A Study of Heat Transfer at the Cavity-Polymer Interface in Microinjection Moulding

The effects of processing conditions, cavity surface roughness and polymer physical properties on the heat transfer coefficient

Maksims BABENKO

Submitted for the Degree of

Doctor of Philosophy

School of Engineering and Informatics

University of Bradford

2015

A Study of Heat Transfer at the Cavity-Polymer Interface in Microinjection Moulding

Maksims Babenko

Abstract

This thesis investigates the cooling behaviour of polymers during the microinjection moulding process. The work included bespoke experimental mould design and manufacturing, material characterisation, infra-red temperature measurements, cooling analysis and cooling prediction using commercial simulation software.

To measure surface temperature of the polymers, compounding of polypropylene and polystyrene with carbon black masterbatch was performed to make materials opaque for the IR camera. The effects of addition of carbon black masterbatch were analysed using differential scanning calorimetry and Fourier transform infrared spectroscopy.

Sapphire windows formed part of the mould wall and allowed thermal measurements using an IR camera. They were laser machined on their inside surfaces to generate a range of finishes and structures. Their topographies were analysed using laser confocal microscope. The surface energy of sapphire windows was measured and compared to typical mould steel, employing a contact angle measurement technique and calculated using Owens-Wendt theory. A heating chamber was designed and manufactured to study spreading of polymer melts on sapphire and steel substrates.

A design of experiments approach was taken to investigate the influence of surface finish and the main processing parameters on polymer cooling during microinjection moulding. Cooling curves were obtained over an area of 1.92 by

1.92 mm of the sapphire window. These experiments were conducted on the Battenfeld Microsystem 50 microinjection moulding machine.

A simulation study of polymer cooling during the microinjection moulding process was performed using Moldflow software. Particular interest was paid to the effect of the values of the interfacial heat transfer coefficient (HTC) on the simulated cooling predictions. Predicted temperature curves were compared to experimentally obtained temperature distributions, to obtain HTC values valid for the material and processing parameters.

Keywords: Heat transfer coefficient, thermal contact resistance, thermal contact conductance, surface roughness, microinjection moulding, polymer, infrared, simulation.

Acknowledgements

It is a pleasure to thank the many people who made this thesis possible.

First I want to thank my supervisors Dr Ben Whiteside and Professor John Sweeney for supporting me during these past four years. Their scientific expertise and high standards in work principles became my personal inspiration for research. I appreciate all their advice, support and encouragement.

My gratitude extends to Ben for believing in me and offering me a great opportunity. It all started with Ben supervising my bachelors dissertation while I was acquiring a degree in civil and structural engineering. After completion he has offered me a summer internship in the centre for micro and nano technology, following by another offer of getting a PhD qualification. It was never my ambition to get a doctoral degree and I have refused when I was asked for the first time. I thank Ben, Cristina Tuinea-Bobe and Keith Norris for believing in me and encouraging me to take this journey. In summary, I would give Ben most of the credit for becoming the kind of scientist I am today.

My sincere gratitude goes to Keith Norris. He was always there and would never say no if someone needed his help, advice or simply a hug. He was heart and soul of the MNT laboratory and I cannot thank him enough for being there when I had my ups and downs.

I would like to thank Fin Caton-Rose and Franco Costa for their expertise, advice and guidance with the Moldflow simulation software.

I would also like to thank Samuel Bigot, Franck Lacan and Petko Petkov from Cardiff University for their contribution to this work with a challenging task of laser machining sapphire windows.

Thanks are also due to the members of staff of the Polymer IRC group led by Professor Phil Coates who have also contributed to my work and time spent at

Bradford. I would like to use this opportunity to express my appreciation to Cristina Tuinea-Bobe, Rob Spares, Gabriela Golzález Castro, John Wyborn, Glen Thompson, Adrian Kelly, Tim Gough, Ken Howell, Ian Smith, Colin Grant and Paul Spencer.

During these four years I have not only gained enormous experience in polymers and micromoulding but also found a true friend. I want to thank Karthik Nair for his continued support and keeping me motivated, especially during writing up stage.

Lastly, I am deeply indebted to my loving family. Their love, care and support throughout life makes me achieve all my goals.

Table of Contents

List of Figures

List of Tables

Nomenclature

A	=	area, (m^2)	*Greek Symbols*		
b	=	Wien's constant = 0.002898 (m · K)	α	=	absorbance
C_p	=	Heat capacity (J/g·C)	γ	=	surface free energy, surface tension, (J/m^2)
g	=	acceleration due to gravity = 9.8 (m/s^2)	γ_c	=	critical surface tension, (J/m^2)
h	=	Plank's constant = 6.6×10^{-34} (J ·s)	γ_L	=	surface tension of liquid, (J/m^2)
h_c	=	thermal contact conductance, conductance through the contact spots, (W/m^2 ·K)	γ_L^D	=	dispersive component of liquid surface tension, (J/m^2)
h_g	=	conductance through the gaps, (W/m^2 ·K)	γ_L^P	=	dispersive component of liquid surface tension, (J/m^2)
h_j	=	joint conductance, (W/m^2 ·K)	γ_{LV}	=	liquid and vapour interfacial tension or surface free energy, (J/m^2)
h_r	=	radiation through the gaps, (W/m^2 ·K)	γ_L^+	=	acid component of liquid surface tension, (J/m^2)
HTC	=	Heat transfer coefficient, (W/m^2 ·C)	γ_L^-	=	base component of liquid surface tension, (J/m^2)
I_{SL}	=	energy of adhesion, (J/m^2)	γ_S	=	solid surface free energy, (J/m^2)
K	=	Boltzmann's constant = 6.6×10^{-23} (J/K)	γ_S^{ab}	=	dispersive component of solid surface free energy, (J/m^2)
Q	=	heat flow, (W)	γ_S^d	=	dispersive component of solid surface free energy, (J/m^2)
Q_{photon}	=	total photon number emittance, ($photons/s/m^2$)	γ_S^h	=	hydrogen bonding component of solid surface free energy, (J/m^2)
$Q_\lambda b$	=	spectral photon emittance, ($photons/s/m^3$)	γ_S^i	=	induction component of solid surface free energy, (J/m^2)
R	=	thermal resistance, (m^2K/W)	γ_S^p	=	polar component of solid surface free energy, (J/m^2)
$R_{t,c}$		thermal contact resistance, (K/W)	γ_{SL}	=	solid and liquid interfacial tension of surface free energy, (J/m^2)
R_1,R_2		R1,R2 = radii of the curvature of the drop	γ_{SV}	=	solid and vapour interfacial tension of surface free energy, (J/m^2)
Sa	=	the arithmetic mean of the absolute height with in a sampling area, (μm)	γ_S^+	=	acid component of solid surface free energy, (J/m^2)
Sq	=	The root mean square value of the ordinates within the sampling area, (μm)	γ_S^-	=	base component of solid surface free energy, (J/m^2)
T	=	Temperature (°C)	ΔP	=	pressure difference, (Pa)
TCR	=	thermal contact resistance, (m^2C/W)	ΔT	=	temperature difference, (K)
T_g	=	glass transition, (°C)	ε	=	emissivity
T_m	=	Melting temperature, (°C)	θ	=	contact angle, (degree)
T_1	=	temperature of the surface 1, (K)	λ	=	wavelength (m)
T_2		temperature of the surface 2, (K)	λ_{max}	=	maximum wavelength (m)
W	=	total radiant emittance (W/m^2)	ρ	=	reflectivity
W_a	=	work of adhesion (J/m^2)	σ	=	Stefan-Boltzmann constant = 5.7×10^{-8} ($W/m^2 \cdot K^4$)
W_c	=	crystallinity	τ	=	transmittance
$W_\lambda b$	=	spectral radiant emittance (W/m^3) =Watts per unit area per unit wavelength			

Chapter 1. Introduction, Aim, Objectives and Thesis outline

1.1 Introduction

Microinjection moulding is a leading technology for manufacturing high volumes of polymer micro components at a relatively low cost. The microinjection moulding is a process where metal mould topography and its features are transferred on to plastic parts. It is a cyclic process where a thermoplastic in the form of granules or powders is placed into a hopper. The mould closes, then from the hopper material is transferred into a heated barrel where material becomes molten and homogeneous. The molten material is then pushed under pressure with the injection plunger into the mould cavity. The holding pressure is then applied for a certain amount of time, to stop material shrinkage. The material freezes after some time, replicating the metal mould features. Once it is cold the mould opens and the final product is ejected from the cavity. Then the same process can start again (Surace et al., 2012).

Polymer microinjection moulding technology was adapted from conventional injection moulding in the late eighties. Microinjection moulding machines normally have 12 to 16 mm screw diameter for melting plastics. The screw size is constrained by the pellet size. A single pellet should not be bigger than the screw channel depth and pitch. A standard pellet size varies between two and five mm in length and width with the mass varying from 11 mg to 40 mg. Figure 1.1 shows a process where polymer pellets are fed into the heated barrel and also examples of polymer pellets that are used for microinjection moulding.

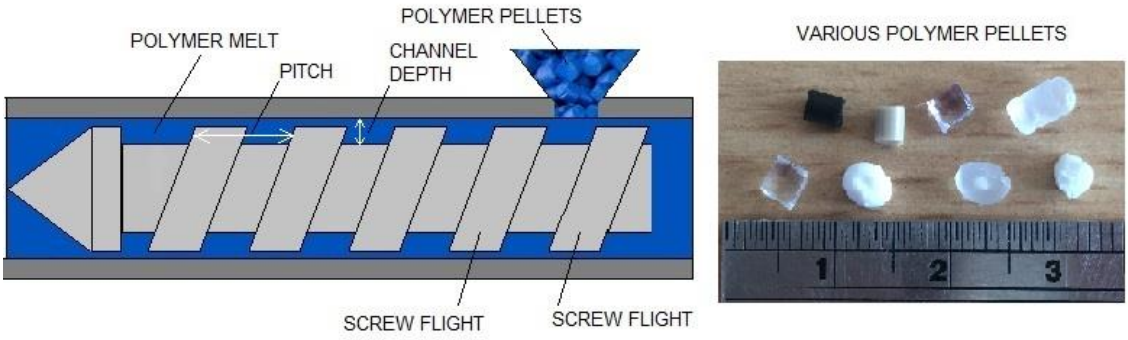

Figure 1.1 Screw in the barrel (left); standard polymer pellets for microinjection moulding (right).

A micro part might require just a few pellets of material, so all the rest of the melted plastic sits in the hot barrel where it can easily degrade. Thermal degradation (molecular deterioration as a result of overheating) of the material affects mechanical and optical properties of the moulded part, as well as flow behaviour of the melt, making traditional injection moulding machines not appropriate for moulding micro components. Moreover, shot size is very difficult to control for making a part which can weigh as little as 0.025 g. Any variation in the process or slight movement of the screw may make the micro part flash or be damaged. In the middle of the nineties new microinjection machines were optimised specially for micromoulded parts production (Piotter et al., 2002).

1.2 What is a Micro Part?

A micrometer (µm) or a micron is a metric unit of length which is equal to one millionth of a meter. Human hair from the head can be around 40 to 120 micrometers in diameter and a healthy human red blood cell is about 7.2 µm. (Blume-Paytavi et al., 2008; Khurana, 2008). Figure 1.2 shows a micro filter for medical industry and micromechanical locking lever made of Polyoxymethylene (POM).

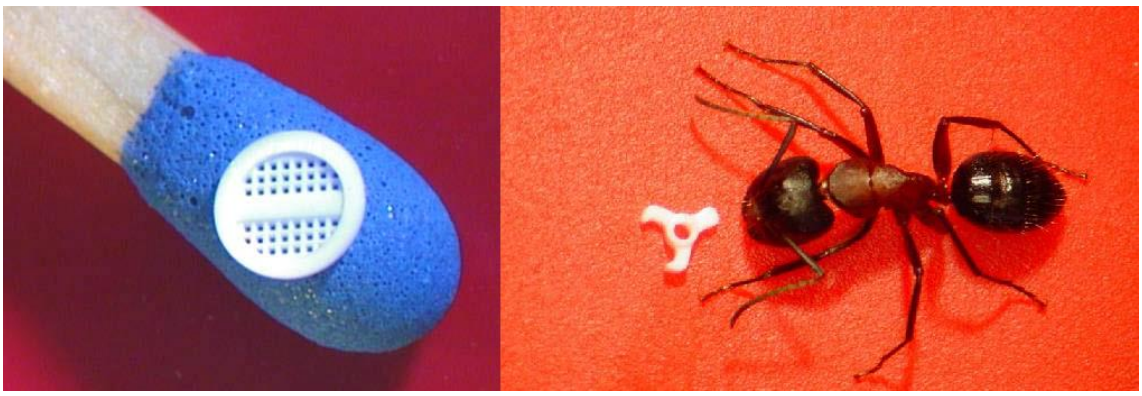

Figure 1.2 (Left) Micro filter with 80 µm mesh size, Part Volume 0.63 cubic mm. (Right) Locking lever, Part Volume 0.70 mm^3 (Battenfeld, no date).

Micro parts can be categorised into 3 groups:

- The final product has a very low mass, less than 1 g.
- The part that is identical to the conventional moulded part, but it has regions or features on the surface in the micrometer range.
- The part where dimensions are irrelevant, but tolerances are in the micrometer range (Whiteside et al., 2003).

1.3 Market and Applications

There is a wide range of applications where polymers are used such as medical, automotive, optics, telecommunications and micromechanics, which shows the significance of microinjection moulding. Some examples of micro injection moulded components are presented in Table 1.1.

A significant development has been achieved in micro fluidics. Micro syringe pumps have been designed which can allow flow rates of 1 - 10,000 nanoliters per second. The MicroFlow system developed by the Micronics company can extract molecules and hormones directly from complex fluids such as blood, urine or saliva. Polymer micro injection moulding is one of the most suitable processes for manufacturing low-cost, disposable micro fluidic devices (Micronics.net, 2012).

A huge demand for micro polymer parts comes from the medical industry. There are already available on the market hearing aid implants, catheter components, heart valve components, micro components for drug delivery system and wound closure devices. Expertise in micro moulding helped a US based high-technology company to develop a device for replacement of metal staples and sutures, which surgeons use after major invasive surgery (Sovrin.com, 2011a). Staples were made of bioabsorable polylactide/polyglycolide copolymer (see Figure 1.3), meaning that after the patients recovery there is no need of further surgical intervention in order to remove staples. Another benefit of bioabsorable copolymer staples is that there is no requirement for special skills to apply them, whereas a suturing procedure requires special training and skills development (Mtdmicromolding.com, 2012; Sovrin.com, 2011a).

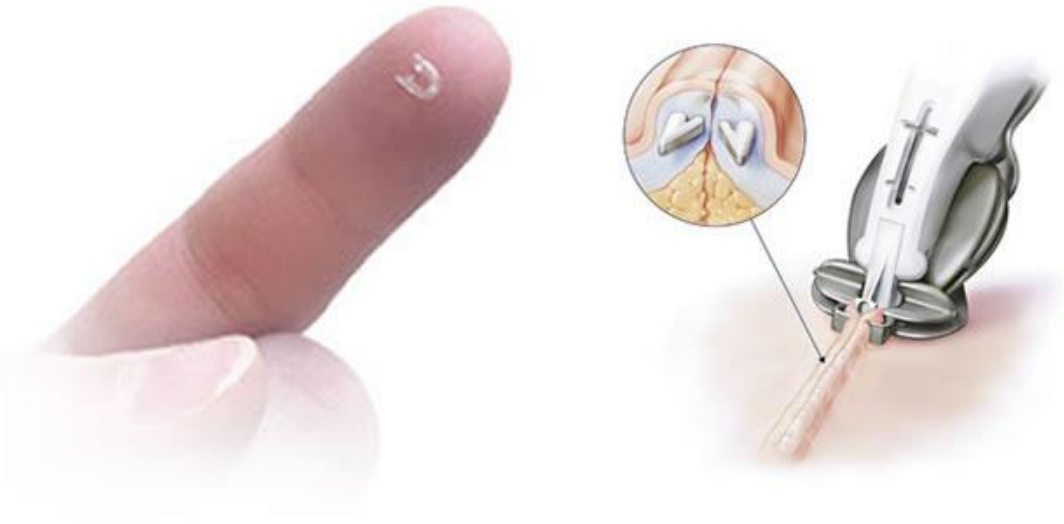

Figure 1.3 Wound closure device (Sovrin.com, 2011b).

Table 1.1 Micro components fields and applications (Surace et. al., 2012; Battenfeld, no date).

Application fields	Examples
Telecommunication, computers	Mobile phones components, fibre optics connectors, head of an ink-jet printer
Automotive	Micro switches, connectors, sensors, ABS-systems
Medical	Micro filter for acoustics, hearing aid, drug delivery systems, implants, catheter components, surgical components, diagnostic devices, wound closure device, micro needles, syringes
Optics	Lenses, displays, light collection devices
Watches	Gear wheels, latches, micro transmissions
Micromechanics	Micro engines, rotators, locking levers, micro switches, catch wheels for micro switches, operating pins
Electronic	Micro parts, circuit boards

1.4 Simulation

The first injection moulding machine was patented by John and his brother Isaiah Hyatt in 1872. Their machine used a plunger to inject plastic through a heated cylinder into a mould. This moulding process continued to be unchanged until 1946, when James Hendry built the first screw injection moulding machine. (Johannaber, 2007). Researchers and engineers noticed that product quality was related to processing conditions. Very often a problem would be discovered during production, resulting in expensive and time consuming mould re-engineering. For that reason simulation of moulding was developed. The major advantage of simulation is that it can help to avoid problems during design stage, saving money and time in production stage. Simulation allows the

moulded part to be analysed, predicting possible defects and optimising the design (Costa et al., 2009).

In 1978, in Australia a company named Moldflow was formed by Colin Austin. It was the first company that focused on injection moulding simulations. Plastic injection moulding software helps manufacturers to predict, optimise and verify the design of plastic products. Software includes finite-element analysis (FEA) tools to simulate various processes in injection moulding, namely:

1) Flow simulation of the melted polymer which can predict potential defects such as weld lines, trapped air and sink marks.

2) Cooling simulation, which includes cooling system modelling and analysis. It helps to predict plastic part warpage, optimising part cooling and minimising cycle time.

3) Shrinkage and warpage simulation helps to control part deformation. It predicts shrinkage and warpage based on process parameters.

4) Fibre orientation simulation, predicting numerically three-dimensional fibre orientation during the mould filling stage.

Other tools include thermoplastic filling, gate location, runner balancing, insert overmoulding, reactive injection moulding, gas-assisted injection moulding and co-injection moulding (Autodesk, 2012a).

1.5 Heat Transfer in Injection Moulding

Injection moulding is a cyclic process that consists of a sequence of phases which includes filling (injection), packing, cooling, solidification, mould opening, part ejection and mould closing. Heat transfer occurs during various phases in the injection moulding cycle. Firstly, when polymer pellets are fed into the heated barrel, melted and injected into the cavity, convection in the melt is the major heat transfer mechanism. During solidification and packing, heat is

removed from the melted polymer by the way of conduction through the mould walls. The thickness of the frozen layer of material will continue to grow from the cavity wall to the centre of the part, demonstrated in Figure 1.4 (Kamal et al., 2009). The cooling phase is of particular interest, because the rate of cooling can have a significant influence on the flow characteristics, morphology and resulting physical properties. These effects are notably relevant to thin components and components with microscale features, where the surface area to volume ratio is high.

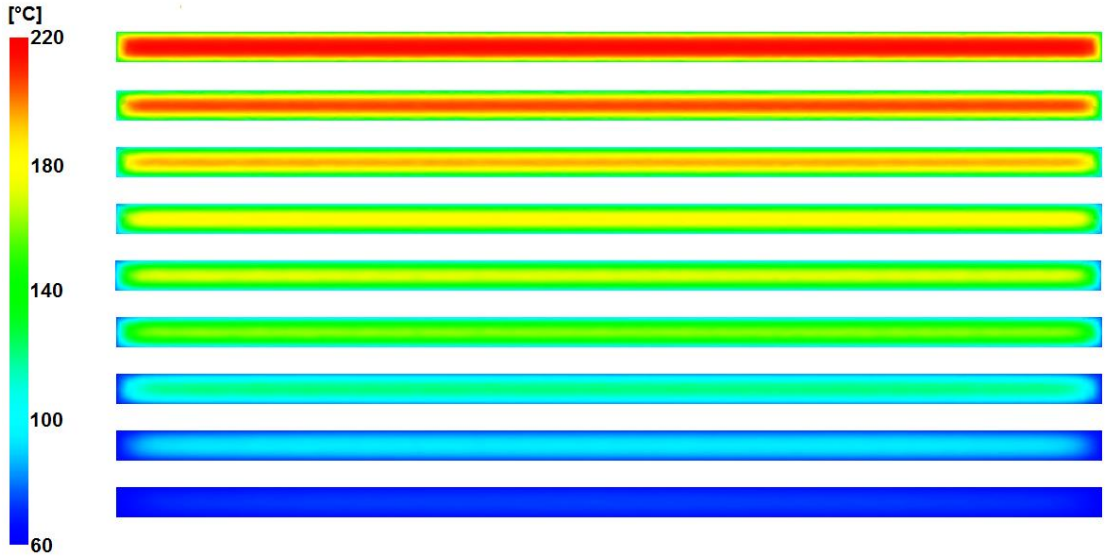

Figure 1.4 Cooling through the part thickness.

Heat transfer between the tool and molten polymer in contact is affected by the area of the contacting surfaces, the temperature of the polymer and steel, the pressure applied and the surface roughness. Surface topography of the mould can be readily measured and can be assumed to be constant during a moulding operation. Temperature can be monitored by thermocouples imbedded in the tool or by using IR technology and pressure can be monitored with the help of pressure sensors. Heat transfer between two contacting surfaces is governed by thermal contact resistance (TCR) or thermal contact conductance (TCC), which is the inverse of TCR. Commercially available

simulation software products use the term heat transfer coefficient (HTC) to describe heat transfer at the polymer-mould interface, which is the same as TCC.

1.6 Thermal Contact Resistance (TCR)

Thermal contact resistance (R) is a resistance to the heat flow (Q) between two bodies in contact and can be defined as:

$$R = \frac{A\Delta T}{Q} \qquad (m^2K/W) \tag{1.1}$$

where A is the area, ΔT is the temperature difference at the interface, and Q the heat flow (Madhusudana, 1996).

Thermal contact conductance (h_c) is defined by Madhusudana (1996) as "the ratio of the heat flux (Q/A) to the additional temperature drop (ΔT) due to the presence of the (imperfect) joint".

$$h_c = Q/A\Delta T \qquad (W/m^2 \cdot K) \tag{1.2}$$

1.7 Flow of the Heat Between Two Bodies in Contact

It is know that every practical solid surface has irregularities, which can be macroscopic or microscopic in size. The existence of these macroscopic and microscopic irregularities is due to surface roughness effects. When two solid surfaces are pressed together only a small part of nominal surface is actually in contact. Research on solid metal-to-metal surface contacts have shown that only a small proportion, approximately 1 – 2% of the apparent surface area is making a real contact. (Madhusudana, 1996; Bowden and Tabor, 1950).

Heat flow through the interface of contacting surfaces can be split into three forms (see Figure 1.5):

- Conduction through the contact spots.

- Conduction through the microscopic or macroscopic voids between the actual contact spots which can be filled with different conducting substances such as air, other gases, foils, wire screens, coatings and greases.

- Radiation across the gaps, which can be ignored if temperature at the interface is lower than 700 K (426.85 ^{o}C). (Bahrami et al., 2006). This can be expressed as:

$$h_j = h_c + h_g + h_r \quad \text{1.3}$$

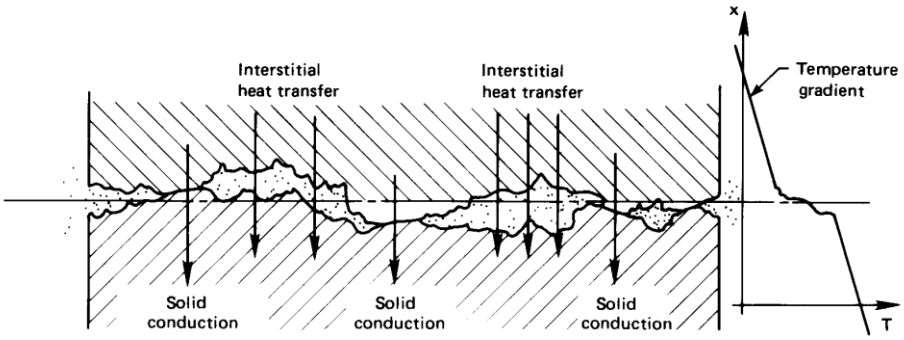

Figure 1.4 Heat transfer between two solid surfaces (Lienhard and Lienhard, 2002).

The thermal resistance of mechanically joined materials has been studied largely because of its remarkable importance in a wide range of engineering applications. The TCR depends on the spacing of surface irregularities and surface deviations as shown in Figure 1.6.

More closely spaced peaks and valleys represent roughness of the surface. Normally roughness is produced by machining processes. These closely spaced irregularities may be cutting tool marks, electrical discharge machine marks, scratches produced by grinding wheels or polishing pads. The waviness (widely spaced irregularities) can be produced by instabilities, deflections or vibrations in the machines. Surface quality or surface texture is mainly defined in terms of roughness. Waviness can be an important problem in

some applications, but roughness is of major interest to engineers (Vorburger and Raja, 1990).

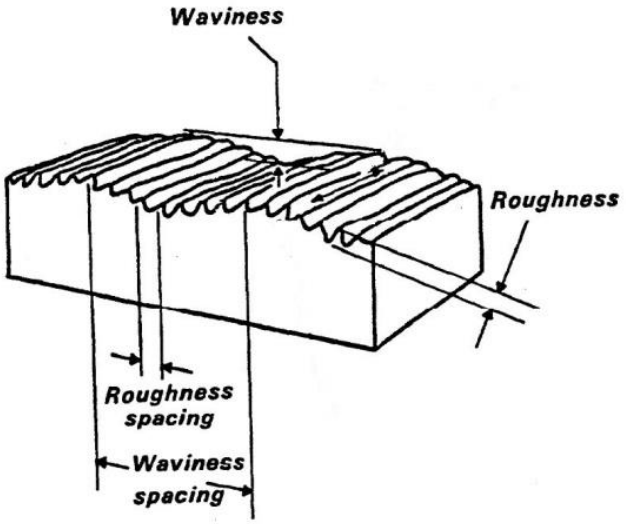

Figure 1.5 Surface characteristics (Vorburger and Raja, 1990).

Generally TCR depends on surface topography, thermal conductivity of two contacting objects, thermal conductance of interstitial gas or liquid, contact pressure and the type of heat transfer (Sridhar, 1999). There are several applications where TCR needs to be maximised. An example is the thermal isolation of spacecraft components. In a vacuum, conduction through the solids is the main mechanism of heat transfer and so a good knowledge of materials with low TCR is essential for keeping temperatures low. Good insulation with high TCR is required for storage and transportation of cryogenic fluids (Snaith et al. 1986). However, the majority of applications require TCR to be minimised, when heat needs to be removed quickly. Such applications include:

1) heat exchangers

2) the interface between fuel and container in a nuclear power reactor

3) the joints of an aircraft which are subjected to aerodynamic heating

4) the interface between gas turbine blades and rotor

5) manufacturing systems such as rolling, forging, extrusion, injection and micro injection moulding which is the area of interest of the present research (Madhusudana, 1996).

1.8 Aim and Objectives

The principal aim of this thesis is to conduct an experimental and parametric study of heat transfer at the cavity-polymer interface in microinjection moulding in order to better understand cooling phenomena of the process and compare it with predictions of commercially available simulation software. To achieve the aim of the research the following objectives were set:

- To prepare and analyse materials to be used in this work. This includes: laser machining of sapphire windows to generate different surface topographies; compounding polymers with carbon black masterbatch to make them IR opaque and analyse the effects of carbon black masterbatch on their thermal properties; analysing surface energy of sapphire and typical mould steel.
- To experimentally obtain cooling curves of selected polymers during microinjection moulding cycles using a high speed infrared camera, employing a special mould where one half of the cavity is represented with a sapphire window.
- To perform a detailed analysis of the polymer cooling. This includes an assessment of the influence of different surface finishes and process parameters such as melt temperature, mould temperature, injection speed and packing pressure.
- To perform cooling simulations using commercially available software and assess the cooling predictions. A particular emphasis is to be paid on heat

transfer coefficient (HTC) values which are used to model the heat flux across the polymer-mould interface.

1.9 Thesis Outline

The following summarises the content of this thesis:

Chapter 2: Microinjection moulding background

This chapter presents the technology of polymer microinjection moulding and limitation of conventional injection moulding machines to produce micro components. The following sections of the chapter include temperature and pressure monitoring techniques for micro moulded part quality.

Chapter 3: Thermal imaging background

This chapter details the thermal imaging technology for polymer temperature measurements. It includes the discussion of main components of the high speed infrared camera and the most significant parameters which need to be considered for surface temperature measurements of polymers during the microinjection moulding.

Chapter 4: Literature review

This chapter presents a review of the literature regarding the thermal contact resistance. The aim of this chapter is to identify the gaps in knowledge of thermal behaviour at the interface between polymer and steel in microinjection moulding.

Chapter 5: Materials and characterisation

This chapter presents materials preparation and characterisation for the experimental study. This includes sapphire windows laser

machining and topography measurements, polymers compounding with carbon black masterbatch with further analysis of their thermal and optical properties. Also energy measurements of the sapphire and steel surfaces and determination of the rate of spreading of polymers on these surfaces.

Chapter 6: Polymer Cooling experimental study

This chapter presents mould design for measuring surface temperature of polymers during the microinjection moulding cycle. It includes visualisation system description and its calibration for the accurate temperature measurements. The work in this chapter is focused on the cooling curves obtained with different surface finishes and different processing parameters. The effect of these factors on polymer cooling has been evaluated using the design of experiments (DOE) approach.

Chapter 7: Simulation of the microinjection moulding

This chapter focuses on the Moldflow cooling analysis of the part surface temperature. Cooling curves predicted with different HTC values were evaluated by comparison with experimentally obtained cooling profiles.

Chapter 8: Conclusions and recommendations

This chapter reports the results from each of the investigations and main research findings. Also, it puts forward some of the future work to be undertaken based on the obtained results and observations.

Chapter 2. Microinjection Moulding Background

2.1 Microinjection Moulding Technology

In the late eighties microinjection moulding was developed from conventional injection moulding (Piotter et al. 2002; Scholz, 2011). At the time it was very difficult to produce parts that would be less than a millimetre in dimension with the mass of a few milligrams using conventional injection moulding machines. The main issues were arising from polymer degradation, shot volume accuracy and lack of high repeatability of the shot size. Moreover, conventional injection moulding machines were typically controlled using hydraulic power which was not accurate enough for manufacturing parts with micro features. A small variation of the shot size could be critical for the replication of polymer micro parts because the parts would flash or become damaged (Scholz, 2011).

Standard systems for injection moulding can also be called a single step systems (see Figure 2.1), because plasticising, metering, and injection happens in the same barrel. Taking into account that typical screw diameter ranges from 16 to 32 mm it is very difficult to control small shot size. A single step system with 14 mm screw diameter would require 0.0056 mm stroke to produce a shot weight of 1 mg. This example clearly shows that conventional injection moulding system is not ideal for micro parts production. Reduction of the screw diameter is limited mainly by the size of the conventional polymer granule which needs to fit into the screw channel. Also, the shaft cross section of the screw has to withstand considerably high torsion moment. Further reduction of the screw diameter would create very high load on the shaft cross section. (Scholz, 2011; Whiteside et al., 2006; Battenfeld no date; Piotter et al., 2009).

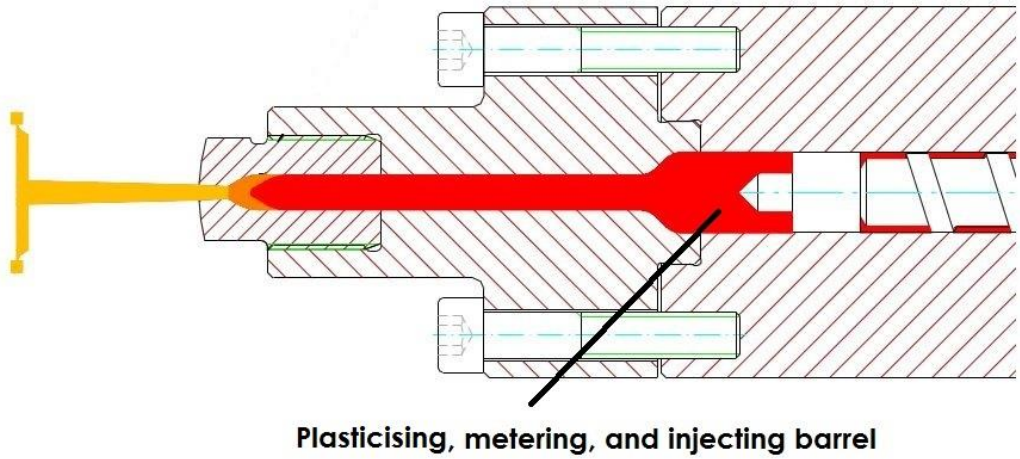

Figure 2.1 Single step system, standard technology (Battenfeld, no date).

A three step system (Figure 2.2) was designed by Battenfeld and partners to overcome the issue of the shot size. The process of shot preparation was divided into three separate stages, namely, plasticising, metering, and injection. The system was implemented into the Microsystem 50 microinjection moulding machine, that was designed and optimised for part weights below 100 mg (Battenfeld, no date).

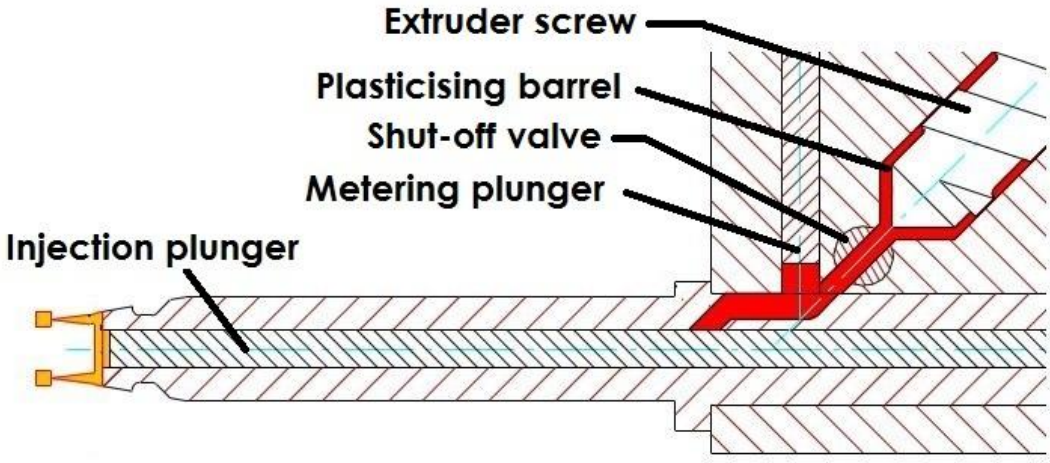

Figure 2.2 Three step system (Battenfeld, no date).

The process of shot preparation in the three step system can be divided into the following process steps:

1. Polymer pellets are plasticised by the 14 mm diameter extrusion screw, which is mounted at an angle of 45° to the injection axis.

2. Melt is extruded into a metering chamber, where a servo-driven plunger meters a dose of material. The servo-driven plunger can prepare a shot of material with the maximum volume of 1100 mm^3 in 0.01 mm^3 increments.

3. The rotating shut-off valve closes to stop material flowing back from the metering chamber.

4. A predefined volume of polymer in the metering chamber is then delivered into the injection chamber.

5. Polymer melt is injected into the cavity with the second servo-driven injection plunger with the maximum velocity of 1000 mm/s (Scholz, 2011; Whiteside et al., 2006).

In microinjection moulding highly accurate tool movements have to be ensured for the screw movement, metering piston, injection plunger, and clamping device. High alignment tolerances of less than 10 µm are required for the movement of the clamping plates and for the linear and rotational precision movements, which cannot be delivered by conventional servo hydraulic systems. Therefore, high precision servo electric drives, positional feedback systems, and advanced software are normally used to guarantee high precision movements (Whiteside et al. 2006; Piotter et al. 2009; Scholz 2011). At the University of Bradford four injection moulding machines were compared experimentally to determine factors affecting part quality and repeatability. Two of the injection machines were servo hydraulic and the other two servo electric. Researchers reported that servo electric machines show better screw

positioning control, comparing to servo hydraulic. Moreover, energy consumption of servo electric machines was reported to be 3.6 times less than of servo hydraulic machines (Kelly et al., 2005).

A variety of microinjection moulding machines are available on the market. A number of machines with their specifications is presented in Table 2.1.

Table 2.1 Commercially available micro injection machines (Scholz, 2011).

Manufacturer	Model	Clamping Force [kN]	Injection Pressure [bar]	Injection Volume [mm³]	Diameter Screw or piston [mm]	Injection Speed [mm/s]
Lawton	Sesame Nanomolder	13.6	3500	0.082	10	1200
APM	SM-5EJ	50	2450	1	14	800
Battenfeld	Microsystem 50	56	2500	1.1	14	760
Nissei	AU3	30	-	3.1	14	-
Babyplast	Babyplast 6/10	62.5	2650	4	10	-
Sodick	TR05EH	49	1970	4.5	14	300
Rondoll	High Force 5	50	1600	4.5	20	-
Boy	12/AM 129-11	129	2450	4.5	12	-
Toshiba	EC5-01.A	50	2000	6	14	150
Fanuc	Roboshot S2000-I 5A	50	2000	6	14	300
Sumimoto	SE7M	69	1960	6.2	14	300
Milacron	Si-B17 A	147	2452	6.2	14	-
MCP	12/90 HSE	90	1728	7	16	100
Nissei	EP5 Real Mini	49	1960	8	16	250
Toshiba	NP7	69	2270	10	16	180
Desma	Formica Plat 1K	10	3000	150	6	500
Wittmann Battenfeld	MicroPower 15	150	2500	3	14	750

The commercially available microinjection moulding machine Battenfeld Microsystem 50 meets all the requirements for production of micro polymer parts.

Table 2.2 Technical characteristics of Battenfeld Microsystem 50 (Battenfeld, 2003).

Injection drive unit specifications		Clamping unit specifications	
Extruder screw diameter	14 mm	Maximum clamping force	50 kN
Maximum screw torque	75 Nm	Maximum opening force	50 kN
Maximum screw speed	300 rpm	Maximum clamping / opening speed	140 mm/s
Injection piston diameter	5 mm	Maximum mould size	150 mm x 196 mm x (100-200 mm)
Maximum calculated shot volume	1100 mm^3	maximum ejector stroke	30 mm
Injection pressure limitation	2500 bar	Maximum ejector force	0.5 kN
Maximum injection speed	760 mm/s	Recommended ejector force	0.1-0.2 kN

2.2 Materials for Microinjection Moulding

Materials used for microinjection moulding must have good processibility, good mechanical and optical properties, where little importance can be given to the aesthetics. The majority of polymers used in micro injection moulding are thermoplastics. Viscosity of the melt is one of the most important requirements. It has to be low enough at high shear rates, to allow polymer melt to fill micro cavities. Therefore, typical materials used in micromoulding are poly methyl methacrylate (PMMA), polycarbonates (PC), polyethylenes (PE), polypropylene (PP), polystyrene (PS), polysulfones (PSU), polybutylene terephthalates (PBT), polyoxymethylenes (POM), polyamides (PA), polyaryletheretherketones (PEEK), and liquid crystal polymers (LCP). To improve mechanical properties thermoplastic materials can be filled with powders, minerals, and additives.

These materials are also used in conventional injection moulding and some of them are commercially available at relatively low costs (Piotter et al., 2009; Whiteside et al., 2006; Scholz, 2011; Coates et al., 2006). In this research two materials commonly used in injection moulding, polypropylene and polystyrene were used to conduct the experimental work.

2.3 Process Monitoring

Process monitoring is very important for quality assurance and process evaluation (Coates et al., 2006). Numerous research studies have shown that the polymer melt temperature and cavity pressure have great influence on the filling process and the quality of the injection moulded parts (Chen and Turng, 2005). Accurate measurements of cavity pressure and melt temperature are required for the research proposed. Whiteside et al. (2003) installed multiple sensors on the Microsystem 50 machine to measure injection pressure, cavity pressure, displacement and velocity of the injection pin, and mould temperature. All the data was recorded and saved using National Instruments CA-1000 series/DAQcard E-Series hardware and LabView software. Researchers have shown that process conditions significantly affect mechanical properties on the micromoulded parts, thus process monitoring is a very useful tool for quality control. Zhao et al. (2003) also performed a study on process monitoring in micromoulding, using a Battenfeld Microsystem 50 for the experimental work, with a force transducer mounted at the back of the injection plunger to measure injection force. Zhao et al. (2003) reported that measured injection pressure correlates with micro moulded part quality.

2.3.1 Pressure Measurements

Pressure sensors convert input pressures to electrical outputs to measure pressure. Piezoelectric pressure sensors are widely used in laboratories, with the main applications in combustion engines, ballistics and injection moulding. A great advantage of piezoelectric sensors is that they do not require any power supply. It was found that some crystalline materials such as quartz, tourmaline, crystals of the CGG (calcium-gallium-germanate) group, gallium orthophosphate, PZT-based (lead zirconate titanate) piezoceramics and Lead-Metaniobate generate an electrical polarization when subjected to a mechanical load. Piezoelectric materials properties are summarised in Table 2.3. The direct piezoelectric effect is when mechanical load or deformation of the crystal generates a proportional charge or electrical potential. The converse piezoelectric effect can be defined as an application of an electrical field to the crystal, where it induces a mechanical deformation proportional to the field (Sommer and Engeler, 2005).

Table 2.3 Piezoelectric materials summary (Sommer and Engeler, 2005).

Material	Working temperature	Advantages	Disadvantages
Quartz	Up to 400° C	- outstanding electrical insulation properties -minimal sensitivity deviation up to 350° C - not pyroelectric - available at low cost	- relatively low sensitivity - tendency to twin under high loads
Tourmaline	Up to 600° C	- higher temperature range than quartz	- lower sensitivity than quartz - pyroelectric -available on as natural crystal
Crystals of CGG group	-	- not pyroelectric - higher sensitivity than quartz - properties remain stable at very high temperatures - no twinning	- growth of crystals is more difficult that for quartz

Gallium	Up to 600° C	- sensitivity is twice that of quartz, which is contact up to 500° C	- very difficult to grow - not available as large crystals
PZT-based piezoceramics and Lead-Metaniobate	-	- very high piezoelectric sensitivity, up to 100 times that of quartz	- aging crystals -poor linearity - highly pyroelectric
High temperature piezoceramics	Up to 600° C	- sensitivity up to 5 - 10 times higher that of quartz	- aging crystals -poor linearity - highly pyroelectric

2.3.1.1 Basic Pressure Sensor

Basic design of a pressure sensor (see Figure 2.3) consists of sensor housing, preload sleeve, diaphragm, connector, spacer ring and the most important - the piezoelectric crystal.

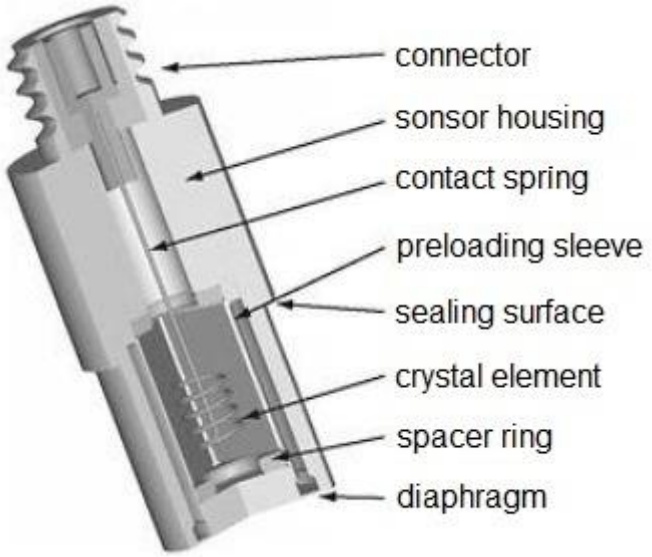

Figure 2.3 Basic design of a pressure sensor (Sommer and Engeler, 2005).

The sensor housing protects the piezoelectric element, serves as an electrical shield, and provides a means of mounting. The preload sleeve guarantees a good linearity and sensitivity stability of the sensor, but not all sensors use preload sleeve. The diaphragm is the most important part of the sensor, because it converts the pressure into a proportional force acting on the

element. A piezoelectric crystal element can have different shape and size, which normally depends on sensor design and application (Sommer and Engeler, 2005).

2.3.2 Cavity Pressure in Injection Moulding

The pressure in the cavity of the mould during the injection moulding process is the vital parameter. It can be used to provide a quality index of the part and to improve control of the injection moulding process. Special pressure sensors were developed for injection moulding processes. These sensors do not have a diaphragm. When polymer melt enters the cavity it freezes by touching the relatively colder cavity wall. This frozen skin layer acts as the diaphragm (Sommer and Engeler, 2005; Gautschi, 2002).

Piezoelectric cavity pressure sensors were compared online from such manufacturers as Kistler, Dynisco, RJG, and Priamus. With Kistler and Priamus providing the smallest piezoelectric cavity pressure sensors with the front diameter of the sensor being one millimetre. The Kistler cavity sensor has an advantage over Priamus, as it can simultaneously measure mould cavity pressure up to 200 MPa and temperature of the melt. Both cavity sensors are compared in Figure 2.4.

Kistler's cavity pressure and temperature sensor has a front diameter of one millimetre. The pressure acts over the entire front of the sensor and is transmitted to the crystal element, which generates a proportional small electric charge measured in Picocoloumb (pC). Obtained electrical charge is converted into a voltage 0 ... 10 V using a charge amplifier and is then available as an amplified output. The melt contact temperature is measured with an integrated K type (NiCr-Ni) thermocouple, which is located at the front of the sensor. Its technical characteristics makes Kistler's cavity pressure and temperature

sensor very useful in the analysis of the part quality and process control of microinjection moulding (Kistler, 2011a).

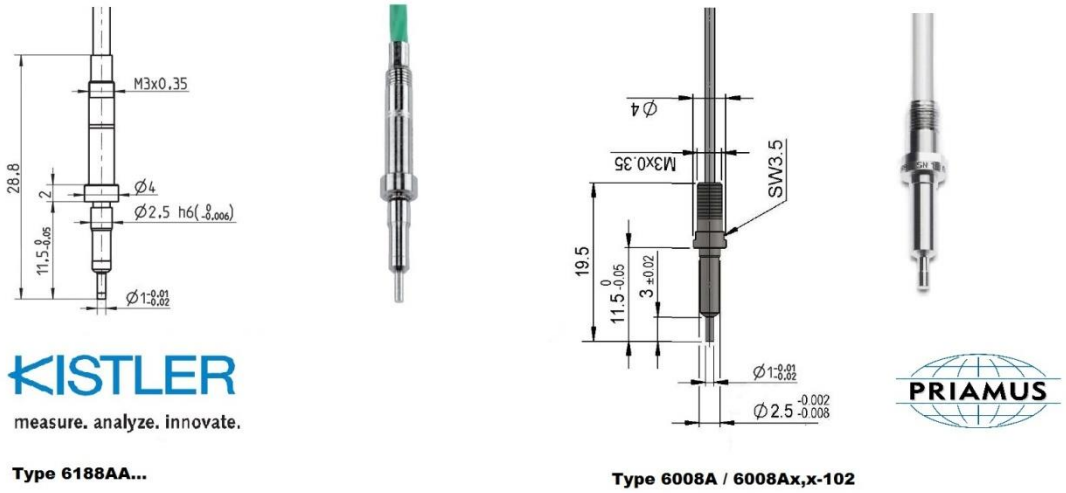

Technical Data	Kistler 6188AA	Priamus 6008A
Range	0...2000 bar	0...2000 bar
Overload	2500 bar	2500 bar
Sensitivity	≈-4.8 pC/bar	2.1 pC/bar
Deviation of linearity	≤ ± 1 %	≤ ± 1 %
Maximum mould temperature	200 °C	200 °C
Maximum melt temperature at the front of the sensor	< 450 °C	< 500 °C

Figure 2.4 Kistler cavity sensor (left) and Priamus cavity sensor (right) (Kistler, 2011a; Priamus, 2013).

2.3.3 Temperature Measurements

There are two commonly used methods to measure temperature of the melt. The first method includes a temperature sensor, such as thermocouple flush mounted in the cavity. The second method is based on the theory of electromagnetic radiation. Every body above the temperature of absolute zero emits infrared radiation (IR). Infrared sensors do not need to be in contact with the object, are highly sensitive and have fast response times, thus they are an

attractive method for measuring cavity or melt temperatures (Manero, 1996; Dininger, 1994).

2.3.3.1 Thermocouples

There are a variety of temperature sensors available on the market, but the thermocouple remains the most commonly used sensor for temperature measurements (Reed, 1999). In the injection moulding process monitoring, resistant temperature detectors (RTDs), thermocouples and thermistors can be used. RTDs are the most accurate (0.1 to 1°C) and stable, but they are very expensive, require electrical input to function, have slow response time (1 to 50 seconds), and are relatively large in size. Thermistors, because of the materials used, have limited operating temperature range. As with RTDs they also require electrical input to function. Normally narrow temperature ranges are measured, because of the nonlinearity, however they have fast response time (0.12 to 10 seconds), are cheaper than RTDs and have good accuracy of 0.05 to 1.5 °C. Thermocouples remain the most commonly used in injection moulding. They are small in size with fast response time of 0.10 to 10 seconds, cheap to produce, have the widest temperature range, and do not require electrical input. However they must be protected from corrosive environments, smaller wire sizes are less stable and have shorter life span, reference junction compensation is required, and they are less stable than RTDs (Fontes, 2005; Rosato et al. 2000; Measurement Specialties, 2003).

Thermocouples consist of two electrical conductors of dissimilar metals or alloys joined at one end of the circuit. The thermocouples are often represented as only one pair of dissimilar conductors joined by two junctions. One junction is the measuring junction, the other, is the reference junction. The measuring junction is in contact with an object of a certain temperature, where as the

reference junction is maintained at 0 °C or at the electronically compensated meter interface. When the junctions are exposed to different temperatures, a current will flow in the wires proportional to their temperature difference. By knowing the type of thermocouple used, the value of millivolt potential and the temperature of the reference junction temperature at the measurement junction can be determined (Fontes, 2005).

Comparing to all temperature sensors technologies thermocouples have the widest temperature range of - 200 to +2315 °C. Various types of thermocouples and their applications are compared in Table 2.5.

Table 2.4 Thermocouples characteristics (ASTM Committee E20 on temperature measurement, 1993; Reed, 1999; Fontes, 2005; Fraden, 2010).

Type	Alloy combinations	Recommended temperature range (°C)	International colour code To IEC 60584.3:2007 BS EN 60584.3:2008	Application
E	Nickel-Chromium (+) / Copper-Nickel (-)	- 200 to 900	Purple	Can be used in oxidising or inert atmospheres. Not subjected to corrosion, so can be used in high-moisture environments.
J	Iron (+) / Copper-Nickel (-)	0 to 760	Black	Can be used in vacuum, reducing or inert atmospheres, oxidising atmospheres with reduced life. Iron oxidises rapidly above 538 °C

K	Nickel-Chromium (+) / Nickel-Aluminium (-)	- 200 to 1260	Green	Recommended for use in oxidising, neutral or completely inert atmospheres. Should not be used in vacuum, reducing or sulphurous atmospheres.
T	Copper (+) / Copper-Nickel (-)	- 200 to 370	Brown	Can be used in oxidising, reducing, inert atmospheres as well as vacuum. Resistant to corrosion in high moisture conditions.
R and S	Platinum-Rhodium (+) / Platinum (-)	0 to 1480	Orange	High resistance to oxidation and corrosion. Must be protected in non-metallic tube and ceramic insulators.

Chapter 3. Thermal Imaging Background

Thermal imaging or thermography is the detection of the radiation emitted by an object as a function of its temperature. All objects above absolute zero (- 273.15 °C) emit electromagnetic radiation (Stemmer Imaging GmbH, 2010; Runciman, 1999).

3.1 The Electromagnetic Spectrum

Electromagnetic radiation is the transmission of energy at the speed of light (3 x 10^8 m/s) in the form of electric and magnetic fields, often referred as to electromagnetic waves. Electromagnetic radiation can be classified by wavelength or frequency into radio, microwaves, infrared, visible light, ultraviolet, X-rays, and gamma rays forming a frequency spectrum. Wavelength is related to the frequency (f) by $\lambda = c/f$, where c is the speed of light. The electromagnetic spectrum is shown in Figure 3.1. Low frequency corresponds to long wavelength and low energy, whereas high frequency corresponds to short wavelength and high energy. At the lower end of the frequency spectrum are radio and micro waves with the frequencies between 10^4 and 10^8 Hz (Hertz). The infrared waves refer to a broad range of frequencies from 3 ^{x} 10^{11} to 4.3 $^x10^{14}$ Hz. Below the visible region are ultraviolet waves with the frequencies between 7.5 x 10^{14} and 3 x 10^{16} Hz. Very high in frequency are X-rays. X-rays are in the range of 3 x 10^{16} and 3 x 10^{19} Hz. Gamma rays are ultra high frequency typically above 10^{20} Hz (AGA infrared systems AB, 1984).

3.2 The Infrared Spectrum

Every object above the temperature of absolute zero emits infrared energy. As the temperature increases the amount of emitted energy increases.

The infrared spectrum can be divided into three regions, namely, near infrared (NIR) or short wave infrared (SWIR) with the approximate wavelength between 0.7 and 1.9 µm, mid infrared (MIR) or mid wave infrared (MWIR) with approximate wavelength of 2 to 5 µm, and long infrared (LIR) or long wave infrared (LWIR) with the wavelength approximately 7 to 14 µm (Kaplan, 2007).

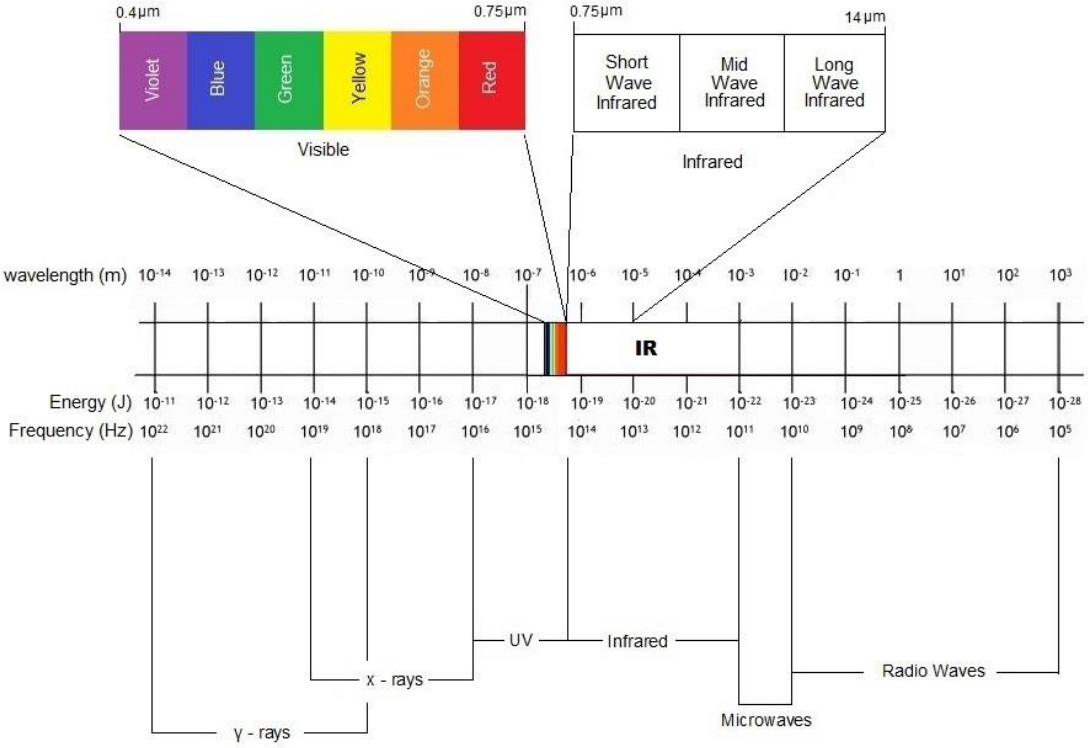

Figure 3.1 Electromagnetic spectrum.

3.3 Surface Thermal IR Radiation

Max Planck derived the law that described the electromagnetic radiation emitted by a black body at a defined temperature over the entire wavelength spectrum. The spectral radiance is measured in terms of power emitted per solid angle, per unit are of the body, per wavelength. Plank's law illustrates that radiance always increases with temperature, and shifts to shorter wavelengths when temperature increases, which is shown in Figure 3.2. The following equation expresses the energy emitted, in terms of wavelength and the temperature.

$$W_\lambda b = \frac{2\,\pi\,h\,c^2}{\lambda^5\left(e^{\frac{hc}{K\lambda T}}-1\right)} \qquad \textbf{3.1}$$

where $W_\lambda b$ is the rate at which a black surface emits radiant energy, h is Planck's constant (6.6×10^{-34} J·s), c is the speed of light (3×10^8 m/s), λ is the wavelength in metres, e is the exponential constant (2.71828), K is Bolzmann's constant (1.4×10^{-23} J/K) and T is the absolute temperature of the blackbody (K).

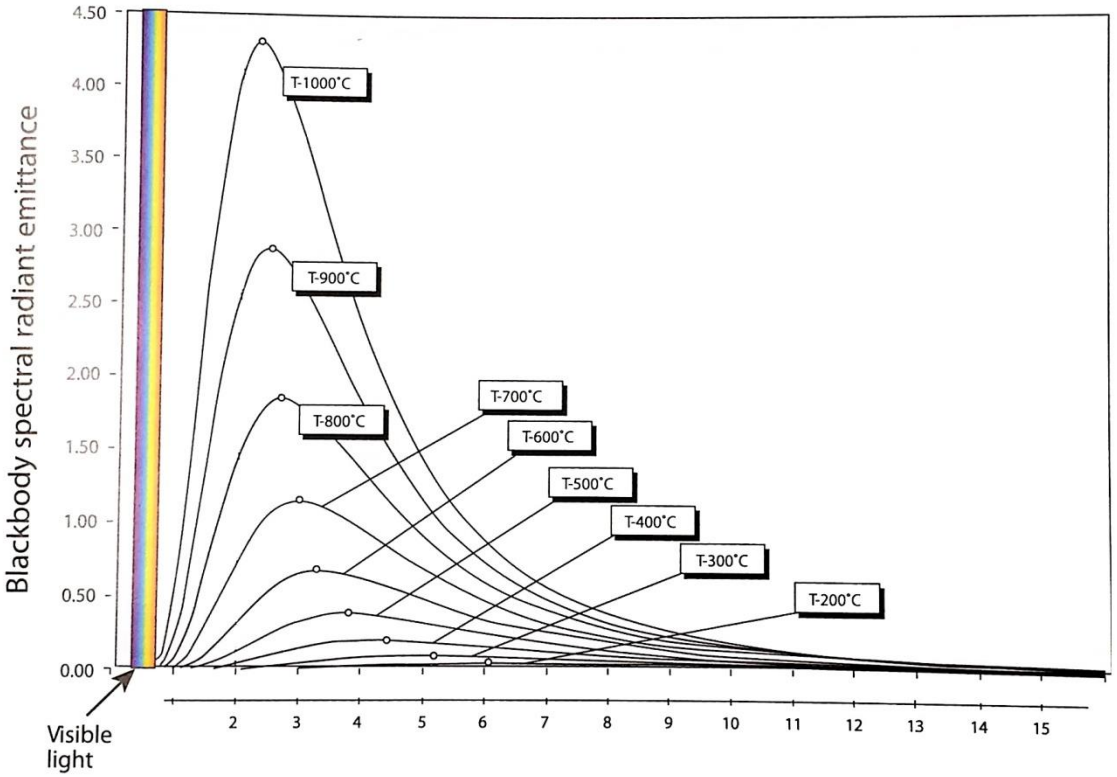

Figure 3.2 Illustration of Planck's Law.

The radiant energy emitted from the surface is defined by the Stefan-Bolzmann law. In the case of real material it is expressed as:

$$W = \sigma\varepsilon T^4 \qquad \textbf{3.2}$$

or in the case of a black body:

$$W = \sigma T^4 \qquad \textbf{3.3}$$

where, W is the radiant flux emitted per unit area (W/cm^2), σ is the Stefan-Boltzmann constant (5.673×10^{-8} W / $m^2 \cdot K^4$) which is independent of material,

surface or temperature, ε is the emissivity, and T is the absolute temperature of the surface. The emissivity of the material can be defined as the ability of a surface to emit radiant energy.

The other law that defines the radiation behaviour is the Wien's displacement law. It states that the wavelength at which surface emits its peak energy is defined as Wien's displacement constant (b) divided by the surface temperature (T) in Kelvin.

$$\lambda_{max} = \frac{b}{T} \quad \textbf{3.4}$$

where λ_{max} is the maximum wavelength (μm), b is the Wien's displacement contact (0.002898 m · K) and T is the surface temperature (K).

The energy emitted from the thermal radiator is not transferred continuously, but occurs as discrete "jumps", or quanta - called photons. The energy of the photon is proportional to the wavelength of the radiated energy emitted and expressed as:

$$E_{photon} = \frac{hc}{\lambda} \quad \textbf{3.5}$$

or

$$E_{photon} = hf \quad \textbf{3.6}$$

where E_{photon} - is the energy of the photon (J), h - is the Planck's constant (6.6×10^{-34} J·s), c - is the speed of light (3×10^{8} m/s), λ - is the wavelength is metres, and f - is the frequency (Hz). The energy of a photon is of interest for this particular research, because the IR camera used in the experimental work is fitted with Indium-Antimonide (InSb) photon detector rather than thermal detector. Therefore, Planck's law, Stefan-Bolzmann law, and Wien's law for a black body can be modified to deal with number of photons (N_b) rather than energy. By dividing Planck's expression by hc/λ, the new expression becomes:

$$Q_\lambda b = \frac{2\,\pi\,c}{\lambda^4\left(e^{\frac{hc}{K\lambda T}}-1\right)}\ (photons/s\ \cdot\ m^3) \quad \textbf{3.7}$$

The Stefan-Bolzmann's equation which expresses the total number of photons emitted from a blackbody at the given temperature becomes:

$$Q_{photon} = \frac{0.37\delta T^3}{k}\ (photons/s \cdot m^2) \quad \textbf{3.8}$$

The Wien's expression for calculating the maximum wavelength of the photon emission remains the same as for the maximum energy emission, but Wien's constant becomes 3663 μm-K. This is due to the wavelength at which maximum occurs, which is about 25 percent greater for photon emission than for the energy emission (AGA infrared systems AB, 1984; Kaplan, 2007).

3.4 Classification of Objects According to Emissivity

The surfaces can be divided into three groups: blackbodies, graybodies and non-graybodies, which is shown in Figure 3.3. The Blackbody is a theoretical surface, which would have an ε = 1 at all wavelengths and would absorb all the energy at its surface. Most solid objects are graybodies and have emissivity higher than zero, but lower than one. The graybodies have a constant value of emissivity, independent of the wavelength. Practically, the blacker the material, the closer its emissivity is to 1. On the other hand, the more reflective the surface is, the lower its emissivity. The emissivity of a body can be defined as the ratio of the amount of radiant energy emitted from the surface to the radiant energy emitted by the blackbody at the same temperature. The non-graybodies have wavelength dependent value of the emissivity. The non-graybodies can be semi-transparent, therefore they emit energy, absorb energy and transmit it.

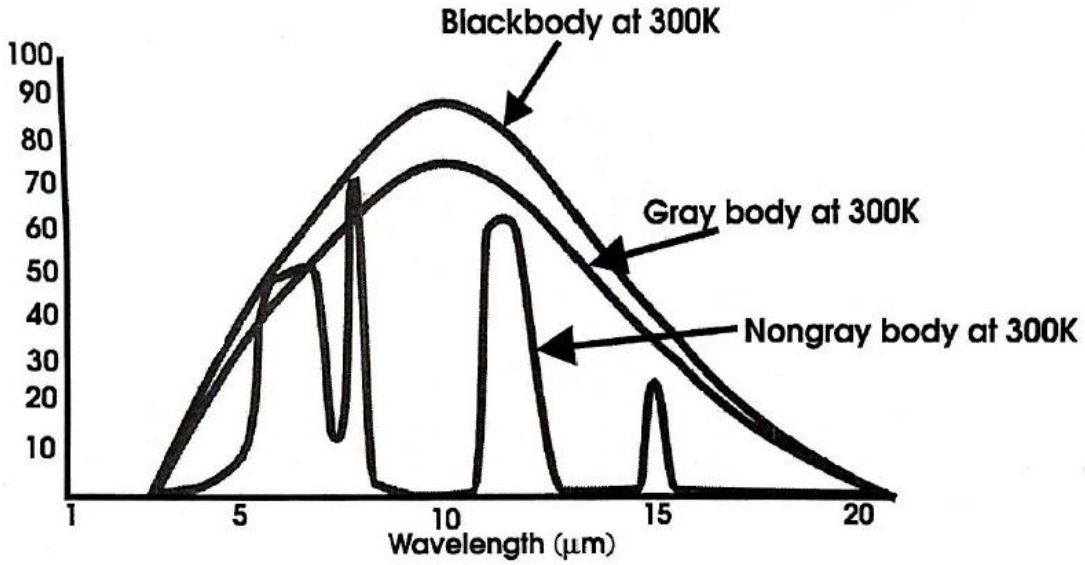

Figure 3.3 Spectral distribution of a blackbody, greybody, and non-greybody at the same temperature (Kaplan, 2007).

3.5 Absorption, Reflection and Transmission

If electromagnetic radiation is incident on surface of a body, there are only three things can happen to this radiated energy: it may be reflected, absorbed, or transmitted through the body. These three processes are described by reflectivity (ρ), absorbance (α), and transmittance (τ), which are dimensionless and the sum of them is always equal to one. The surface that absorbs energy has also to emit it at the same wavelength. This is known as Kirchhoff's law, where for a blackbody α = ε = 1, whereas for a real body it is normally less than one. When semi-transparent material (non-graybody) is considered the radiation balance equation can be written as:

$$\varepsilon + \rho + \tau = 1 \qquad \textbf{3.9}$$

where, ε - is the emissivity, ρ - is the reflectivity, and τ - is the transmittance. An example of surface properties and energy measured by the IR camera is shown in Figure 3.4. The opaque material (graybody) would not transmit any energy i.e. τ = 0. The emissivity in this case would be:

$$\varepsilon = 1 - \rho \qquad \textbf{3.10}$$

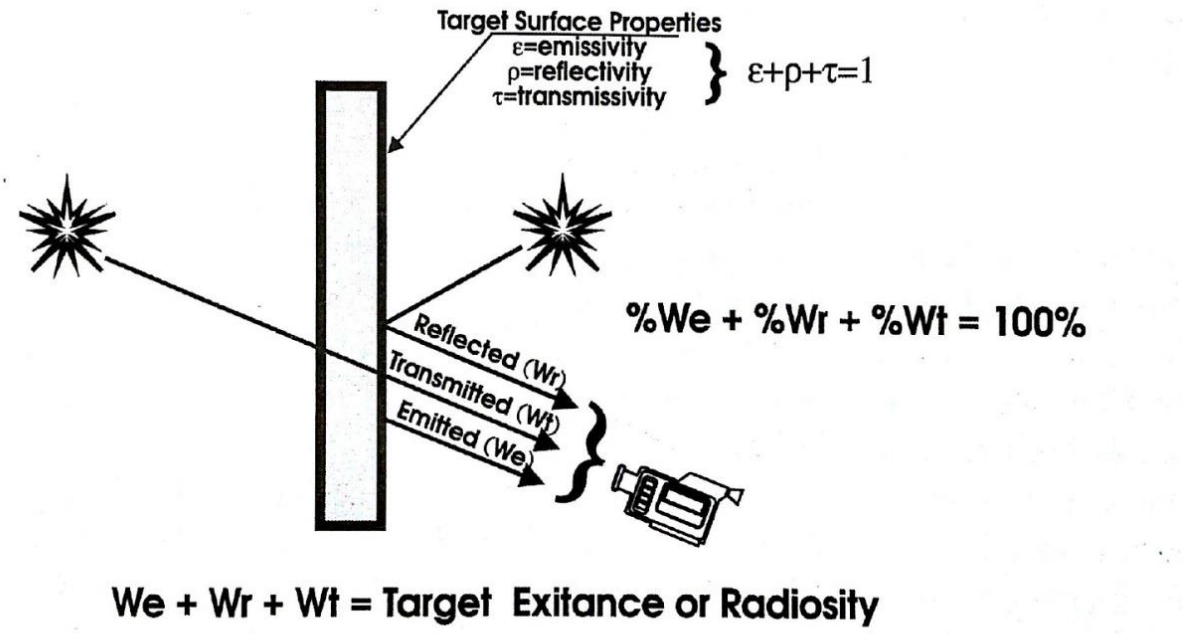

Figure 3.4 The surface properties and energy measured by the IR camera (Kaplan 2007).

In the case of the blackbody the IR camera measures only emitted energy, in the case of the graybody, the camera sees emitted and reflected energy, and in the case of a non-graybody the IR instrument see all three energy components, namely emitted, reflected and transmitted energies (Kaplan, 2007; Breitenstein et al., 2010).

3.6 High Speed IR Camera

The main aim of the thermal imaging camera is to convert infrared radiation into a visual image which can be used to quantitatively analyse the temperature of the surface. The study of polymer cooling in a microinjection moulding process requires a very fast response IR camera, as cooling of a micro part can take less that a second.

Modern IR cameras consist of the following key parameters: IR optics, IR focal plane array (IRFPA) detectors, and electronics. The IR optics are required to focus the emitted energy by the body surface onto the IR detector, which

converts the absorbed energy into the electrical signal. The electronics amplify and condition the signal from the IR detector. The electric impulse is then sent to a processing unit which transmits the signal into data to be displayed. The displayed image can be presented in monochrome or colour (see Figure 3.5), where grey shades or colour hues represent the thermal level of the specimen depending on the emission of the infrared light from the surface (Kaplan, 2007; Vollmer and Mollmann, 2010; Breitenstein et al., 2010).

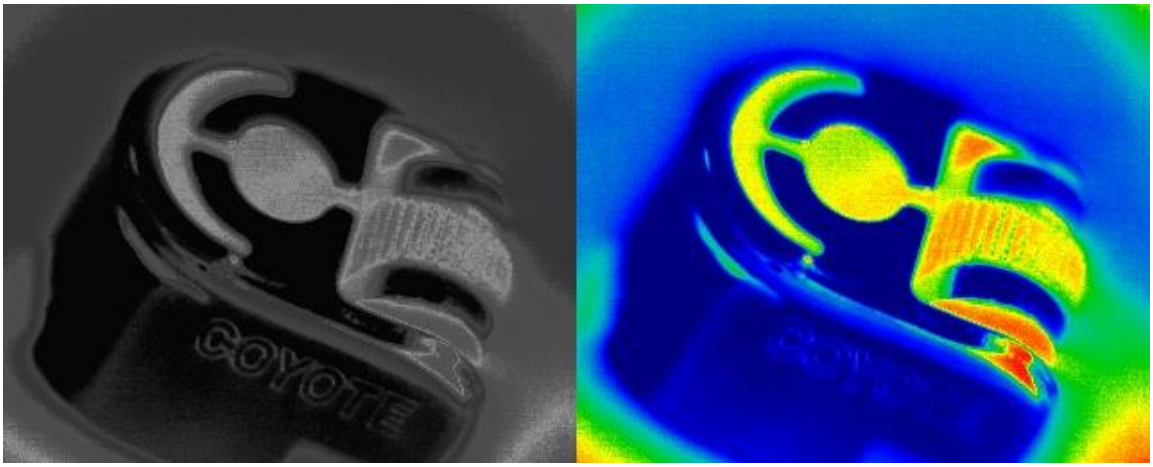

Figure 3.5 Monochrome and colour IR images.

3.6.1 Infrared Detectors

The heart of any infrared imaging system is an infrared detector or an array of detectors, which is shown in Figure 3.6. They work as transducers by converting thermal radiation or photons into an electrical signal. IR detectors can be divided into two categories, namely thermal detectors and photon detectors. Thermal detectors normally operate at room temperature; they have broad spectral response, lower sensitivities and a slow response time of a few ms. They operate by producing an electrical response in reference to the temperature change of the sensor. The photon detectors have high sensitivities, high response time down to a fraction of μs, but limited spectral

responses. Unlike thermal detectors, photon detectors convert absorbed photons directly into an electrical signal. To achieve a very fast response (in order of microseconds) and low signal-to-noise ratio, photon detectors have to be cryogenically cooled. Cryogenic cooling reduces noise and increases sensitivity (Vollmer and Mollmann, 2010).

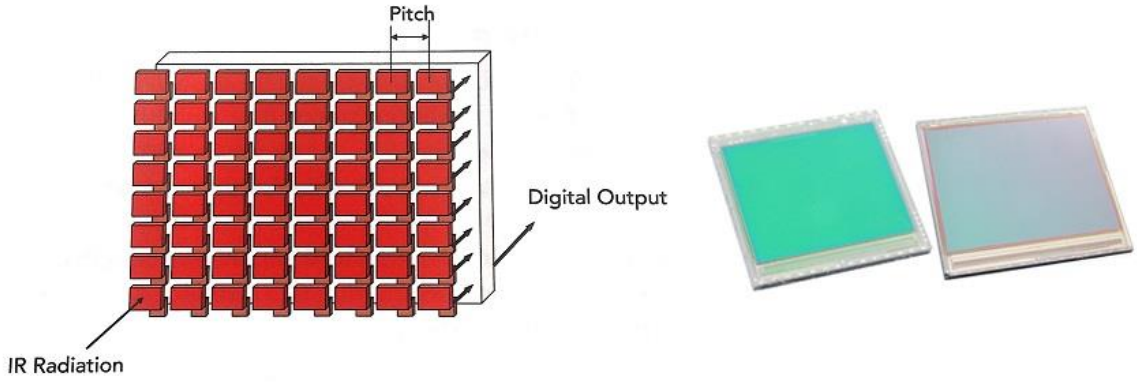

Figure 3.6 Basic IR Focal Plane Array principle (left) and FLIR (InSb) Focal Plane Arrays (right) (FLIR Advanced Thermal Solution, 2013).

3.6.2 Detector Selection

Selection of the IR camera should be based on its detector performance, where major parameters are the wavelength region of interest, integration time and sensitivity.

The wavelength region of interest for polymers is governed by their absorption or transmittance. The transmittance depends on material and thickness of the specimen. Polymers such as polyethylene, polypropylene and polystyrene are non-gray bodies or as they are also called selective emitters. A thin film of many polymers including polyethylene, polypropylene, polystyrene and nylon would appear transparent to most IR wavelengths, but they would absorb at specific wavelengths. Figure 3.7 shows spectral transmittance of 30 μm and 130 μm thick films. Polyethylene films show strong absorption at

approximately 3.4 and 6.7 µm, whereas polyester has a strong absorption band at approximately 8.5 µm (Vollmer and Mollmann, 2010).

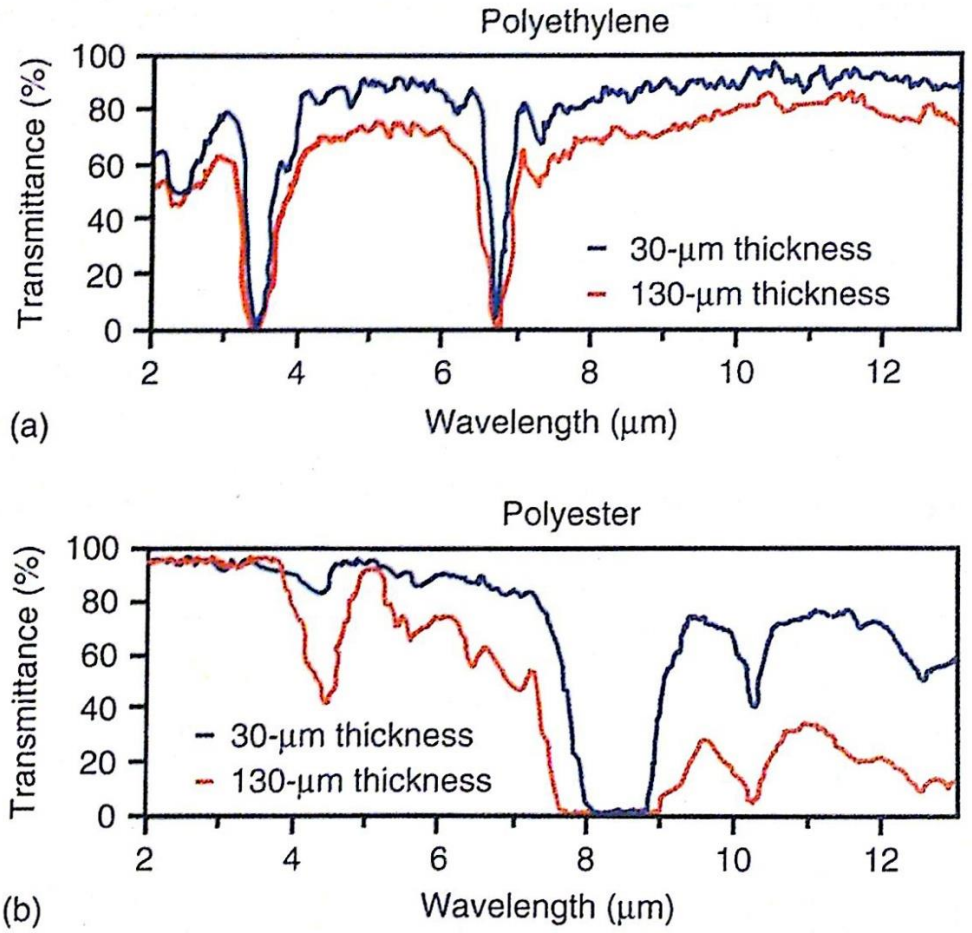

Figure 3.7 Spectral transmittance of polyethylene (a) and polystyrene (b) with different thickness (Vollmer and Mollmann, 2010).

The majority of organic polymers have a very strong but narrow carbon-hydrogen (C - H) absorption band at 3.4 µm. This means that at 3.4 µm the polymer film will appear opaque and will emit maximum energy. There are also polymers that exhibit a strong (C - O) absorption band at 7.9 µm. Polymers can be divided into 3 groups, namely materials that have strong absorption at 3.4 µm, 3.4 or 7.9 µm, or 7.9 µm only (Bendada et al., 2004b; Vollmer and Mollmann, 2010; Kaplan, 2007).

Table 3.1 Polymers and their absorption bands.

3.4 μm	3.4 or 7.9 μm	7.9 μm
Polyamide, polyethylene, polypropylene, polystyrene, nylon, polybutylene, glassine	PVC, acrylic, polyurethane, polycarbonate	Polyester, PTFE, polyamide, cellophane, cellulose acetate, fluoroplastic

To measure the surface temperature of these materials, an IR camera has to be spectrally adapted to the wavelengths at which the material exhibits strong absorption. This is available by using spectral filters. A narrow bandpass (NBP) filter of 3.4 μm or 7.9 μm wavelength will make the array of sensors blind to all the energy outside the 3.4 μm and 7.9 μm, enabling polymer surface temperature measurements (Kaplan, 2007; Vollmer and Mollmann, 2010).

3.6.3 Integration Time

The integration time of the IR camera is the exposure time of the detector to produce a single frame. This property is vital for dynamic events. Selection of the appropriate integration time will eliminate motion blur and capture enough energy to produce an image. In microinjection moulding, polymers enter the cavity at the high speed to prevent premature solidification of the part. The correct temperature measurement can only be determined when melt is at rest, therefore a short integration time is required for accurate temperature measurement (Vollmer and Mollmann, 2010).

3.6.4 Sensitivity

The IR camera sensitivity is a measure of the smallest signal, which can be detected by the sensor. It is the most commonly described by the Noise Equivalent Temperature Difference (NETD) and is measured in milliKelvins

(mK). It plays an important role when accurate and detailed images and videos are required. Highly sensitive detectors produce more detailed images and show more colour/temperature differences, in other words, a camera with good sensitivity can differentiate areas on the picture with very little temperature difference. Cryogenically cooled detectors have sensitivities in the range of 10 - 30 mK, whereas un-cooled sensor experience more noise, hence have sensitivity in the range of 30 - 120 mK (Vollmer and Mollmann, 2010; Van Anda, no date).

3.6.5 FLIR X6540SC Infrared Camera

An ultra high speed, high sensitivity infrared camera FLIR X6540SC was used for the experimental work (see Figure 3.9). The camera has a cooled Indium antimonide (InSb) focal plane array (FPA) detector with the spectral range of 1.5 - 5.1 µm, pixel pitch of 15 µm and aperture of F/3. The detector sensitivity (NETD) is <20 mK at 25 °C which can capture the smallest image details and temperature difference of less than 20 mK (0.02 ˚C). The FLIR X6540SC is capable of capturing 125 frames per second at the fullframe size of 640 x 512 pixels. The frame size is user adjustable in 16 by 4 pixel steps with the frame rate up to 4 KHz. The software allows integration time to be adjusted in the nanoseconds increments in the range of 160 nanoseconds to full frame. The camera is fitted with Gigabit Ethernet (GigE) interface which provides image streaming and IR camera control over Ethernet network with data transfer rates up to 1 Gb/s. The FLIR X6540SC outputs 14-bit data, but with "superframing" dynamic range can be effectively extended to 16-bit. Cooling of the detector is achieved by a rotary Stirling engine cryocooler which removes

the heat from the cold finger with the detector by a thermodynamic cycle. One of the FLIR rotary Stirling cryocoolers is shown in Figure 3.8.

Figure 3.8 FLIR Systems cryogenic cooling engine (Flir.com, 2015).

The IR camera is fitted with an external trigger which can be activated and configured in the software allowing synchronisation of the image recording. To measure the surface temperature of polymers, the camera can be spectrally adapted to the wavelengths at which polymer materials exhibit high emissivity. The IR camera is fitted with a motorised filter wheel which is located between the detector and the lens. The FLIR X6540SC meets all the necessary requirements for the application of the polymer cooling study in microinjection moulding process.

Figure 3.9 FLIR X6540SC IR camera (FLIR Systems, 2014).

Chapter 4. Literature Review

4.1 Introduction

A significant number of scientific papers about thermal contact resistance have been published in various journals, namely International Journal of Heat and Mass Transfer, International Journal of thermophysics, AIAA Journal of Thermophysics and Mass Transfer, and Journal of Heat Transfer. Research papers cover TCR in general heat transfer applications, aerospace heat transfer, microelectronics cooling, nuclear engineering, and heat exchangers. The effects of TCR between two solid bodies in contact, were mainly studied for metal-to-metal interfaces.

Electronic devices continue to decrease in size and their internal clock speeds continue to increase. Heat management in electronic packaging is required to provide reliability and stable performance. The TCR between electronic packages and a heat sinks play a vital role in removal of heat from the semiconducting devices (Peterson and Fletcher, 1988; Grujicic et al., 2005; Khan et al., 2005).

Thermal contact resistance has also been studied in polymer processing, especially in injection moulding. Thermal contact between steel mould surface and polymers was studied experimentally and numerically (Bendada, 2004b). Masse and his colleagues (2004) carried out a study on cooling of polymer parts in the injection moulding process. They concentrated on major parameters affecting heat transfer such as, thermal contact resistances, residual stresses and PvT diagrams.

4.2 Analytical and Theoretical Work

Thermal contact resistance and thermal contact conductance have been studied extensively because of their importance in many engineering and mechanical applications. The majority of research publications on TCR are concerned with metal-to-metal contacts and applications where it is of importance. For almost 80 years analytical, experimental and numerical models have been developed to predict heat transfer between two solid bodies in contact (Bahrami et al., 2006). The thermal resistance problem consists of a heat flow model, a geometrical model and a deformation model.

TCR has been studied analytically by many researchers. Cooper, Mikic and Yovanovich (1969) carried out a study on resistance of heat flow between two thick bodies in contact in a vacuum. Theoretical studies were based on a simplified model, where ideal heat flow through a single contact was assumed and analysed. Then, an extended model was applied to predict thermal conductance of multiple contact spots. They have also considered a relationship between the pressure applied and the true contact area in order to predict thermal conductance. At the time very few results were available for experimentally obtained values of contact conductance and measure surface profiles. Therefore, comparison could not be performed between experiment and theory. Further work was undertaken by Mikic (1974) on rough, but nominally flat surfaces. Mikic concentrated his theoretical and analytical work on modes of deformation affecting the value of conductance. He presented expressions for the estimation of thermal conductance based on three modes of deformations, namely pure plastic deformation, plastic deformation of asperities together with elastic deformation of the substrate, and pure elastic deformation.

Developed expressions were restricted to the rough nominally flat surfaces. Song and Yovanovich (1988) also worked on the analytical problem of thermal conductance. They have developed a novel expression capable of predicting contact heat transfer, which was dependent on surface roughness and Vickers microhardness. The resulting expression simplified the prediction of heat transfer significantly. Reported results of contact conductance showed that their theoretical predictions were in a good agreement with experimental values obtained for four different materials (stainless steel (SS304), nickel 200, zircaloy-4, zirconium-2.5% niobium) obtained by Hegazy (1985). McWaid and Marschall (1992) also aimed to improve prediction of TCR. They adapted existing elastic models, which were previously developed by Greenwood and Williamson (1966) (GW model) and McCool (1986). The original GW model estimates the average size and number of contacts as the function of load. Then, the GW model was expanded by adding determination of non-dimensional separation of two contacting surfaces, determination of actual contact area, determination of the average value of the ratio of micro-contact to flux tube radius and by adding average contact radius. They managed to achieve relatively accurate prediction values of TCR. McWaid and Marschall have validated the model with experimental work, based on contacts between rough, similar materials. They have reported results for four pairs of specimens out of ten pairs studied. They have used two materials namely, aluminium (6061-T61) and stainless steel (SS 304) with different types of surface finishes. The average error between the predicted and measured values was less than 25% for isotropic rough surfaces, and around 50% for anisotropic surfaces.

Historically, to use deformation models researchers have had to choose elastic or plastic models initially and then do the calculation. Sridhar and

Yovanovich (1994) compared for the first time both elastic and plastic models on the same set of data. They used experimental data for contact conductance of isotropic surfaces and reduced it to a dimensionless form. They compared elastic and plastic deformation models with data obtained by Antonetti (1983), Hegazy (1985) and McWaid (1990). The Mikic elastic model and The Cooper, Mikic, Yovanovich (CMY) plastic model were compared based on the set of data from five different materials: nickel 200, stainless steel (SS304), zirconium-2.5% niobium, zircaloy-4 and aluminium (6061). The finding led to the conclusion, that some materials undergo elastic deformation, some plastic deformation and some could undergo both elastic and plastic deformation, and suggested that a new elastoplastic model of deformation had to be developed and more experimental data was required to test all the deformation models. Based on the results from their previous research Sridhar and Yovanovich (1996a) proposed a new elastoplastic model for isotropic conforming rough surfaces. The new model was developed based on the one previously proposed CMY plastic model. Again, experimental data was reduced into a dimensionless form in order to compare models with themselves as well as experimental results. Elastic and plastic models were compared against data obtained by Antonetti (1983), Hegazy (1985), McWaid (1990), and Maddren (1994) for nickel 200, stainless steel (SS304) and zirconium-2.5% niobium. Results showed that nickel 200 underwent plastic deformation, five out of eleven pairs of SS304 underwent elastoplastic deformation, whilst the remaining pairs experienced full plastic deformation. Zirconium alloys Zirconium-2.5% niobium and zircaloy-4 showed significant elastic deformation. Further experimental work on thermal contact conductance of tool steel and comparison results with elastoplastic models of deformation was performed (Sridhar and Yovanovich,

1996b). Three sets of steel specimens were prepared: untreated, heat treated to 40 HRC (hardness Rockwell "C") and heat treated to 58 HRC. Prior to thermal conductance measurements surface roughness and microhardness were examined. Test results were compared with the proposed elastoplastic model (Sridhar and Yovanovich, 1996a), which revealed, that untreated tool steel specimens underwent elastoplastic deformation, while other heat treated specimens underwent fully elastic deformation.

4.3 Experimental Work

Various types of apparatus have been built to measure thermal contact conductance experimentally between either similar or dissimilar materials. One of the most commonly used is the axial heat flow apparatus. Peterson and Fletcher (1988), Sridhar and Yovanovich (1996), Lambert and Fletcher (1995), Marotta and Fletcher (1998), Sunil Kumar and Ramamurthi (2003) and Zhang et al. (2006) used axial heat apparatus to measure thermal contact resistance of solid spot contacted surfaces. All of the experimental work was performed in vacuum, so that heat transfer between the gaps could be ignored. On the other hand, Wahid and Madhusudana (2000), Bahrami et al. (2004) focused their work on gap conductance. Their experimental studies involved both methods: in the vacuum and with interstitial gases. The principles of the axial heat flow experiments are similar, but they differ in details. Figure 4.1 shows a schematic representation of the axial flow heat apparatus.

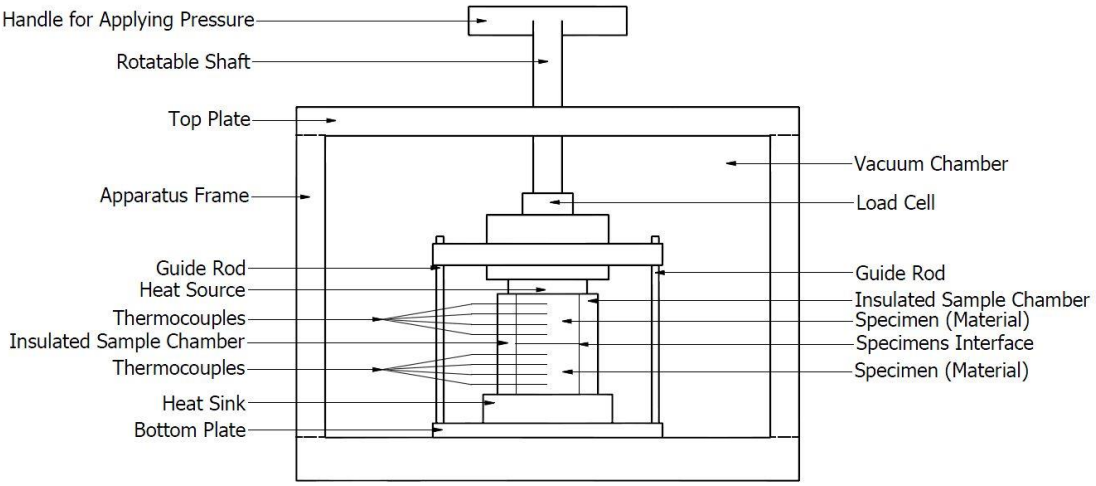

Figure 4.1 Schematic drawing of the axial heat flow apparatus (Narh and Sridhar, 2000).

Sridhar and Yovanovich (1996) used the axial heat flow apparatus to verify their elastoplastic deformation model. Thermal contact conductance was measured experimentally for the tool steel interfaces with different roughness and microhardness. Marotta and Fletcher (1998) conducted an experimental investigation on TCC for nominally flat, uncoated surfaces of dissimilar alloys, namely aluminium (6101-T6-T61)/aluminium (A356-T61) and aluminium (6101-T6)/stainless steel (SS 304). Experiments were performed on surfaces with different roughness in vacuum using axial heat flow apparatus. The data obtained was used in the development for theoretical models of uncoated aluminium/aluminium and aluminium/stainless steel surface contacts. After comparing both elastic and plastic models, Marotta and Fletcher (1998) concluded that experimental data of dissimilar materials contacts was better predicted by the elastic deformation model.

The axial heat flow apparatus was used in experimental work carried out by Sunil Kumar and Ramamurthi (2003). They have performed a study on the influence of roughness, waviness and flatness of surfaces on TCC. Samples of stainless steel and aluminium with different levels of roughness, waviness and

flatness were tested in vacuum. Theoretically predicted values of thermal contact conductance showed a close match with experimentally derived ones. Similar experimental work was performed by Zhang et al. (2006). In both publications researchers looked at the influence of thespecimens roughness and used an axial heat flow apparatus. Zhang et al. (2006) performed a study on TCR at the interface of brass surfaces with various roughness levels. Four pairs of sand-blasted brass specimens were used to measure TCC. Experimental data was processed and compared with numerical simulations. Experimental data showed good agreement with numerical predictions based on the effects of contact pressure, thermal conductivity of the interstitial medium (air) and mean absolute slope of the rough surfaces. However, the published work does not specify if experiments were performed in vacuum or otherwise, whilst the corresponding numerical simulations considered both vacuum and air-filled cases.

Other applications involved the study of TCC at mould compound/heat spreader material interfaces and coatings applied onto metal surfaces. In microelectronic devices heat spreaders transfer heat from electronic components to the heat sinks, maintaining performance levels of the device. Results obtained by Peterson and Fletcher (1988) showed that thermal conductance between mould compound and heat spreader is strongly dependent on the interface pressure. Also, they have proven that models for predicting thermal conductance for metal-to-metal contacts can be used to predict thermal conductance at the interface between metal and plastic as well.

Lambert and Fletcher (1995) also studied TCR in electronic devices. They have focused their research on coating materials which are mainly used in electronic modules. Low operating temperature of standard electronic modules

(SEM) guarantees better performance and decrease in failure rates. Thermal contact conductance of silver coated aluminium alloys and electroless nickel-plated copper were determined using axial heat flow apparatus. Bare, vapour-deposited silver, electroplated silver, and flame-sprayed silver coating techniques were applied onto aluminium alloy surfaces. Surface topography, microhardness measurements and thickness of the coatings were also considered (Lambert and Fletcher, 1995).

It is known that the main heat flow mechanisms at the interface between two bodies are conduction through the contact spots and conduction through the gaps. Wahid and Madhusudana (2000) have proven that at low contact pressures heat flow through the gaps becomes main mechanism of heat transfer at the interface. They have conducted a set of experiments where solid spot conductance and the gap conductance were studied. Conductance for a range of surfaces with different RMS roughness and a range of interstitial gases and gas mixtures was measured using an axial heat flow apparatus. First, experiments were performed in vacuum to determine solid spot conductance and afterwards, with interstitial gases. Helium, argon, carbon dioxide, nitrogen and mixtures of argon and helium were considered. The gap conductance was calculated by subtracting solid spot conductance from the total one. Bahrami et al. (2004) went further and developed an expression for predicting heat transfer of the interstitial gases between conforming rough contacts. Experiments were conducted with argon, helium and nitrogen, which were also used in experimental work performed by Wahid and Madhusudana (2000). Prepared specimens were made of stainless steel (SS 304) and nickel 200. Collected experimental data by Bahrami et al. (2004) and data obtained by Hegazy (1985) and Song et al. (1993) were compared with the expression developed.

Predicted heat transfer values were in a good agreement with the data obtained by Hegazy (1985) and Song et al. (1993).

The TCR plays an important role in a quasisteady-state heat transfer across two surfaces coming into regular, periodic contact. This type of contacts is encountered in an internal combustion engine where the contact between the exhaust valve and valve seat changes periodically (Madhusudana, 1996).

A modified axial heat flow apparatus, where the upper plate of the apparatus was spring loaded and operated with a pneumatic cylinder to cause contact and separation of the surfaces was used by Moses and Johnson (1989). They have studied the quasisteady-state heat transfer condition for similar metallic surfaces in a regular, periodic contact. Behaviour of TCR and the influence of the cycle contact and separation times were studied experimentally. Results for heat transfer and temperature distribution were reported for low contact pressures between similar materials (brass, aluminium, copper) at a mean temperature of 33 $^{\circ}$C at the interface. Reported experimental results were in a good agreement with the results previously published by other researchers namely Vick and Ozisik (1981), Howard and Sutton (1973) and Howard (1976). Prediction models for quasisteady periodic contacts were proven to be able to predict surface interactions accurately.

Several reviews have been written discussing the problem of thermal contact resistance in various applications. The TCR was reviewed by Snaith et al. (1986) aiming to help designers to understand the problem and factors affecting heat transfer between two bodies in contact. The review included a general overview of processes of heat transfer across metal/metal interfaces, parameters affecting TCR, such as heat flux and direction of heat, surface

topography, and interstitial materials. Experimental techniques and analytical predictions for determining TCR have been discussed and compared.

Table 4.1 Summary of effects of varying the stated parameters (Snaith et al., 1986).

Parameter which is changed	**Effect on the thermal resistance of the pressed contact in:**	
	High vacuum $(< 10^{-3}\ torr\ pressure)$	Air or other fluid at atmospheric pressure
Applied mechanical load increased	Decrease: significant effect	Decrease: significant effect
Mean interfacial temperature increased	Expect to decrease: over the 0-100°C range little effect	May increase or decrease depending upon thermophysical properties of the interfacial fluid
Period of heating extended	Expect to decrease as duration increases	Expect decrease
Applied load (or interface temperature) is cycled	Decrease	May increase as sheared particles oxidise
Surface films thickened	Increase	Increase with film thickness
Surface roughness increased	Increase	May decrease as surface films are penetrated
A soft, high thermal conductivity, material is inserted at the interface	Decrease: careful material selection can lead to a significant reduction	Decrease (as for in high vacuum)
A hard, low thermal conductivity, material is inserted at the interface	Increase: careful material selection can lead to a significant increase	Increase (as for in high vacuum)

Another review was written by Mantelli and Yovanovich (2002) where they have focused on a specific application of TCR of contacting surfaces in vacuum, which is an important parameter in spacecraft thermal design. They have stated that there was no universal model to predict joint resistance. They have performed a survey of the available models which potentially could be used in spacecraft thermal design. The review included thermal constriction models, surface geometry models and surface deformation models. Parameters that affect TCR, such as effects of oxidation and the effects of interstitial materials

were also considered. TCR of nonconforming rough surfaces in a vacuum environment was also reviewed by Bahrami et al. (2006). The authors have analysed and compared a number of geometrical, mechanical and thermal models of TCR. The models were compared with experimental data consisting of more than 400 TCR data points, which were divided into two limiting groups: conforming rough and elastoconstriction. The authors showed that existing models do not cover both of the limiting groups and that better models needed to be developed.

4.4 Thermal Contact Resistance of Metal/Polymer Joints

Marotta and Fletcher (1996) have studied thermal contact resistance at metal/polymer interfaces on an experimental basis. A range of polymers, namely ABS, Delrin, Teflon, Nylon 6-6, LE phenolic, Polycarbonate, UHMW polyethylene, Polypropylene and PVC were tested in an axial heat flow apparatus in a vacuum environment, where aluminium 6101-T6 was used as a base material. Experimental results included thermal conductivity measurements for a range of temperatures between 10 and 100°C maintaining the interface pressure at 200 psi (1.38 MPa). Thermal contact conductance for each material was measured at 20°C with a range of contact pressures between 75-400 psi (0.51 - 2.76 MPa) which is shown in Figure 4.2. The data obtained for thermal contact conductance was compared with an elastic model of deformation proposed by Mikic (1974) and a plastic model by Cooper, Mikic and Yovanovich (1969), which were initially developed for metal/metal contacts. Experimental work showed that thermal conductivity of materials is independent of the temperature at the range of 10 - 100°C, whereas analytical work showed that there was a disagreement between elastic and plastic deformation models and experimental data and models are not suitable for metal/polymer interfaces.

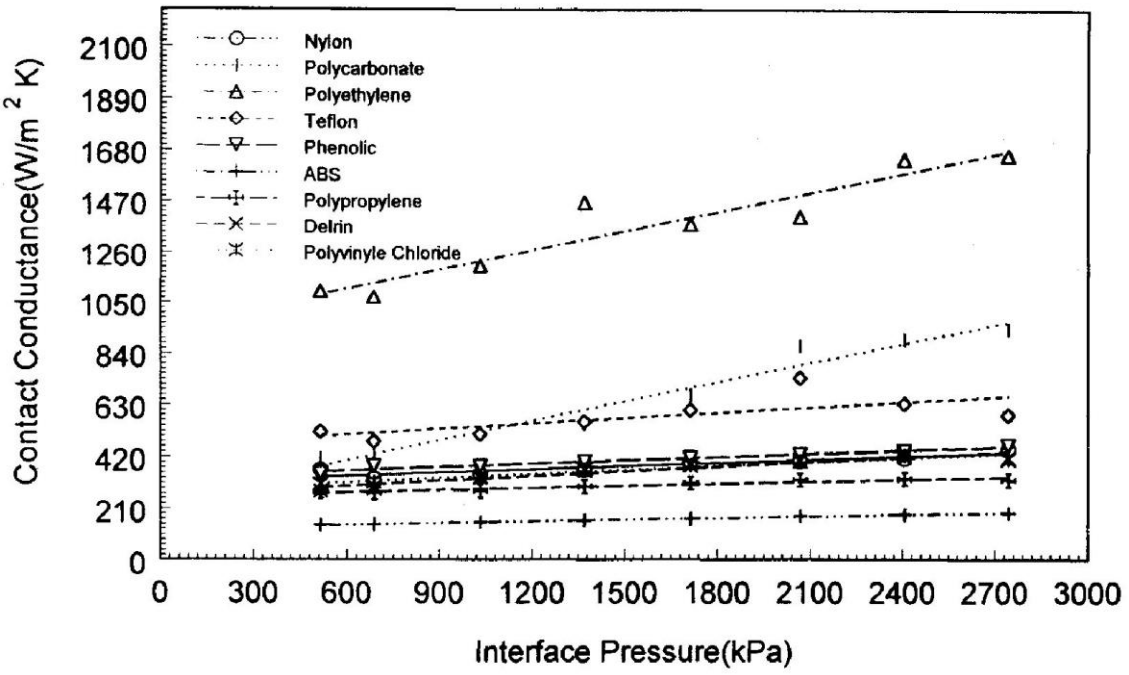

Figure 4.2 Thermal contact conductance for various polymers at an interface temperature of 20°C for a range of interface pressures (Marotta and Fletcher, 1996).

Parihar and Wright (1997) were also unsuccessful in using existing contact resistance models to predict TCR at metal/elastomer interfaces. Because of the intrinsic properties of the elastomers, elastic and plastic models were not suitable. Despite that, they have performed and experimental study on a thick (4.76 mm) cylindrical silicone rubber sample measuring total thermal resistance of the whole joint and thermal resistance at hot and cold interfaces under low contact pressures of 0.02 to 0.25 MPa. Figure 4.3 shows thermal resistance network of metal-elastomer-metal joint, where R_t - the total resistance of the joint, R_1 - resistance at the hot interface, R_2 - resistance at the cold interface, R_b - bulk resistance of the elastomer, T_1 and T_4 the apparent metal temperatures at the hot interface and cold interfaces, and T_2 and T_3 the apparent elastomer temperatures at the hot interface and cold interfaces. The axial heat flow apparatus was used where silicone rubber samples were placed between two stainless steel (SS 304) cylinders in ambient air environment. The total joint

resistance decrease was governed by increase in applied pressure and reduction of flux levels (see Figure 4.4 left).

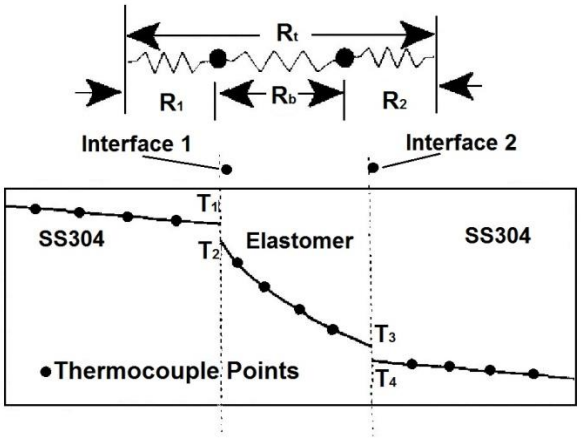

Figure 4.3 Resistance network and temperature distribution of the joint (Parihar and Wright, 1997).

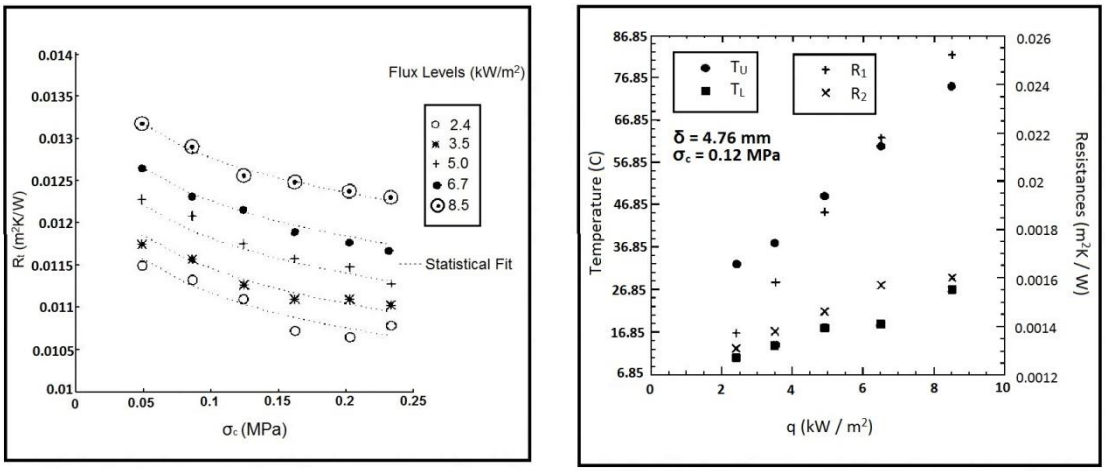

Figure 4.4 Total resistance R_t of the joint (left) and the resistance at the hot interface R_1, cold interface R_2 , T_U and T_L mean interface temperatures upper and lower interfaces (right) (Parihar and Wright, 1997).

Figure 4.4 (right) shows how mean interface temperatures and thermal resistance at the interfaces changes with the increase of flux levels. With an applied pressure of 0.12 MPa thermal resistance at the hot interface was varying from approximately 0.0016 to 0.025 m^2K/W, whereas at the cold interface it ranged from 0.0013 to 0.0016 m^2K/W.

Narh and Sridhar (1997) proposed a model for prediction of TCR at metal/polymer interfaces. The authors have considered glass transition

temperature as the driving mechanism of their model, also including pressure, surface asperities and hardness, as well as the specific volume of the polymer. The TCR at steel/polystyrene interfaces was measured using axial heat flow apparatus under various contact pressures ranging from approximately 0.25 MPa to 2 MPa, below and above glass transition temperatures. The authors have reported that the proposed model was able to predict TCR values quite accurately, but unfortunately the data obtained was very limited. Figure 4.5 (a) shows total resistance (R_t) as a function of thickness at constant temperature and pressure. Figure 4.5 (b) demonstrates change of thermal contact resistance of the samples below T_g with applied pressure at mean temperatures of 65°C and 75°C.

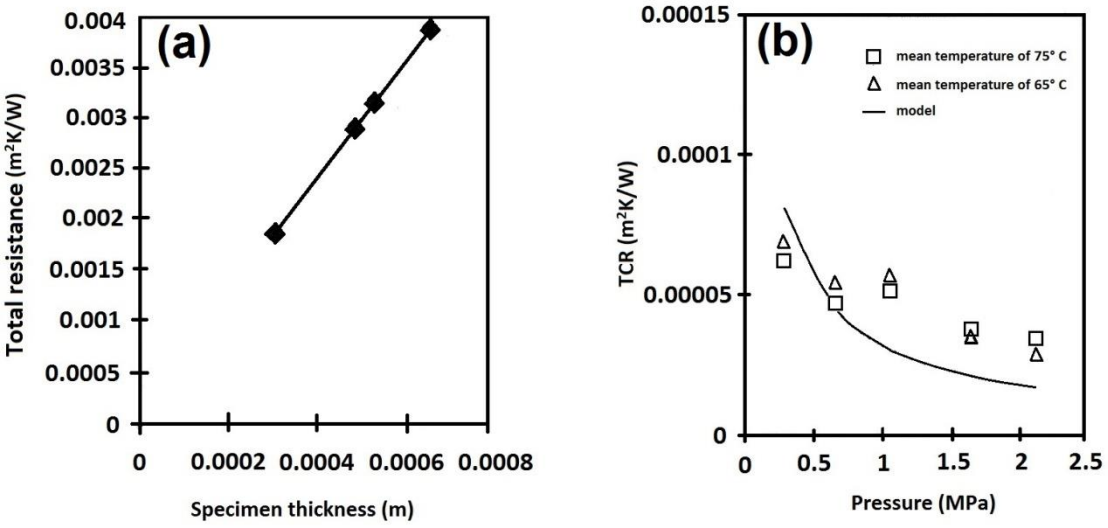

Figure 4.5 Total thermal resistances of PS specimens (a) and variation of TCR with pressure at two mean temperatures (b) (Narh and Sridhar, 1997).

Fuller and Marotta (2001) developed another model for the prediction of thermal joint conductance. They modified an already existing elastic conductance model by adding surface contact mechanics and basic properties of the polymers. Analytical and experimental work by Fuller and Marotta was based on the same materials that were used by Marotta and Fletcher (1996) in their work, namely Delrin® 1, Delrin® 2, polycarbonate and PVC. Thermal joint conductance was measured at 40 °C for a range of contact pressures between

20 - 400 psi (0.14 - 2.76 MPa) with specimens approximately 2 mm thick. The joint resistance as a function of pressure for the range of materials is presented in Figure 4.6. Predicted values showed good agreement with experimentally obtained values with maximum uncertainty of 17%.

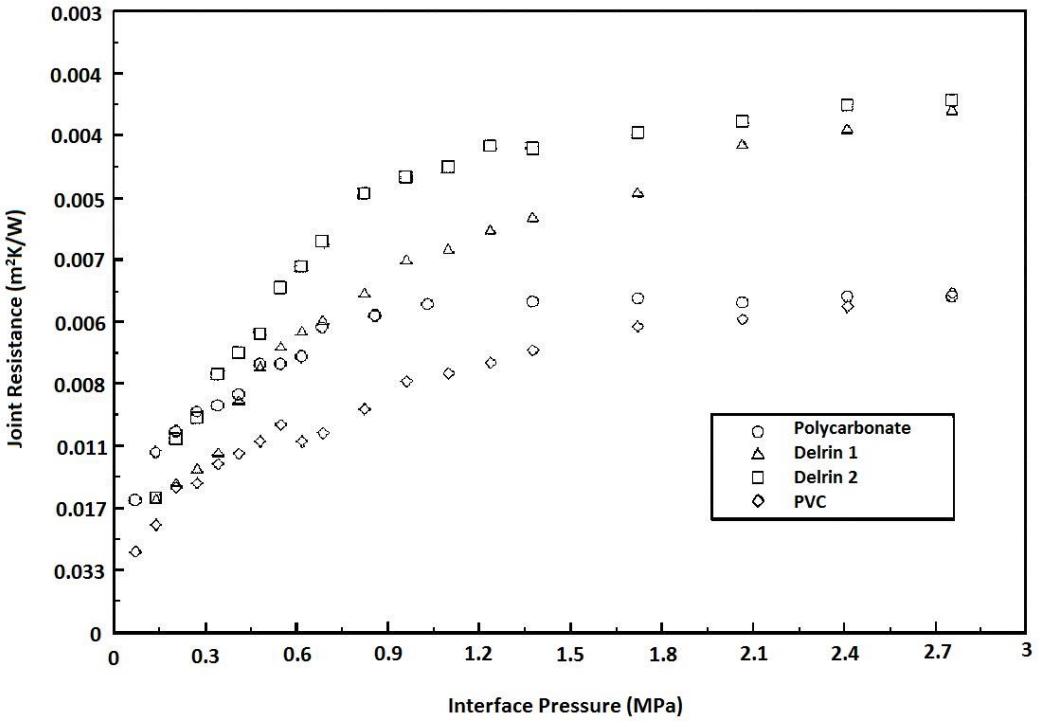

Figure 4.6 Experimental joint resistance (Fuller and Marotta, 2001).

Another instrument for measuring the thermal contact resistance at the polymer/mould interfaces was developed by Dawson et al. (2008) at the National Physical Laboratory. The apparatus developed is slightly different from axial heat flow apparatus used by Peterson and Fletcher (1988), Sridhar and Yovanovich (1996), Lambert and Fletcher (1995), Marotta and Fletcher (1998), Sunil Kumar and Ramamurthi (2003), Zhang et al. (2006), Wahid and Madhusudana (2000) and Bahrami et al. (2004). The top plate of the apparatus can be raised to a required height, to simulate gap formation between the polymer part and cavity surface when it shrinks while cooling. This allowed researchers to quantify TCR at the interface with and without the gap. The thermal resistance of the gaps was determined at the PMMA-air-steel interface

with introduced air gaps between PMMA sample and top (cold) plate. Gaps of approximately 0.1, 0.2, 0.5, 0.8, and 1.3 mm spacing were used. Other experimental arrangements included a TCR measurement without a PMMA specimen, with 1 and 3 mm PMMA specimens and 1 mm PMMA/ 0.9 mm steel plate/ 3 mm PMMA 'sandwich' structure.

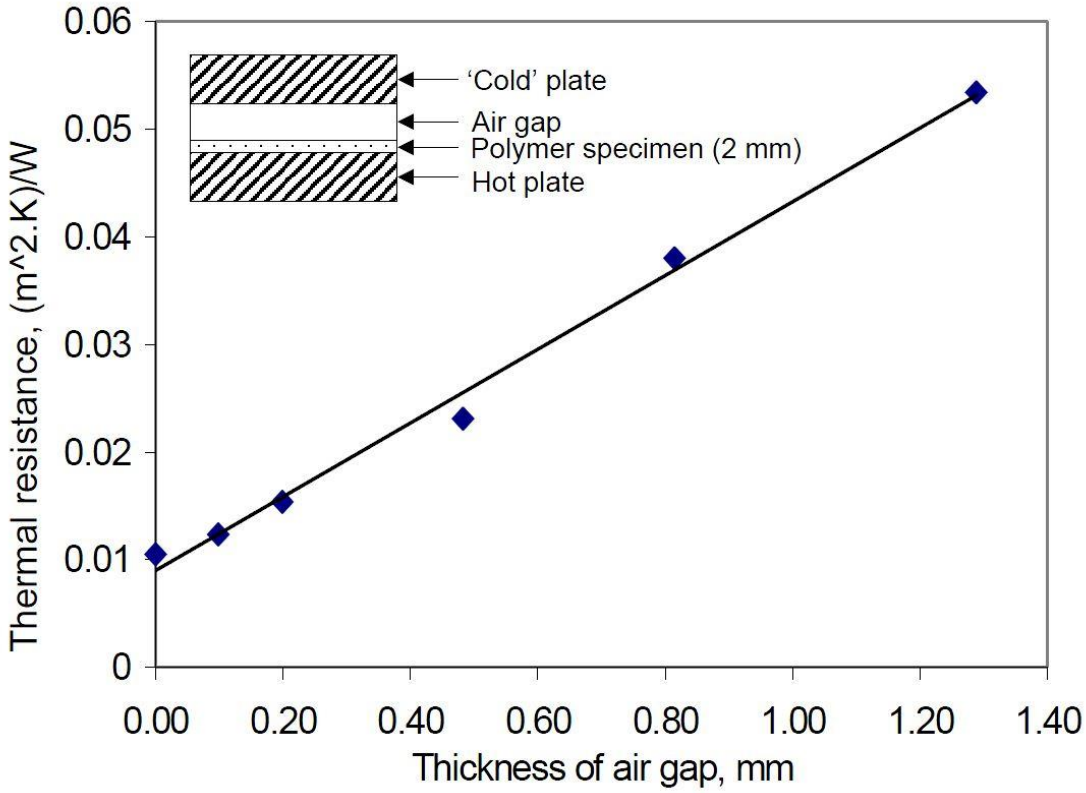

Figure 4.7 Thermal resistance of 2 mm thick PMMA specimen with increasing thickness of the air gap (Dawson et al., 2008).

Figure 4.7 demonstrates a rapid increase in thermal resistance as the thickness of the air gap increases. Measurements of the thermal resistance at the PMMA-steel interface provided values of 0.00019, 0.00015 and 0.00013 m^2K/W, which is equivalent to HTC values of 5200, 6600 and 7900 W/m^2K respectively. Through the modelling work authors also showed that the effect of varying HTC was greatest for thin-walled specimens with a thickness of 0.5 mm which is shown in Figure 4.8.

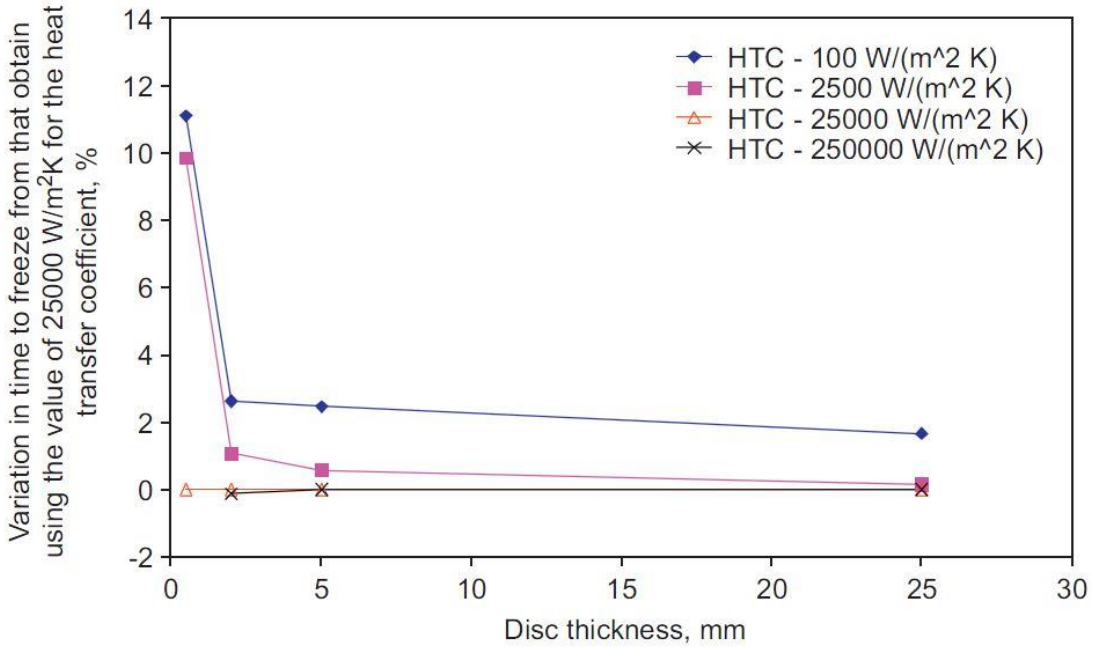

Figure 4.8 the effects of HTC values on time to freeze (Dawson et al., 2008).

4.5 Thermal Contact Resistance in Injection Moulding

Yu et al. (1990) performed an analytical and experimental study on the importance of TCR in injection moulding. They have shown that when TCR effects are not considered, computer aided engineering (CAE) software for cooling simulations in injection moulding (Polycool II) predicts a significantly lower cooling time when compared with the experimental data. They measured surface temperatures for both Acrylonitrile butadiene styrene (ABS) and the steel mould, to calculate TCR at the metal/ABS interface during the cooling phase. Operating settings such as injection pressure and injection temperature were monitored. The effects of inside cavity pressure, temperature, part thickness, and TCR were modelled as a function of time. Surface roughness, which was one of the most important parameters in metal/metal contacts, was ignored in both analytical and experimental analysis. Researchers have

experimentally obtained TCR values ranging from $0.35x10^{-3}$ to $8x10^{-3}$ m^2K/W for different materials and different thicknesses.

Table 4.2 Average TCR for different materials and different thickness (Yu et al., 1990).

	TCR, 10^{-3}, m^2K/W		
Material	**2 mm**	**3 mm**	**4 mm**
PC	4.5 ~ 8	0.9 ~ 1.1	0.85 ~ 1
Acetal	2.5 ~ 3	1.6 ~ 2.1	1.2 ~ 1.6
PC20%GF	2 ~ 4	0.85 ~ 1	0.8 ~ 0.95
PPO	2 ~ 3.8	0.7 ~ 0.9	0.6 ~ 0.8
PS	1 ~ 2	1 ~ 1.16	0.5 ~ 0.9
PP	0.65 ~ 1.7	0.35 ~ 0.65	0.4 ~ 0.7

The values obtained were later tested by Sridhar and Narh (1999). They have studied the simulation of the injection moulding process to show that TCR is time dependent and to show that TCR may underpredict the required cooling time by up to 15%. A tensile test specimen part was modelled using commercial simulation software - C-MOLD. Constant values for TCR equal to $4x10^{-5}$ m^2K/W as the minimum, and 10^{-3} m^2K/W, as the maximum, were selected in the software. Results have shown that lower TCR improves simulation of shrinkage and warpage, whereas a higher TCR value improves cooling time prediction. They have concluded that the use of time dependent TCR is essential.

Another parametric study was performed based on the same TCR values by Sridhar et al. (2000). Simulation analysis in C-MOLD was performed on three polymer part geometries looking on the effects of cavity pressure and mid-plane shrinkage. Results have shown that that higher TCR increases cooling time because, during the post-filling phase, when packing pressure is applied, heat is removed by conduction through the contact spots. Under high pressure metal/polymer interface will contain only microscopic gaps. Microscopic gaps in this case can be related to surface roughness of the mould. When the cavity pressure drops to atmospheric pressure, macroscopic gaps will form at the

interface. Macroscopic gaps are formed because of the effects of polymer shrinkage. Research showed that thermal contact resistance in injection moulding is strongly dependent on time and gap formation during post-filling phase.

Some interesting findings were published by Delaunay and Le Bot (2000). They have proven experimentally that constant mould temperature cannot be used as a boundary condition for injection moulding simulation. When hot polymer is injected, mould surface temperature is increased by approximately 10 $^{\circ}$C immediately after injection. Perfect contact between polymer and mould cannot be assumed either. Research shows that once the pressure in the cavity starts to drop, TCR increases. When cavity pressure reaches zero a sudden increase in TCR occurs, which can be connected with shrinkage of the polymer part. A gap between the part and mould surface appears. At the surface of the polymer part, a temperature increase was observed. Heat that escapes from the core of the part to the surface shows slower conduction due to the appearance of the gap and the polymer part gets reheated at the surface. Bendada et al. (2004b) have confirmed the observations made by Delaunay et al. (2000) and Sridhar et al. (2000) regarding the formation of the gap due to shrinkage when the pressure inside the cavity drops to atmospheric pressure. Bendada et. al (2004a) have designed a novel system for measuring polymer temperature during injection moulding. A hollow waveguide infrared device designed was able to measure temperature of the surface and bulk temperature of the polymer. The concept was based on polymer semi-transparency in the spectral band of photon detector and the temperature of polymer part. In practice the hollow waveguide collects the thermal radiation diffused from polymer melt and sends this energy to the photon detector. They have also confirmed that during

cooling and under packing pressure, the contact between the mould and polymer is very good and low TCR is observed. Temperature values obtained by a radiometric device were compared with the results obtained from the thermal sensor that was located close to the mould/polymer interface. Good agreement was observed between the two methods used. Later, Bendada et al. (2004b) improved the methodology for analysis of TCR that they have used in previous research. The infrared waveguide pyrometer was used to measure the temperature at the surface of the polymer, while two-thermocouple probe was used to measure the surface temperature of the mould. An inverse heat conduction algorithm was used to calculate heat flux at the mould/polymer interface from temperatures monitored inside the cavity. Experimentally, they have shown that TCR does not change when high cavity pressure is applied, but when pressure drops to zero, TCR suddenly increases. Also they have shown that TCR is higher when lower injection temperature is used. A similar effect was observed with the lower mould temperature.

Masse et al. (2004) studied the cooling stage of polymer within an injection moulding process, taking into account parameters such as TCR, residual stresses, and PvT diagram. They have tested three surfaces with different roughness (Ra = 0.05 µm, Ra = 1 µm, Ra = 5 µm) at different pressures. Results showed that resistance increases when roughness increases. If the number of peaks on the surfaces increases, more air is trapped at the interfaces. Based on experimental work, they have proposed an expression to predict TCR depending on roughness measurements. This expression is only valid for TCR prediction while polymer part is under packing pressure i.e. there are only microscopic gaps due to surface imperfection. The authors mentioned that they have proposed two constants that depend on the roughness; however,

the values were not published for the confidentiality reasons. Numerical simulations were based on temperature dependant Young's modulus and Poisson's ratio. The equation to simulate cooling of the polymer part was expressed as a combination of the state equation, displacement equation and the energy equation. The expression was validated by experimental work, which showed good agreement between the results. The whole study was based on amorphous material (ABS) and it cannot be applied onto semi-crystalline material.

Nguyen-Chung et al. (2010) focused on determination of HTC during the filling stage in microinjection moulding. A short-shot study on two geometries with thickness of 0.2 mm and 0.5 mm was performed. The relationship between the injection pressure and filling degree allowed the authors to determine the heat transfer coefficients during the filling stage. The experimental work showed that cavity pressure, thickness of the cavity and injection speed has an effect on HTC. It is shown in Figure 4.9 that a decrease in thickness of the specimen and a decrease of injection speed increases the heat transfer coefficient. The authors have suggested that there is a need for pressure-dependent model for heat transfer coefficients, because cavity pressure seemed to be a major parameter involved in heat transfer at polymer/steel interface. Figure 4.9 shows a relationship between injection pressure and filling degree for micro-spirals with a thickness of 0.2 and 0.5 mm. It can be seen that the values of heat transfer coefficient for thicker components are lower comparing to the thinner micro-spirals. For thicker micro-spirals HTC was varying between 0 and 8000 W/m^2K, whereas for thinner it was in the range of 1500 to 25000 W/m^2K.

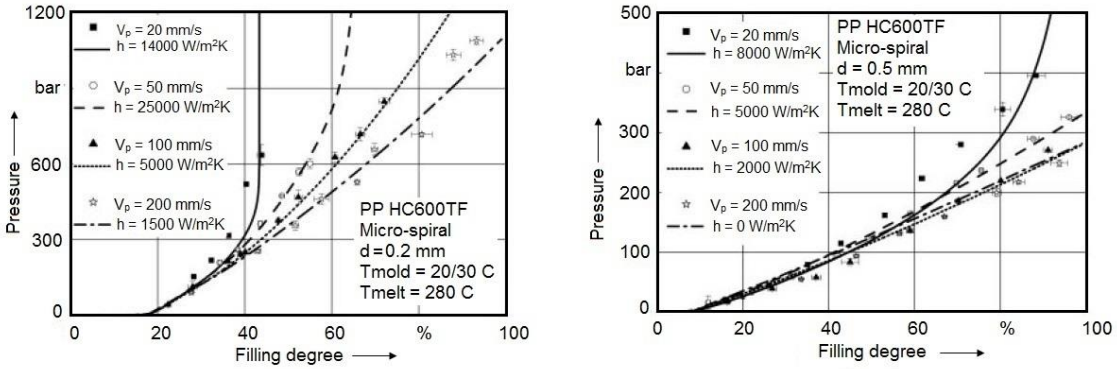

Figure 4.9 Pressure vs. filling degree for micro-spirals with thickness 0.2 mm (left) 0.5 mm (right) (Nguyen et al., 2010).

4.6 Microscale Surface Interactions

In conventional injection moulding the main parameters that control polymer flow in the cavity are melt temperature, mould temperature, injection speed, holding pressure and cooling time. The same parameter are also essential for microinjection moulding, but there is some evidence that microscale flow is different from macroscale flow. When features become smaller several interfacial effects such as surface tension, wall slip and wall adhesion might influence microscale cavity filling (Yao and Kim, 2002; Choi and Kim, 2010; Tofteberg and Andreassen, 2010).

Choi and Kim (2010) have performed microscale filling simulation for different channel sizes of 0.1, 0.5, 1, 5, 10, 50 and 100 µm and showed that slip and surface tension have important roles in micro filling. Their work suggests that slip model needs to be employed for channel diameters smaller than 10 µm and surface tension becomes powerful for channel of 0.1 µm. Yao and Kim (2002) also performed a simulation study on micro-channel filling. Their calculations showed that surface tension effect can be neglected for channel sizes above 1 µm, however wall slip effects need to be included to predict micro filling behaviour.

Anastasiadis and Hatzikiriakos (1998) performed an experimental study on the work of adhesion at polymer/steel interfaces to find out its effect on wall slip phenomena. They have used a sessile drop method and by measuring contact angle at the interface they could determine the work of adhesion. From their experimental work on a variety of polymer/substrate interfaces they have found that slip happens due to the adhesive failure at the interface.

4.7 Summary

The problem of TCR in injection moulding has been studied by several research groups. All the experimental and analytical work agrees that TCR at the mould/polymer interface is not negligible and perfect contact between mould and polymer cannot be assumed. Thermal contact resistance is not constant as assumed in simulation software. Researchers have shown that TCR is dependant strongly on the roughness of the mould surface, the material properties, and process conditions such as melt temperature, mould temperature, injection speed and cavity pressure.

Microinjection moulding is highly precise and sensitive in comparison with conventional injection moulding. At the present time, availability of data on TCR/HTC in microinjection moulding is limited and despite its importance in solidification prediction it remains poorly understood. HTC values reported in the literature were mainly obtained from experiments using conventional injection moulding machines or axial heat flow apparatus. These values may be invalid for microinjection moulding. Lack of data on microscopic rheology, wall slip phenomena, and polymer surface tension are other limitations in studying the cooling process in micromoulding.

Chapter 5. Materials and Characterisation

5.1 Sapphire Windows

Transparent sapphire windows were used as a surface of one half of the mould. These windows need to fit into the mould and be suitable for the application. To this end, sapphire windows were ordered with the following specifications: C-plane orientation +/- 0.5°, diameter of 26.5 +/- 0.05 mm, thickness of 4 +/- 0.1 mm, both sides polished to 10/5 scr/dig, with the minimal protective chamfer on both sides of the windows. Thermal properties of the sapphire are very similar to P20 mould steel. Specifically, thermal conductivity at 20° C is 29 W/mK for P20 tool steel and 23 W/mK for sapphire. Specific heat capacity at 20° C is 460 J/kgK for P20 steel and 750 J/kgK for sapphire. Moreover, optical properties make a sapphire window ideal for the application. Sapphire window has a transmission range of 0.17 - 6.5 μm (see Figure 5.1) allowing the measurements in the short to medium IR spectrum. (Globalopticsuk, 2012; Bohler-Uddeholm, 2000).

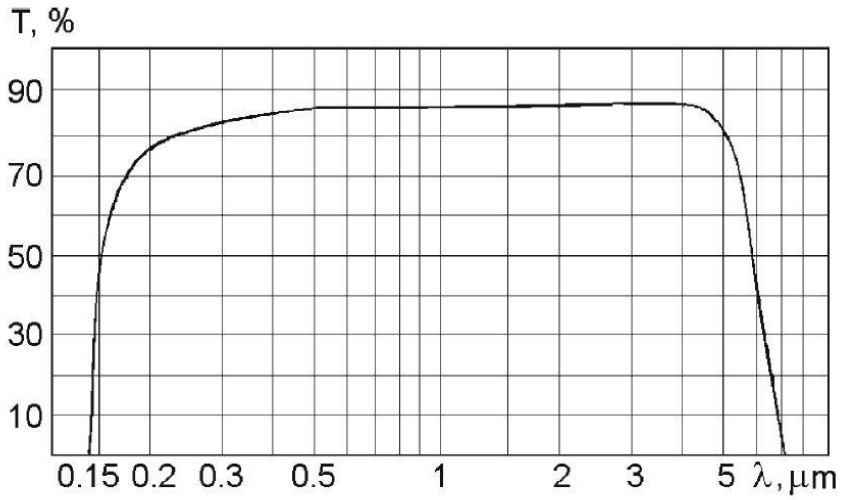

Figure 5.1 Transmission range of the sapphire window (Dobrovinskaya et al., 2009).

5.1.1 Sapphire Windows Micromachining

In order to study the effects of surface roughness on polymer cooling, sapphire windows were machined using an Oxford Lasers PicoLase 1000 micromachining system at Cardiff University.

During micromachining a high density optical energy is focused on a very small region of the work piece and in doing so the material is removed by melting, breaking chemical bonds, evaporation and material elimination at the region of incidence. This region is also referred to as a focus area and can be as small as 2 μm. The brittle and hard nature of the sapphire makes it extremely difficult to machine by conventional methods mainly due to unacceptable tool wear and damage. Major advantages of laser micromachining is that it is a non-contact technique and in combination with a multi-axis position system it can be used for drilling, milling out, cutting and patterning microscopic features on the same machine. By using the laser ablation technique a range of surfaces were prepared with different roughness as well as micro pillars arrays of different heights. Different surface roughnesses can be achieved by increasing the power density of the laser (Karnakis et al., 2007a; Karnakis et al., 2007b; Samant et al., 2009; Chen et al., 2005). Figure 5.2 shows two sapphire windows which were used in experimental work. One of the sapphire windows is optically flat and the other one has a three by three millimetres laser micro machined square patch in the centre of the window.

Figure 5.2 Optically flat sapphire window on the left and laser machined sapphire window on the right.

5.1.2 Surface Topography Measurements

A total of five sapphire windows were used in experimental study. One of them was optically flat (N1), two roughened (N2, N3) and two structured with micro pillars (N4, N5). Their topography was analysed using Olympus LEXT OLS4000 laser confocal microscope. The laser microscope employs a laser beam with a wavelength of 405 nm allowing visualisation with 120 nm lateral resolution and 10 nm Z resolution. The surface area roughness parameters conform to ISO 25178 standard for analysis of 3D areal surface texture. The evaluation area was selected based on the infrared camera's frame size of 128 x 128 pixels, which is equal to 1.92 x 1.92 millimetres. The average surface roughness was measured for sapphire windows N1, N2 and N3, whereas analysis of the sapphire windows N4 and N5 was based on the average height of 20 micro pillars randomly selected in the centre of the array. Measurements were taken with 20X lens using a stitching function with 20 percent overlap to produce an area of 3 mm x 3 mm. Then a region of interest of 1.92 mm x 1.92 mm was selected in the middle of the scanned region and surface roughness calculated in terms of Sa and Sq shown in Figure 5.3 and summarised in Table 5.1.

Sa - expresses the average of the absolute values of the height within a sampling area. It is equal to the arithmetic mean of the measured region on the three-dimensional display diagram when valleys have been changed to peaks by conversion to absolute values. Sq - expresses the root mean squared value of Z(x,y) within a sampling area. It is equal to the average mean squared value of the measured region on the three-dimensional display diagram when valleys have been changed to high peaks by squaring. (Leach, 2010; Olympus, 2015a).

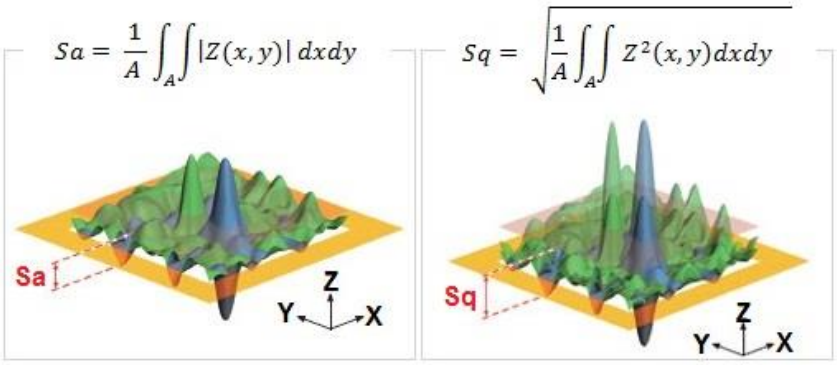

Figure 5.3 Height parameters. Arithmetic mean height (Sa) and root mean square height (Sq) (Olympus-ims.com, 2015b).

Table 5.1 Sapphire windows surface topography measurements.

	Sa (µm)	**Sq (µm)**	**Evaluation area (µm)**
N1 (Polished)	0.007	0.011	1920 x 1920 1920 x 1920 1920 x 1920
N2 (1 µm)	1.089	1.335	
N3 (4.2 µm)	4.214	5.091	
	Average height (µm)	**Standard Deviation (µm)**	**Number of Pillars**
N4 (15 µm pillars)	15.14	0.277	20
N5 (30 µm pillars)	33.2	1.245	20

Figure 5.4 shows the topography of sapphire window N1 which in the text is referred to as polished sapphire and sapphire N2 referred to as 1 µm sapphire window. Figure 5.5 shows the topography of sapphire window N3, referred to as 4.2 µm sapphire window and window N4, referred to as 15 µm pillars sapphire window. Figure 5.6 shows the topography of window N5 referred to as 30 µm pillars sapphire window.

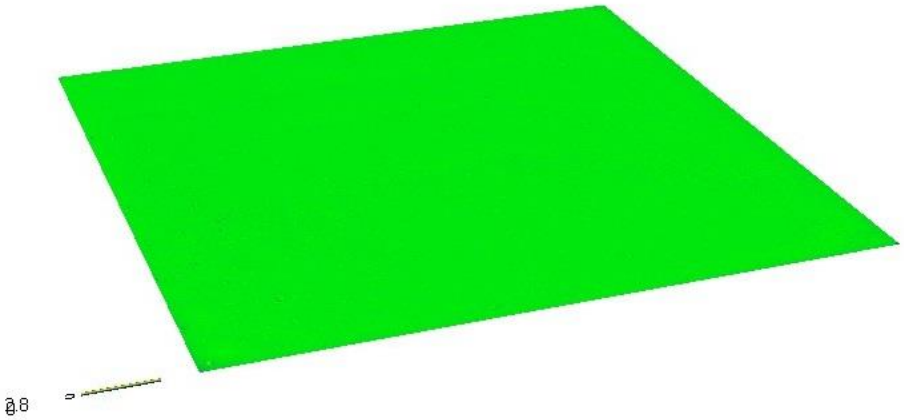

(a)

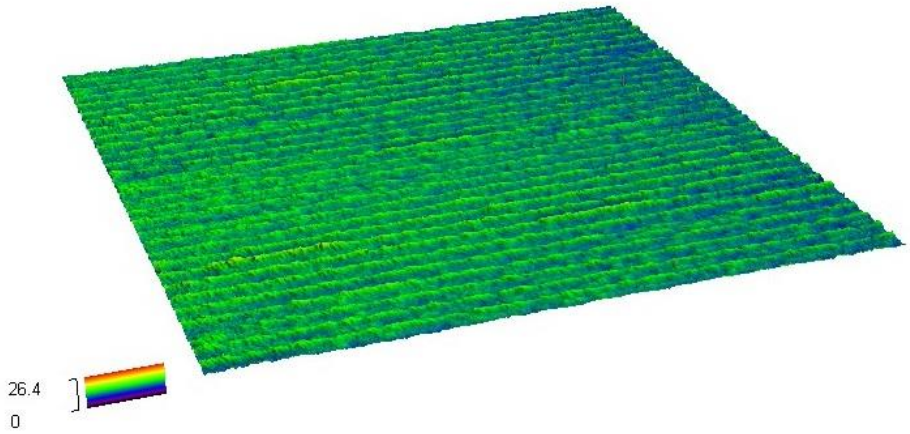

(b)

Figure 5.4 The surface roughness of sapphire N1 and (b) sapphire N2.

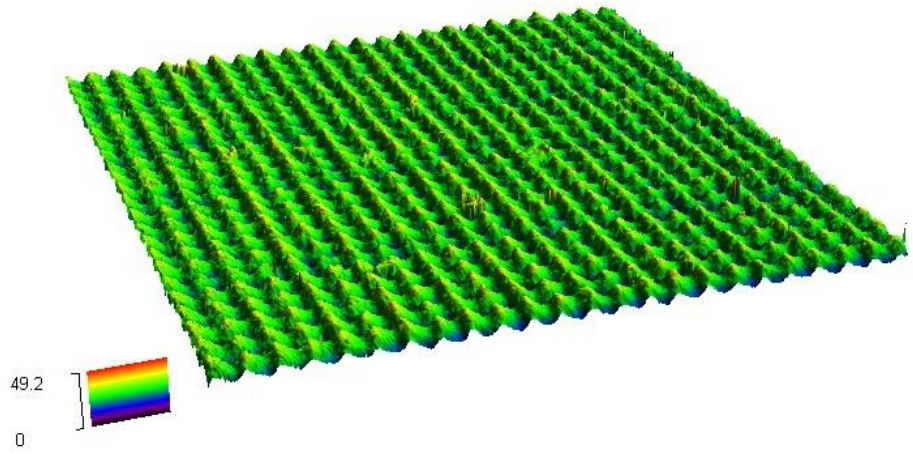

(a)

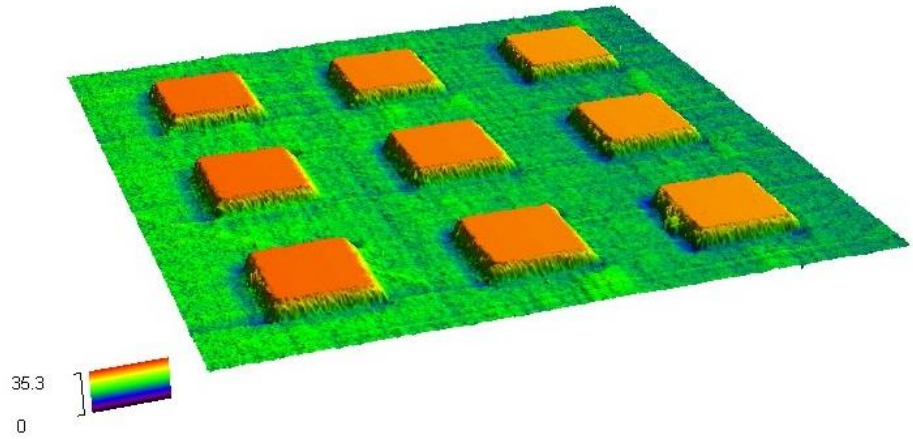

(b)

Figure 5.5 The surface roughness of (a) sapphire N3 and surface topography of (b) sapphire N4.

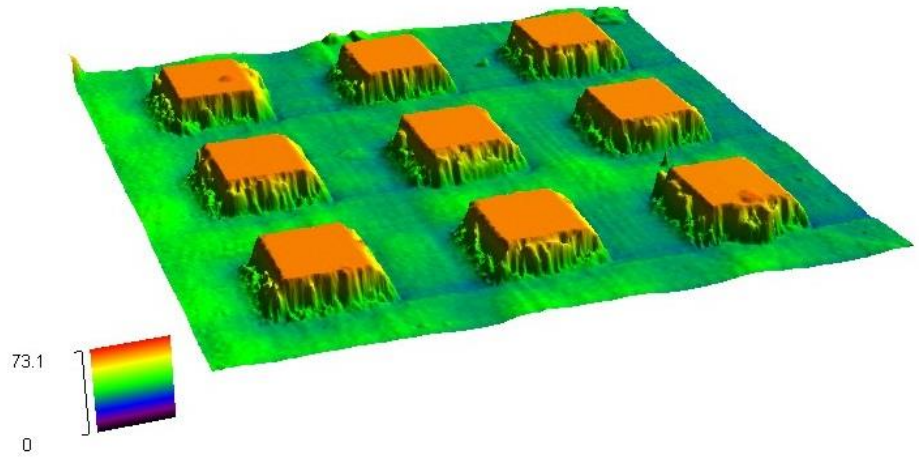

Figure 5.6 surface topography of sapphire N5.

5.2 Polymers Used in the Study

Two commonly used materials in injection moulding, polypropylene (PP) and polystyrene (PS), were selected to perform the planned design of experiments (DOE). Their properties are provided in Table 5.2. Both materials are selective emitters and appear transparent to most IR wavelengths. To overcome IR transparency of the selected materials it was decided to compound them with carbon black (CB) masterbatch, as carbon materials show strong absorption in the IR region of the spectrum (Bansal and Goyal, 2005).

Table 5.2 Polymer materials properties (Moldflow material database). Note: * – the number in the brackets is the material melt temperature in (°C), the other four digits signify its viscosity (Pa s) measured at a shear rate of 1000 (1/s).

Material	Ineos 100-GA12	BASF Polystyrol 158K
Category	Crystalline	Amorphous
Moldflow Viscosity Index*	VI(240)0071	VI(230)0096
Transition Temperature (°C)	182	106
Specific heat (J/kg-C)	2720	1975
Thermal Conductivity (W/m-C)	0.16	0.155

Coefficient of thermal expansion (1/C) [E-005]	9.05	8
Melt density (g/cm^3)	0.75967	0.94609
Solid density (g/cm^3)	0.92889	1.0499
Elastic modulus (MPa)	1340	3300
Poisson's ratio	0.392	0.35
Shear modulus (MPa)	481.3	1220

5.3 Materials Preparation

5.3.1 Carbon Black Masterbatch

Carbon black can be described as a universal additive, as it can provide pigmentation, anti-static properties, electrical conductivity, UV screening, and high absorption of light, the last of which is important for this research. The major use of carbon black is in elastomers, particularly in the production of tyres, where relatively high loading of carbon black contributes to reinforcement, resistance to tearing and abrasion. In thermoplastics they are used at lower loadings to reduce degradation due weathering (Murphy, 2001; Rothon, 2003).

The black universal masterbatch PLASBLAK UN2014 was provided by Cabot free of charge to support the research project. PLASBLAK UN2014 is a jet black masterbatch specially designed for colouration of thermoplastics. It can be used in compounding, injection moulding and extrusion application and will retain good physical properties in the final products. It has 50% jet carbon black pigment, compatible with LDPE, LLDPE, PP, ABS, SAN, PS, ethylene copolymers. It also offers limited suitability in some PA, PVC, PET and PC. Density of the CB masterbatch is 1220kg/m^3 at 23° C and MFI 21.6 kg/190°C of

36g/10 min. PLASBLAK UN2014 is supplied in regular pellet form. The addition rate depends on the requirements of the application with recommended rates of 1% to 2% masterbatch (Cabot Corporation, 2012).

5.3.2 Extrusion Compounding

Due to high demand for coloured plastics, compounding became a separate industry. Based on this, compounders have extended their activities for production of reinforced plastics and other homogeneous blends where several different ingredients can be mixed. Modern compounding instruments are based principally on extrusion mixing which is the main method of compounding thermoplastics.

Compounding of PP and PS with carbon black masterbatch was performed on a twin-screw extruder due to its high efficiency in mixing action comparing to single screw extruders. A Prism TSE 16 TC bench-top co-rotating twin-screw extruder was used for materials compounding. Specifications are provided in Table 5.3.

Table 5.3 Prism TSE 16 TC twin-screw extruder specifications.

Model		TSE-16-TC
Screw Diameter	mm	16
Barrel Length	L/D	15:1
Screw Speed	rpm	0-300
Barrel Temperature	°C	up to 400
Pressure Range	bar	0-100
Typical Output	Kg/hr	5

Prior to extrusion polystyrene was dried using a Motan dryer set at 70°C for 4 hours. The polymer was cooled and mixed with black masterbatch in a tumble blender with 4% of masterbatch to 1 kg of polystyrene. Polypropylene does not

require drying, therefore it was mixed in the same proportion but without drying. Mixed pellets of materials were then compounded on a twin-screw Prism 16 extruder. The throat of the extruder was fitted with an extended tube delivery system with a sealing lid. Each pre-blend was introduced into the throat in one process and the throat lid sealed. The screw speed was set to 150 rpm and barrel temperatures from throat zone to die were 180-200-215°C for both material blends. The molten blends were cooled with water, air dried and then fed into a Varicut pelletiser unit. The pellets of each batch were collected in polythene bags and labelled. These were then dried using Motan drier for 4 hours and placed in foiled punches. The carbon black polystyrene pouches were purged with nitrogen and heat sealed to exclude moisture.

5.4 Polymers Characterisation

Addition of any filler changes nearly every property of the polymer which can give advantages or disadvantages to the materials. Semi-crystalline and amorphous polymers react to the addition of fillers in the same way. The addition of pigment or colour masterbatch affects thermal and mechanical properties in the same way as any other filling materials, but concentration of it is in the range of 0.5 – 10% (usually 2%) by weight which is very low to significantly affect its properties (Rothon, 2003; Murphy, 2001). Two techniques, namely Fourier transform infrared spectroscopy and differential scanning calorimetry were employed to analyse the effects of carbon black on IR transparency and thermal properties of the compounded materials.

5.4.1 Fourier Transform Infrared Spectroscopy (FTIR) Analysis

Transmission spectroscopy is one of the most widely used techniques for obtaining infrared spectra, where a sample is placed in the optical path of the

infrared beam. The advantage of this method is that transmission spectra has high signal-to-noise ratios and it works on solids, liquids, gases, and polymers. The FTIR spectrometers measure the frequencies and intensities of the radiation that is transmitted through the specimen (Bart, 2006; Smith 2011).

Each chemical bond in a polymer has different vibrational, rotational, torsional and bending modes of excitation and infrared light is used to excite each of these modes. When IR radiation passes through the material it is absorbed only at frequencies corresponding to the molecular modes of vibration and each kind of bond may absorb infrared radiation at one or more specific frequencies. For example, both polypropylene and polystyrene have strong but narrow absorption band in the range between 3000 and 2850 wavenumbers which corresponds to a stretching motion of the bond (Koenig, 1999; Stuart, 2004).

The main optical components of a spectrometer are:

- The infrared source, which provides the infrared light beam that travels through the spectrometer, passing though the specimen.
- The interferometer, which consists of the beamsplitter and two mirrors.
- The beamsplitter, which separates one infrared beam into two beams and then recombines these beams into one. One of the beams is reflected from the beamsplitter to a fixed mirror and the back to the beamsplitter. The other beam is transmitted through the beamsplitter to a moving mirror and back to the beamsplitter where the beams recombine.
- The infrared detector, which turns light intensity into the proportionate electrical signal and passes it to the computer for processing.
- Laser, which is used measure mirror movements, align and calibrate the spectrometer.

All of the components listed above generate an infrared spectrum. The infrared spectrum is a two-dimensional plot where intensity is reported in terms of percent transmittance or absorbance (Smith, 2001; Thermo Scientific, no date).

$$\%\boldsymbol{T} = (\boldsymbol{S}/\boldsymbol{B}) \times \mathbf{100} \quad \textbf{5.1}$$

where S in the intensity of IR energy through the sample and B is the background.

5.4.1.1 Experimental Procedures

Moulded samples of polypropylene (PP), polystyrene (PS), carbon black filled polypropylene (CB PP) and carbon black filled polystyrene (CB PS) were analysed for IR transmission using a Nicolet iS50 FTIR spectrometer. The FTIR spectrometer is equipped with a Mid-IR DTGS detector with KBr (Potassium Bromide) beamsplitter. The DTGS stands for deuterated triglycine sulphate and refers to the materials the detector is made from. Figure 5.7 shows PP and CB PP samples mounted in a special holder which allows the infrared beam to pass through. The samples are round disks with diameter 16 mm and thickness of 0.5 mm.

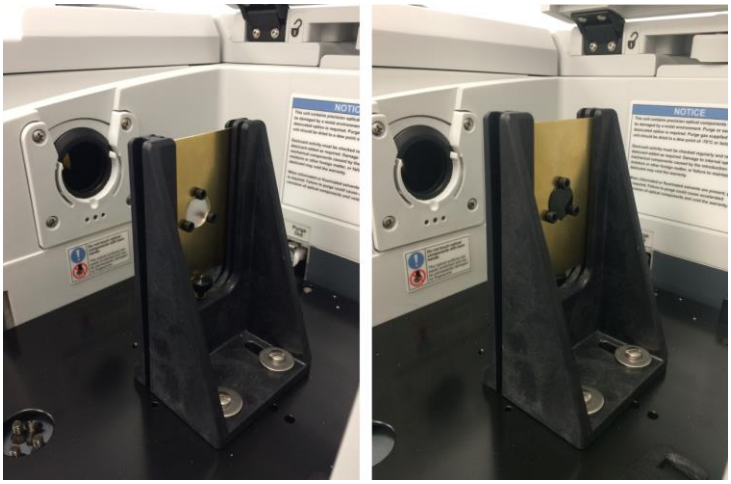

Figure 5.7 PP (left) and CB PP (right) specimens mounted in a sample holder of the Nicolet iS50 FTIR spectrometer.

All spectra were recorded at the resolution of 4 cm^{-1} and spectral range of 4000 – 1960 cm^{-1} (2.5 – 5.1 µm wavelength). A total of 32 scans were accumulated for each spectrum. The spectra was analysed by Omnic 9.0 software.

5.4.1.2 Results

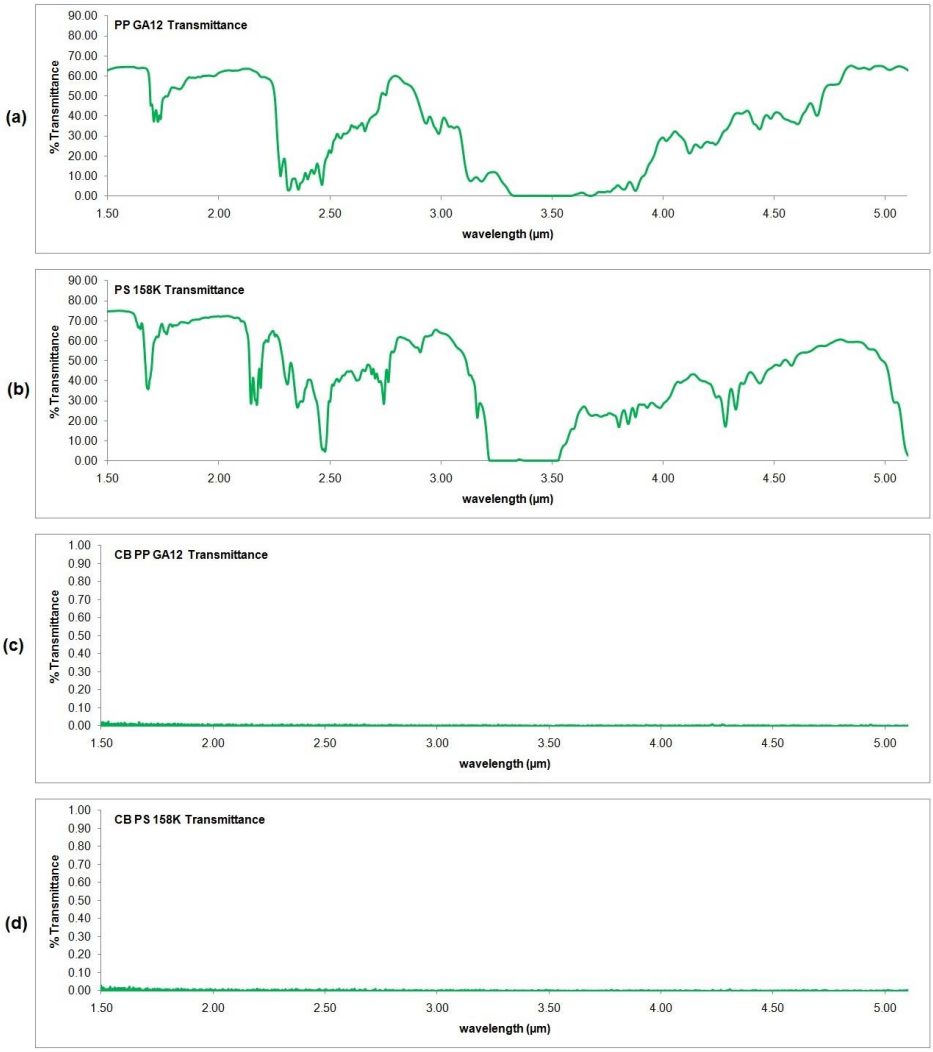

Figure 5.8 IR spectra of PP (a), PS (b), CB PP (c) and CB PS (d).

The obtained IR spectra for PP and PS shows strong absorption around 3.4 µm wavelength which is a carbon-hydrogen (C-H stretching) IR band. Because of the samples thickness, peaks around 3.4 µm appear “chopped-off”. This means

that samples absorb all the light in this wavelength region, but they transmit some of the IR light outside of the region. Figure 5.9 shows the effect of sample thickness on IR transmission. A thin film of polystyrene is highly transparent in Mid-IR range, but shows a narrow and strong band at 3.4 µm wavelength.

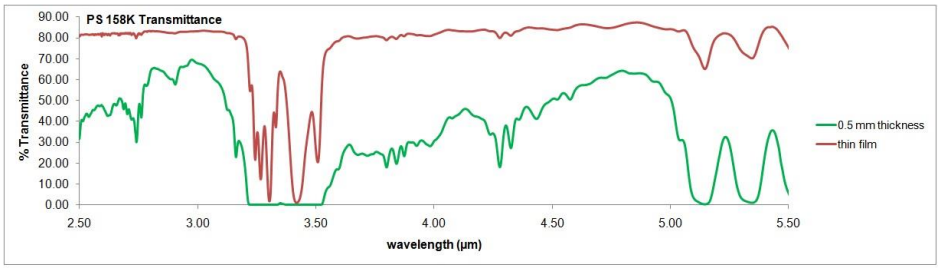

Figure 5.9 IR transmittance of 0.5 mm thick polystyrene sample and thin film.

The main purpose of using this technique was to identify how carbon black masterbatch affects IR transmission of the selected polymers. The IR spectra for CB PP and CP PS in Figure 5.8 shows, that all IR light in Mid-IR range is absorbed. The conclusion was made that addition of 4% of carbon black masterbatch to PP and PS makes it possible to accurately measure surface temperature of the polymers during the microinjection moulding cycle.

5.4.2 Differential Scanning Calorimetry (DSC) Analysis

Differential scanning calorimetry is an effective thermal analytical technique to characterise physical properties of polymers as a function of temperature. Differential scanning calorimeters normally have two sample positions, shown in Figure 5.10. One position is for the specimen under the investigation and the other is for the reference sample, which often is an empty pan. DSC measures the difference in heat flow rate (mV) between a sample and inert reference at a defined heating rate as a function of time and temperature. The heat flow is described as below,

$$\frac{dH}{dt} = Cp\frac{dT}{dt} + f(T,t) \qquad \textbf{5.2}$$

where $\frac{dH}{dt}$ is the heat flow signal, Cp is the sample heat capacity, $\frac{dT}{dt}$ is the heating rate, and $f(T,t)$ is a function of time and temperature.

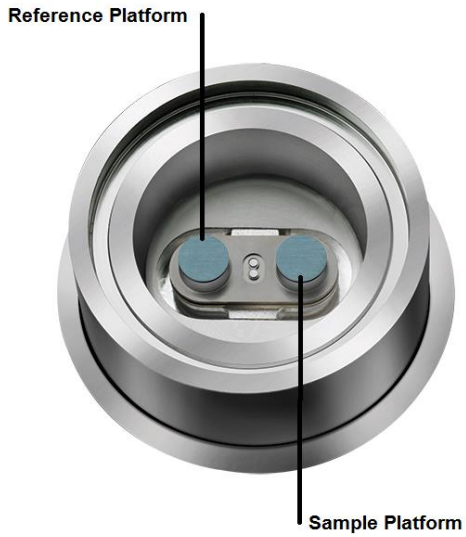

Figure 5.10 DSC cell.

DSC results plot normally shows differential heat flow versus temperature or time. When the specimen absorbs energy the enthalpy change is called endothermal and it is found in the glass transition (T_g), melting and vaporisation. During exothermal transitions energy is being released, which happens as a result of crystallisation, curing, oxidation and other exothermic processes. A DSC can detect and measure any transition in a material that involves a change in the heat content of the material (Bart, 2006; Schick, 2009).

The T_g is the reversible transition in amorphous materials due to a change in chain mobility. Bellow the T_g an amorphous polymer is hard and brittle, while above T_g it becomes more rubbery. The T_m is a melting point, where polymer chains do not have ordered arrangement and can move freely, which is characteristic for crystalline or semi-crystalline polymers (Sandler, 1998).

In this project, DSC was chosen to study the effect of addition of carbon black masterbatch on thermal properties of PP and PS.

5.4.2.1 Experimental Procedures

A Discovery DSC by TA Instruments was used to analyse the melt temperatures (T_m) for PP and CB PP, the glass transition temperatures (T_g) for PS and CB PS, and measurement of heat capacity for all four materials.

The performance of DSC mainly depends on baseline stability, reproducibility, sensitivity and resolution. Prior to experimental study with polymers a test run was performed with a sapphire sample which is one of the reference materials. The test run has showed an exothermal transition around 60 °C which is not characteristic for sapphire. The transition was suggesting that cell was contaminated; therefore cell cleaning and new calibration was required.

5.4.2.1.1 DSC Calibration

A number of calibration procedures were performed, including Tzero calibration, enthalpy (cell) constant calibration, temperature calibration, standard heat capacity calibration, and modulated heat capacity (MDSC) calibration.

Tzero calibration is a two step calibration, first without samples (baseline); second with sapphire disks with known thermal properties. Both experiments used the same method, where cell was equilibrated at -90 °C, held isothermally for 10 minutes and heated to 400 °C at the constant rate of 20 °C/min. The calibration curve showed a 25 µW change of heat flow in the baseline which is within an acceptable range.

The enthalpy (cell) constant calibration was performed with indium (temperature standard) where it was heated through its melting transition. The calculated heat of fusion was then compared with the theoretical value. The cell constant is the ratio between these two values.

Temperature calibration was also performed with indium. The recorded melting point of this standard was compared with the known melting point, and the difference was recorded for temperature calibration (TA Instruments, 2013). All the resultant calibration data was saved and applied to the instrument.

5.4.2.1.2 Samples Preparation

Material samples were prepared from microinjection moulded components. Samples with a big melt cushion of more than 10 mm were moulded. The melt cushion was afterwards machined into cylinders with diameter of 5 mm and finally machined into the thin disks. Flat components work best comparing for example to irregular shape of a sliced pellet, because good thermal contact is achieved between the sample and platform within the DSC cell.

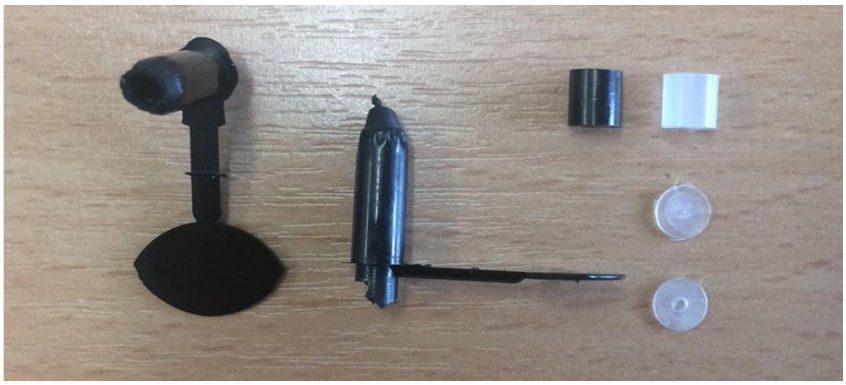

Figure 5.11 Material samples preparation for DSC analysis.

Glass transition temperatures and melting temperatures of the polymer samples were measured. Samples were accurately weighted using a Mettler Toledo analytical balance (AB265-S). In an ideal DSC experiment sample would be placed directly on to a platform to provide best thermal transfer. However, from the practical point of view this is not feasible due to potential contamination of the cell. Therefore, DSC measurements require that samples are placed in a sample pan to eliminate direct contact between the sample with surface or

sensor. In measuring T_g and T_m as a function of temperature samples (7-9 mg) were encapsulated in aluminium pans and an empty aluminium pan was used as a reference. The samples were heated from 40 °C to 300 °C at a heating rate of 10°C/min. Subsequently samples were cooled down at the same rate, and heated again from 40 °C to 300 °C. During the experiments cell was purged with N_2 at a flow rate of 50 ml/min. Running heat/cool/heat cycle erases thermal history of the sample, therefore, normally the second heat cycle is analysed.

The reported T_g values represent the midpoint temperature for the glass transition of the second heating cycle. The T_m is defined as the temperature at the peak apex.

5.4.3 Results for Glass Transition and Melting Temperature

Figure 5.12 shows a comparison of melt temperatures for polypropylene and carbon black filled polypropylene during second heat cycle. The addition of 4% carbon black masterbatch did not affect the T_m of polypropylene, as only a change of 0.019 °C was observed. Figure 5.13 represents T_g measurements for polystyrene and carbon black filled polystyrene. Measured midpoint for PS was 102.751 °C and 102.119 °C for CB PS respectively. Observations of T_g range and midpoint for PS and CB PS suggest that addition of carbon black masterbatch does not affect T_g significantly.

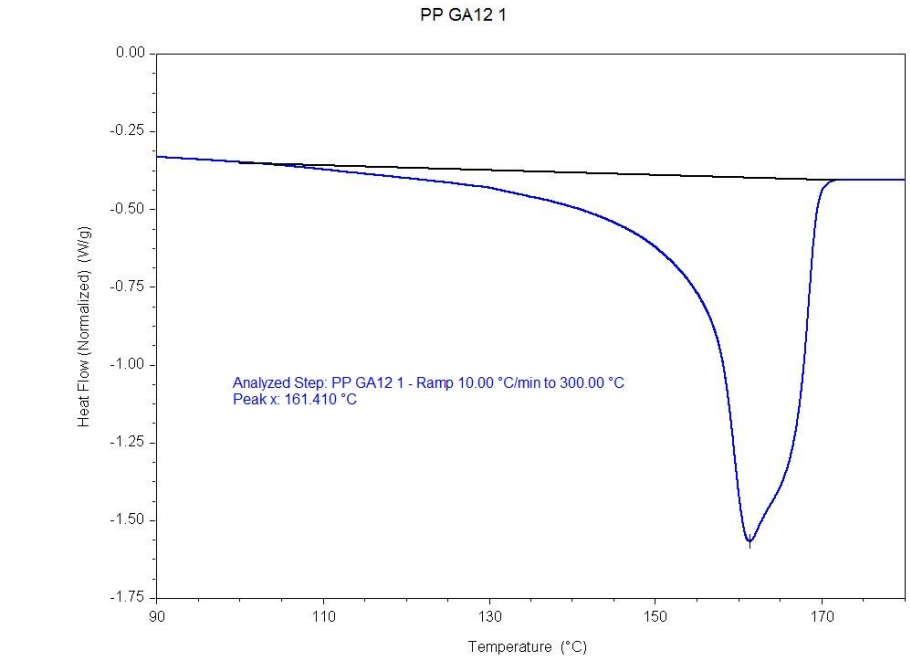

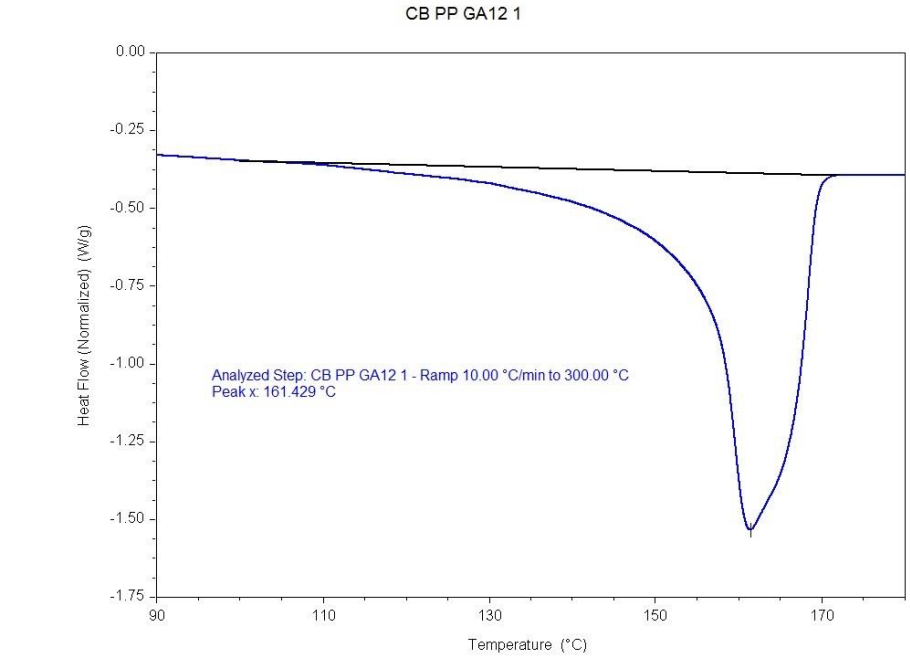

Figure 5.12 Comparison of Tm for PP and CB filled PP.

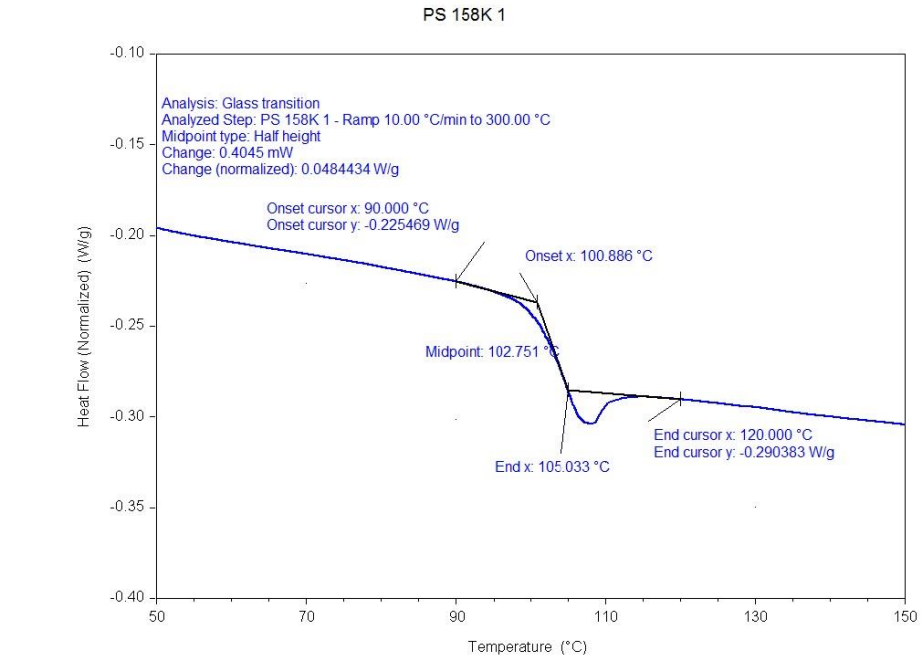

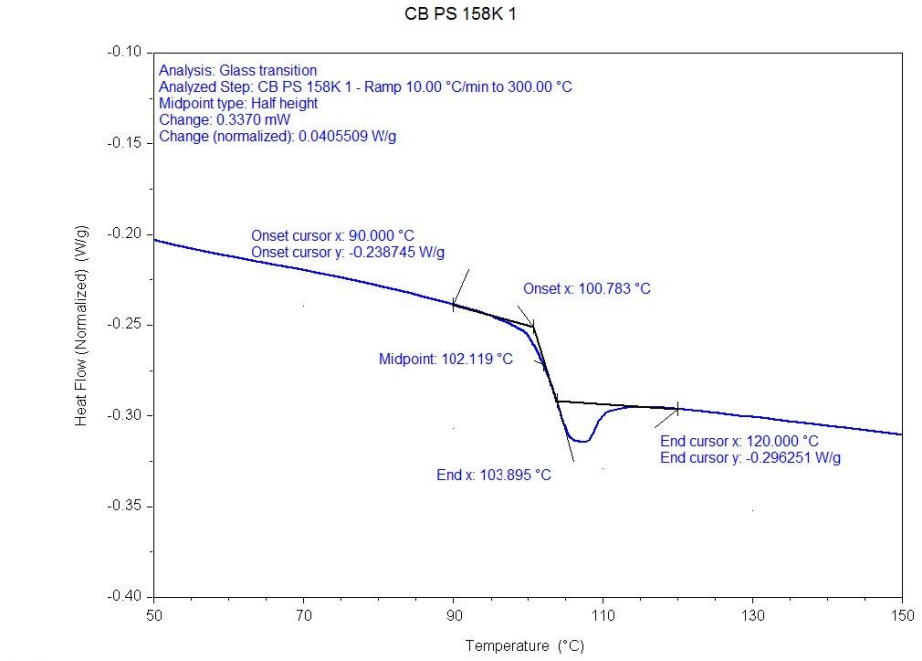

Figure 5.13 Comparison of Tg for PS and CB filled PS.

5.4.4 Specific Heat Capacity Measurements (C_p)

Specific heat capacity ($C_{p)}$ is a fundamental, thermodynamic property of material and is the one of the best ways to compare samples. C_p is the amount of energy required to heat one gram of the material by one degree Celsius (Bruce Cassel, no date). Measurement of heat capacity can readily be achieved using conventional differential scanning calorimetry by heating a test sample at a fixed heating rate over a temperature range. The resulting heat flow response, normalised for specimen mass and heating rate is proportional to specific heat.

The Discovery DSC can directly measure C_p in a single run with better accuracy comparing to traditional methods for measuring heat capacity. The Modulated DSC (MDSC) can generate C_p data within an accuracy of 2-3%. Moreover, traditional three run method (ASTM E1269 Standard) requires a number of separate experiments for baseline, calibration and sample analysis which is more time consuming than MDSC.

In MDSC experiments a sinusoidal oscillation is overlaid on the conventional linear heating, resulting in cyclic heating profile which is demonstrated in Figure 5.14. The resultant heat flow from this cyclic treatment is a combination of heat capacity related (reversing) heat flow and heat flow due to kinetic events (nonreversing), but DSC measures the sum of two. It must be emphasized that MDSC does not measure heat capacity directly. Heat capacity units are obtained by dividing heat flow by heating rate, therefore glass transition and melting transition are included in C_p signals, shown in Figure 5.15 and 5.17. The absolute values of C_p are obtained in the temperature regions where there are no transitions and they are presented in Tables 5.4 and 5.5.

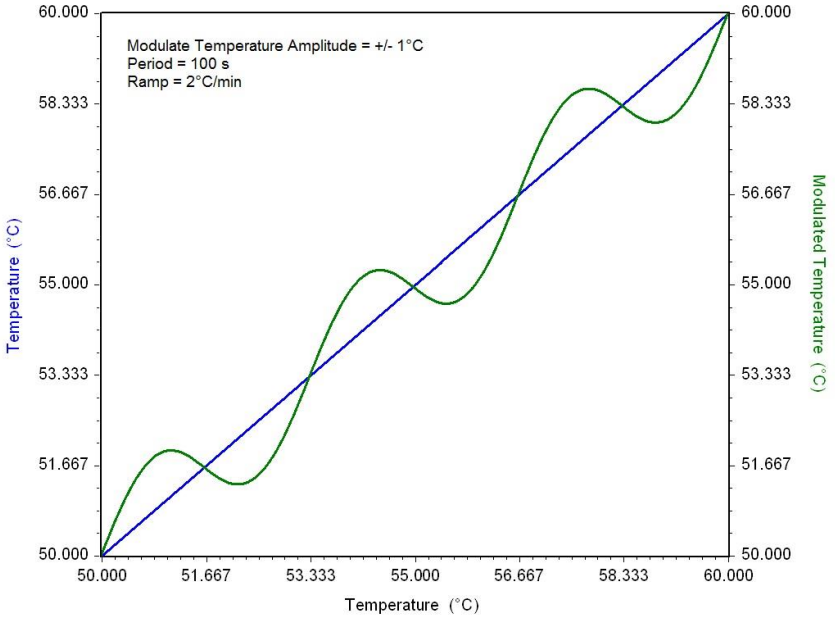

Figure 5.14 Modulated DSC heating profile.

MDSC heat capacity calibration was done prior to C_p determination of the samples. Sapphire was used to perform this calibration. The calibration experiment was performed under the same conditions to those that were selected to be used for polymer samples, including pan type, modulation amplitude, period, and heating rate. The reversing heat capacity calibration curve was calculated by dividing the theoretical value of heat capacity, by the measured one. Thin polymer disks of PP, CB PP, PS and CB PS were encapsulated in standard aluminium pans. Three samples of each material were tested. Modulation conditions were as follows; heating rate 2 °C/min, modulation amplitude ±1 °C, and modulation period 100 s. Measured C_p data was averaged for each of the materials.

5.4.5 Results

5.4.5.1 Comparative Specific Heat Capacities of Polystyrene and Polypropylene

Figure 5.15 shows C_p results of polystyrene with some of the measured and literature values.

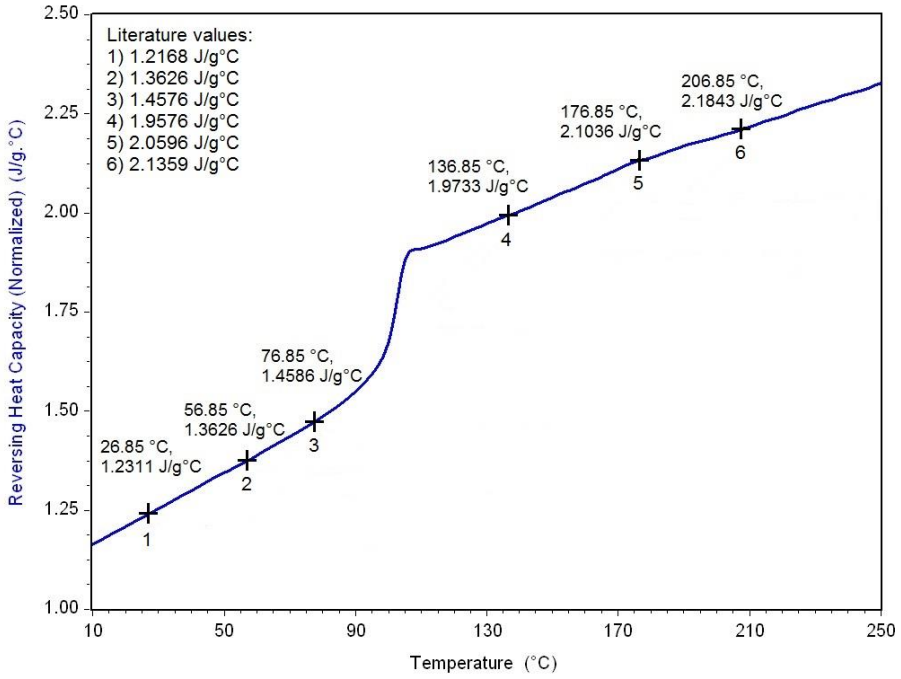

Figure 5.15 Specific heat capacity plot of polystyrene.

Table 5.4 shows a comparison between specific heat capacities for polystyrene in the literature obtained measurements from 29 different samples and measurements from MDSC in the present work. The measured C_p values agree well with the values reported by Gaur and Wunderlich in 1982a within ± 0.05 J/g°C, with the maximum error of 2.4 %. Moreover, polystyrene is well known to be used as a reference material for a range of physicochemical analysis including thermal resistance, infrared transmission, melt flow rate, enthalpy and heat capacity (Montgomery and Sauerwein, 2011). TRIOS, TA

instruments' software package contains a reference C_p data for polystyrene, but only for the glassy state, with the temperature range of 1 to 75 °C. This data was also compared with experimentally obtained values of heat capacity of polystyrene. Figure 5.16 shows both experimental data over the range of 10 to 75 °C for C_p which is a blue line and reference data from the software, represented by green line. The maximum error observed was 0.003 J/g°C, or 0.2 %.

Table 5.4 Comparative specific heat capacities of polystyrene.

Polystyrene

Temperature (°C)	Experimental Cp (J/g°C)	Literature (J/g°C)	Difference (%)
16.85	1.1874	1.1775	0.8
26.85	1.2311	1.2168	1.2
36.85	1.2761	1.2691	0.5
46.85	1.3206	1.3156	0.4
56.85	1.3626	1.3626	0.0
66.85	1.4098	1.4100	0.0
76.85	1.4586	1.4576	0.1
86.85	1.5159	1.5056	0.7
106.85	1.8856	1.8812	0.2
116.85	1.9098	1.9067	0.2
126.85	1.9423	1.9322	0.5
136.85	1.9733	1.9576	0.8
146.85	2.0028	1.9832	1.0
156.85	2.0358	2.0086	1.3
166.85	2.0721	2.0340	1.8
176.85	2.1036	2.0596	2.1
186.85	2.1322	2.0803	2.4
196.85	2.1570	2.1105	2.2
206.85	2.1843	2.1359	2.2

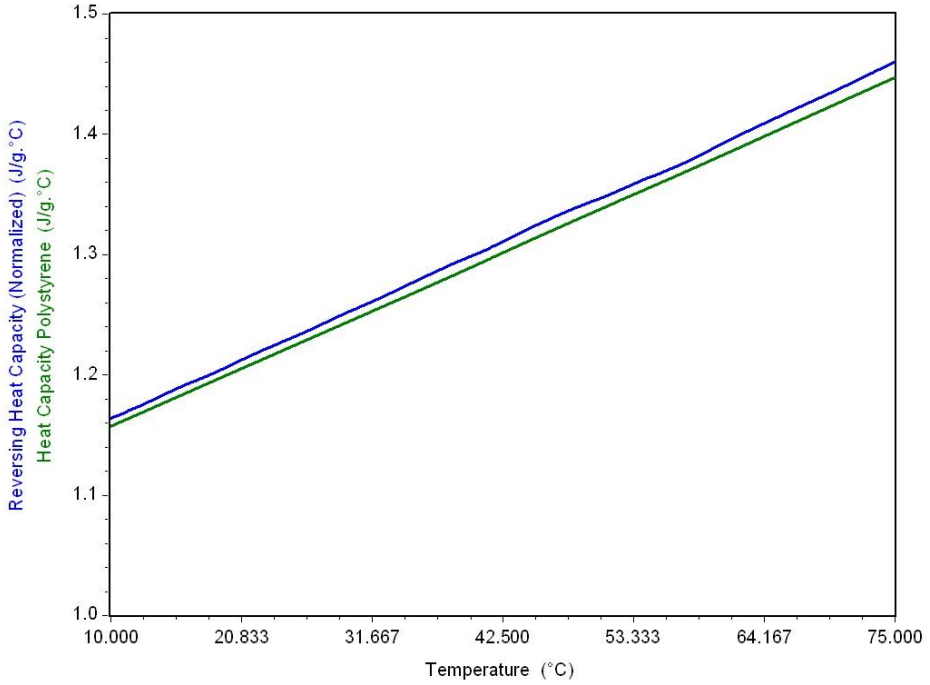

Figure 5.16 measured C_p of polystyrene (blue) and TRIOS software reference C_p data (green).

Figure 5.17 shows C_p results of polypropylene with some of the measured and literature values reported by Gaur and Wunderlich in 1982b. Gaur and Wunderlich (1982b) analysed data from 16 samples of polypropylene with crystallinity (w^c) ranging between 0.25 and 0.67. They have reported the importance of crytallinity on the heat capacity of polypropylene. The reported values of C_p were based on curve fitting and represent the best estimate of the heat capacity. The maximum difference of 2.84 J/g°C was observed between literature and MDSC obtained values of heat capacity, which is 12.4 % difference.

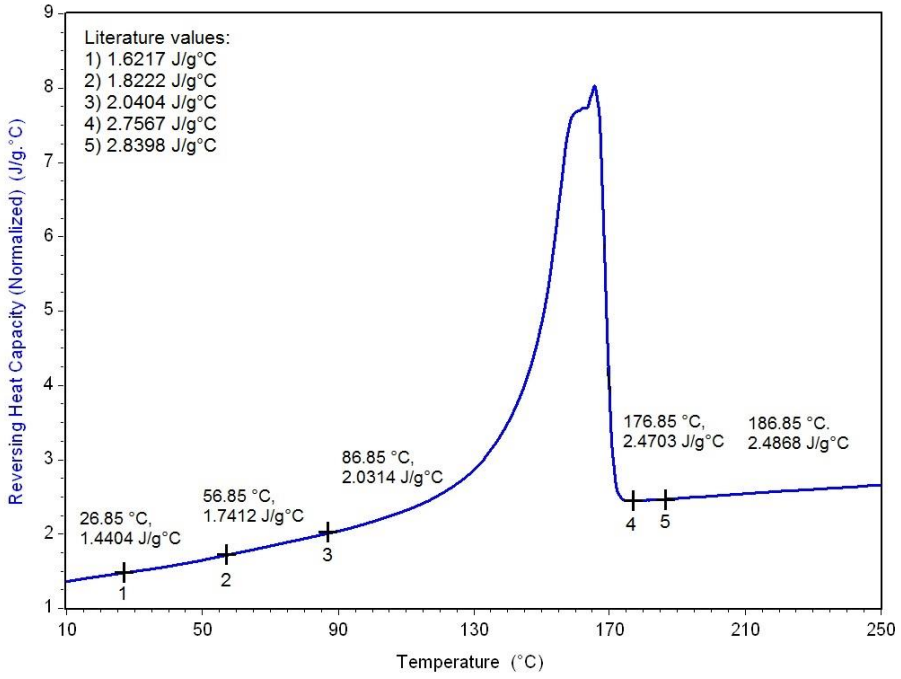

Figure 5.17 Specific heat capacity plot of polypropylene.

Table 5.5 Comparative specific heat capacities of polypropylene.

Polypropylene

Temperature (°C)	Experimental Cp (J/g°C)	Literature (J/g°C)	Difference (%)
16.85	1.4404	1.5599	7.7
26.85	1.5060	1.6217	7.1
36.85	1.5710	1.6861	6.8
46.85	1.6507	1.7531	5.8
56.85	1.7412	1.8222	4.4
66.85	1.8343	1.8933	3.1
76.85	1.9298	1.9660	1.8
86.85	2.0314	2.0404	0.4
96.85	2.1504	2.1160	1.6
106.85	2.2996	2.1927	4.6
176.85	2.4703	2.7567	10.4
186.85	2.4868	2.8398	12.4

5.4.5.2 Effect of Carbon Black Masterbatch on C_p

The effect of the addition of 4% of carbon black masterbatch to polystyrene and polypropylene was analysed. A two-sample T-test was performed for each temperature listed in Tables 5.6 and 5.7. The maximum standard deviation between three samples of PS and CB PS was 0.03 J/g°C for both materials. The maximum difference between the average C_p of PS and CB PS was 0.0381 J/g°C with 95% confidence interval between the means in the range of -0.0242 to 0.1004 J/g°C. P-values were in the range of 0.147 to 0.869 which suggests that difference in C_p is statistically insignificant.

Table 5.6 Comparative specific heat capacities of PS and CB PS.

Temperature (°C)	Cp PS (J/g°C)	Cp CB PS (J/°C)	Difference (J/g°C)	Change (%)
16.85	1.1874	1.1789	-0.0084	-0.7
26.85	1.2311	1.2245	-0.0066	-0.5
36.85	1.2761	1.2694	-0.0067	-0.5
46.85	1.3206	1.3178	-0.0028	-0.2
56.85	1.3626	1.3656	0.0030	0.2
66.85	1.4098	1.4183	0.0085	0.6
76.85	1.4586	1.4768	0.0181	1.2
86.85	1.5159	1.5415	0.0256	1.7
106.85	1.8856	1.8572	-0.0283	-1.5
116.85	1.9098	1.8717	-0.0381	-2.0
126.85	1.9423	1.9048	-0.0375	-1.9
136.85	1.9733	1.9358	-0.0375	-1.9
146.85	2.0028	1.9665	-0.0363	-1.8
156.85	2.0358	1.9987	-0.0371	-1.8
166.85	2.0721	2.0346	-0.0374	-1.8
176.85	2.1036	2.0696	-0.0340	-1.6
186.85	2.1322	2.0998	-0.0324	-1.5
196.85	2.1570	2.1277	-0.0293	-1.4
206.85	2.1843	2.1569	-0.0274	-1.3

The maximum standard deviation between three samples of PP and CB PP was 0.02 J/g°C and 0.03 J/g°C respectively. The maximum difference between the average C_p of PP and CB PP was 0.2187 J/g°C with 95 % confidence interval between the means in the range of -0.2664 to -0.1711 J/g°C. P-values for a range of temperatures were between 0 and 0.007 which suggests that difference in C_p is statistically significant. An increase of heat capacity ranging from 6.4 to 12.7 % was observed with the addition of carbon black masterbatch. The results from two-sample T-test for PS, CB PS, PP and CB PP over the range of temperatures listed in Tables 5.6 and 5.7 can be found in Appendix 2.

Table 5.7 Comparative specific heat capacities of PP and CB PP.

Temperature (°C)	Cp PP (J/g°C)	Cp CB PP (J/g°C)	Difference (J/g°C)	Change (%)
16.85	1.4404	1.6240	0.1836	12.7
26.85	1.5060	1.6908	0.1848	12.3
36.85	1.5710	1.7645	0.1935	12.3
46.85	1.6507	1.8534	0.2027	12.3
56.85	1.7412	1.9443	0.2031	11.7
66.85	1.8343	2.0408	0.2065	11.3
76.85	1.9298	2.1409	0.2111	10.9
86.85	2.0314	2.2485	0.2171	10.7
96.85	2.1504	2.3691	0.2187	10.2
106.85	2.2996	2.4742	0.1745	7.6
176.85	2.4703	2.6288	0.1585	6.4
186.85	2.4868	2.6562	0.1695	6.8

5.5 Sapphire and Steel Surface Energy

5.5.1 What is a Surface Free Energy, Surface Tension?

Surface free energy, (γ) of a material is the work that should be done to bring the molecules from the interior bulk phase to its surface to create a new surface having a unit area ($1\ m^2$). It is measured in energy per square meter (J/m^2). Definition of the surface free energy is the same for the liquid and solid states (Erbil, 2006; Aveyard and Haydon, 1973).

For the liquid surfaces, surface tension γ has two definitions. Surface tension can be defined as the force that operates inwards from the boundaries of its surface perpendicularly, tending to contact and minimize the area of the surface. Its unit is force per meter (N/m). In thermodynamics it is defined as the energy per unit area of the surface of a liquid and measure in J/m^2. It can be regarded as the thin skin formed at the surface of the liquid by attraction between the molecules. For a solid surface, surface tension can be defined as the restoring force necessary to bring the freshly exposed surface to its equilibrium (Erbil 2006; Aveyard and Haydon, 1973).

5.5.2 Contact Angle

The contact angle, θ, (see Figure 5.18) is formed by a liquid drop which is in the state of equilibrium by balancing three forces, namely, interfacial tensions between solid and liquid (SL), between solid and vapour (SV), and liquid and vapour (LV). The contact angle equilibrium was first described as the summation of forces at the three-phase intersection point by Young (1805):

$$\gamma_{SV} = \gamma_{SL} + \gamma_{LV} \cos\theta \qquad \textbf{5.3}$$

where γ is the surface tension or surface free energy (Erbil, 2006; Finn, 2004).

The measurement of contact angle is a straightforward procedure, where a tangent (angle) between liquid drop and solid surface is measured. In equation 5.3 γ_{SV}, γ_{SL} and γ_{LV} are thermodynamic properties of the liquid and solid therefore it entails a single, unique contact angle. In reality nearly all solid surfaces exhibit contact angle hysteresis, which is a difference between advancing and receding contact angles. Contact angle hysteresis can be present due to heterogeneity or surface roughness of the solid substrate. If surface of the substrate is rough it will not represent surface energetics, it will rather reflect surface roughness and lead to errors in surface energy calculations. Stable contact angle equilibrium can be achieved if the following conditions are met:

1. The surface is ideally solid and not deformable.
2. The surface is smooth.
3. The surface is compositionally homogenous
4. The solid surface and liquid do not interact (Wu, 1982, Meiron et al., 2004).

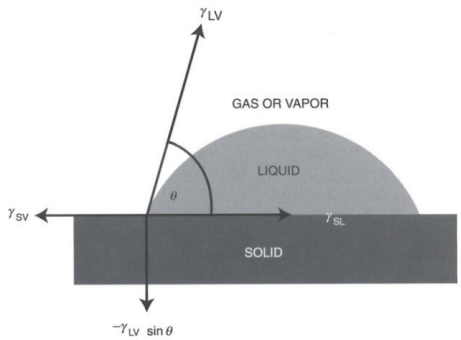

Figure 5.18 Vectorial equilibrium for a drop of a liquid resting on a solid surface to balance three forces, namely, the interfacial tensions, between solid and liquid, γ_{SL}, that between solid and vapor, γ_{SV}, and that between liquid and vapor, γ_{LV}, resulting in Young's equation: ($\gamma_{SV} = \gamma_{SL} + \gamma_{LV} \cos\theta$), where θ is the contact angle. The down component of the vector forces ($-\gamma_{LV} \sin\theta$) is also shown (Erbil, 2006).

The contact angle also represents the wetting of the solid by a liquid and is determined by equilibrium contact angle, θ. If θ is less than $90°$, then the liquid is said to wet the solid. A zero contact angle represents complete wetting, if θ is higher than $90°$, liquid is said to be non-wetting (Erbil, 2006; Barnes and Gentle, 2001).

The contact angle is a useful measurement tool for the work of adhesion (W_a). The thermodynamic work of adhesion is the work required to separate a unit area of two phases in contact, and it is related to Dupre equation of surface free energies:

$$W_a = \gamma_{SV} + \gamma_{LV} - \gamma_{SL} \quad \textbf{5.4}$$

where, W_a is the work of adhesion, $\gamma_{SV}, \gamma_{LV}, and\ \gamma_{SL}$are the surface free energies at solid/vapour, liquid/vapour, and solid/liquid interfaces. The better the adhesion, the better polymer replication, therefore steel and sapphire being high energy solids will have good wettability.

There are two types of contact angles, namely static and dynamic. Static contact angle is measured when liquid is stationary. Dynamic contact angle is determined when liquid is in motion and it is governed by the balance of the interfacial driving force and viscous retarding force (Wu, 1982).

Measuring surface tension of polymer melts has several complications. Firstly, polymer melts have high viscosities and therefore long relaxation times. Secondly, polymers require high temperature to become fluid. The combination of these factors makes the conventional methods for measuring surface tension difficult. A long time is required to get stable contact angle equilibrium, moreover thermal stability of polymers at high temperatures also restricts surface tension measurements of polymer melts (Sauer and Dee, 2002).

5.5.3 Surface Tension of Solids

4.5.3.1 Sessile Drop Method

The surface tension of solids cannot be measured directly. The general method involves placing a drop of liquid with a known surface energy also called the probe liquid onto the surface of the solid. Table 5.8 shows surface tension of most commonly used probe liquids. The contact angle and the known surface energy of the probe liquid are used to estimate solid surface tension (Erbil, 2006; Pocius, 2002).

It is very important to understand that the surface energy of a solid is not an absolute value. It depends on the methodology, probe liquids used, and theory applied for calculation of surface energy of the solid (Rulison, 1999).

Table 5.8 The surface tensions of probe liquids.[a]- Comyn (1997), [b] - Barnes and Gentle (2001), [c]Erbil (2006).

Probe Liquid	$\gamma_{LV}(mJ/m^2)$	$\gamma_{LV}^{d}(mJ/m^2)$	$\gamma_{LV}^{p}(mJ/m^2)$
Water	72.8[abc]	21.8 ± 0.7[a]21.8 ± 3[c]	51[a]
Glycerol	63.4[a b] , 64[c]	37.0 ± 4[a c]	26.4[a]
Ethane diol	48.3[a]	29.3[a]	19[a]
Diiodomethane	50.8	50.8	0
Formamide	58.2[a], 58[c]	39.5 ± 7[a c]	18.7[a]
Ethanol	22.4[a b]	17[a]	5.4[a]
Dimethyl sulfoxide	43.54[a], 44[c]	34.86[a]	8.68[a]
2-ethoxyethanol	28.6[a]	23.6[a]	5[a]
Dimethyl formamide	37.30[a]	32.42[a]	4.88[a]

Tricresyl phosphate	40.9[a]	29.2 ± 4[a]	1.7[a]
Trichlorobiphenyl	45.3[a]	44 ±6[a]	1.3[a]
Pyridine	38.00[a], 37.2 [b]	37.16[a]	0.84[a]
n-Hexadecane	27.6[a]	27.6[a]	0[a]
Ehylene glycol	48.4 [b], 48[c]	-	-
Chloform	27.2 [bc]	-	-

5.5.4 Most Common Surface Energy Theories

There is no universal method for calculating surface energy from contact angle measurements and several theories are used nowadays including:

1) Zisman theory

2) Fowkes theory

3) Owen/Wendt theory

4) Van Oss theory

The surface energy of a solid is not a direct measurement. It is vital to understand that value of surface free energy depends on which probe liquids are used and which theory is chosen for the analysis (Rulison, 1999).

5.5.4.1 Zisman Theory

The Zisman method is used to determine critical surface free energy (γ_c). According to Zisman, the surface energy of a solid is defined as the highest surface tension of the liquid that will completely wet the solid (contact angle θ = 0°). The plot is constructed, where cosine values of the contact angle are on the y axis and liquid surface tension values on the x axis.

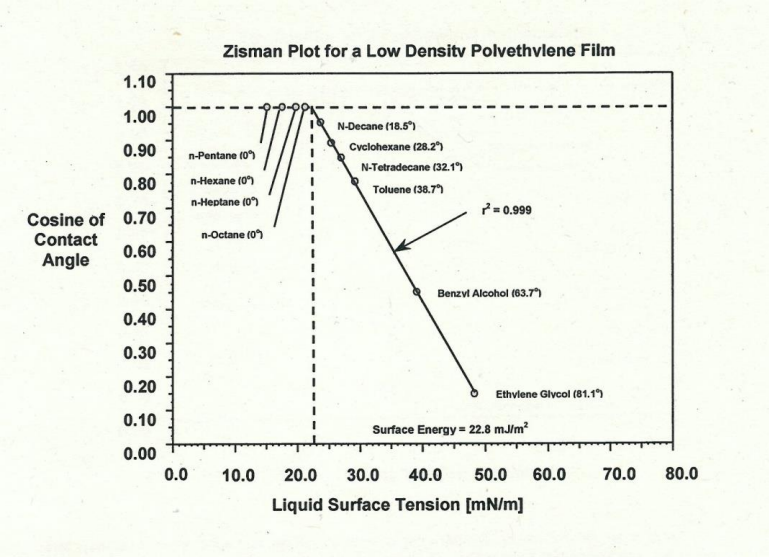

Figure 5.19 Zisman plot for a low density polyethylene film (Rulison, 1999).

In Figure 5.19, the contact angle data is plotted in the form of liquid surface tension versus cosine of contact angle and extrapolated to $\cos\theta = 1$ ($\theta = 0°$), a surface tension value is obtained for the highest surface tension liquid that will completely wet polyethylene with a contact angle of $0°$. This theory works well for non-polar surfaces, such as polyethylene and polypropylene, but becomes unacceptable for polar surfaces, including some polymers, glasses, ceramics, and metals (Rulison, 1999; Zenkiewicz, 2007).

5.5.4.2 Fowkes Theory

Fowkes was the first one who assumed that surface free energy is a sum of independent components with specific interactions:

$$\gamma_s = \gamma_s^d + \gamma_s^p + \gamma_s^h + \gamma_s^i + \gamma_s^{ab} + \gamma_s^o \quad \textbf{5.5}$$

where d is the dispersion force, p - polar force, h - hydrogen bonding force, i - induction force, ab - acid-base force, o - remaining forces. The Fowkes theory is based on three equation, namely, Young's equation, Dupre's equation of

adhesion energy, and Fowkes theory that adhesive energy can be divided into dispersion on polar components.

Young's Equation:

$$\gamma_S = \gamma_{SL} + \gamma_L \cos\theta \quad \textbf{5.6}$$

Drupe's definition of adhesion Energy:

$$\mathrm{I}_{\mathrm{SL}} = \gamma_S + \gamma_L - \gamma_{SL} \quad \textbf{5.7}$$

Where (I_{SL}) = energy of adhesion per unit area between a liquid and a solid surface.

The Fowkes theory states that adhesion energy between solid and liquid can be divided into dispersion and polar components:

$$\mathrm{I}_{\mathrm{SL}} = 2\left[\left(\gamma_L^D\right)^{1/2}\left(\gamma_S^D\right)^{1/2} + \left(\gamma_L^P\right)^{1/2}\left(\gamma_S^P\right)^{1/2}\right] \quad \textbf{5.8}$$

Where: (γ_L^D) - dispersive component of the surface tension of the probe liquid, (γ_L^P) - polar component of the surface tension of the probe liquid, (γ_S^D) - dispersive component of the surface energy of the solid and (γ_S^P) - polar component of the surface energy of the solid.

Combination of all three equations gives an equation of Fowkes surface free energy:

$$\frac{\gamma_L(\cos\theta+1)}{2} = \left(\gamma_L^D\right)^{0.5}\left(\gamma_S^D\right)^{0.5} + \left(\gamma_L^P\right)^{0.5}\left(\gamma_S^P\right)^{0.5} \quad \textbf{5.9}$$

Normally, two liquids are used to measure contact angles, polar (water) and non polar - Diidomethane or methylene iodide (Rulison, 1999; Zenkiewicz, 2007).

5.5.4.3 Owen/Wendt Theory

Owen/Wendt method is similar to Fowkes method mathematically, but the way of calculation surface free energy is different. The theory is based on two equations:

Young's Equation:

$$\gamma_S = \gamma_{SL} + \gamma_L \cos\theta \quad \textbf{5.10}$$

Good's Equation:

$$\gamma_{SL} = \gamma_S + \gamma_L - 2(\gamma_L^D \gamma_S^D)^{0.5} - 2(\gamma_L^P \gamma_S^P)^{0.5} \quad \textbf{5.11}$$

where γ_S - surface energy of solid, γ_S^D - dispersive component of the surface energy of solid, γ_S^P- polar component of the surface energy of solid, γ_L- surface tension of probe liquid, γ_L^D - dispersive component of the surface tension of the probe liquid, γ_L^P - polar component of the surface tension of the probe liquid, γ_{SL}- interfacial tension between solid and liquid, θ - the contact angle between solid and liquid.

The combination of Young's and Good's equations is as follows:

$$\frac{\gamma_L(\cos\theta+1)}{2(\gamma_L^D)^{0.5}} = (\gamma_S^P)^{0.5} \frac{(\gamma_L^P)^{0.5}}{(\gamma_L^D)^{0.5}} + (\gamma_S^D)^{0.5} \quad \textbf{5.12}$$

The equation has a linear form $y = mx + c$ where:

$$y = \frac{\gamma_L(\cos\theta+1)}{2(\gamma_L^D)^{0.5}} \quad \textbf{5.13}$$ **Equation 4.13**

$$m = (\gamma_S^P)^{0.5} \quad \textbf{5.14}$$

$$x = \frac{(\gamma_L^P)^{0.5}}{(\gamma_L^D)^{0.5}} \quad \textbf{5.15}$$

$$c = (\gamma_S^D)^{0.5} \quad \textbf{5.16}$$

Once the contact angles between a range of probe liquids and solid are obtained, the contact angle data can be plotted in the Owens/Wendt format (see Figure 5.20). Surface tension values of probe liquids including, overall, polar and dispersive are also required. The best fit line is to be applied on the plotted data. The polar component of the solid surface free energy is calculated from the slope of the line; whereas dispersive component of the solid surface free energy is calculated from the intercept (Rulison, 1999; Zenkiewicz, 2007).

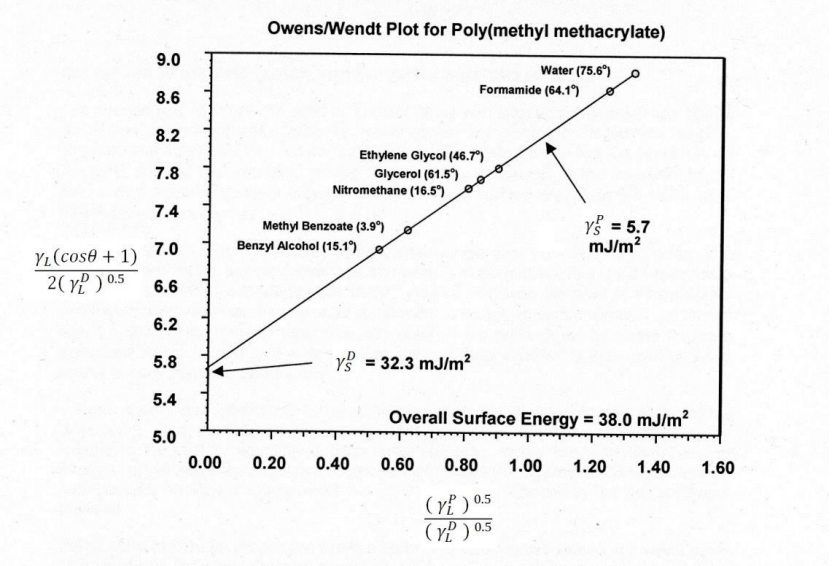

Figure 5.20 Example of the Owens/Wendt plot. (Rulison, 1999).

5.5.4.4 Van Oss Theory

The methods discussed above are a one component model (Zisman) and two component models (Fowkes and Owens/Wendt). This means that a minimum of one probe liquid is enough for the Zisman method and at least two probe liquids need to be used for Fowkes' and the Owen/Wendt methods. In the Van Oss theory the surface energy is divided into three components, namely, a dispersive component, an acid component, and a base component. At least three probe liquids need to be used, where one of the probe liquids is non-polar, and the other two are bipolar liquids. The first contact angle measurement is to be made with the probe liquid that has only a dispersive component and the following equation is to be used to find dispersive component of the surface energy of the solid:

$$\gamma_L(1+cos\theta) = 2\,[(\gamma_S^D\gamma_L^D)^{0.5}] \qquad \textbf{5.17}$$

The second probe liquid must have only a base component, to calculate the acid component of the solid surface energy and the following equation to be used:

$$\gamma_L(1 + cos\theta) = 2\,[(\gamma_S^D \gamma_L^D)^{0.5} + (\gamma_S^+ \gamma_L^-)^{0.5}] \quad \textbf{5.18}$$

where γ_S^+ is the acid component of the surface energy of the solid and γ_L^- - the base component of the surface tension of the liquid.

The third probe liquid must have only an acid component to its surface tension to calculate the base component of the solid surface energy. The following equation is to be used in this case:

$$\gamma_L(1 + cos\theta) = 2\,[(\gamma_S^D \gamma_L^D)^{0.5} + (\gamma_S^- \gamma_L^+)^{0.5}] \quad \textbf{5.19}$$

where γ_S^- - the base component of the surface energy of the solid, γ_L^+ - the acid component of the surface tension of the liquid.

The Van Oss theory is more suitable for inorganic surfaces, organometallic surfaces, and surfaces containing ions, such as pharmaceutical powders and papers (Rulison, 1999; Zenkiewicz, 2007)

5.6 Rate of Spreading of Polymers on Solids

When a polymer pellet starts melting on a metal surface it normally does not exhibit an equilibrium contact angle. A number of studies have been performed on spreading of polymers on solid surfaces including metals, glass and clay. Schonhorn (1966) studied the kinetics of wetting of high and low surface energy polymers, where change in the length of the drop base was studied as a spreading parameter. Silberzan and Leger (1992) has shown that low molecular polymers spread faster compared to high molecular polymers on the same substrates. Rogers et al. (2005) have performed an analysis of contact angles at polymer-clay interfaces. Results showed that polymers that

showed complete wetting were more suitable for nano-composites. Lau and Burns (1973) have studied the spreading behaviour of small polystyrene drops on place glass surfaces in terms of contact angle, contact area and surface tension.

All these studies give an idea as to how polymer melt contact angle measurements can be used for the investigation of wetting behaviour of polymer melt on solid surfaces. A sessile drop shape method was used in this study to investigate the effect of carbon black masterbatch on polymer spreading behaviour.

5.6.1 Experimental Procedures

5.6.1.1 Surface Energy of the Substrates

In microinjection moulding experiments a sapphire window was used in one half of the mould cavity. Sapphire has similar thermal properties to typical tool steel, but it was required to understand if the surface energy of the sapphire differs significantly from the steel surface energy.

5.6.1.2 Contact Angle Measurement System

The VCA Optima contact angle measurement system (Figure 5.21) was used for determining contact angles of the probe liquids on steel and sapphire substrates. The apparatus consists of the high resolution video camera and solid state lighting for sharper and brighter images. The system is equipped with motorised syringe, which accurately dispenses probe liquids of the specified volume. Software of the VCA Optima captures static and dynamic images of the droplets and determines contact angles manually or automatically within repeatability of 1 degree and accuracy 0.5 degree.

Figure 5.21 VCA Optima contact angle measurement system.

Sapphire substrates received from the supplier were polished to 0.007 µm Sa, whereas steel substrates were mechanically polished in-house down to 0.009 µm. In the literature it is generally accepted that if surface roughness (Ra) is less than 0.5 µm, the effect that it has on contact angle is insignificant (Rudawska and Jacniacka, 2009). Surface free energy and its polar and dispersive components were determined from a set of contact angles made by the probe liquids, namely distilled water and diiodomethane. Water is considered as a liquid with the dominant polar component (γ_l^d = 21.8 mJ/m^2 and γ_l^p = 51.0 mJ/m^2) and diiodomethane as the dispersion liquid (γ_l^d = 50.8 mJ/m^2). The Owens/Wendt method for surface energy determination requires only two probe liquids.

A number of drops of both probe liquids with the volume of 2 µl were deposited on the surface with the motorised syringe. After each drop surfaces were cleaned to be ready for the next experiment. Every drop was rotated several times and five images per each drop were recorded. The contact angles were determined by the image analysis software and exported to Excel where average contact angles were calculated. Once the entire contact angle data for both probe liquids was collected total surface free energy of the substrates was calculated using the Owens/Wendt theory. Measurements of contact angle

surfaces of the sapphire and steel surface with water and diiodomethane are presented in Table 5.9.

Table 5.9 Measurements of contact angle of the examined sapphire and steel surfaces with distilled water and diiodomethane.

No. Of Drops	CA of water on Polished Sapphire	CA of Diiodomethane on Polished Sapphire	CA of water on Polished Steel	CA of Diiodomethane on Polished Steel
1	50.8	50.7	83.7	45.6
	54.4	49.9	82.6	46.5
	49.7	49.6	83.6	46.4
	51	49.6	82.3	46
	51.5	46.5	84.9	44
2	56.6	49.8	81.2	45
	54	49.7	81.5	44.4
	52	48	84.3	42.3
	53.4	49.8	84.3	42.2
	55.3	47.9	82.6	43
3	54.7	53.2	84.5	48.2
	54.6	47.7	84.6	44.4
	53.9	47.2	83.6	45.3
	54.6	47.2	82.8	44.6
	54.2	47.9	80.3	45.9
4	49.7	54.1	80.2	48.6
	49.1	55.2	81.7	49.6
	53.5	55.3	82.9	48.8
	51.7	52.8	79.6	46.3
	50.1	50.7	76.8	43.9
5	56.2	52.1	80.4	47.2
	55.8	53.7	84	46.9
	57.4	51.2	77.3	43.2
	52.5	51.6	76.5	41.2
	54.3	51.5	82	41.9
Average	**53.24**	**50.52**	**81.93**	**45.26**

5.6.1.3 Results

The surface free energies of steel and sapphire surfaces have been calculated from contact angles made by distilled water and diiodomethane

according to the Owens/Wendt theory. Table 5.10 shows all the determined and calculated values required to plot contact angle data in Owens/Wendt format. Values of the overall surface tension (σ_L) of probe liquids were taken from the literature and dispersive surface tension components (σ_L^D) calculated from equation 5.12, the polar surface energy components were calculated by subtracting dispersive surface tension component from the overall surface tension. X and Y values were calculated from equations 5.15 and 5.13. From the data plotted the polar component of the solid surface free energy is calculated from the slope of the line; whereas dispersive component of the solid surface free energy is calculated from the intercept.

Table 5.10 Results for the probe liquids of sapphire and steel surfaces.

Liquid	Polished Sapphire (θ)	Rad	Cos(θ)	σ_L	σ_L^D	$(\sigma_L)^2$	σ_L^P	X	Y	Polar	Dispersive	Total (mJ/m2)
Water	53.24	0.93	0.60	72.80	36.83	5299.77	35.97	0.99	9.59	14.46	33.97	48.43
diiodomethane	50.52	0.88	0.64	50.80	50.80	2580.64	0.00	0.00	5.83			

Liquid	Polished Steel (θ)	Rad	Cos(θ)	σ_L	σ_L^D	$(\sigma_L)^2$	σ_L^P	X	Y	Polar	Dispersive	Total (mJ/m2)
Water	81.93	1.43	0.14	72.80	36.83	5299.77	35.97	0.99	6.84	0.60	36.86	37.47
diiodomethane	45.26	0.79	0.70	50.80	50.80	2580.64	0.00	0.00	6.07			

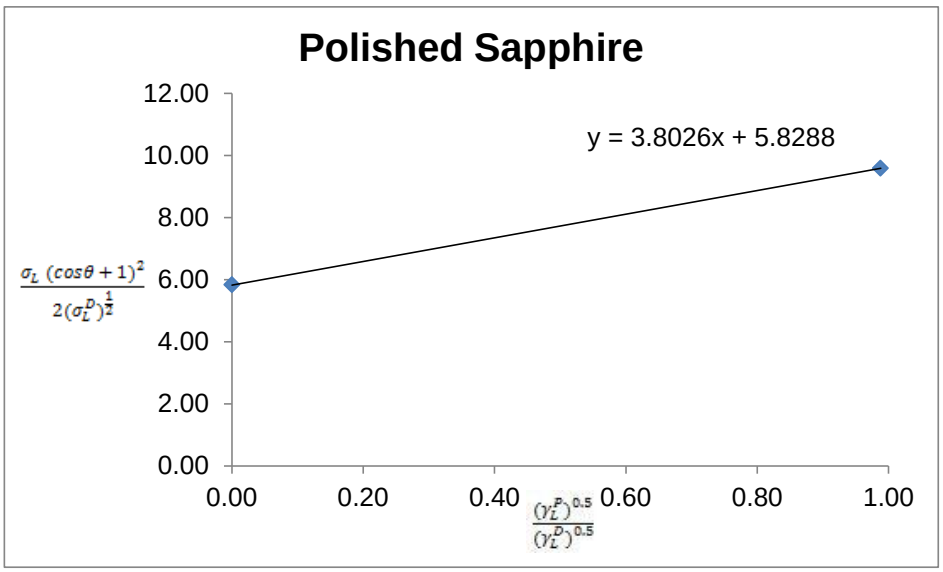

Figure 5.22 Owens/Wendt plot for sapphire surface.

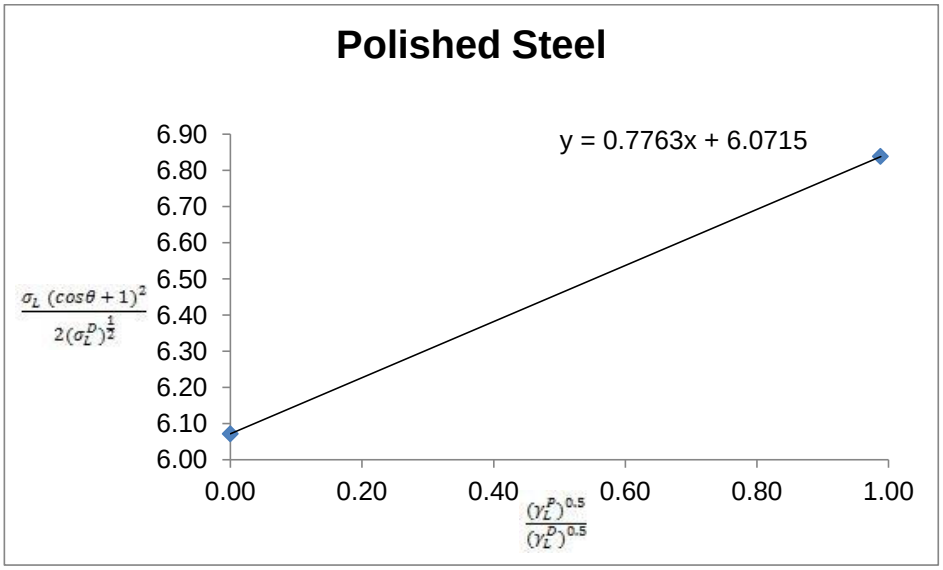

Figure 5.23 Owens/Wendt plot for steel surface.

Using the determined contact angles, the total free energy of sapphire was 48.32 mJ/m^2 and 37.47 mJ/m^2 for steel. Both surfaces have similar dispersive components of the surface free energy. On the steel surface mainly dispersive interactions occur, with the polar interaction very small. On the sapphire surface both dispersive and polar interactions are present. Borosilicate Glass, quartz, sapphire, soda-lime glass, metals and metal oxides are all high energy surfaces and have similar wettability and surface tension. The critical surface tension for high energy solids reported in the literature is in the range of 36 to 47 mJ/m^2 (Wu 1982). However, it has to be noted that critical surface energy (Zismann method) of a solid is defined as the highest surface tension of the liquid that will completely wet the solid and both methods cannot be compared directly. Surface free energy of sapphire is higher than steel by more than 10 mJ/m^2 which suggests that wettability of this surface should be higher compared to a steel surface. However, spreading of polymer melts on these surfaces has shown that the difference in surface free energy of substrates has no significant effect.

5.6.2 Rate of Spreading of Polymers on Solids

The contact angle variation as a function of time was studied using the same contact angle apparatus, but with modifications. A heating chamber was designed and manufactured to allow measurements of contact angles at elevated temperatures. The chamber has a cylindrical steel body with a heater formed as a coil wrapped around it (Figure 5.24). Other components shown in Figure 5.24 are:

- Sapphire windows (1) at both ends allowing illumination and camera recording of the drops spreading on the surface inside the chamber. Diameter 10 mm, thickness 1 mm.
- Elmatic SQ5 heater formed to coil (2), 250 watts x 240 volts, fitted with a type K thermocouple.
- Thermal insulating bulk fibre (3), between the heater and stainless steel clamp band (4).
- Inlet (5) for inert gas to prevent polymer drop degradation.
- A hole (6) for a K type wire thermocouple. A thermocouple was inserted into the chamber and was located few millimetres beside the drop resting on a surface. This thermocouple was used to monitor the temperature of the environment inside the chamber. A number of experiments with thermocouples showed that environment temperature was equal to substrate surface temperature and was also interpreted as the temperature of the polymer drop.
- Chamber base (10), top cover (11) and substrate support (9) machined out of Macor glass ceramic.
- Solid substrate (7), steel or sapphire with the maximum diameter of 12 mm and height 10 mm.

- A lever (8) that was used to lift the substrate into to the chamber and lock it into the position.

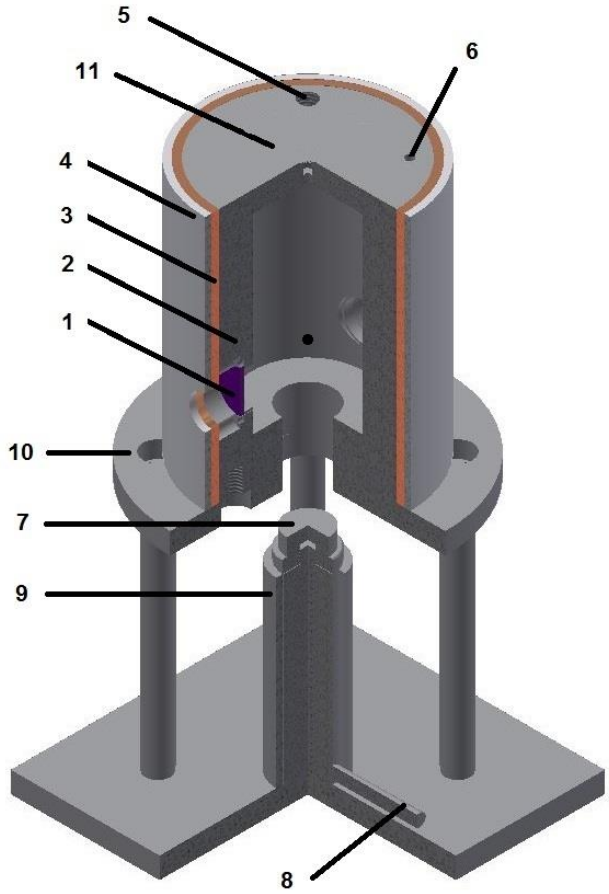

Figure 5.24 High temperature chamber for measuring sessile contact angles of polymer melts.

5.6.3 Polymer Samples

To eliminate any variability caused by difference in weight of the drops, small cylinders were microinjection moulded from polypropylene, polystyrene, carbon black filled polypropylene and carbon black filled polystyrene. The cylinders are 1.5 mm in diameter and height. The average mass of PS and CB PS cylinders was 3.1 mg with standard deviation of 0.02 mg. The average mass of PP and CB PP was 2.5 mg with standard deviation of 0.06 mg.

Prior to each experiment, substrates were ultrasonically cleaned in acetone. A cylinder of a given polymer was then located on the surface of the substrate. The chamber was preheated to a given temperature and once isothermal conditions were reached, the polymer sample sitting on the surface was introduced inside the chamber. The temperature of the environment would initially drop, because cold body was introduced, but it would thermally stabilise within approximately 10 minutes. Image acquisition of the drop profile was started once the cylinder was introduced inside the chamber. A constant flow of nitrogen (1 l/min) was supplied to the chamber to prevent polymer degradation. A sequence of images was then acquired at a frame rate of 4 images per minute. A DropSnake analysis which is based on ImageJ image processing package was used to analyse a sequence of images. It is based on cubic B-spline snakes (active contours) which allow good description of the drop contours (Stalder et al., 2006). To confirm values of spreading each experiment was performed three times. Experimental conditions are listed in Table 5.11.

Table 5.11 Experimental conditions for measuring rate of spreading.

220 °C	Polished Sapphire	PS 158K
		CB PS 158K
		PP GA12
		CB PP GA12
	Polished Steel	PS 158K
		CB PS 158K
		PP GA12
		CB PP GA12
240 °C	Polished Sapphire	PS 158K
		CB PS 158K
		PP GA12
		CB PP GA12
	Polished Steel	PS 158K
		CB PS 158K
		PP GA12
		CB PP GA12

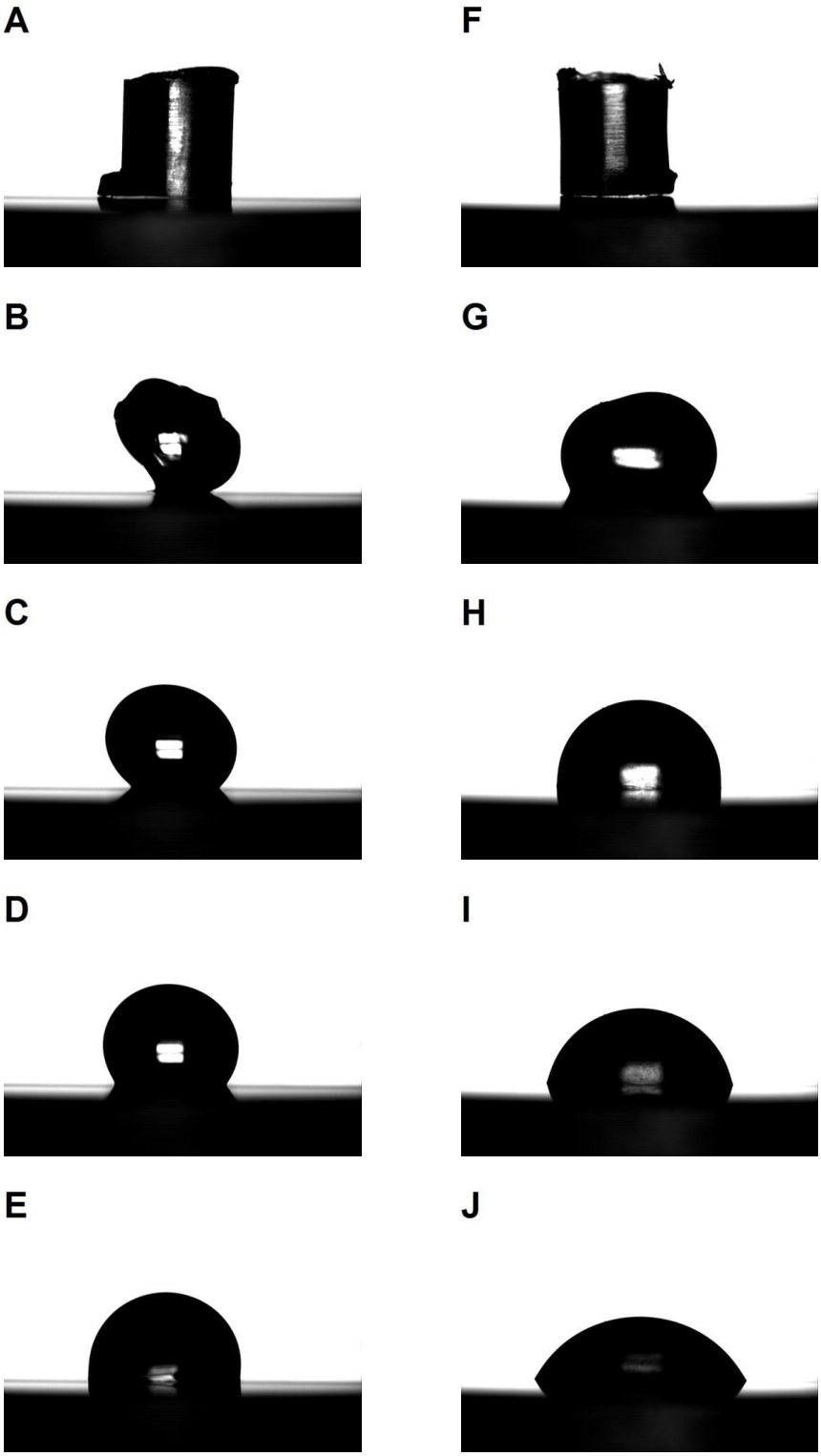

Figure 5.25 (A) PS at t = 0 min, (B) PS at t = 5 min, (C) PS at t = 10 min, (D) PS at t = 15 min, (E) PS at t = 20 min, (F) PP at t = 0 min, (G) PP at t = 5 min, (H) PP at t = 10 min, (I) PP at t = 10 min, (J) PP at t = 15 min.

5.6.4 Results

Figure 5.25 shows melting of the cylinders and formation of spheres from polystyrene and polypropylene on sapphire substrate. Images A - E represent polystyrene, image F – J represent polypropylene. Each of the images was taken at an interval of 5 minutes. It can be observed that polypropylene has higher spreading rate comparing to polystyrene under the same experimental conditions.

Spreading of the drops was determined by plotting the change of contact angles with time and fitting a linear regression line. A faster spreading rate is represented by the higher slope.

Table 5.12 Magnitude of rate of spreading.

	220 C		240 C	
	Sapphire	Steel	Sapphire	Steel
PS 158K	-1.94	-2.02	-2.53	-2.82
CB PS 158K	-1.11	-1.04	-1.55	-1.91
PP GA12	-2.88	-2.52	-3.79	-3.53
CB PP GA12	-2.78	-2.73	-3.94	-3.67

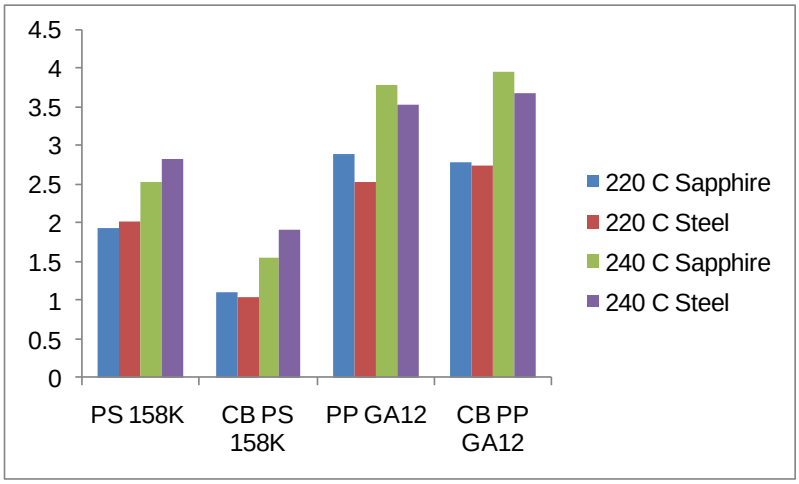

Figure 5.26 Graph showing comparative rate of spreading at 220 °C and 240 °C on sapphire and steel surfaces.

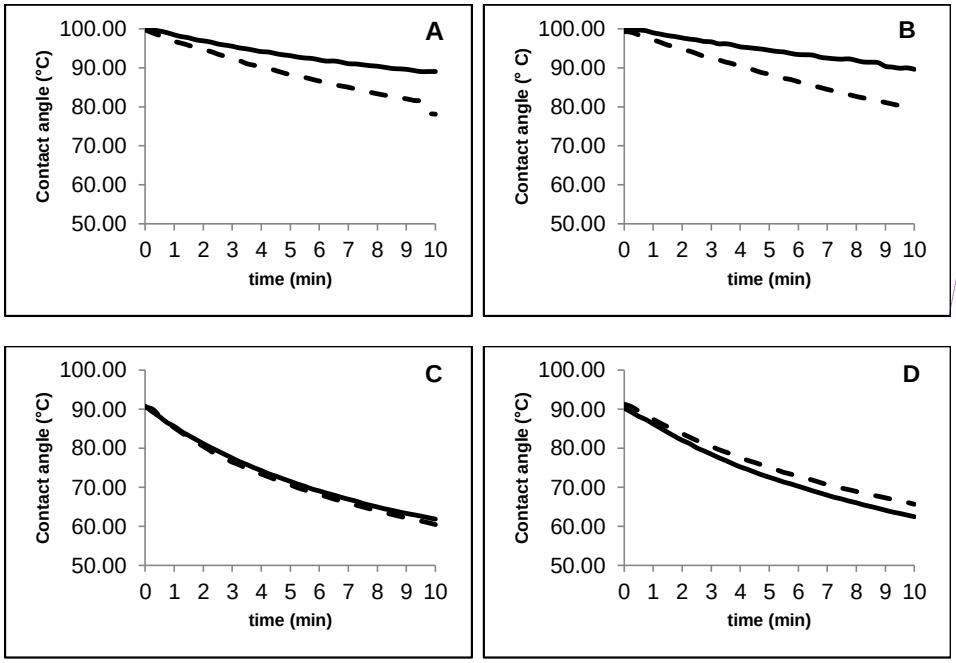

Comment [m1]: Added axis titles

Figure 5.27 Change of contact angle with time at 220 °C (A) PS and CB PS on sapphire, (B) PS and CB PS on steel, (C) PP and CB PP on sapphire, and (D) PP and CB PP on steel. Solid line – carbon black filled materials, dashed line – unfilled materials.

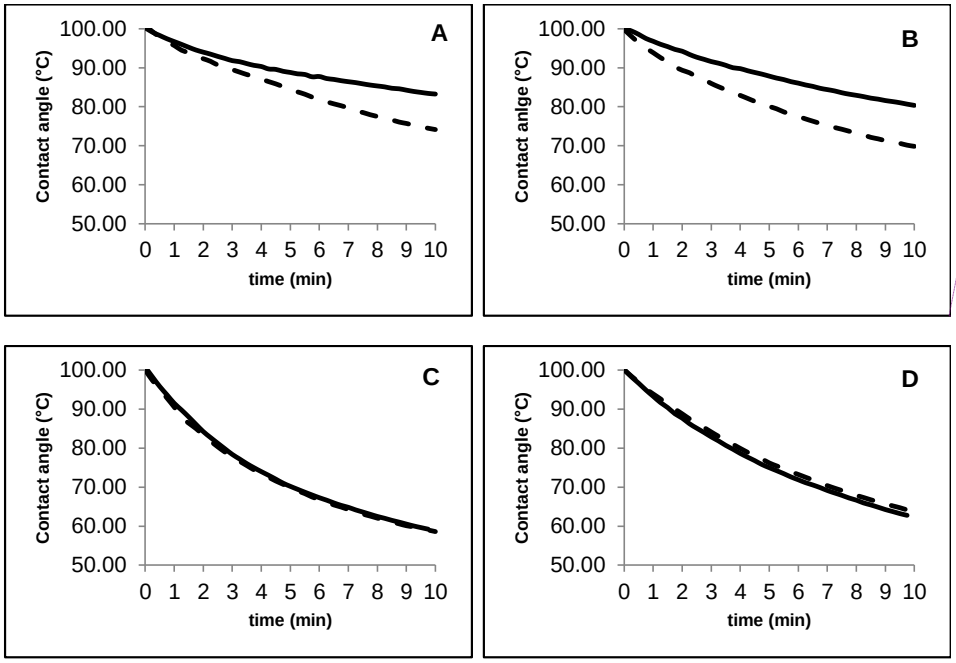

Comment [m2]: Added axis titles

Figure 5.28 Change of contact angle with time at 240 °C (A) PS and CB PS on sapphire, (B) PS and CB PS on steel, (C) PP and CB PP on sapphire, and (D) PP and CB PP on steel. Solid line – carbon black filled materials, dashed line – unfilled materials.

PS and CB PS have shown nearly identical spreading rates at 220 °C on both sapphire and steel surfaces. However, an increased spreading of PS and CB PS was observed on the steel surface at the temperature of 240 °C. The magnitude of slopes for PP and CB PP did not show high variation comparing to PS and CB PS. The addition of carbon black masterbatch reduced the spreading rate of polystyrene, on both surface and at both low and high temperatures which is shown in Figure 5.27 (A, B) and Figure 5.28 (A, B). The effect of the addition of carbon black masterbatch to PP did not change spreading behaviour by much, which can be seen from the magnitude of slope in Table 5.12. Moreover, Figure 5.27 (C) shows that at 240 °C PP and CB PP had very similar drop spreading rates. Overall, polymers exhibit similar spreading rates on sapphire and steel which suggests that 10mJ/m^2 higher free surface energy of sapphire is not significant. It can be clearly seen that the rise in temperature increases the spreading of polymers on the surfaces. Figure 5.26 summarises all the magnitudes of slopes.

Chapter 6. Polymer Cooling Experimental Study

In order to study polymer cooling directly, a special mould was designed based on a flow visualisation tool previously developed at the University of Bradford. The tool was used to study polymer flows in a range of micromoulding cavities. A transparent sapphire window was used as one half of the mould cavity. The fixed half of the mould was fitted with 45° first surface mirror, which enabled visibility within the cavity through the sapphire window (Whiteside et al., 2009). A number of publications based on the experimental technique described in this chapter can be found in Appendix 1.

6.1 Mould Construction

The main tasks of the microinjection moulding tool are to distribute the melt inside the cavity, form and cool down a part and remove it from the mould. A mould consists of the following standard components: clamping plates, cavity plates, back-up plate, core plates, risers, ejector assembly, ejector pins, guide bushes and guide pillars. A three dimensional model of the designed mould is shown in Figure 6.1. The mould base was customised and ordered from Hasco Ltd, a company specialising in mould making for the plastic industry. The mould machining was performed at the University of Bradford. The selection of the mould steel is important as it affects both the functionality and the lifespan of the mould. General requirements for mould materials are high wear resistance, high corrosion resistance, high dimensional stability and good thermal conductivity (Unger, 2006). Mould steel 1.1730 was selected for the clamping plates, risers and ejector assembly, because generally in mould construction these parts can be unhardened. Cavity plates and core plates are subjected to high pressures, therefore harder mould steels are generally used for these components. Mould

steel 1.2311 was used for cavity plates and tool steel P20 was selected for the core plates. A summary of the materials used for the mould construction are presented in Table 6.1.

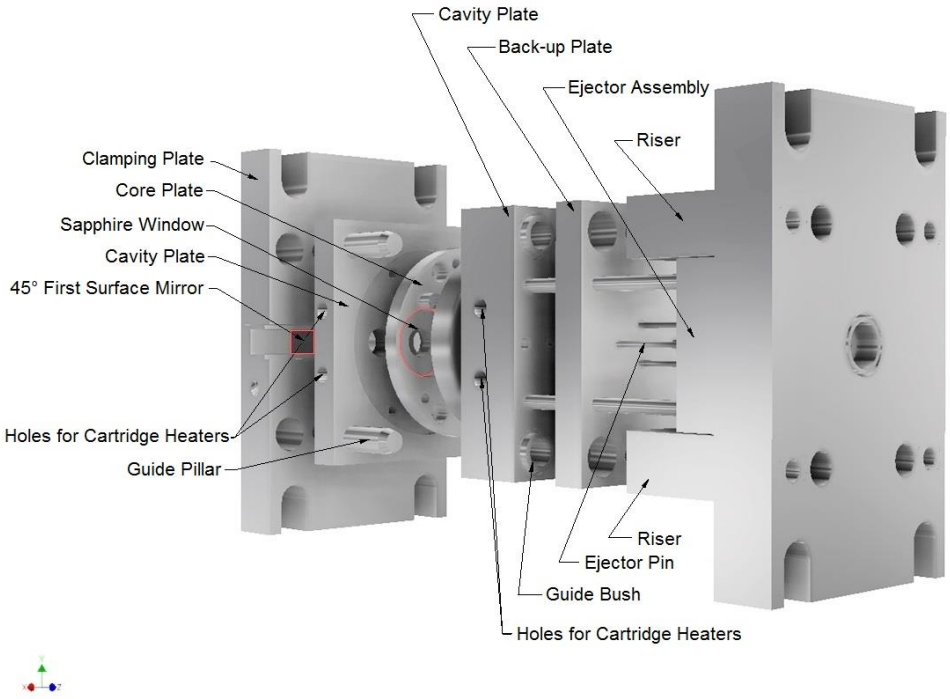

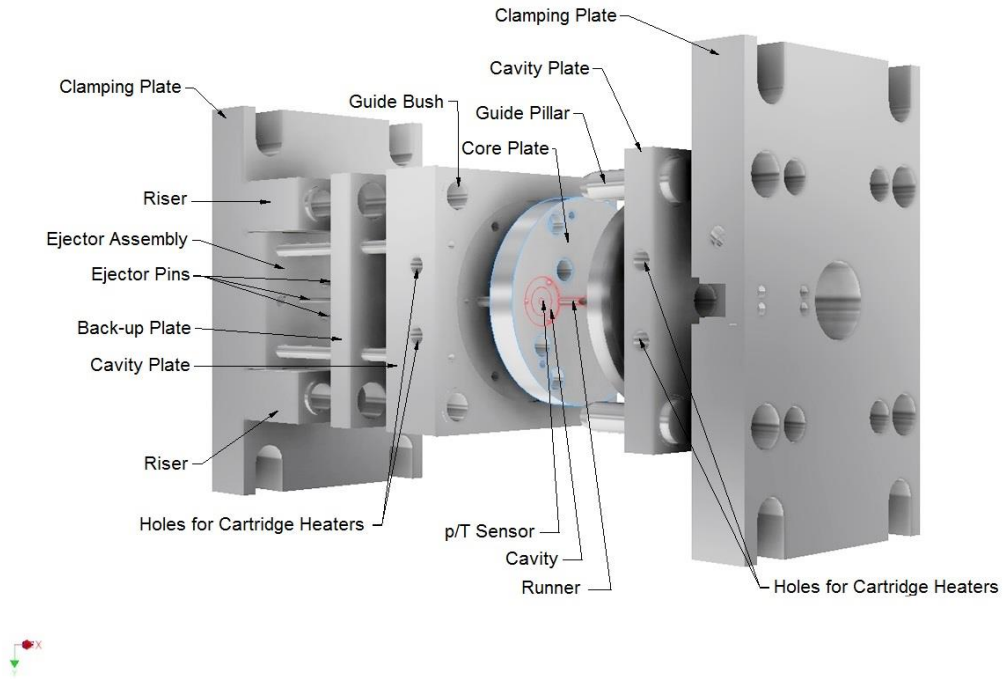

Figure 6.1 3D model of the two-plate mould.

Table 6.1 Mould materials summary.

Material	Mould steel 1.1730	Mould Steel 1.2311	Tool Steel P20
Chemical composition (%)	C - 0.45; Si - 0.27; Mn - 0.7	C - 0.40; Si - 0.30; Mn - 1.45; P ≤ 0.035; S ≤ 0.035; Cr - 1.95; Mo - 0.2	C - 0.37; Cr - 2; Mn - 1.4; Mo - 0.2; Ni - 1; Si - 0.3; S ≤ 0.010
Hardness (HB)	Approx. 190	Approx. 280 - 325	Approx. 290 - 341
Thermal Conductivity (W/m-K) at 20° C	50	34.5	29
Components used for	Clamping plates, risers, ejector assembly	Cavity plates, back-up plate	Core plates

6.1.1 Mould heating

Heating of the mould is required to prevent premature melt freezing during the filling stage and for uniform part cooling in microinjection moulding. The most commonly used method for mould heating is heating with electrical cartridge heaters. Cartridge heaters are easy to install and easy to use. Specialists from Watlow Ltd assisted in the selection of the optimised cartridge heaters based on the mass of the mould and heaters watt density. Watlow Firerod cartridge heaters (see Figure 6.2) have a Nickel-chromium resistance wire, which provides even and efficient heat distribution to the stainless steel sheath. The maximum operation temperature of the heaters is 538 °C, with the maximum energy density of 62 W/cm^2 and maximum voltage of 240 Volts. Swaged-in fibreglass leads are stainless steel braided to protect them from abrasion against sharp edges (Watlow Ltd, 2013).

Figure 6.2 Watlow Firerod cartridge heaters.

6.2 Cavity Pressure Measurements

Cavity pressure is one of the factors which can be used to monitor and achieve consistent replication quality of the moulded parts. It was shown that when cavity pressure is consistent for each cycle, then properties of the moulded parts are identical and reject rates are practically negligible (Rosato et al., 2000). Inappropriate cavity pressure may result in a number of defects. For example, excessive cavity filling pressure may result in flashing of the part, whereas low cavity pressure may result in unfilled parts or warpage.

The TCR/HTC is another parameter that is dependent on cavity pressure. When packing pressure is applied a good contact between the cavity surface and polymer part is maintained and heat is removed by conduction through the contact spots. Once cavity pressure starts decaying or drops to atmospheric pressure formation of macroscopic gaps occurs. Heat that escapes from the core of the part to the surface shows a decrease in conduction due to formation of the gaps at the interface. These macroscopic gaps are formed due to the effects of polymer shrinkage. Experimental work by a number of researchers suggests that cavity pressure is a major parameter in heat transfer at polymer/steel interface (Marotta and Fletcher, 1996; Parihar and Wright, 1997; Narh and Sridhar, 1997; Fuller and Marotta, 2001; Sridhar et al., 2000; Delaunay and Le Bot, 2000; Masse et al., 2004; Nguyen-Chung et al., 2010).

In this research a Kistler (6189A) cavity pressure and temperature (p-T) sensor was flush mounted with the cavity wall of the moving part of the mould. The cavity p-T sensor specifications are presented in Table 6.2. It was used to monitor cavity pressure during the experimental work and for verifying the temperature recorded by the IR camera. Assuming symmetry of the temperature distribution through the thickness of the moulded part, the p-T sensor was used to calibrate the

IR camera and calculate calibration curves for polymers used in the study. Figure 6.3 shows a schematic diagram of the system, where a sapphire window is fitted into the fixed part of the mould and the p-T sensor into the moving part of the mould.

Table 6.2 Kistler (6189A) p-T sensor specifications (Kistler, 2011b).

Technical Data		
Range (bar)	0 ... 2000	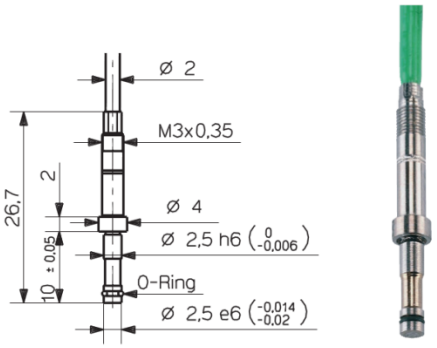
Overload (bar)	2500	
Sensitivity (pC/bar)	- 6.5	
K type thermocouple	NiCr-Ni	
Operating temperature range of the sensor, cable and connector box (°C)	0 ... 200 (allowed to rise to 240 °C without damaging the sensor) measuring error may occur	
Melt temperature at the front of the sensor (°C)	< 450	

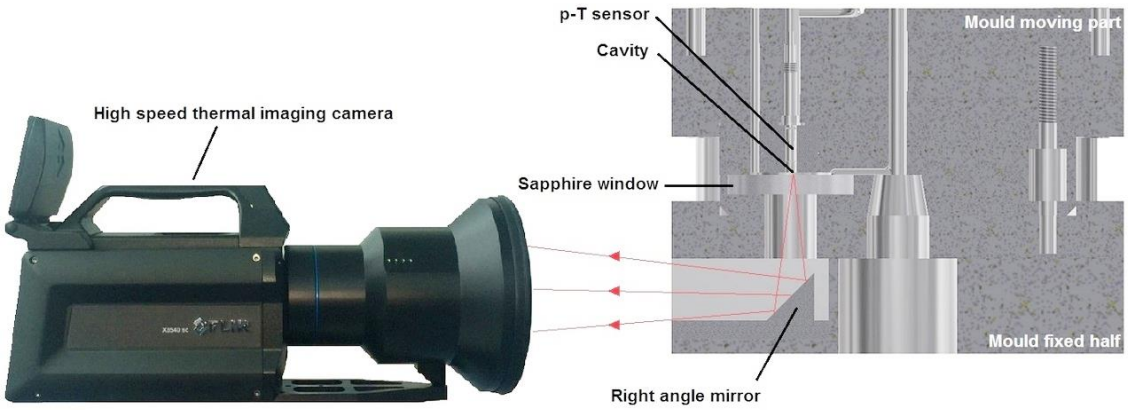

Figure 6.3 Schematic representation of the visualisation system.

When the sensor is subjected to a pressure, the quartz measuring element produces a proportional electrical charge that is converter into a proportional voltage using a Kistler charge amplifier. The amplifier has a measuring range of 5000 pC and an output range from 0 to 10V. The output signal was analysed with SCC DAQ system which consists of the SC-2345 series shielded carrier and NI

PCI-6250 DAQ device on a computer employing National Instruments Labview 11 software. The data acquisition was triggered with the injection start digital input for both p-T sensor and IR camera. Both acquisition devices were operating at the rate of 1KHz for 6 seconds.

6.3 Materials Calibration

The optical train of the visualisation system is quite complex due to the reflections at the surfaces, absorption and different materials emissivities. Therefore it is impractical to compensate for the IR attenuation analytically. Instead, the system was calibrated in-situ using the following method:

1) Polymer was injected into the cavity.
2) It was left there for 5 minutes to thermally stabilise with the mould temperature.
3) After 5 minutes the cameras digital level (DL) value was recorded.

This process was performed over a temperature range of 55 °C to 200 °C, at 5 °C increments. The actual temperature of the polymer was verified with the p-T sensor mounted in the moving part of the mould. This data was used to create a calibration curve for the materials. Then a curve fitting algorithm, namely fourth order polynomial, was fitted to the data points. Initially calibration curves were created for CB PP in combination with sapphire windows of different roughness, namely (Sa) 0.007 µm, 0.5 µm and 1 µm. The same sapphire windows were used for CB PS calibration. A plot of all six curves is shown in Figure 6.4. Based on the observation from the calibration curves in Figure 6.4 and FTIR results in Figure 5.8, one calibration curve could have been used. However, it was decided that two calibration curves were to be used, namely one for CB PP and one for CB PS obtained through a polished sapphire window.

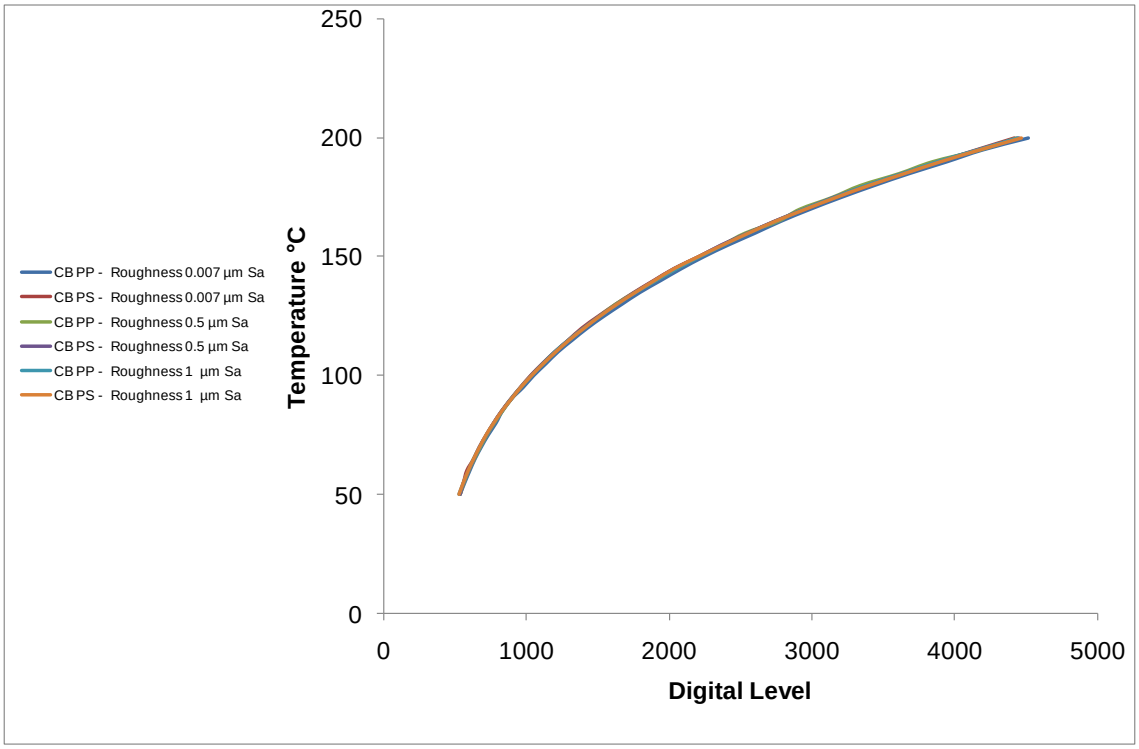

Figure 6.4 Calibration curves of CB PP and CB PS obtained with sapphire windows of different roughness.

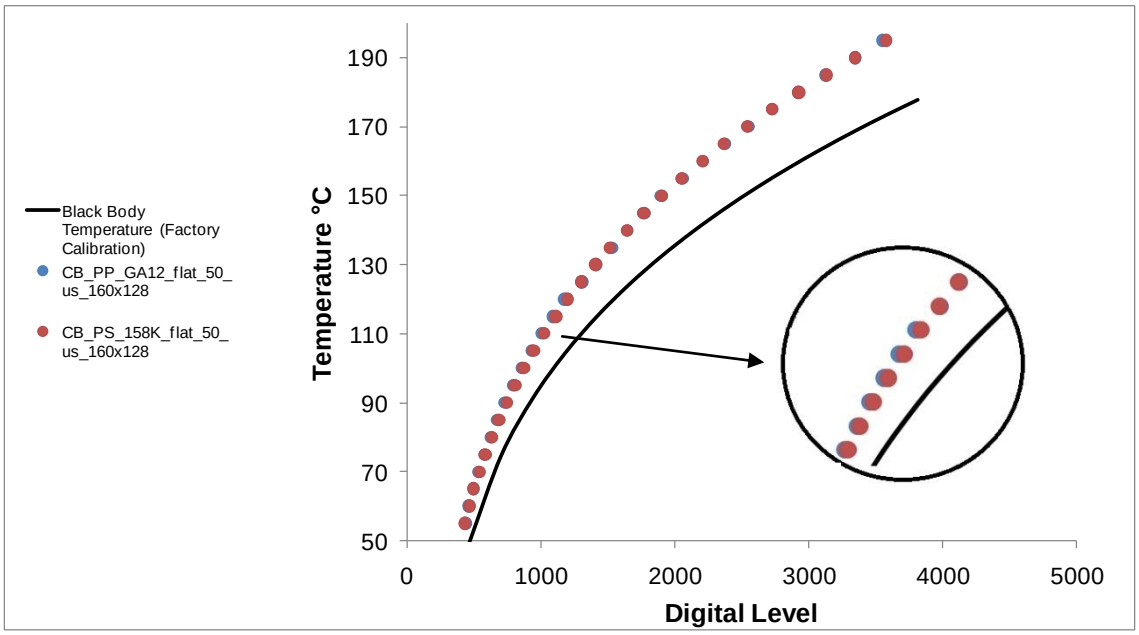

Figure 6.5 Comparison of black body calibration curve and experimentally obtained curves for CB PP and CB PS.

The reason for the need for two calibration curves can be seen in Figure 6.5, where a deviation can be observed at around 115 °C between CB PP and CB PS calibration curves. At the same digital level, the temperature of CB PP is slightly higher and this increase corresponds to the crystallisation temperature of CB PP, as demonstrated in Figure 6.6. Also, IR transmission measurements of the

polymers were performed at room temperature and showed that the addition of carbon black to PP and PS makes them opaque to IR. Measurements of IR transmission or emissivity of carbon black filled materials were not possible at the melt condition. Therefore, it can be concluded that the effect of the temperature on emissivity of carbon black materials is not well understood. Figure 6.5 shows a comparison between experimentally obtained calibration curves and black body calibration curve which has an emissivity of 1. From the graph it can be seen that there is a smaller deviation at lower temperatures compared to higher temperatures between a black body curve and experimentally obtained curves. It suggests that emissivity of carbon black filled polymers reduces with increase in temperature.

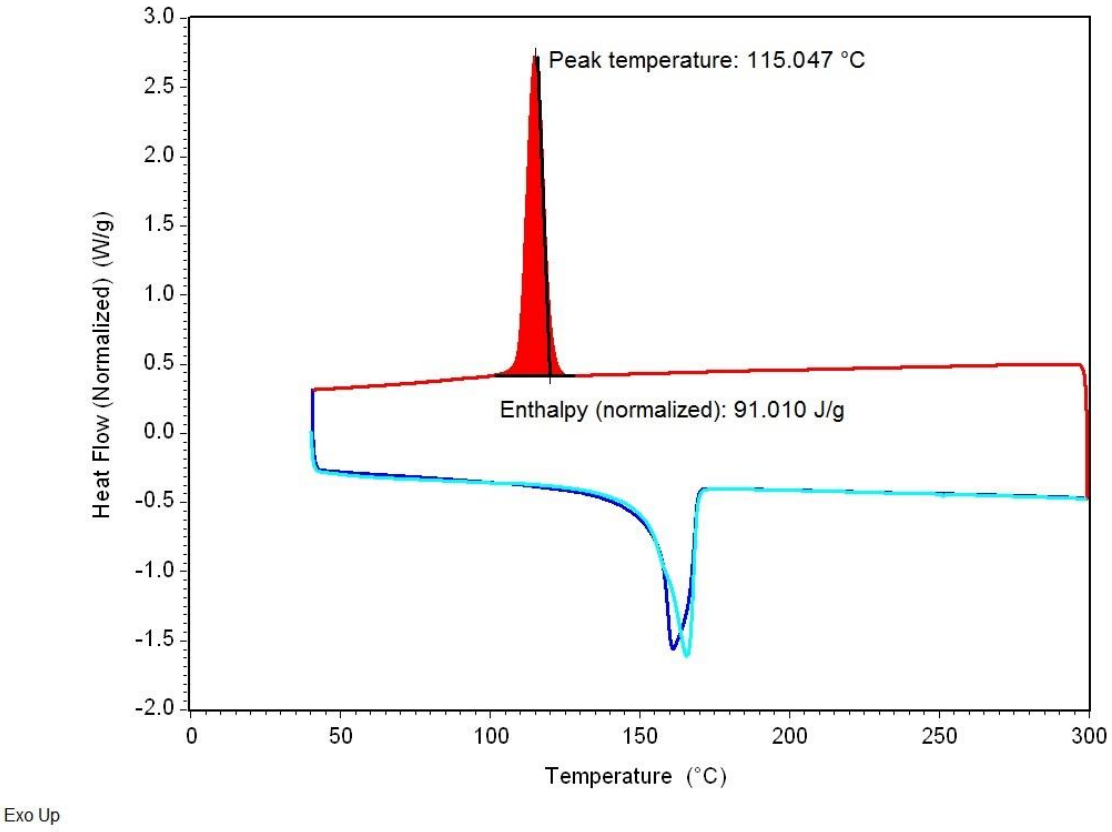

Figure 6.6 DSC curves for CB PP showing crystallisation temperature.

6.4 IR Camera Settings

There are a number of important factors which need to be considered when performing calibration and operation of the camera. These interconnected parameters are frame size, frame rate and integration time and they need to be adjusted for the process to be analysed. The integration time is the exposure time of the IR sensor. Normally a short integration time is used for higher temperature applications to prevent saturation. Moreover, a shorter integration time increases frame rate and produces sharp images on fast thermal events. A number of experiments were performed where polymer was injected into the cavity at different injection speeds. This small trial has shown that 50 µs integration time was adequate to capture flow front up to an injection speed of 500 mm/s. Calibration of materials and further experiments were performed with a frame size of 160 x 128 pixels, integration time of 50 µs and frame rate of 1000 frames per second.

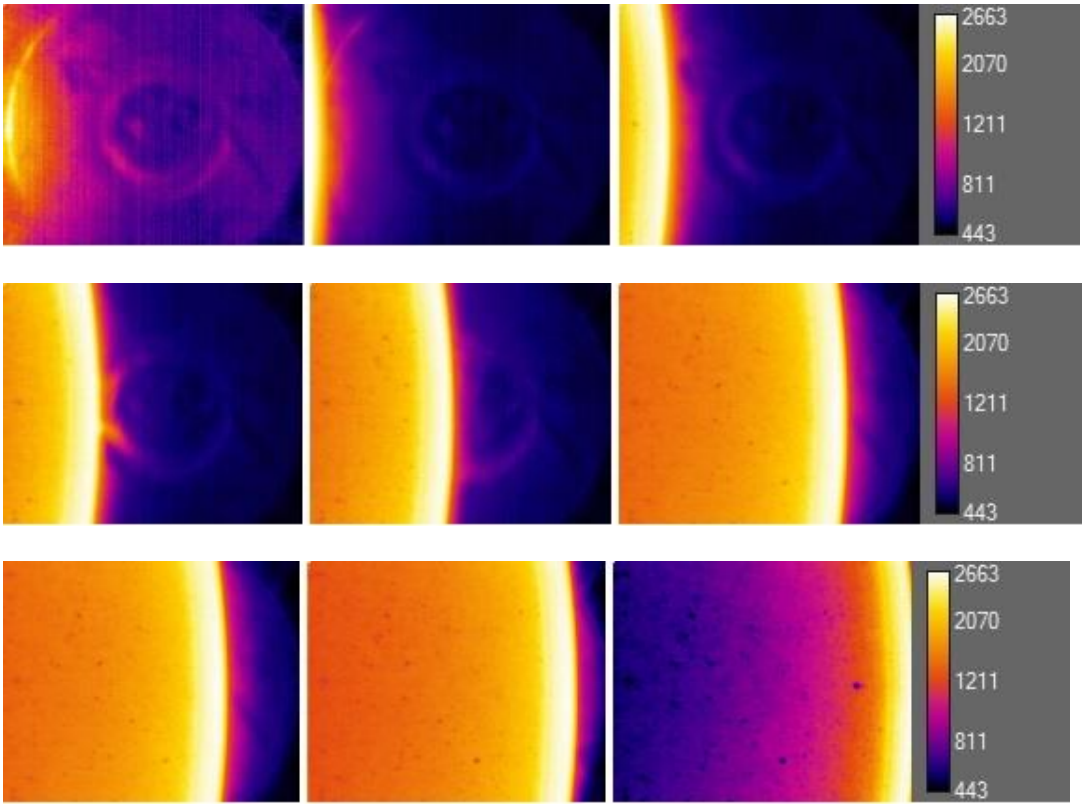

Figure 6.7 Filling of the centre of the cavity.

Figure 6.7 shows filling in the centre of the cavity. The frame size was 160 x 128 pixels (2.4 x 1.92 mm). The circular front of the p-T sensor fitted in the other half of the mould can be observed in images before the flow front covers it.

6.4.1 Focusing on Sapphire/Melt Interface

Focusing at the interface between the sapphire and melt is not an easy task, as cavity filling happens in a fraction of a second. A special IR target was machined from 2 mm aluminium sheet which was painted in black. Then a 1 mm hole was drilled which corresponds to the centre of the cavity. The target disk was then attached to the fixed half of the mould shown in Figure 6.8. When the edge of the hole was in the best focus that meant that IR camera was focused on the sapphire surface. Figure 6.8 also shows image recorded during focusing of the camera. Very small scratches can be observed on the surface of the target which also suggests that camera is in focus at the interface.

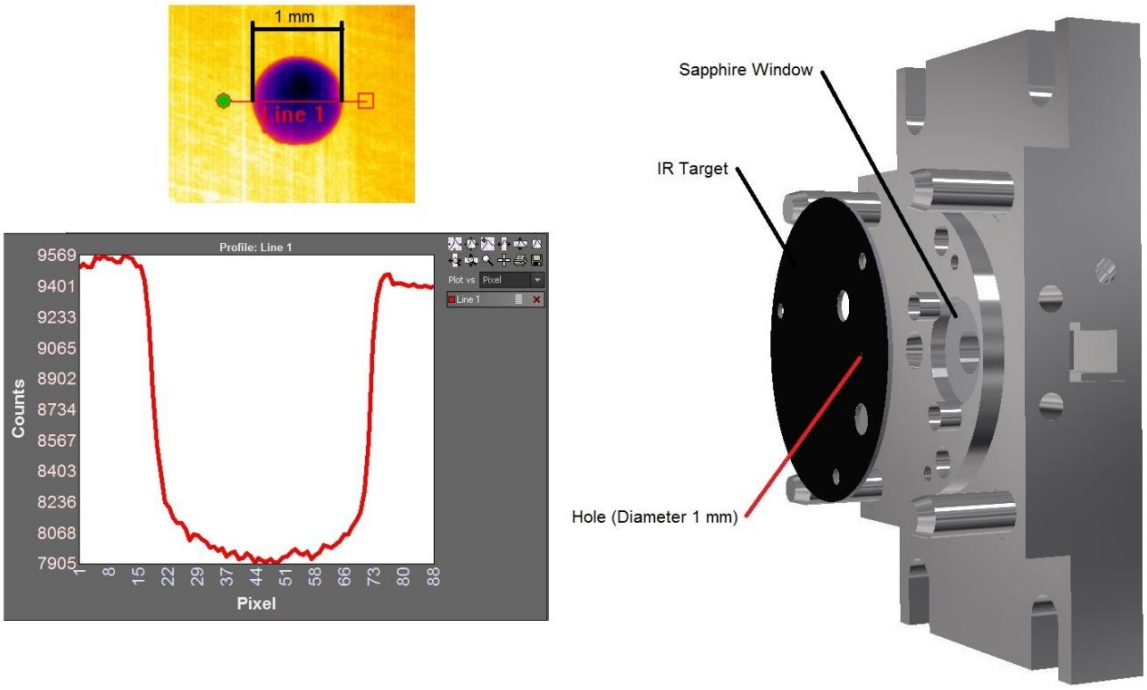

Figure 6.8 Focusing at the interface with IR target.

6.5 Part Geometry

Part geometry is a small disk component shown in Figure 6.9. The area of interest is located in the centre of the disk.

Figure 6.9 Part geometry and dimensions.

6.6 Design of Experiments

Prior to the DOE (Design of experiments) robust processing settings had to be identified. These are the minimum and maximum settings at which good parts can be produced. This was achieved by identifying lower and higher limits of injection speed and packing pressure at two melt temperatures (220 and 240 °C) and two mould temperatures (60 and 80 °C). All the parts were visually analysed for undesirable short shots and sink marks at low settings and flashing of the parts at high settings.

The design of experiments was used to determine which of the controllable process variables have the most influence on the output (Montgomery et al., 2007). In terms of microinjection moulding these variables can be injection speed, melt temperature, mould temperature, injection pressure, switch-over pressure, cavity pressure and many more processing conditions. In the DOE approach two or more factors can be taken into account simultaneously in the analysis of the main factor or interaction between them. When implementing DOE there are two approaches, namely full factorial design and fractional factorial design. Within full factorial design, responses at all combinations of the factor levels are measured. Fractional

factorial designs are used to reduce experimental efforts in large DOEs. In this approach only a selected subset of the runs in the full factorial design is performed (Montgomery et al., 2007; Support.minitab.com, 2015).

Analysis of the results obtained from DOE was performed in Minitab 16 software employing the analysis of variance (ANOVA). In general, the purpose of the ANOVA is to test the significant differences between the group means.

In this work the factors selected to be studied within the full factorial DOE were, surface roughness, melt temperature, mould temperature, injection speed and packing pressure. As it can be seen from Tables 6.3 and 6.4, a five-factor with two-level for melt temperature, mould temperature, injection speed and packing pressure and five-level for surface roughness full factorial design has been carried out. Tables 6.5 and 6.6 show full factorial design of experiments for two materials employed in the investigation.

Table 6.3 Process parameters settings for CB PP.

Factors and Level Settings (CB PP)						
Factors	Name	Level 1	Level 2	Level 3	Level 4	Level 5
A	Surface Roughness	0.007 µm	1 µm	4.2 µm	15 µm pillars	30 µm pillars
B	Melt Temperature	220 °C	240 °C			
C	Mould Temperature	60 °C	80 °C			
D	Injection Speed	200 mm/s	500 mm/s			
E	Packing Pressure	300 bar	600 bar			

Table 6.4 Process parameters settings for CB PS.

Factors and Level Settings (CB PS)						
Factors	Name	Level 1	Level 2	Level 3	Level 4	Level 5
A	Surface Roughness	0.007 µm	1 µm	4.2 µm	15 µm pillars	30 µm pillars
B	Melt Temperature	220 °C	240 °C			
C	Mould Temperature	60 °C	80 °C			
D	Injection Speed	200 mm/s	500 mm/s			
E	Packing Pressure	500 bar	1000 bar			

Table 6.5 Full factorial design of experiments for CB PP used in the investigation.

RunOrder	Surface Roughness (µm)	Melt T (°C)	Mould T (°C)	Injection speed (mm/s)	Packing Pressure (bar)
1	Polished	220	60	200	300
2	Polished	220	60	200	600
3	Polished	220	60	500	300
4	Polished	220	60	500	600
5	Polished	220	80	200	300
6	Polished	220	80	200	600
7	Polished	220	80	500	300
8	Polished	220	80	500	600
9	Polished	240	60	200	300
10	Polished	240	60	200	600
11	Polished	240	60	500	300
12	Polished	240	60	500	600
13	Polished	240	80	200	300
14	Polished	240	80	200	600
15	Polished	240	80	500	300
16	Polished	240	80	500	600
17	1 um	220	60	200	300
18	1 um	220	60	200	600
19	1 um	220	60	500	300
20	1 um	220	60	500	600
21	1 um	220	80	200	300
22	1 um	220	80	200	600
23	1 um	220	80	500	300
24	1 um	220	80	500	600
25	1 um	240	60	200	300
26	1 um	240	60	200	600
27	1 um	240	60	500	300
28	1 um	240	60	500	600
29	1 um	240	80	200	300
30	1 um	240	80	200	600
31	1 um	240	80	500	300
32	1 um	240	80	500	600
33	4.2 um	220	60	200	300
34	4.2 um	220	60	200	600
35	4.2 um	220	60	500	300
36	4.2 um	220	60	500	600
37	4.2 um	220	80	200	300
38	4.2 um	220	80	200	600
39	4.2 um	220	80	500	300
40	4.2 um	220	80	500	600
41	4.2 um	240	60	200	300
42	4.2 um	240	60	200	600
43	4.2 um	240	60	500	300
44	4.2 um	240	60	500	600
45	4.2 um	240	80	200	300
46	4.2 um	240	80	200	600
47	4.2 um	240	80	500	300
48	4.2 um	240	80	500	600
49	15 um pollars	220	60	200	300
50	15 um pollars	220	60	200	600
51	15 um pollars	220	60	500	300
52	15 um pollars	220	60	500	600
53	15 um pollars	220	80	200	300
54	15 um pollars	220	80	200	600
55	15 um pollars	220	80	500	300
56	15 um pollars	220	80	500	600
57	15 um pollars	240	60	200	300
58	15 um pollars	240	60	200	600
59	15 um pollars	240	60	500	300
60	15 um pollars	240	60	500	600
61	15 um pollars	240	80	200	300
62	15 um pollars	240	80	200	600
63	15 um pollars	240	80	500	300
64	15 um pollars	240	80	500	600
65	30 um pillars	220	60	200	300
66	30 um pillars	220	60	200	600
67	30 um pillars	220	60	500	300
68	30 um pillars	220	60	500	600
69	30 um pillars	220	80	200	300
70	30 um pillars	220	80	200	600
71	30 um pillars	220	80	500	300
72	30 um pillars	220	80	500	600
73	30 um pillars	240	60	200	300
74	30 um pillars	240	60	200	600
75	30 um pillars	240	60	500	300
76	30 um pillars	240	60	500	600
77	30 um pillars	240	80	200	300
78	30 um pillars	240	80	200	600
79	30 um pillars	240	80	500	300
80	30 um pillars	240	80	500	600

Table 6.6 Full factorial design of experiments for CB PS used in the investigation.

RunOrder	Surface Roughness (μm)	Melt T (°C)	Mould T (°C)	Injection speed (mm/s)	Packing Pressure (bar)
1	Polished	220	60	200	500
2	Polished	220	60	200	1000
3	Polished	220	60	500	500
4	Polished	220	60	500	1000
5	Polished	220	80	200	500
6	Polished	220	80	200	1000
7	Polished	220	80	500	500
8	Polished	220	80	500	1000
9	Polished	240	60	200	500
10	Polished	240	60	200	1000
11	Polished	240	60	500	500
12	Polished	240	60	500	1000
13	Polished	240	80	200	500
14	Polished	240	80	200	1000
15	Polished	240	80	500	500
16	Polished	240	80	500	1000
17	1 um	220	60	200	500
18	1 um	220	60	200	1000
19	1 um	220	60	500	500
20	1 um	220	60	500	1000
21	1 um	220	80	200	500
22	1 um	220	80	200	1000
23	1 um	220	80	500	500
24	1 um	220	80	500	1000
25	1 um	240	60	200	500
26	1 um	240	60	200	1000
27	1 um	240	60	500	500
28	1 um	240	60	500	1000
29	1 um	240	80	200	500
30	1 um	240	80	200	1000
31	1 um	240	80	500	500
32	1 um	240	80	500	1000
33	4.2 um	220	60	200	500
34	4.2 um	220	60	200	1000
35	4.2 um	220	60	500	500
36	4.2 um	220	60	500	1000
37	4.2 um	220	80	200	500
38	4.2 um	220	80	200	1000
39	4.2 um	220	80	500	500
40	4.2 um	220	80	500	1000
41	4.2 um	240	60	200	500
42	4.2 um	240	60	200	1000
43	4.2 um	240	60	500	500
44	4.2 um	240	60	500	1000
45	4.2 um	240	80	200	500
46	4.2 um	240	80	200	1000
47	4.2 um	240	80	500	500
48	4.2 um	240	80	500	1000
49	15 um pollars	220	60	200	500
50	15 um pollars	220	60	200	1000
51	15 um pollars	220	60	500	500
52	15 um pollars	220	60	500	1000
53	15 um pollars	220	80	200	500
54	15 um pollars	220	80	200	1000
55	15 um pollars	220	80	500	500
56	15 um pollars	220	80	500	1000
57	15 um pollars	240	60	200	500
58	15 um pollars	240	60	200	1000
59	15 um pollars	240	60	500	500
60	15 um pollars	240	60	500	1000
61	15 um pollars	240	80	200	500
62	15 um pollars	240	80	200	1000
63	15 um pollars	240	80	500	500
64	15 um pollars	240	80	500	1000
65	30 um pillars	220	60	200	500
66	30 um pillars	220	60	200	1000
67	30 um pillars	220	60	500	500
68	30 um pillars	220	60	500	1000
69	30 um pillars	220	80	200	500
70	30 um pillars	220	80	200	1000
71	30 um pillars	220	80	500	500
72	30 um pillars	220	80	500	1000
73	30 um pillars	240	60	200	500
74	30 um pillars	240	60	200	1000
75	30 um pillars	240	60	500	500
76	30 um pillars	240	60	500	1000
77	30 um pillars	240	80	200	500
78	30 um pillars	240	80	200	1000
79	30 um pillars	240	80	500	500
80	30 um pillars	240	80	500	1000

For each run order shown in Tables 6.5 and 6.6, the first 20 parts were discarded. After 20 cycles process was stabilised and the following 10 parts were collected together with recorded temperature and cavity pressure distributions.

6.7 Data Processing

Figure 6.10 demonstrates two temperature distributions recorded with the IR camera. The only difference between the two cooling curves is the injection speed, run 1 is 200 mm/s and run 3 is 500 mm/s; other processing condition can be seen in Table 6.5. The temperature measured is the average temperature shown in a blue square which is a region of interest (1.92 x 1.92 mm). The black arrow shows temperature before the injection. These two curves cannot be compared directly, because filling of the cavity starts earlier at 500 mm/s. To compare cooling curves directly they were aligned to their peak temperatures as shown in Figure 6.11. Therefore t = 0 is the peak temperature measured.

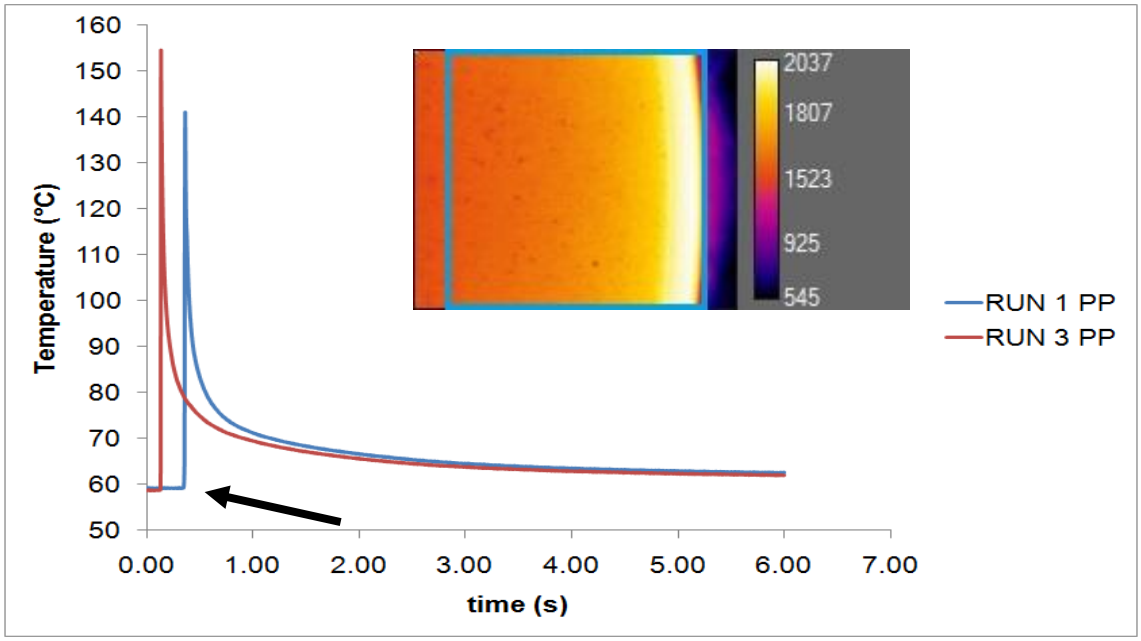

Figure 6.10 Difference in cooling curves with injection speed of 200 mm/s (blue) and 500 mm/s (red).

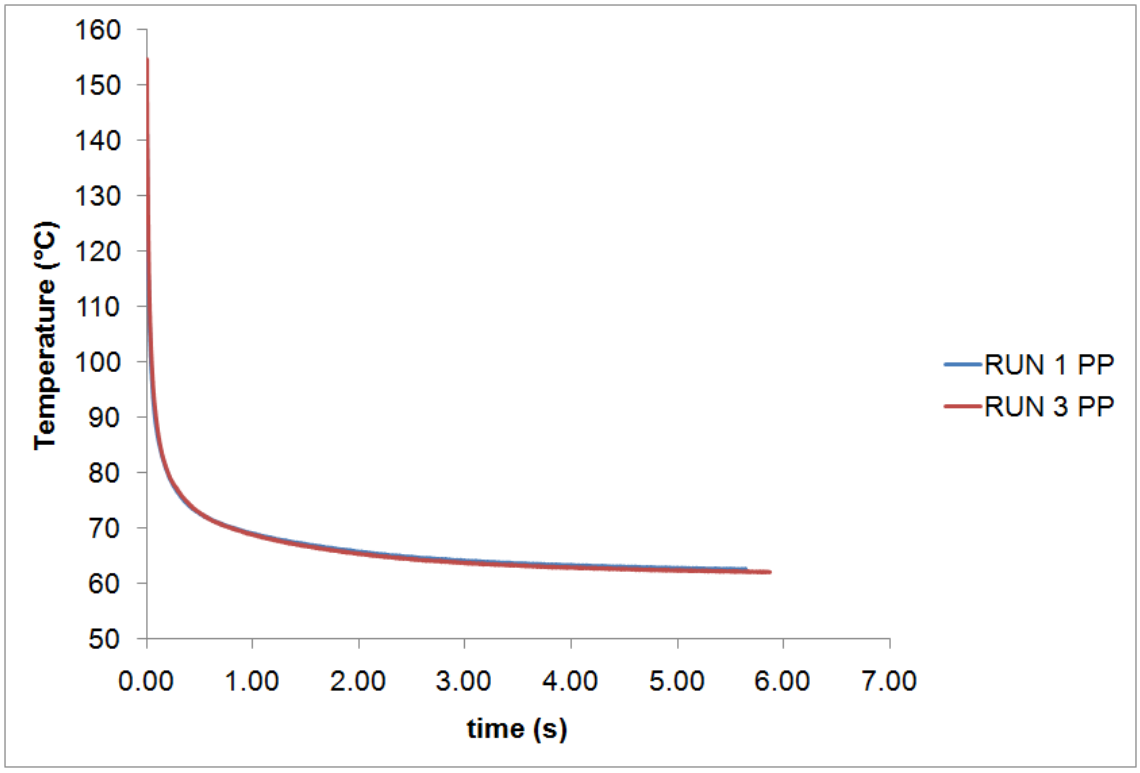

Figure 6.11 Cooling curves with aligned peaks with injection speed of 200 mm/s (blue) and 500 mm/s (red).

The peak average temperature measured is nowhere near melt set temperature of 220 °C. Melt touches the cold surface and cools down extremely rapidly. This can also be observed during cavity filling shown in Figure 6.12. The difference between the flow front and material approximately 2 mm behind is nearly 20 °C.

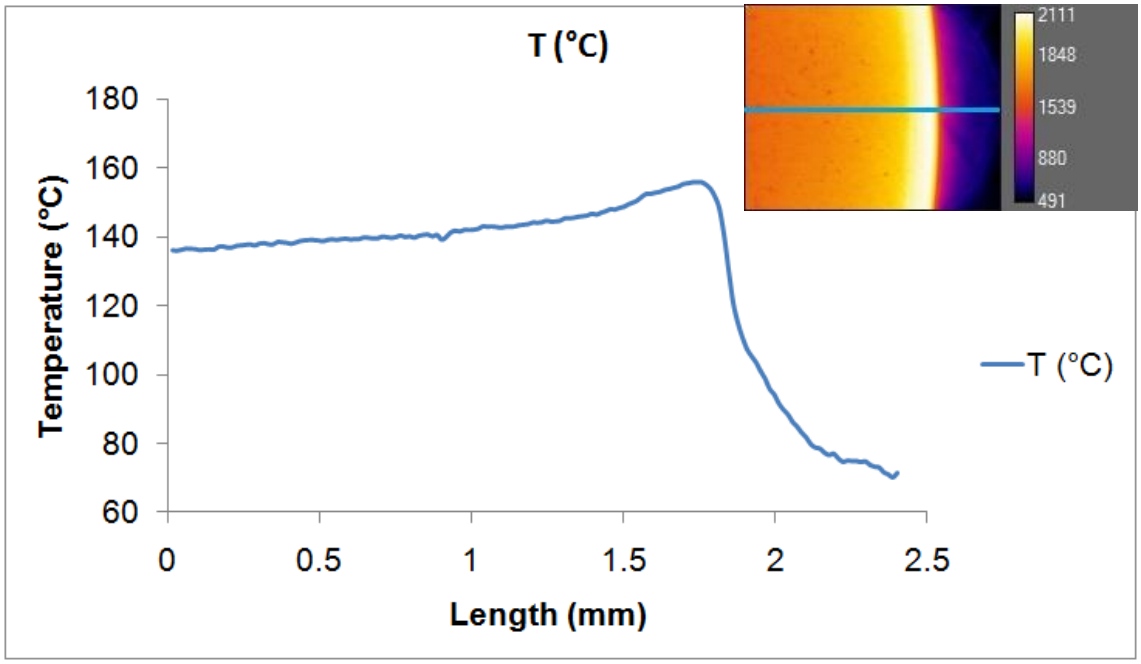

Figure 6.12 Temperature line profile of the melt during cavity filling.

Another interesting observation is that flow front temperature decreases further as it moves into the cavity. Figure 6.13 shows eight frames captured during the filling centre of the cavity. In the graph line profiles are plotted together with the maximum temperature values. The geometry of the part is 16.6 mm diameter disk and what is plotted is an area in the centre of the disk (H = 1.92, W = 2.4 mm). This suggests that temperature of the flow front is higher when it just starts filling the cavity.

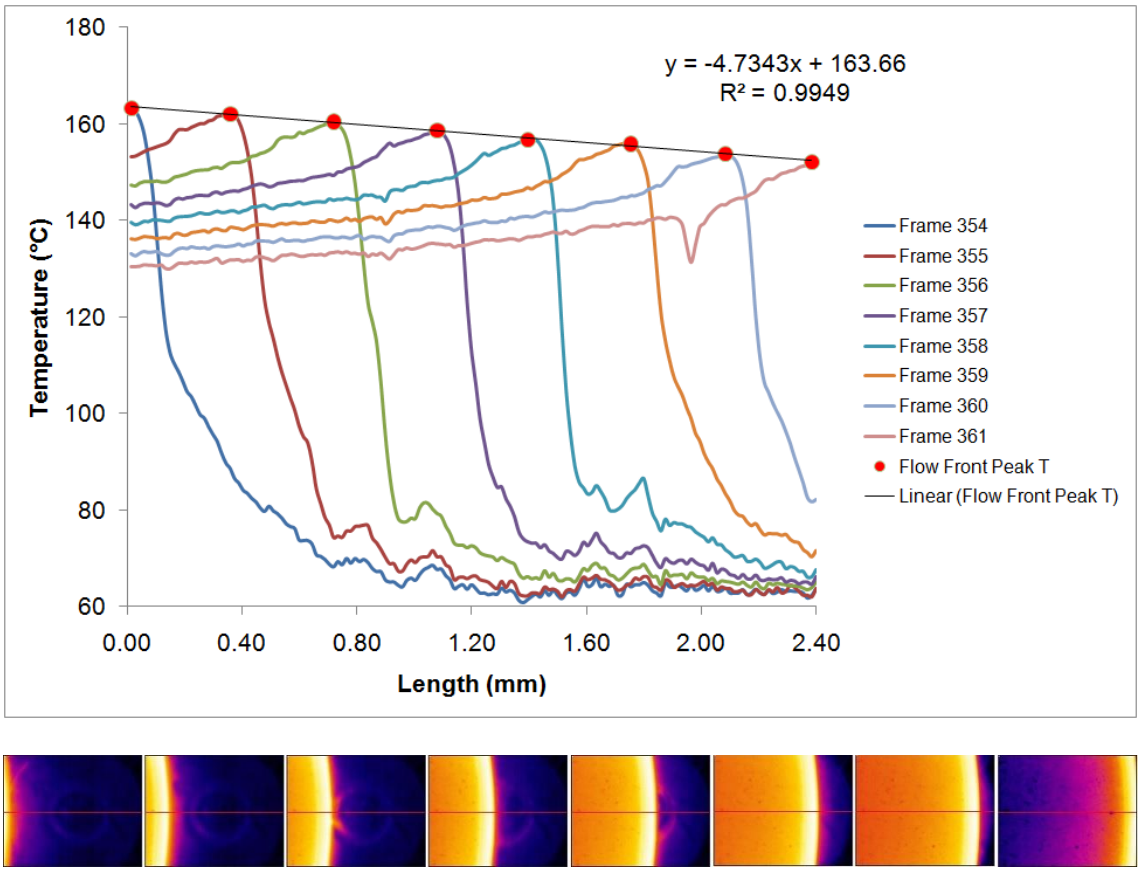

Figure 6.13 Temperature line profiles of the melt showing flow front temperature decreasing while melt moving progressively the measurement field.

6.8 Analysis of the Results

6.8.1 CB PS - Effects of Processing Settings

Figures 6.14 and 6.15 show typical cooling profiles together with cavity pressure distributions recorded through polished sapphire. Figure 6.14 represents low processing settings (melt T = 220 °C, mould = 60 °C, injection speed = 200

mm/s, packing pressure 500 bar), whereas Figure 6.15 represents high processing settings (melt T = 240 °C, mould = 80 °C, injection speed = 500 mm/s, packing pressure 1000 bar). Cooling profiles demonstrate how quickly temperature drops from its peak temperature to the mould set temperature.

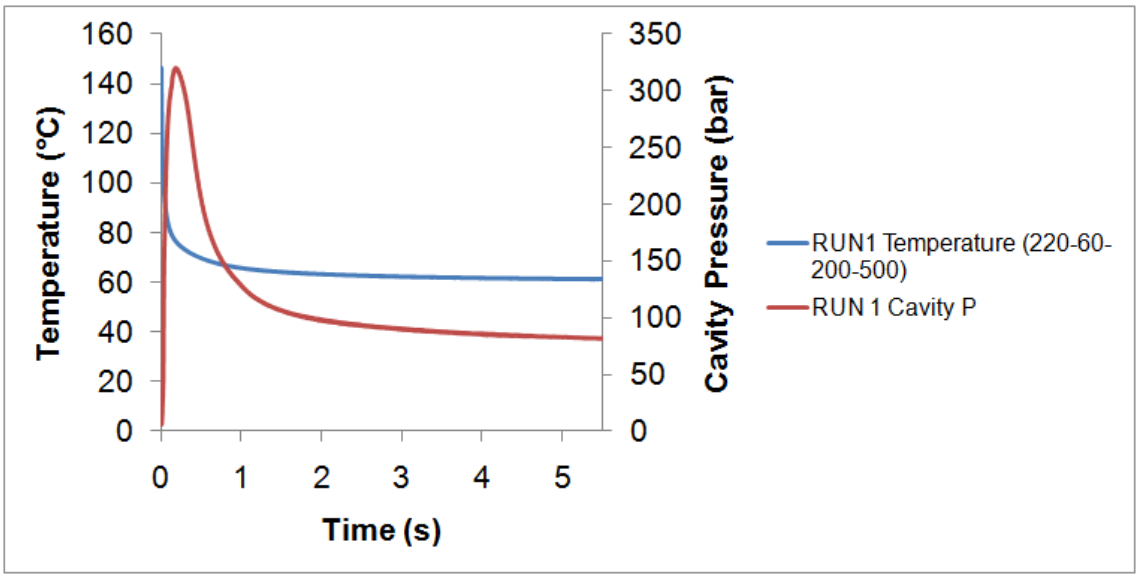

Figure 6.14 Cooling curve and cavity pressure profile at low processing parameters.

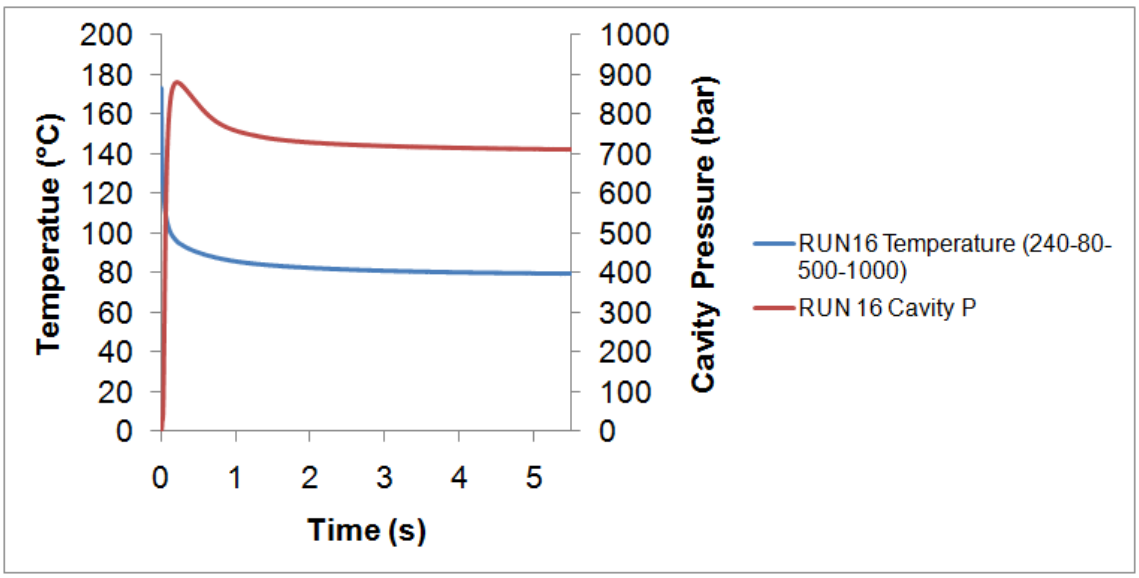

Figure 6.15 Cooling curve and cavity pressure profile at high processing parameters.

In this research Minitab 16 analysis software was used to perform the statistical analysis of the experimental results. Significant effects were analysed

depending on the temperature of the polymer at different time steps which are t = 0 s (peak T), t = 0.25 s, t = 0.5 s, t = 1 s, and t = 1.5 s.

A Pareto chart graphically summarises and displays the magnitude and the importance of the main effects of the processing settings on polymer temperature. It is a bar chart where factors are plotted from largest to smallest according to their importance. All the bars that go beyond red line on the Pareto chart are statistically significant. On the chart the standardised effects are the t-statistics and calculated by dividing each coefficient by its standard error. (Support.minitab.com, 2015).

The most influential process parameters on the peak temperature during filling were injection speed, melt temperature and mould temperature which are shown in Figure 6.16. Injection speed was found to be the most significant factor during filling of CB PS.

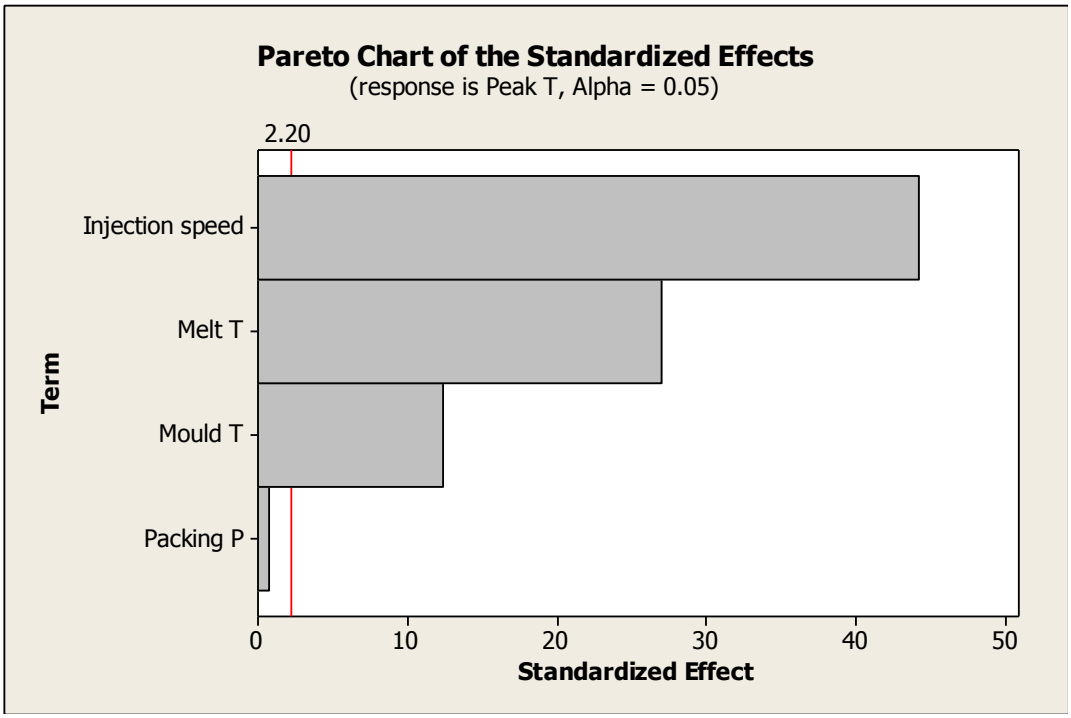

Figure 6.16 Pareto analysis of the processing parameters during cavity filling of CB PS.

Figure 6.17 represents Pareto analysis of polymer temperature at four different time steps, namely t = 0.25 s, t = 0.5 s, t = 1 s, and t = 1.5 s. With confidence limit of 95% it shows that mould temperature and melt temperature, are both statistically significant parameters with the mould temperature being the most influential.

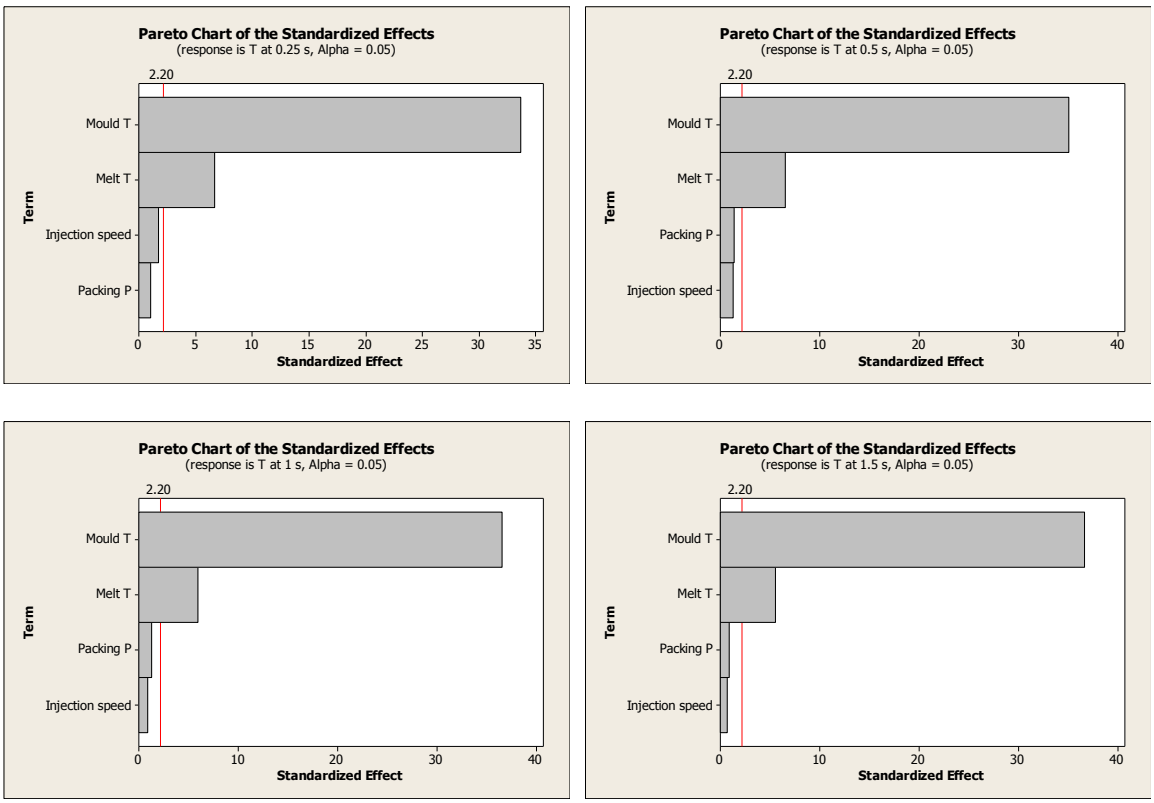

Figure 6.17 Pareto analysis of the processing parameters during polymer cooling of CB PS at four different time steps.

Figures 16.18 - 6.22 show the main effect plots for the four factors (Melt T, Mould T, Injection speed and Packing P) and two-levels for each factor for a range of sapphire windows, namely polished sapphire, 1 µm sapphire, 4.2 µm sapphire, 15 µm pillars sapphire and 30 µm pillars sapphire. Each main effect chart shows directly the effect it produces on the response, where the slope of the line represents the magnitude and direction of the effect on polymer temperature. Vertical axes represent the means of the temperature at a given time for the each factor level. At t = 0 the effects of melt temperature, mould temperature and injection are clearly visible. The analysis of the temperature at t = 0.25 s, t = 0.5 s, t = 1 s, and t = 1.5 s permits to say that mould temperature is the most influential parameter on polymer cooling for all the surfaces.

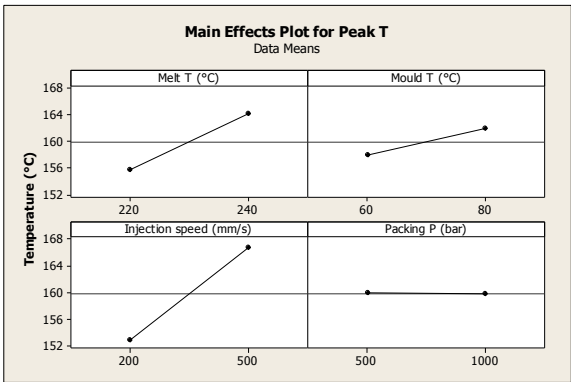

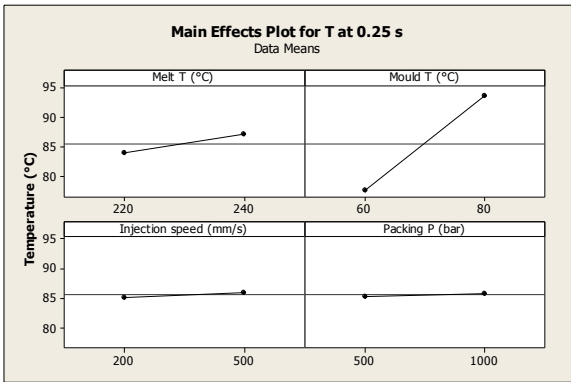

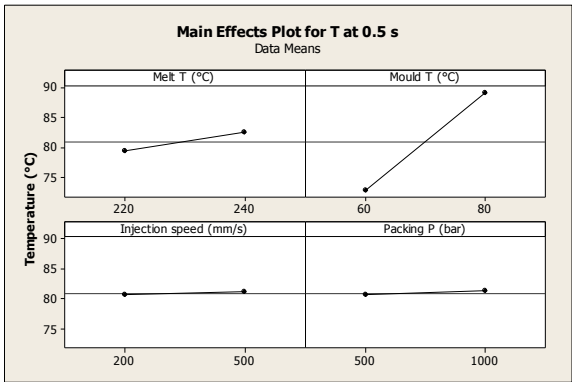

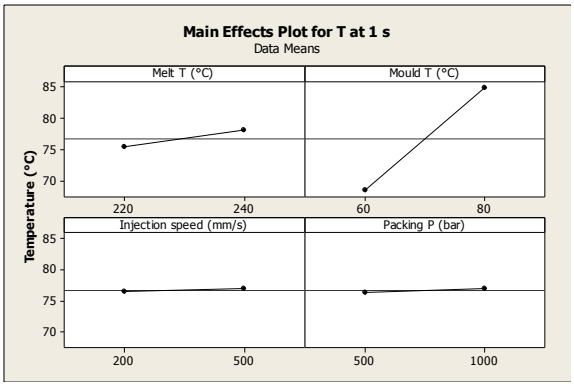

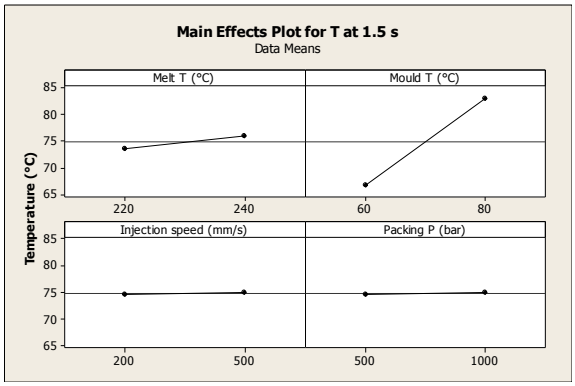

Figure 6.18 Sapphire N1 (Polished) - main effect plot of the temperature of CB PS at t = 0 s, t = 0.25 s, t = 0.5 s, t = 1 s, and t = 1.5 s.

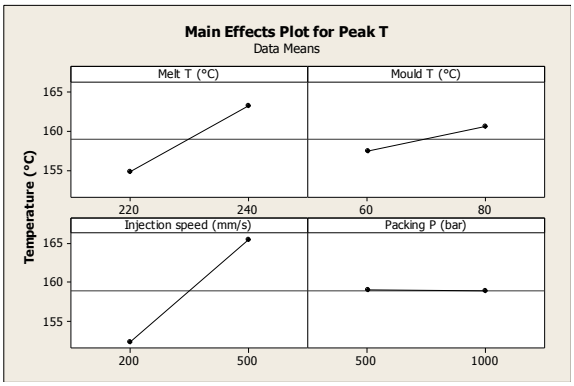

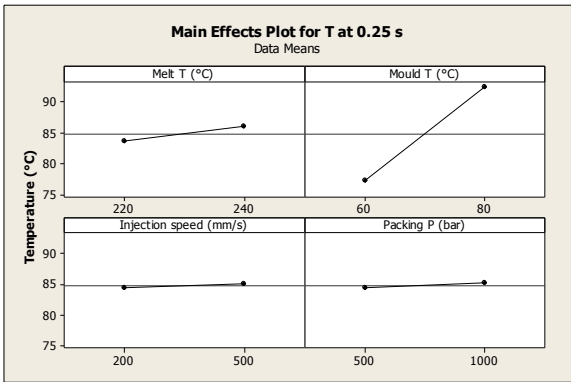

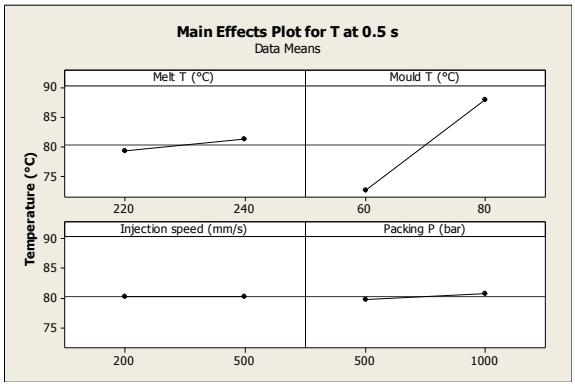

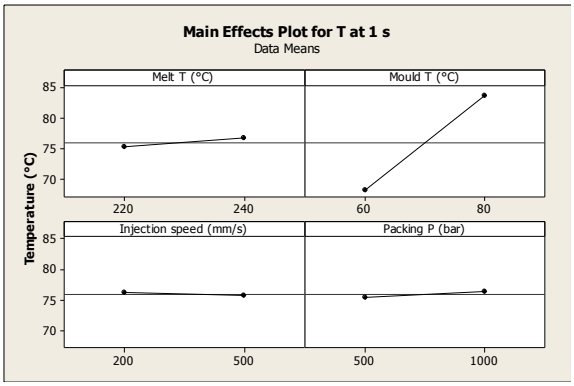

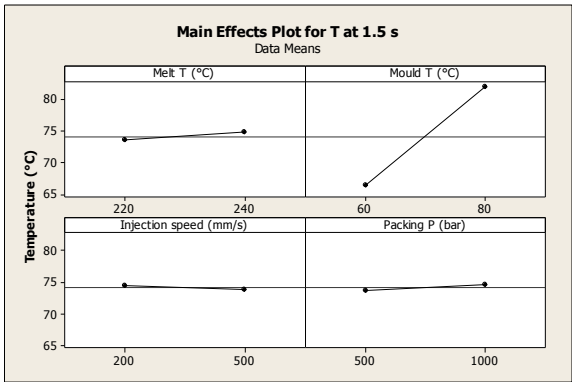

Figure 6.19 Sapphire N2 (Sa = 1.089 µm) - main effect plot of the temperature of CB PS at t = 0 s, t = 0.25 s, t = 0.5 s, t = 1 s, and t = 1.5 s.

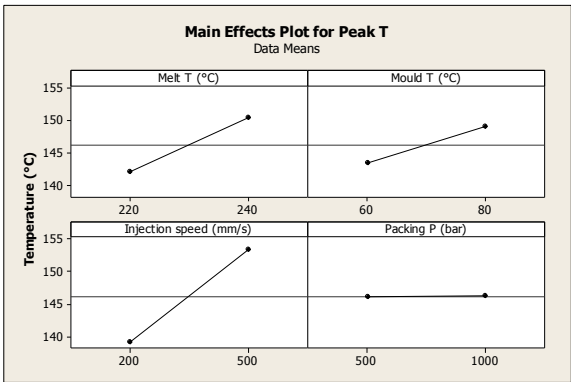

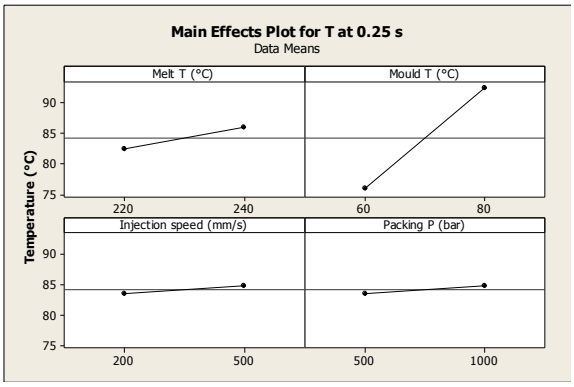

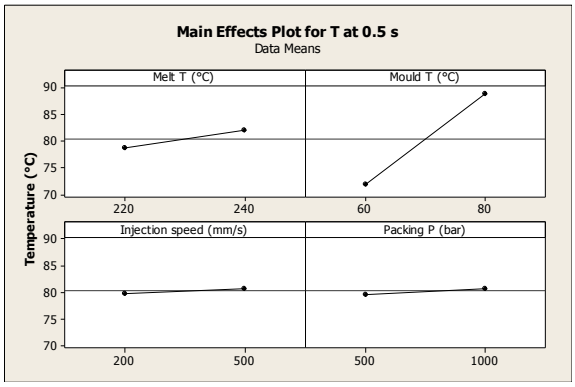

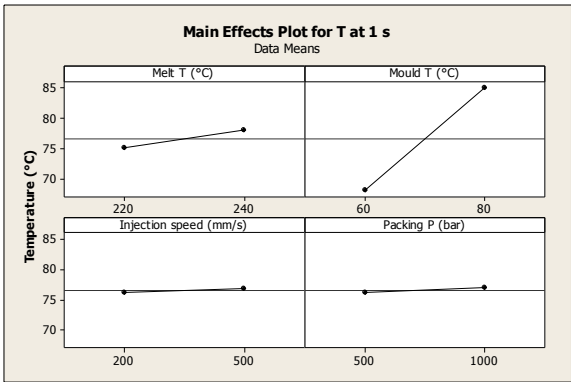

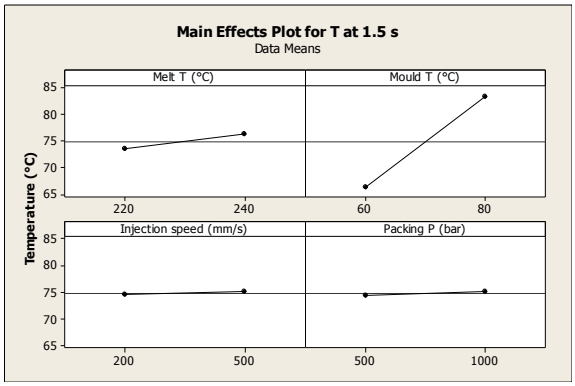

Figure 6.20 Sapphire N3 (Sa = 4.214 µm) - main effect plot of the temperature of CB PS at t = 0 s, t = 0.25 s, t = 0.5 s, t = 1 s, and t = 1.5 s.

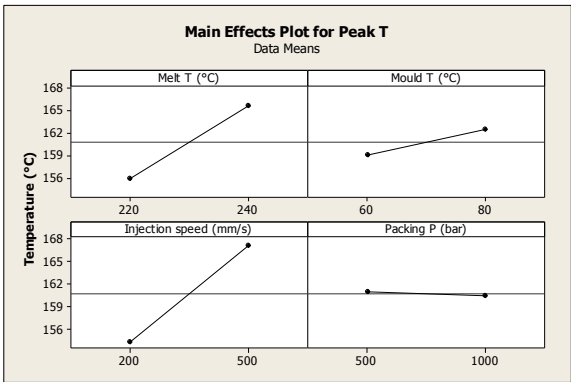

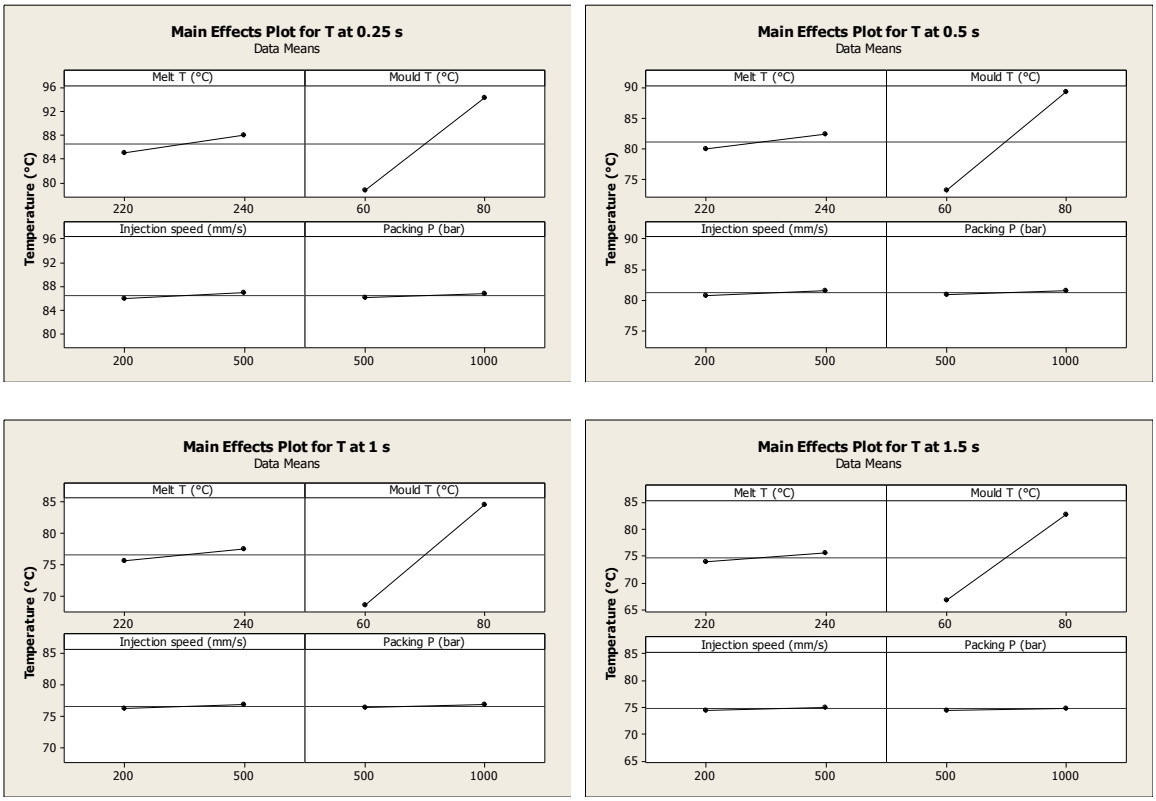

Figure 6.21 Sapphire N4 (15 µm pillars) - main effect plot of the temperature of CB PS at t = 0 s, t = 0.25 s, t = 0.5 s, t = 1 s, and t = 1.5 s.

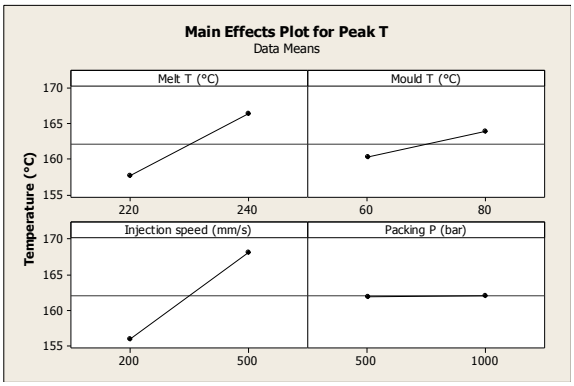

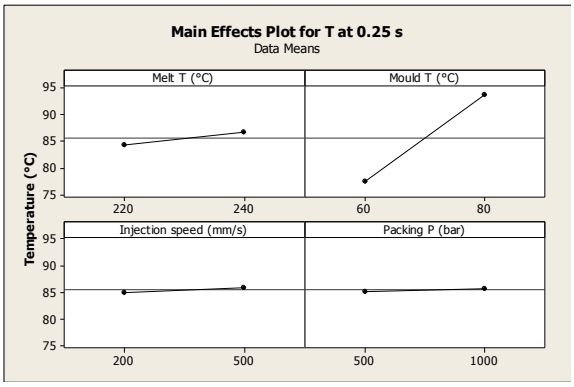

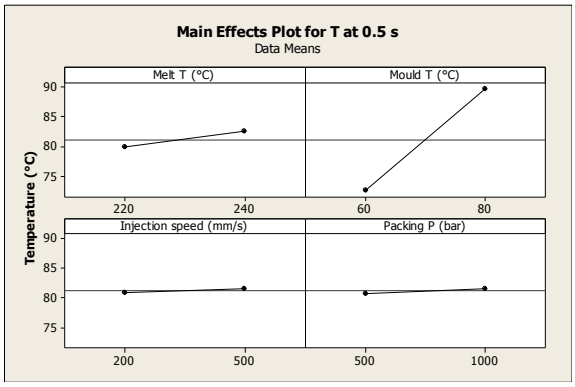

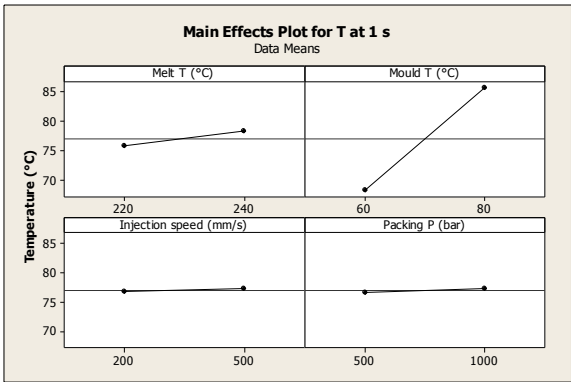

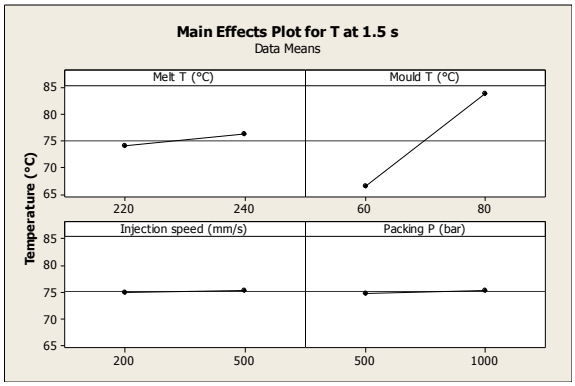

Figure 6.22 Sapphire N5 (30 µm pillars) - Main effect plot of the temperature of CB PS at t = 0 s, t = 0.25 s, t = 0.5 s, t = 1 s, and t = 1.5 s.

6.8.2 CB PP - Effects of Processing Settings

Figure 6.23 reports the Pareto chart of polymer temperature for CB PP recorded through polished sapphire. Three factors had statistically significant effects on the temperature during filling: the injection speed, melt temperature and mould temperature. Similarly to CB PS the injection speed was the most significant parameter. During the cooling or at times t = 0.25 s, t = 0.5 s, t = 1 s, and t = 1.5 s two parameters had statistically significant effect on polymer temperature, namely mould temperature and melt temperature shown in Figure 6.24.

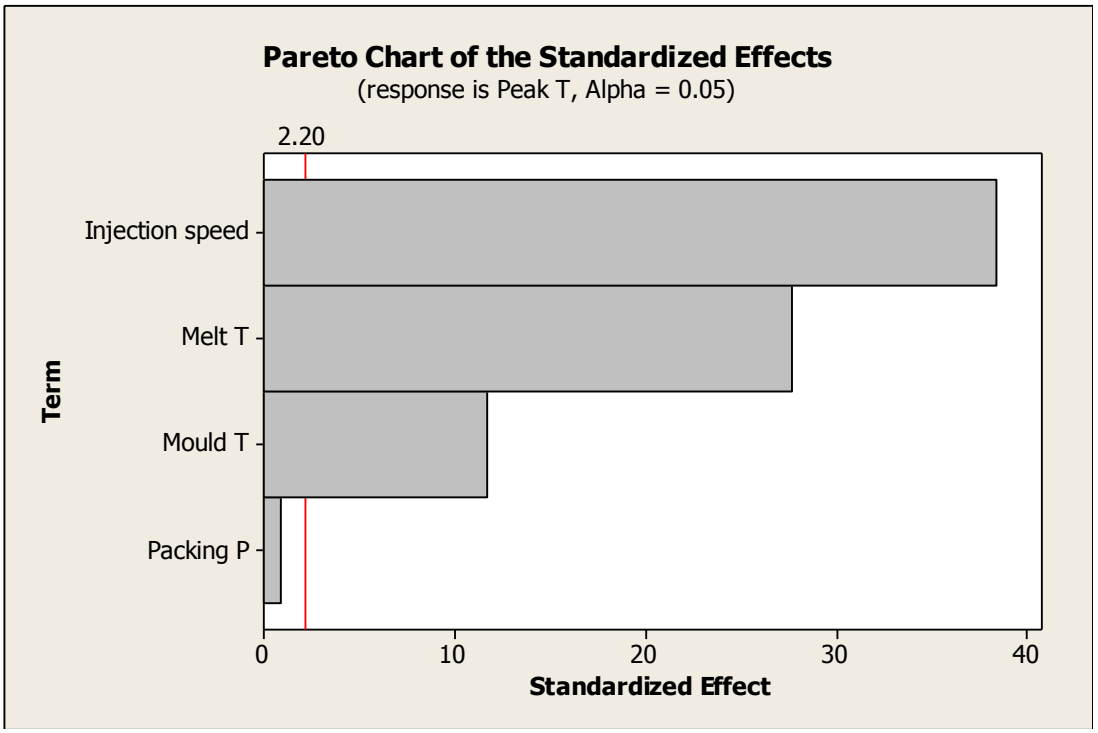

Figure 6.23 Pareto analysis of the processing parameters during cavity filling of CB PP.

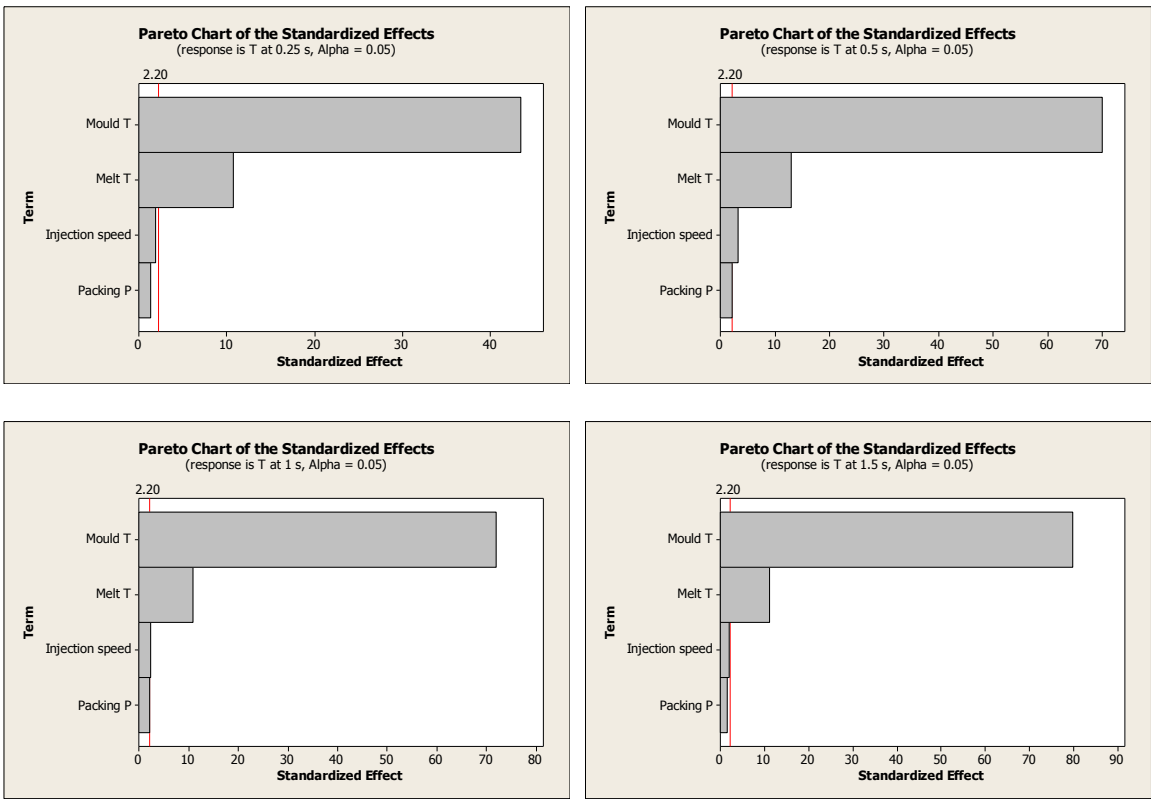

Figure 6.24 Pareto analysis of the processing parameters during polymer cooling of CB PS at four different time steps.

Figures 6.25 - 6.29 show the main effect plots for the four factors (Melt T, Mould T, Injection speed and Packing P) and two-levels for each factor for a range of surfaces, polished sapphire, 1 µm sapphire, 4.2 µm sapphire, 15 µm pillars sapphire and 30 µm pillars sapphire windows. At t = 0 the effects of melt temperature, mould temperature and injection speed are clearly visible. The analysis of the temperature at t = 0.25 s, t = 0.5 s, t = 1 s, and t = 1.5 s permits to say that mould temperature is the most influential parameter on polymer cooling for all the surfaces. Melt temperature is less significant, whereas injection speed and packing pressure remain virtually the same when comparing low and high levels.

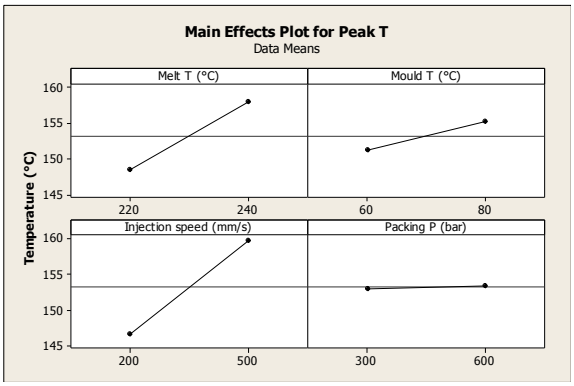

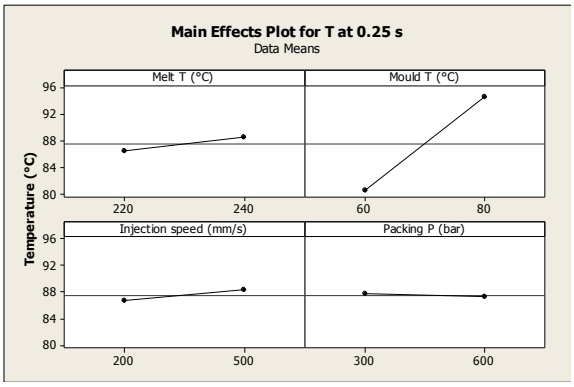

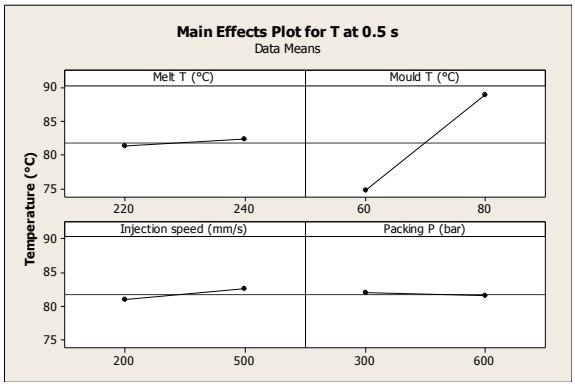

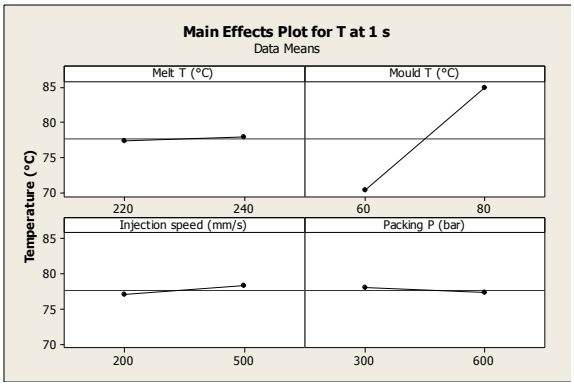

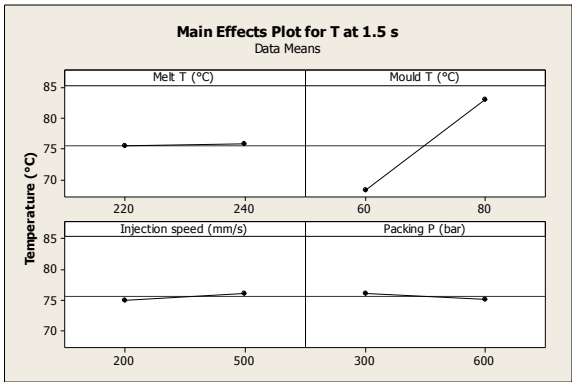

Figure 6.25 Sapphire N1 (Polished) - main effect plot of the temperature of CB PP at t = 0 s, t = 0.25 s, t = 0.5 s, t = 1 s, and t = 1.5 s.

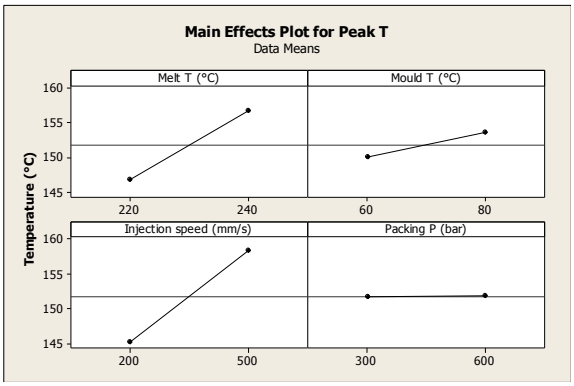

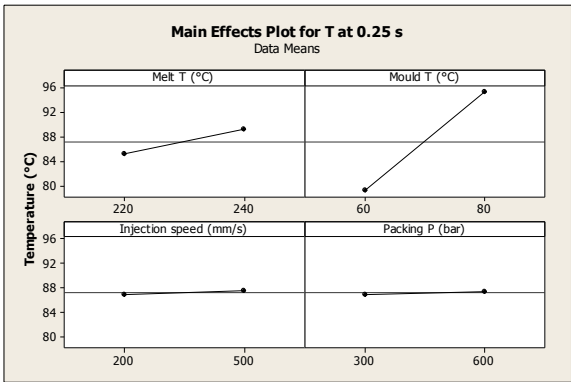

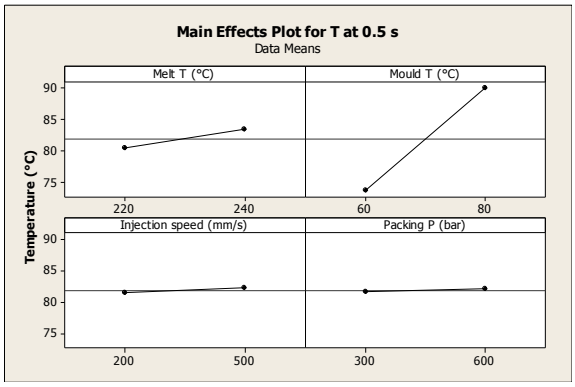

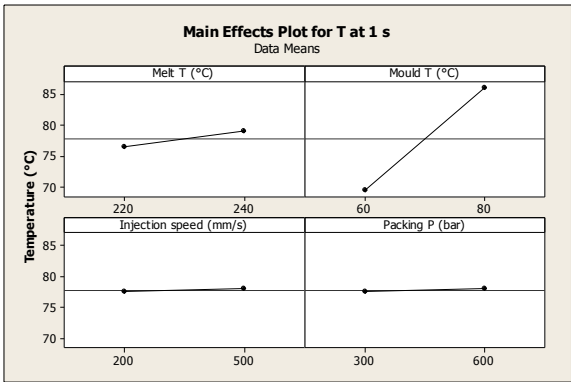

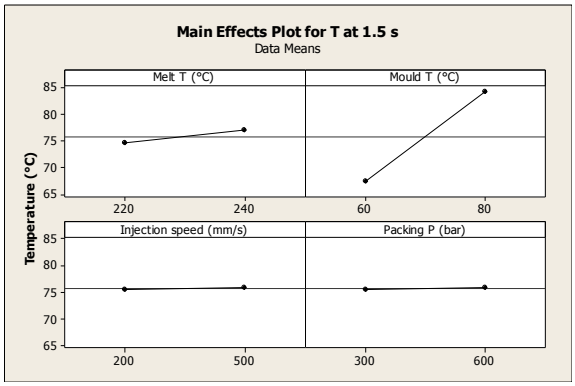

Figure 6.26 Sapphire N2 (Sa = 1.089 µm) - main effect plot of the temperature of CB PP at t = 0 s, t = 0.25 s, t = 0.5 s, t = 1 s, and t = 1.5 s.

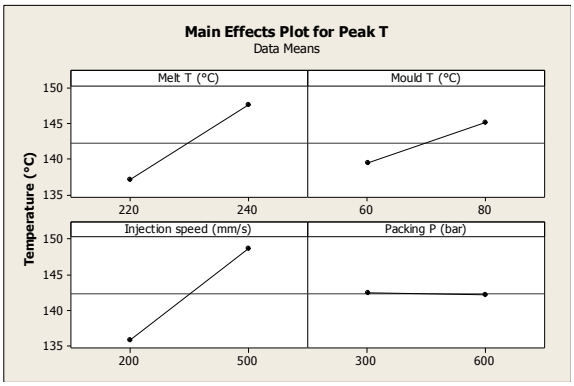

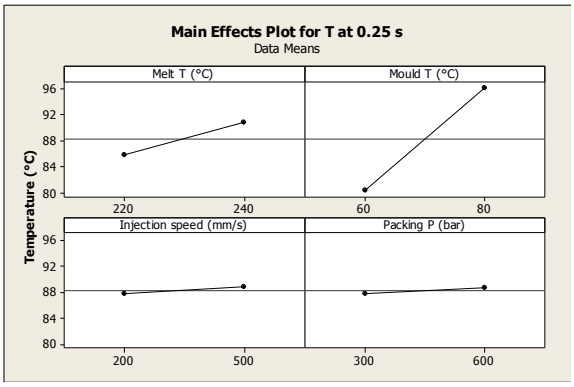

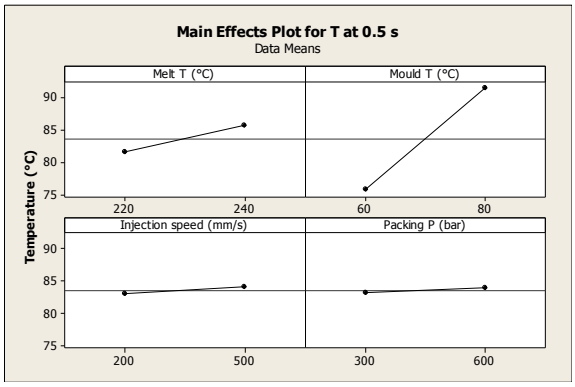

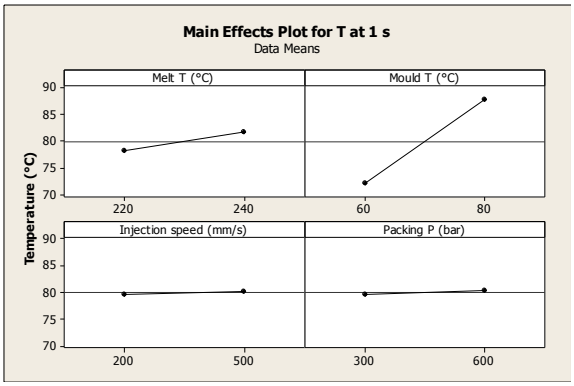

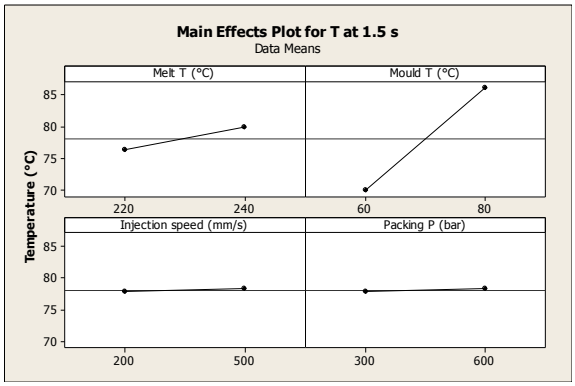

Figure 6.27 Sapphire N3 (Sa = 4.214 µm) - main effect plot of the temperature of CB PP at t = 0 s, t = 0.25 s, t = 0.5 s, t = 1 s, and t = 1.5 s.

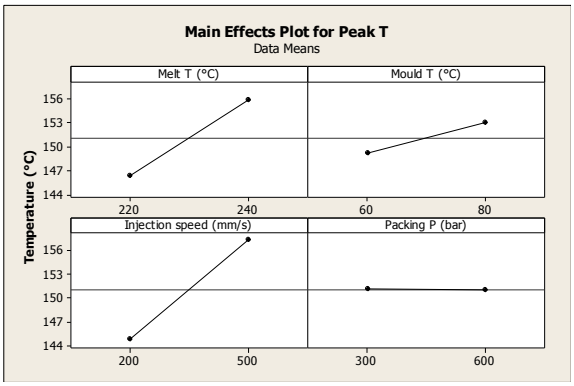

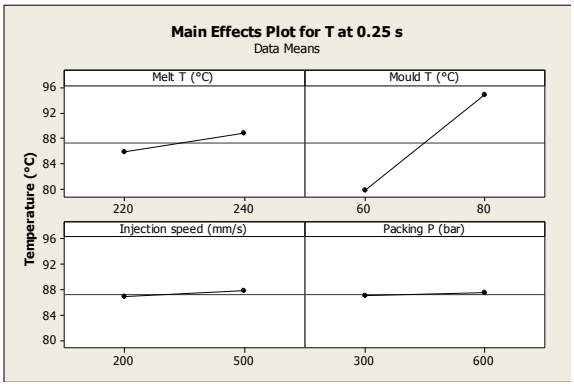

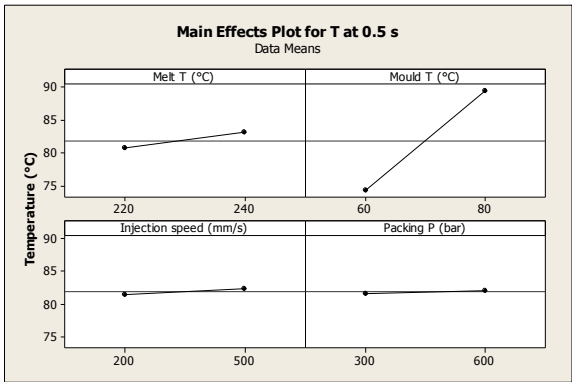

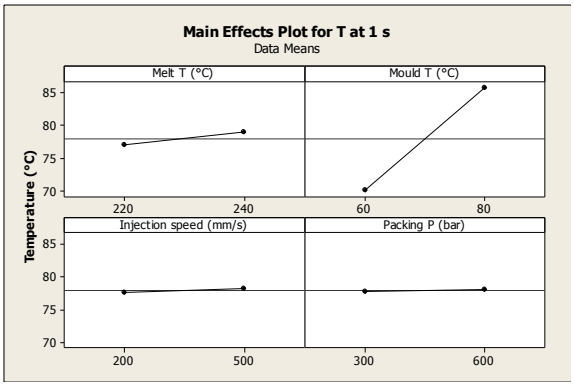

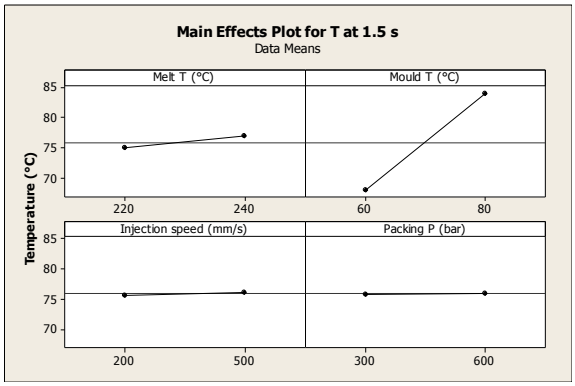

Figure 6.28 Sapphire N4 (15 µm pillars) - main effect plot of the temperature of CB PP at t = 0 s, t = 0.25 s, t = 0.5 s, t = 1 s, and t = 1.5 s.

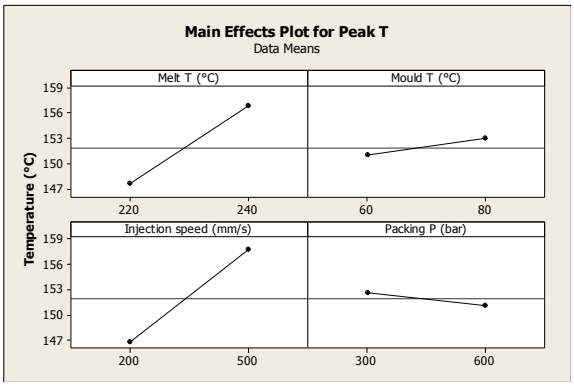

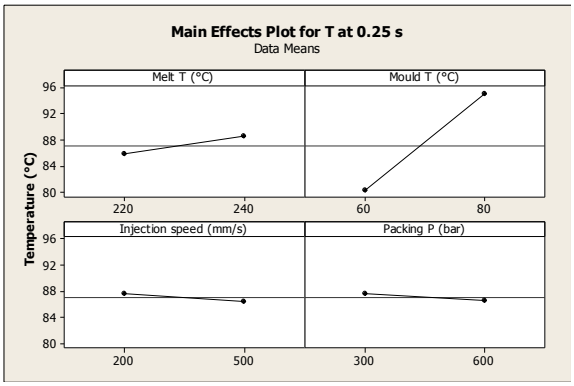

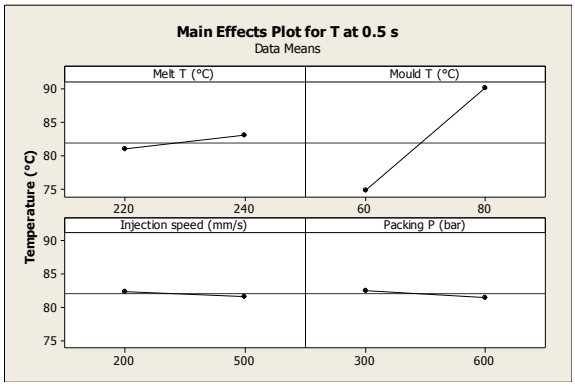

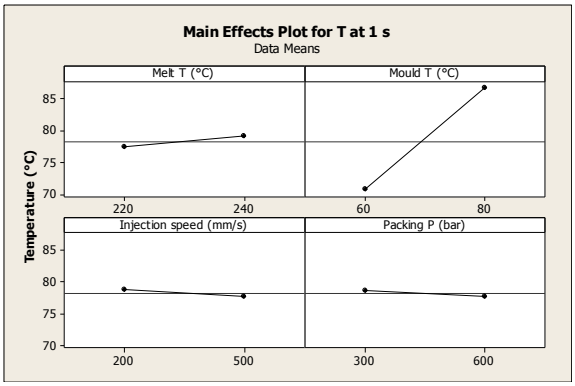

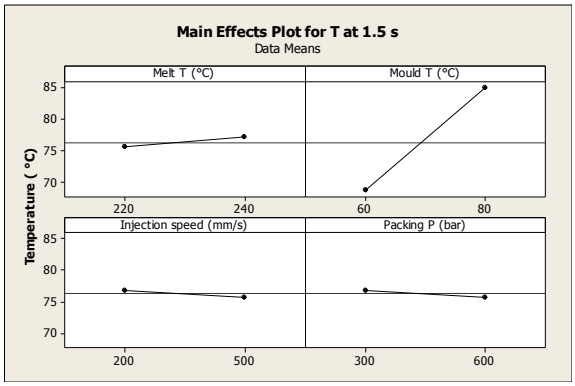

Figure 6.29 Sapphire N5 (30 µm pillars) - main effect plot of the temperature of CB PP at t = 0 s, t = 0.25 s, t = 0.5 s, t = 1 s, and t = 1.5 s.

6.8.3 CB PS - Effects of Surface Roughness

The effects of surface roughness on polymer cooling were analysed separately. The effective surface area was measured using Olympus LEXT OLS4000 laser confocal microscope. It was expected that high effective surface area would increase cooling rate. Table 6.7 shows five surface topographies measured. Increase of effective surface area can be observed with an increase in surface roughness and height of the pillars.

Table 6.7 Measurement of the effective surface area.

	ROI (mm)	Area (mm²)	Effective Surface area (mm²)
Polished Sapphire	1.92 x 1.92	3.68	3.68
1 µm Sapphire		3.70	5.08
4.2 µm Sapphire		3.71	7.88
15 µm Pillars		3.70	5.20
30 µm Pillars		3.70	15.05

Figure 6.30 shows temperature values (the response) recorded through polished, 1 µm, 4.2 µm, 15 µm pillars and 30 µm pillars sapphire windows for both materials together with the average and standard deviation. During cooling the maximum standard deviation was 1.68 °C for CB PP and 1.38 °C for CB PS. During the filling (Peak T) temperature deviation was higher; however this was only due to the 4.2 µm sapphire window. It was observed that for both materials peak temperatures recorded were lower by 7 - 18 °C. Figure 6.31 represents cooling curves for CB PS at low settings. A bump in curves around 0.02 s can be observed and it corresponds to an increase of pressure in the cavity. Figure 6.32 represents cooling curves for CB PS at high settings. Here bump in curves was not observed.

CB PP Polished

T at 0.25 s	T at 0.5 s	T at 1 s	T at 1.5 s	Peak T
78.50	73.28	69.52	67.56	140.08
78.48	73.51	69.47	67.43	139.22
78.65	73.39	69.35	67.24	152.70
79.40	74.02	69.53	67.31	154.06
93.48	88.27	84.80	83.15	144.13
93.85	88.86	85.32	83.39	143.66
94.71	89.23	85.32	83.49	157.44
94.93	89.48	85.58	83.56	156.80
81.70	75.42	71.11	68.84	149.12
82.91	76.16	71.47	69.01	150.24
81.72	75.64	71.20	68.90	161.13
82.34	76.27	71.52	69.04	163.21
96.30	90.30	86.15	84.33	153.69
96.31	90.77	86.74	84.69	153.46
97.07	91.10	86.57	84.69	166.09
97.73	91.56	87.17	85.04	166.25

CB PP 1 um

T at 0.25 s	T at 0.5 s	T at 1 s	T at 1.5 s	Peak T
76.14	71.00	67.26	65.26	137.27
76.76	71.69	67.76	65.67	138.53
77.22	72.37	68.46	66.35	151.47
77.83	72.75	68.47	66.21	152.06
92.73	87.86	84.40	82.79	142.10
93.23	88.55	85.13	83.25	141.81
93.74	88.83	84.98	83.25	155.54
94.22	89.56	85.80	83.78	155.49
81.89	75.49	70.99	68.78	148.33
82.05	75.63	71.23	68.85	148.83
81.01	75.27	70.94	68.70	162.44
80.81	75.53	71.26	68.89	160.94
95.46	90.30	86.27	84.55	152.16
96.69	91.14	87.11	85.07	152.52
97.54	91.55	86.91	85.02	164.11
98.05	91.98	87.60	85.44	164.42

CB PP 4.2 um

T at 0.25 s	T at 0.5 s	T at 1 s	T at 1.5 s	Peak T
77.01	72.59	69.35	67.47	127.39
77.85	73.40	69.80	67.78	127.06
77.63	73.24	69.63	67.66	141.46
78.61	74.06	70.21	68.10	141.10
92.92	88.72	85.72	84.24	134.07
93.48	89.43	86.43	84.78	133.30
93.82	89.73	86.41	84.81	146.01
94.88	90.69	87.31	85.42	145.89
81.77	77.10	73.54	71.62	137.72
83.35	78.04	74.33	72.18	138.19
82.86	78.06	74.26	72.26	151.25
84.17	79.18	75.13	72.85	151.72
97.43	92.37	88.50	86.88	145.09
97.91	93.00	89.33	87.40	144.31
98.72	93.52	89.29	87.53	156.53
99.81	94.19	90.06	88.02	155.91

CB PP 15 um

T at 0.25 s	T at 0.5 s	T at 1 s	T at 1.5 s	Peak T
76.78	71.27	67.50	65.30	138.50
77.27	71.81	67.71	65.72	137.95
78.99	73.86	69.87	67.51	151.12
78.91	73.88	69.66	67.52	151.18
93.19	88.34	85.08	83.49	142.06
93.98	89.05	85.61	83.74	142.27
93.50	88.50	84.94	83.18	153.98
93.52	88.71	85.21	83.29	153.21
81.03	75.57	71.72	69.62	147.29
81.58	75.84	71.70	69.44	147.51
81.39	75.67	71.45	69.21	159.86
82.04	76.26	71.69	69.33	159.94
95.40	89.68	85.74	83.99	151.75
95.49	90.11	86.28	84.29	151.15
96.66	90.71	86.22	84.37	164.68
97.16	91.03	86.74	84.60	164.78

CB PP 30 um

T at 0.25 s	T at 0.5 s	T at 1 s	T at 1.5 s	Peak T
78.31	72.59	68.51	66.46	139.75
78.07	72.50	68.71	66.70	139.81
77.39	72.63	68.85	66.82	151.69
77.96	73.19	69.15	67.07	151.68
93.65	89.06	85.69	84.14	143.58
93.61	89.11	86.09	84.34	142.69
93.55	89.16	85.86	84.22	155.50
94.49	89.94	86.58	84.62	156.30
82.25	76.66	72.74	70.68	149.98
83.06	76.99	72.92	70.63	150.24
82.57	77.01	72.71	70.51	161.90
82.52	77.32	73.12	70.84	163.23
96.13	90.89	87.17	85.50	154.24
96.13	91.28	87.82	85.91	153.64
97.08	91.78	87.66	85.89	164.45

CB PS Polished

T at 0.25 s	T at 0.5 s	T at 1 s	T at 1.5 s	Peak T
74.57	69.96	65.95	64.37	146.41
74.99	70.47	66.38	64.68	146.51
75.59	70.64	66.38	64.73	160.31
75.85	71.15	66.91	65.07	160.73
92.14	87.77	83.77	82.08	151.62
92.56	88.32	84.30	82.52	151.27
92.97	88.42	84.24	82.43	165.06
93.32	88.97	84.74	82.84	163.42
79.50	74.56	70.20	68.44	155.35
79.77	75.21	70.76	68.81	155.39
79.97	74.86	70.30	68.45	169.90
80.72	75.76	70.99	68.88	168.94
93.52	89.10	84.88	83.03	158.54
94.46	90.03	85.56	83.49	158.67
94.57	89.82	85.39	83.42	172.67
94.96	90.48	86.03	83.94	173.21

CB PS 1 um

T at 0.25 s	T at 0.5 s	T at 1 s	T at 1.5 s	Peak T
75.02	70.66	66.82	65.19	146.75
75.65	71.38	67.39	65.65	146.69
75.94	71.33	67.31	65.60	159.07
76.72	72.17	67.96	66.16	159.09
91.21	86.94	82.98	81.27	150.54
91.70	87.67	83.65	81.86	150.76
90.92	85.93	81.50	79.65	162.44
92.27	88.19	84.10	82.23	162.42
78.38	73.94	69.89	68.20	154.09
79.29	74.85	70.49	68.56	154.66
78.33	72.51	67.53	65.57	169.94
78.69	73.21	68.16	66.09	168.76
91.99	87.79	83.72	81.95	158.18
92.86	88.88	84.69	82.75	157.69
93.73	88.39	83.55	81.50	171.25
94.42	89.97	85.45	83.29	170.84

CB PS 4.2 um

T at 0.25 s	T at 0.5 s	T at 1 s	T at 1.5 s	Peak T
72.64	68.88	65.45	63.95	131.44
73.44	69.70	66.06	64.41	131.50
73.32	69.39	65.86	64.31	146.44
74.20	70.33	66.66	64.95	145.84
89.80	86.39	83.18	81.69	138.39
91.28	87.68	84.15	82.43	138.67
91.44	87.77	84.20	82.52	151.56
92.72	88.98	85.17	83.30	152.11
77.04	73.13	69.52	67.91	140.83
78.57	74.52	70.46	68.55	140.57
78.55	74.13	70.02	68.21	155.42
79.60	75.28	70.95	68.87	155.67
92.23	88.64	85.02	83.34	145.69
93.56	89.89	86.00	84.07	145.71
93.75	89.68	85.76	83.86	159.53
94.58	90.65	86.61	84.57	159.99

CB PS 15 um

T at 0.25 s	T at 0.5 s	T at 1 s	T at 1.5 s	Peak T
75.86	70.56	66.26	64.65	148.10
76.11	71.01	66.67	65.01	147.00
77.09	71.96	67.54	65.78	159.53
77.49	72.58	68.14	66.23	160.00
92.72	87.90	83.75	82.07	152.27
93.51	88.65	84.20	82.42	152.60
93.68	88.57	84.07	82.32	164.39
93.87	88.95	84.48	82.68	162.87
80.05	74.43	69.67	67.86	156.90
80.42	74.91	70.00	68.12	157.00
80.64	74.77	69.90	67.93	172.32
81.41	75.49	70.36	68.25	171.58
94.12	89.13	84.63	82.80	160.42
94.78	89.79	85.15	83.21	159.99
95.42	89.98	85.20	83.22	173.93
96.28	90.75	85.68	83.58	172.48

CB PS 30 um

T at 0.25 s	T at 0.5 s	T at 1 s	T at 1.5 s	Peak T
74.94	70.31	66.23	64.58	150.06
75.34	70.85	66.74	64.96	149.88
75.79	71.00	66.84	65.12	161.15
75.89	71.30	67.07	65.25	161.11
92.23	87.92	83.94	82.18	154.70
93.14	89.01	84.99	83.16	154.10
93.23	88.93	84.90	83.06	164.87
93.97	89.69	85.47	83.51	165.51
78.62	73.76	69.48	67.65	158.12
79.25	74.62	70.13	68.13	158.63
79.39	74.25	69.64	67.67	171.57
79.67	74.89	70.26	68.14	171.56
93.02	89.48	85.82	83.96	160.63
94.26	90.63	86.85	84.73	161.43
94.65	90.61	86.51	84.45	174.75
95.20	91.35	87.38	85.16	175.21

CB PP Mean (°C)

T at 0.25 s	T at 0.5 s	T at 1 s	T at 1.5 s	Peak T
77.35	72.15	68.43	66.41	136.60
77.69	72.58	68.69	66.66	136.51
77.98	73.10	69.23	67.12	149.69
78.54	73.58	69.40	67.24	150.02
93.20	88.45	85.14	83.56	141.19
93.63	89.00	85.72	83.90	140.75
93.86	89.09	85.50	83.79	153.69
94.41	89.67	86.09	84.13	153.54
81.73	76.05	72.02	69.91	146.49
82.59	76.53	72.33	70.02	147.00
81.91	76.33	72.11	69.92	159.32
82.38	76.91	72.54	70.19	159.81
96.14	90.71	86.76	85.05	151.39
96.50	91.26	87.45	85.47	151.02
97.41	91.73	87.33	85.50	163.17
98.19	92.19	87.89	85.77	162.84

CB PP Standard Deviation (°C)

T at 0.25 s	T at 0.5 s	T at 1 s	T at 1.5 s	Peak T
1.02	0.97	1.03	1.12	5.27
0.68	0.85	0.96	0.96	5.33
0.79	0.60	0.57	0.54	4.64
0.66	0.58	0.65	0.69	5.10
0.38	0.46	0.57	0.63	4.08
0.30	0.33	0.54	0.65	4.22
0.49	0.46	0.63	0.70	4.47
0.58	0.72	0.84	0.88	4.49
0.44	0.78	1.10	1.23	5.00
0.74	0.99	1.29	1.39	5.05
0.78	1.17	1.38	1.49	4.61
1.20	1.42	1.62	1.68	4.74
0.82	1.02	1.10	1.17	3.67
0.90	1.08	1.19	1.23	3.87
0.80	1.08	1.22	1.27	3.79
1.14	1.39	1.49	1.53	4.69
MAX	**1.20**	**1.42**	**1.62**	**1.68**	**5.33**

CB PS Mean (°C)

T at 0.25 s	T at 0.5 s	T at 1 s	T at 1.5 s	Peak T
74.61	70.08	66.15	64.55	144.55
75.11	70.68	66.65	64.94	144.32
75.55	70.87	66.79	65.11	157.30
76.03	71.51	67.34	65.53	157.35
91.62	87.39	83.52	81.86	149.50
92.44	88.27	84.26	82.48	149.48
92.45	87.92	83.78	82.00	161.66
93.23	88.96	84.79	82.91	161.27
78.71	73.96	69.75	68.01	153.06
79.46	74.82	70.37	68.44	153.25
79.37	74.10	69.48	67.56	167.83
80.02	74.93	70.14	68.05	167.30
92.98	88.83	84.81	83.02	156.69
93.98	89.84	85.65	83.65	156.70
94.42	89.70	85.28	83.29	170.43
95.09	90.64	86.23	84.11	170.35

CB PS Standard Deviation (°C)

T at 0.25 s	T at 0.5 s	T at 1 s	T at 1.5 s	Peak T
1.20	0.72	0.50	0.45	7.47
1.02	0.64	0.49	0.46	7.29
1.38	0.95	0.68	0.61	6.12
1.22	0.89	0.66	0.61	6.48
1.16	0.69	0.42	0.38	6.40
0.94	0.59	0.48	0.46	6.18
1.20	1.19	1.32	1.34	5.74
0.73	0.53	0.54	0.51	5.26
1.15	0.57	0.30	0.31	7.00
0.69	0.27	0.30	0.30	7.25
0.97	0.94	1.11	1.15	7.02
1.06	1.01	1.16	1.15	6.65
0.89	0.65	0.76	0.74	6.25
0.77	0.63	0.83	0.77	6.30
0.71	0.81	1.09	1.10	6.23
0.73	0.50	0.78	0.76	6.00
MAX	**1.38**	**1.19**	**1.32**	**1.34**	**7.47**

Figure 6.30 Temperature values used in the statistical analysis with mean temperatures and standard deviation.

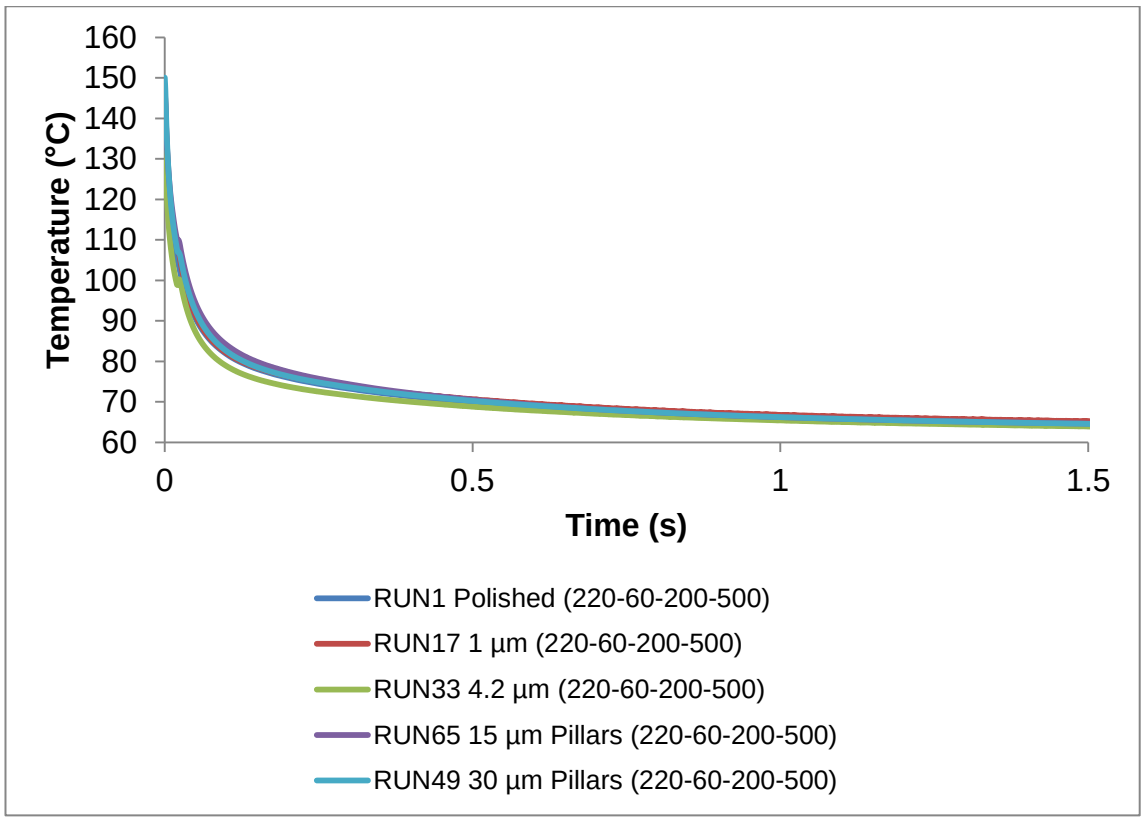

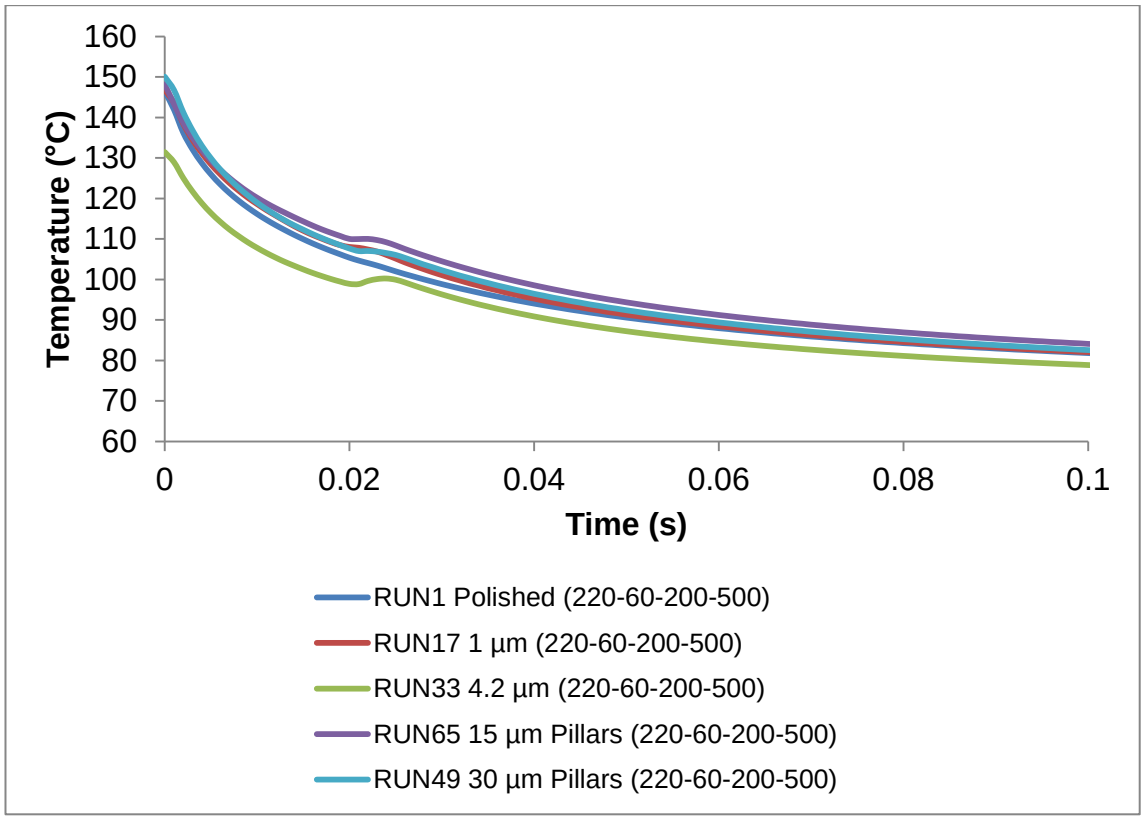

Figure 6.31 Cooling curves of CB PS at low processing parameters.

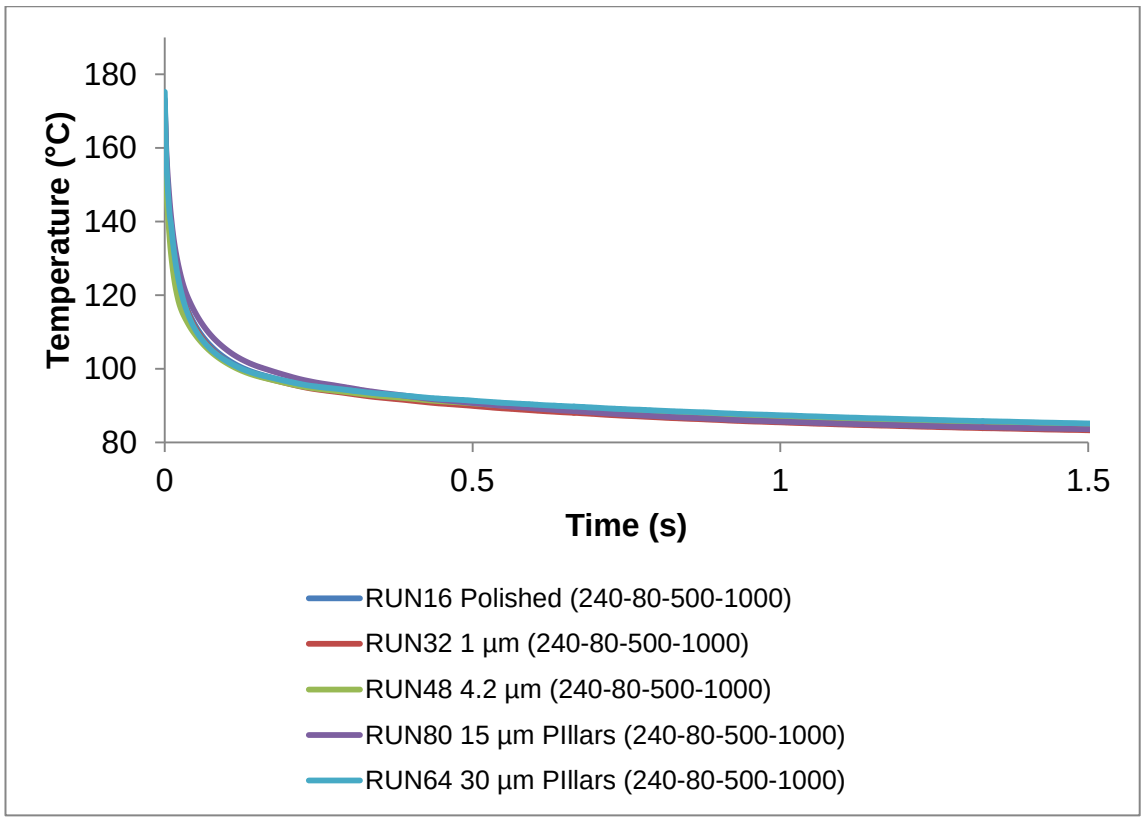

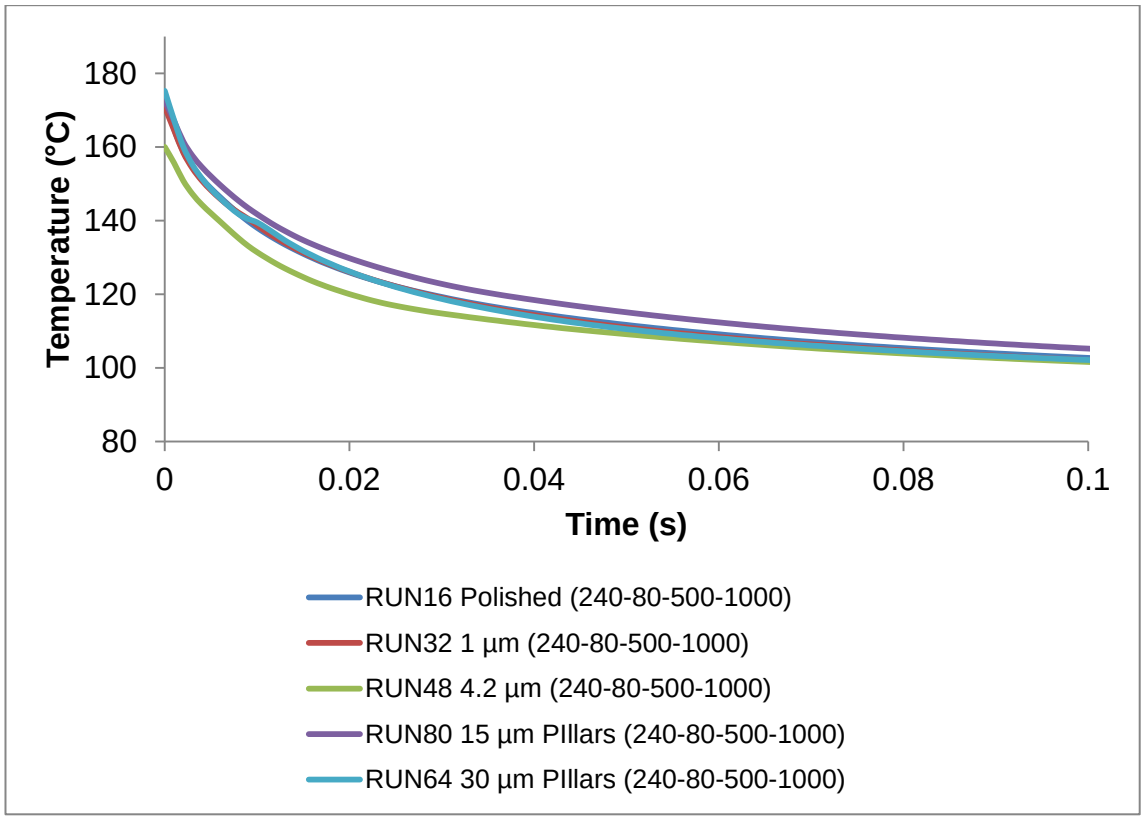

Figure 6.32 Cooling curves of CB PS at high processing parameters.

From Figures 6.31 and 6.32 it appears that 4.2 µm sapphire which has the highest effective surface area comparing to polished sapphire and 1 µm sapphire cools down faster at both low and high settings. This can also be observed from main effects plots but only at t = 0 s and t = 0.25 s. Repeatable results can be observed when comparing polished sapphire and 1 µm sapphire surfaces at all temperatures. However the difference in temperatures is no more than 1 °C. The effect of 4.2 µm sapphire surface on the peak temperature remains not fully understood. Possibly the surface structure of the 4.2 µm sapphire (see Figure 5.5a) is subjected to scattering mechanism, but it doesn't explain why it only happens during filling, as temperature at t = 0.5 s, t = 1 s and t = 1.5 s temperature measured was higher comparing to 1 µm sapphire window.

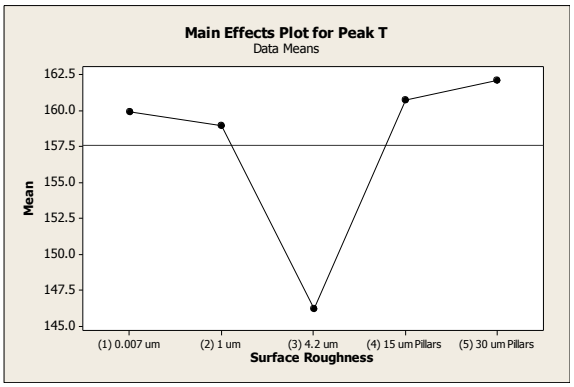

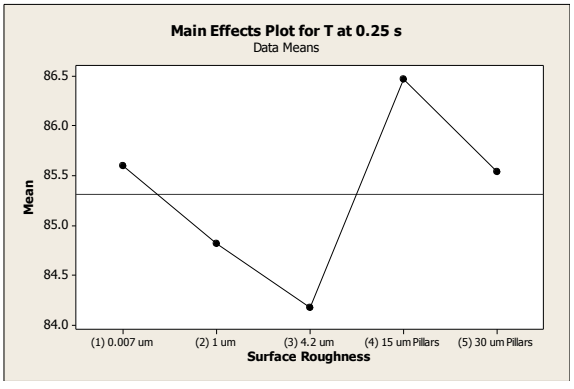

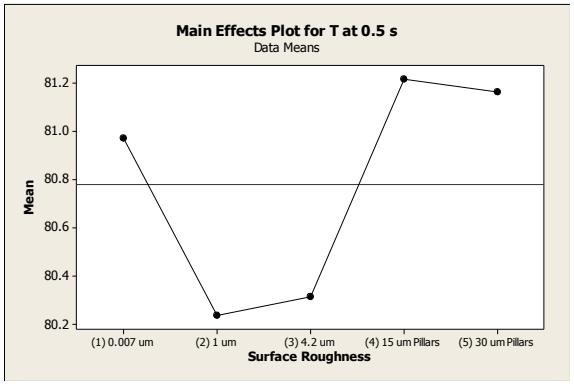

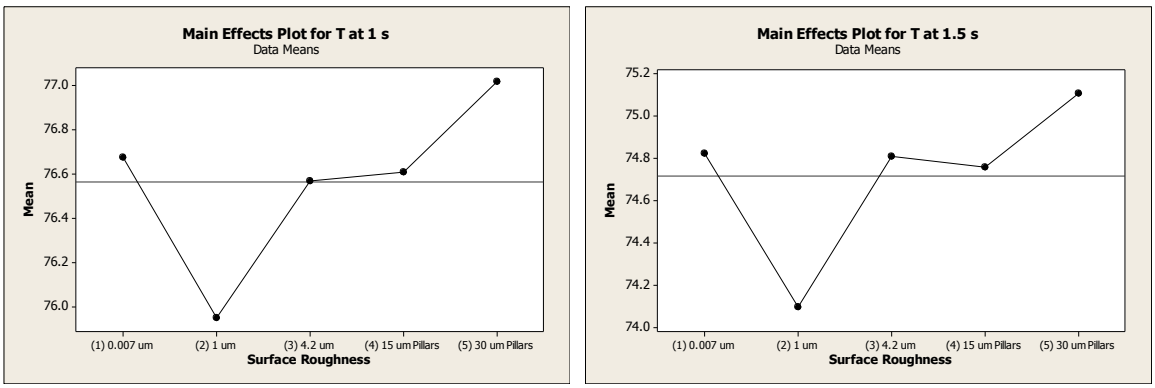

Figure 6.33 Temperature main effects plot for CB PS.

6.8.4 CB PP - Effects of Surface Roughness

Figures 6.34 and 6.35 represent cooling profiles of CB PP at low settings and high settings. Similarly to CB PS peak temperatures recorded with the 4.2 µm sapphire window were considerably lower compared to the rest of the surfaces. Figure 6.35 is missing one cooling curve recorded with 30 µm pillars sapphire window. The sapphire window has cracked during the test shots before last run of the DOE. The nature of the crack was not identified, as there was no excessive cavity pressure recorded. Experimental work could not be continued, because one of each surface topographies were laser machined. The analysis of variance was performed without last runs of the DOE. Results of the statistical analysis of the DOE were summarised using main effect plot, shown in Figure 6.36. Main effects plot for peak temperature looks similar to the one for CB PS. The main effects plots at t = 0.25 s, t = 0.5 s, t = 1 s and t = 1.5 s were more repeatable comparing to CB PS. An interesting observation was that during cooling, the mean temperature recorded through the 4.2 µm sapphire window was higher compared with the polished surface and 1 µm surface. It was expected that due to the higher effective surface area the mean temperature recorded through the 4.2 µm rough surface would be lower.

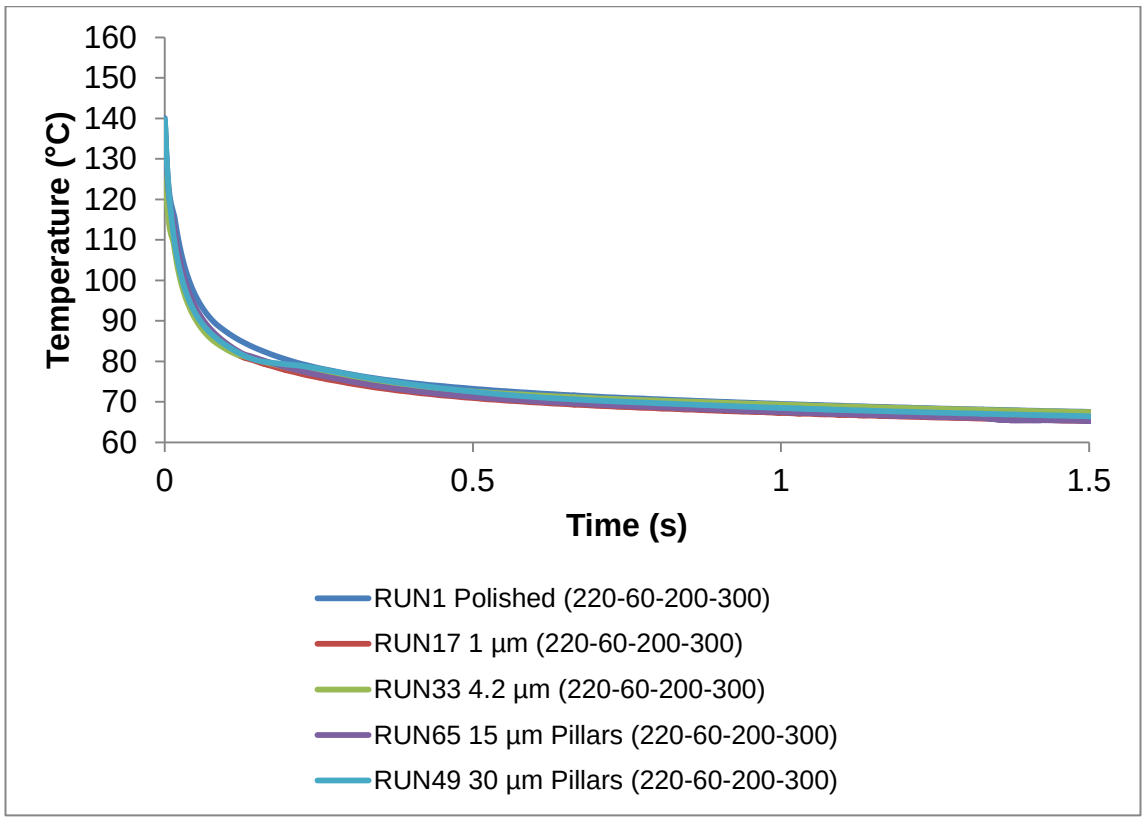

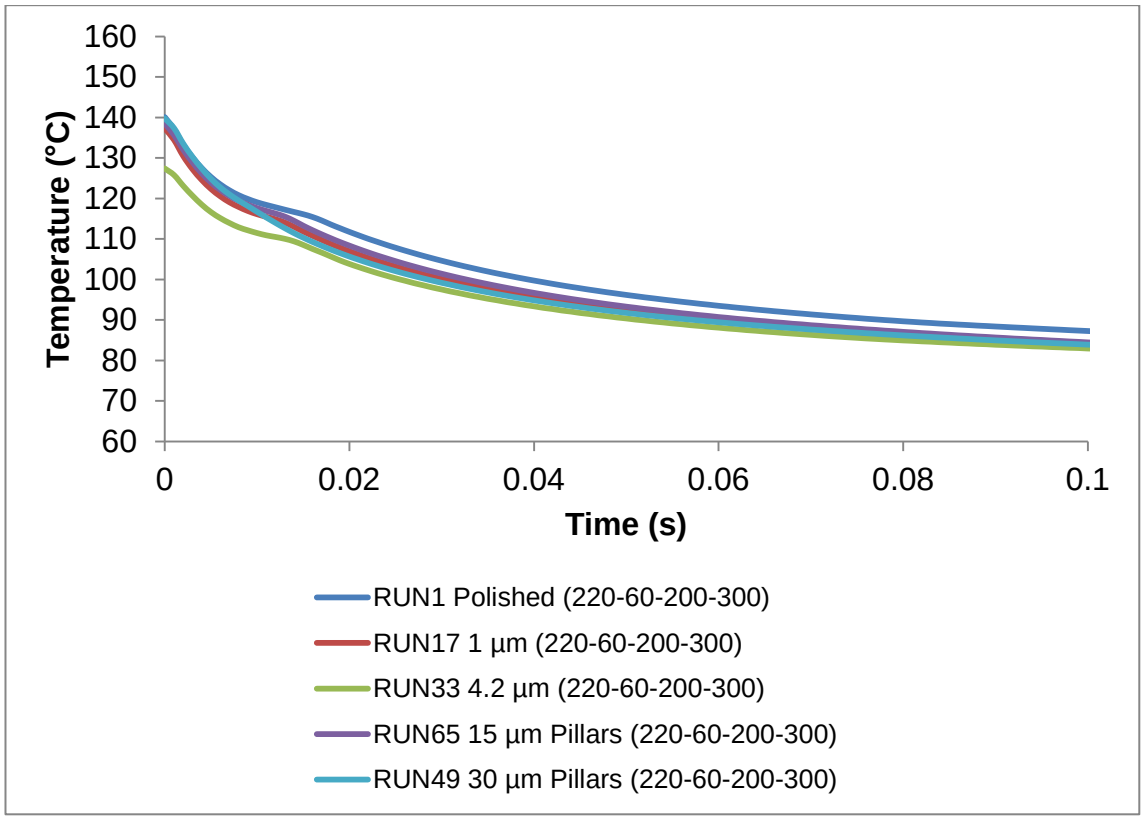

Figure 6.34 Cooling curves of CB PP at low processing parameters.

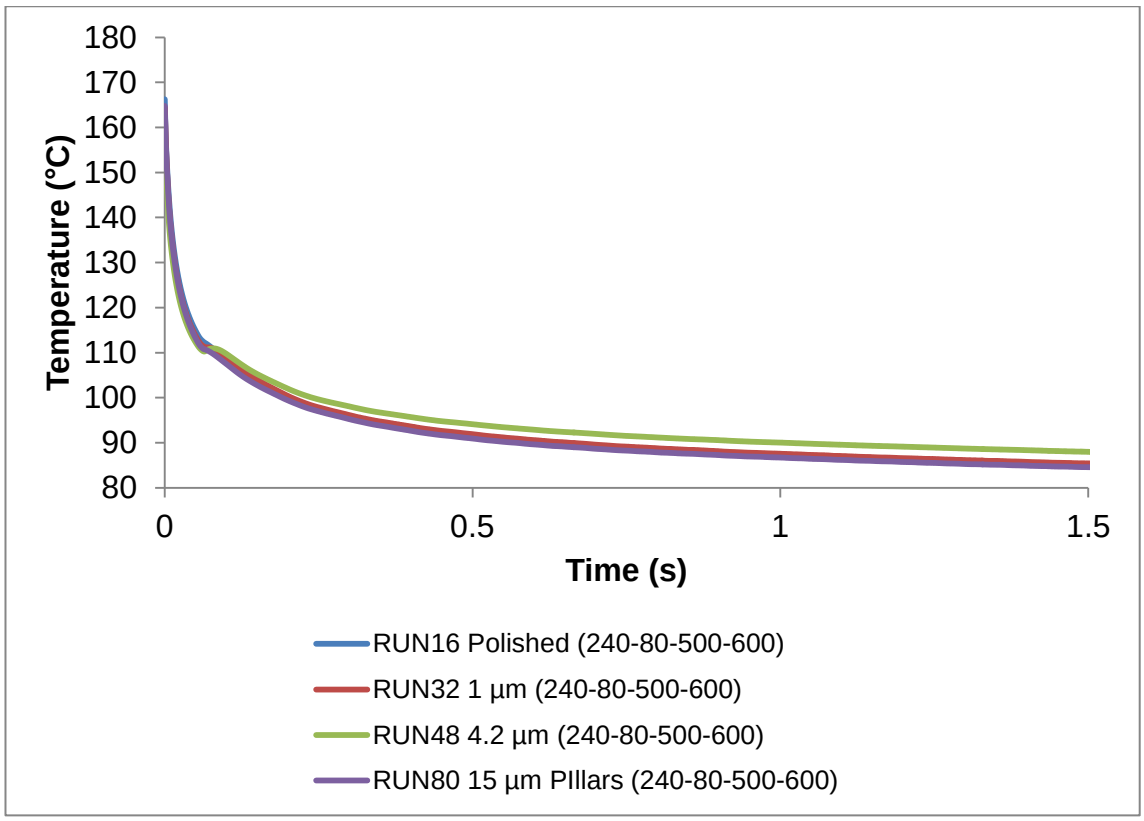

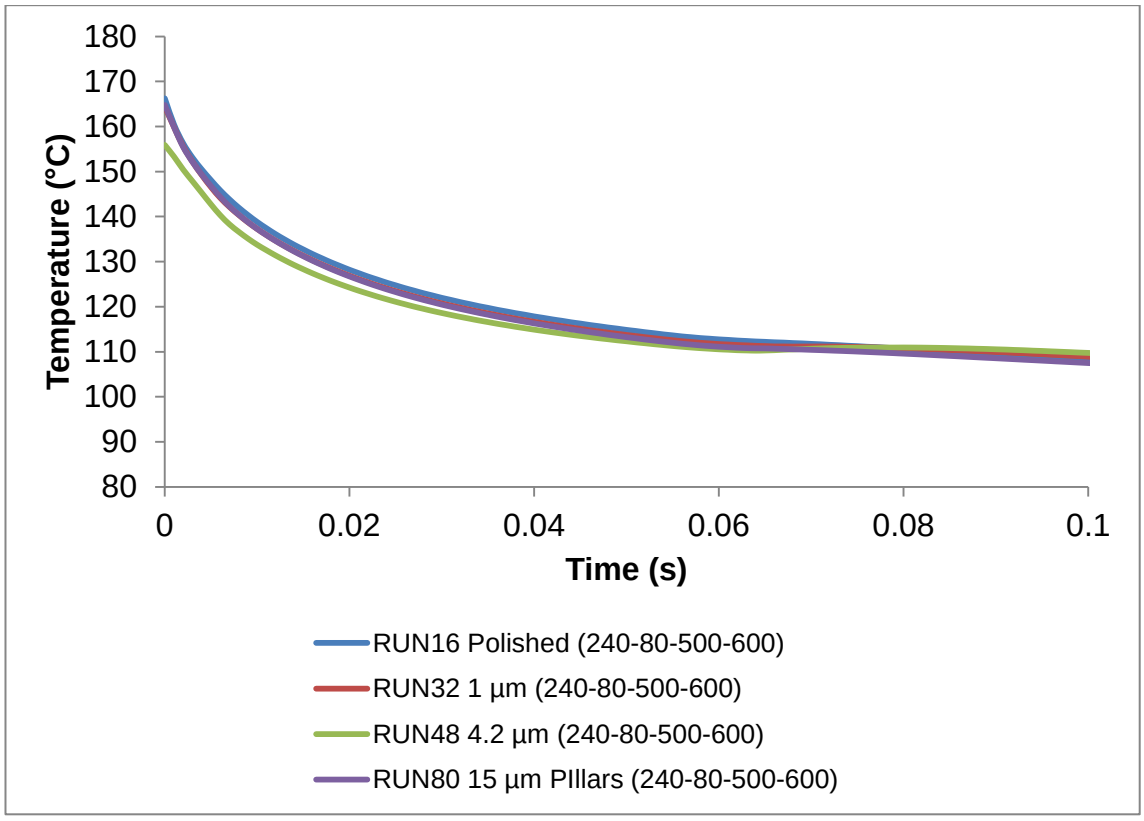

Figure 6.35 Cooling curves of CB PP at high processing parameters.

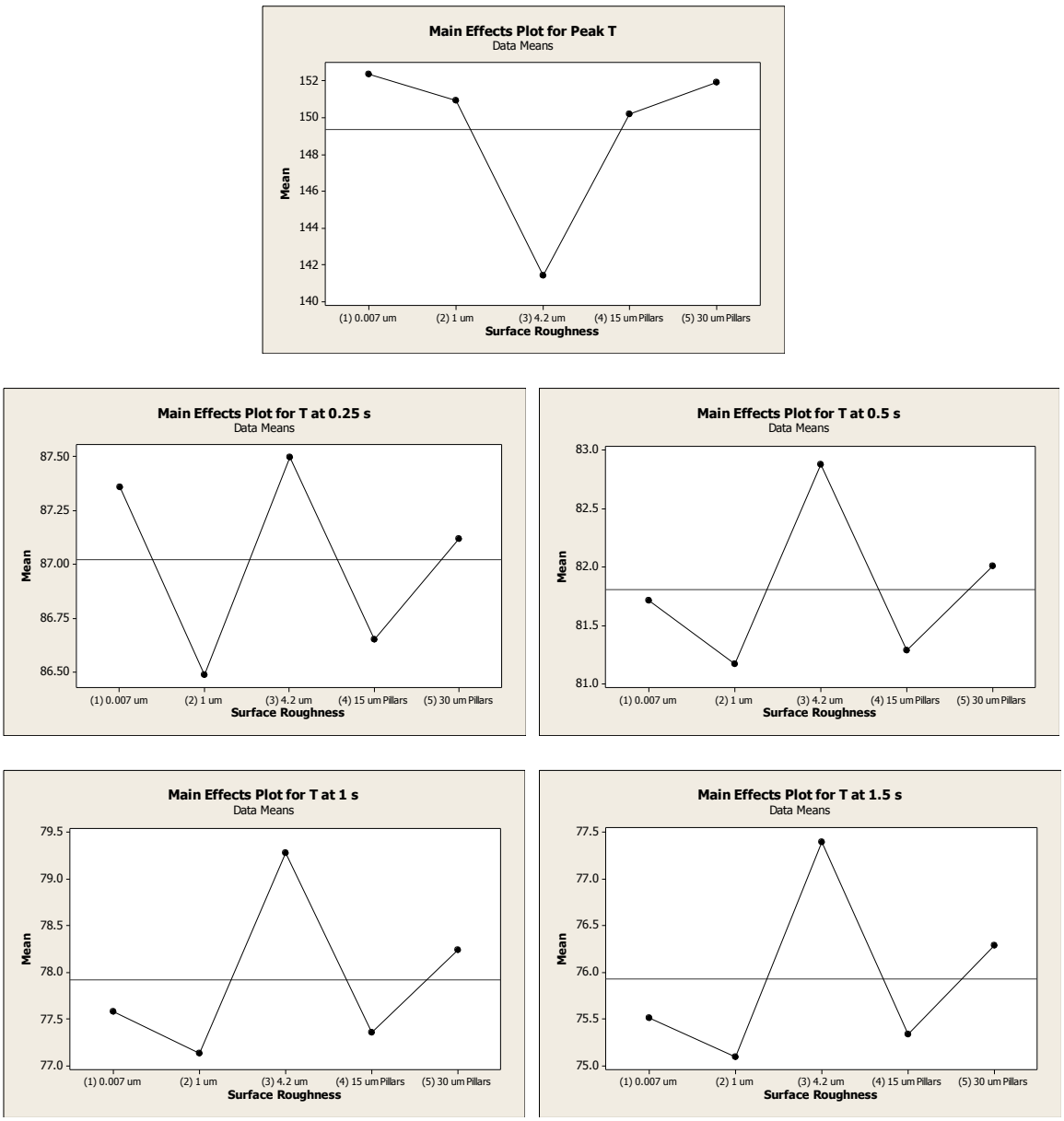

Figure 6.36 Temperature main effects plot for CB PP.

6.9 Conclusion

This chapter reports an experimental approach for studying polymer cooling directly during microinjection moulding process. To measure the temperature of the polymer, a special tool was designed and manufactured where the fixed half of the mould was fitted with a sapphire window. Temperature profiles were recorded by employing a high speed infrared camera, which was calibrated in-situ with carbon black filled polypropylene and carbon black filled polystyrene. Particular interest was paid to the relationship between sapphire windows surface finish and polymer cooling. A range of sapphire windows were laser machined to represent varying

surface roughness and an ordered pillars structure with different height. Then, a design of experiments approach was employed to study polymer cooling with different processing parameters. In particular, the effects that mould temperature, melt temperature, injection speed, cavity pressure and surface topography have on polymer cooling. The following conclusions can be made based on the obtained results:

- Polymer cooling during microinjection moulding is very rapid and polymer temperature at the flow front is significantly lower than melt set temperature.
- By conducting an ANOVA analysis it was possible to identify significant processing parameters on polymer cooling. It was shown that during cavity filling injection speed is a dominant parameter, followed by melt and mould temperatures, whereas cavity pressure had no effect. During polymer cooling mould temperature dominates as the most influential parameter, followed by melt temperature. The injection speed and cavity pressure had virtually no effect. The effects of the processing parameters have followed the same trends for both materials and range on surface topographies.
- The relationship between sapphire surface finish and polymer cooling was not conclusive. Same trend was observed for both materials at peak temperatures; however results were different during polymer cooling. It was expected that polymer cooling rate would increase with an increase of the effective surface area, however the main effects plot did not show it. Generally, the difference in polymer cooling curves was minimal, with maximum standard deviation values of 1.68 °C for CB PP and 1.38 °C for CB PS.

Chapter 7. Simulation of the Microinjection Moulding Process

Computer-aided simulation programs of injection moulding are used to provide information on the moulding process and approximate process parameters before the start of the actual tool manufacturing. This helps to avoid design errors which could lead to expensive tool re-engineering or modifications. Challenges in simulating microinjection processes arise from the fact that software was adapted from conventional injection moulding simulations and experimental work was based on conventional injection moulding. A number of factors such as lack of rheological data for micro structures, wall slip effects and surface tension play a role on the filling of micro parts but are neglected in macro moulding (Costa, Tosello, Whiteside, 2009; Piotter et al., 2009).

The market offers a number of commercial software packages for simulation of injection/microinjection moulding, such as Moldflow, Moldex3D, Simpoe-Mold and other simulation programs. During the investigation Moldflow Insight 2015 (Service Pack 2) was employed to perform simulation studies. Moldflow is a CAE (computer aided engineering) simulation software which employs the finite-element method and requires a 3D solid geometry prior to use of the simulation software. The software generates a mesh of connected simple parts which is then used for the finite-element analysis. Moldflow offers several mesh solutions:

- Midplane mesh – where geometry mesh consists of three-node, triangular elements. Mesh is formed by identifying the thickness of the component and assigning a surface plane through the middle of the thickness.

- Dual Domain mesh – where each surface of the geometry consists of three-node triangular elements which are matched across opposing faces.
- 3D mesh – where geometry consists of solid, four-node, tetrahedral elements.

Good meshing is the basis of the high quality simulation analysis.

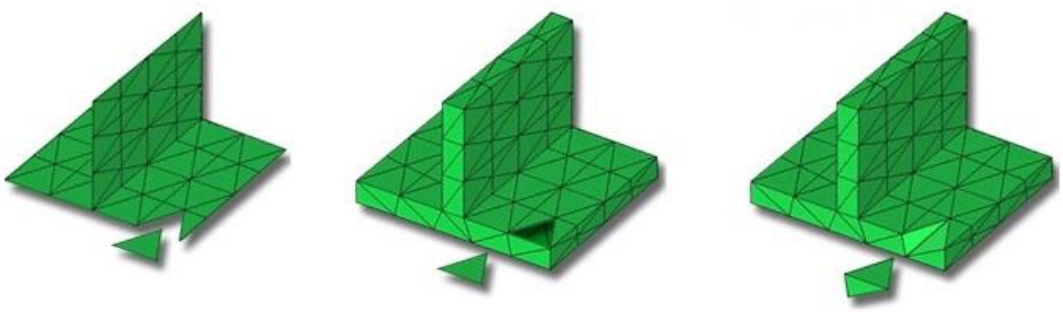

Figure 7.1 Mesh types (help.autodesk.com, 2015).

The Moldflow software package allows the simulation of the mould filling, packing and cooling. The user can set process parameters, such as melt temperature, mould temperature, fill time, injection speed, packing pressure packing time and other parameters. Moldflow can also automatically recommend parameters. The Moldflow simulation software can be characterised by the following capabilities:

- Filling analysis – which simulates the filling stage of the thermoplastic injection moulding process and helps to predict the flow of the melted plastic in the mould.
- Packing analysis – can help optimise packing profiles and visualise magnitude and distribution of volumetric shrinkage. Also, can help to reduce warpage and appearance of surface defects.
- Cooling – can help optimise cooling system to provide uniform heat removal from the part. This is turn will minimise part warpage, internal stresses, provide smooth surfaces and reduce cycle time. Cooling line

placement, coolant temperature modification and mould material selection are the parameters that lead to meet these objectives.

Other capabilities of the simulation software include shrinkage and deformation analysis, venting analysis, crystallisation analysis, transient mould cooling or heating, induction heating, heating elements and fibre orientation.

A wide range of results from the simulation analysis are available. The results depend on the analysis chosen are available in difference forms, including graphs, texts and animation (help.autodesk.com, 2015).

7.1 Cooling Analysis

In Moldflow simulation software cooling of the part is governed by the heat transfer coefficient (HTC). The HTC describes the heat transfer of the interface between the polymer melt and the mould surface and it is a dominant parameter in calculating temperature distribution. It depends on the contact area, which itself must be a function of mould surface topography, pressure, materials properties, surface energy and interfacial fluids. Temperature distribution in the polymer has a great influence on flow during the filling process and the replication quality of the final product. In addition the cooling process can have a significant influence on the internal structure, morphology and resulting physical properties. Therefore, understanding of the heat flux is essential for prediction of final product quality.

In the simulation a number of approximations are made for conventional moulding simulations, which may be invalid for microinjection moulding simulations. The heat transfer coefficient is one of the examples. The HTC values typically used in simulation were obtained from experiments performed with conventional injection moulding and typically with cavity thickness above 1 mm. Moreover, HTC is assumed to be a constant value and it cannot describe

the flow through micro channels (Costa, Tosello, Whiteside, 2009). Simulation programs implement HTC values differently; they can have a single value of several values. For example, Moldflow and Moldex3D use 3-stage HTC for the filling stage, packing stage and the detached condition (pressure is zero). The default values in Moldflow are 5000 W/m^{2}C for filling, 2500 W/m^{2}C for packing and 1250 W/m^{2}C for detached, whereas Moldex3D recommends to use 5000 W/m^{2}C for filling and 25000 W/m^{2}C for both packing and detached. Moldex3D can also determine the HTC values automatically based on moulding processes, material properties and model geometry. However, it is unclear how it is performed and it wasn't possible to test this function.

Moldflow offers a number of solvers for studying part cooling behaviour including midplane, dual domain and 3D cool analysis. The solver of the 3D cool analysis obtains a full three-dimensional transient finite-element solution for temperatures of the part. This then used to calculate heat flux into the mould. Within the 3D cooling analysis, two different solution are available, namely Cool and Cool (FEM).

- Cool (BEM) – is the boundary element method, which determines surface temperatures of the part, cooling channels and outer surface of the mould, then uses the boundary element integrals to calculate the internal temperatures of the mould. Minimum requirements are the part and cooling channel geometries. This method does not require a 3D mould to be modelled, however it does offer cuboid mould outer surface around the cavity.
- Cool (FEM) – is a superior method where the heat fluxes from the part are used as boundary condition for the steady-state finite-element solution that calculates the temperature through the depth of the mould. The Cool

(FEM) method calculates temperature at every node through the mould and was used in this work. Firstly, complicated 3D moulds can be meshed within this method which provides more accurate results when compared with the cuboid outer surface mould. This is important for mould design with a sapphire window. Secondly, a number of attempts were performed to run Cool (BEM) method with heaters instead of cooling channels, which were unsuccessful.

Within Cool (FEM) method there are two solvers available for calculation of the temperature distribution in the part:

- Conduction solver – is a fast solver, which only considers conduction. It assumes that the entire cavity is instantly full of polymer melt at the set melt temperature.
- Flow solver – is more complex and more accurate. It includes the effects of cavity filling, packing, temperature convection in the flowing polymer and shear heating effects. The entire flow solution in the part is solved, then the data is passed for the mould temperature distribution calculation, following by the recalculation of the entire flow solution in the part. This process is repeated many times, until results converge (Autodesk Moldflow Insight, 2012; help.autodesk.com, 2015).

Both methods were used for the simulation analysis.

7.2 The Process of Performing Simulation

A 3D mould (see Figure 7.2) together with part geometry was imported in the Moldflow simulation software and meshed to meet the demand of the simulation process. All imported CAD bodies were assigned a property type so that software can distinguish components of the assembly. These are fixed and moving mould blocks (3D) and part (3D). Different mesh size was used for part

geometry and mould components according to their importance. Part geometry was designed with a fine mesh (~1 900 000 elements), having cavity volume of 0.232 cm^3 and identical volume of tetrahedral elements. The minimum number of elements through the thickness was selected to be ten. Once the mesh was created it was checked with mesh repair tool for errors, such as holes and overlaps. As soon as the part mesh was satisfactory, a 3D mould mesh was generated, which consisted of ~1 300 000 elements. Cartridge heaters were designed as beam elements and were assigned constant temperature values according to processing conditions.

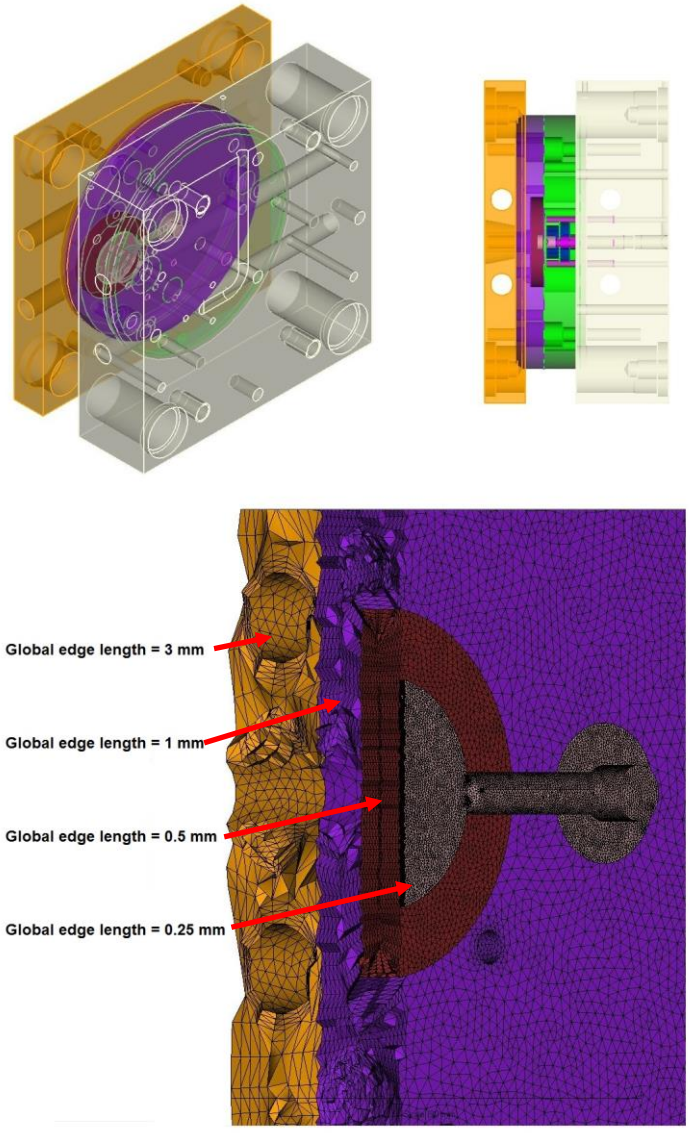

Figure 7.2 The CAD model of the mould and part and its complete three-dimensional mesh.

On the surface of the part that faces the sapphire window a number of nodes were created. These were 25 nodes within a 2 by 2 mm area in the middle on the part shown in Figure 7.3. The newly created nodes were then merged with the existing nodes from the part mesh. The temperature profile at each node was then exported and averaged to simulated experimentally obtained cooling profiles.

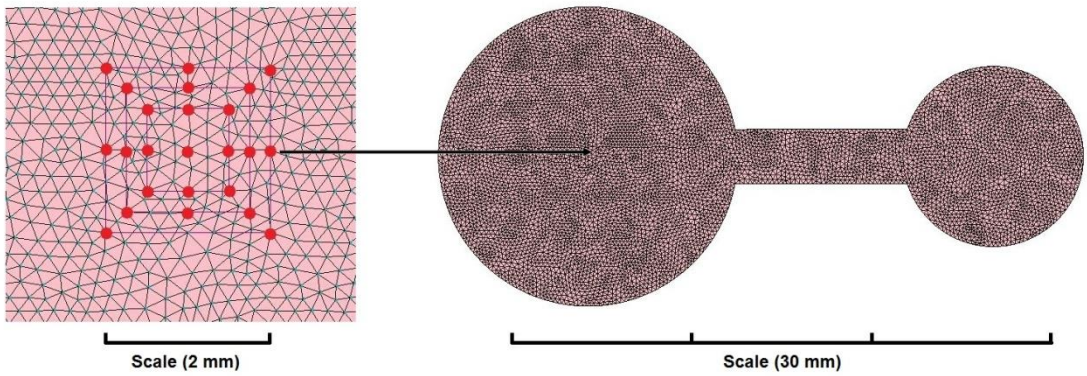

Figure 7.3 Part mesh with additional nodes.

7.3 Analysis Sequence

7.3.1 Conduction Solver

The conduction solver is a default solver for part heat flux calculation. Results of the temperature distribution are available through Cool (FEM) analysis sequence. Because the conduction solver assumes that the cavity is instantly filled with polymer melt, there are only two processing parameters that can be changed, namely melt and mould temperatures. Table 7.1 shows simulation parameters that were used with the conduction solver. Because effects of injection speed and packing pressure are not taken into account, four runs were required which totally represent 16 runs of the experimental DOE shown in Tables 6.5 and 6.6. Mould temperature calculation was set to transient within the cycle, which simulates change in mould temperature with time.

Transient mould temperature convergence tolerance and maximum number of transient mould temperatures cycles were left at default settings, which are 0.1 and 50 respectively.

Table 7.1 Simulation parameters that were used with conduction solver.

Runs	Melt T (°C)	Cartridge heaters T (°C)	Ambient T (°C)	Number of part heat flux time steps
1	220	60	25	250
5	220	80		
9	240	60		
13	240	80		

7.3.1.1 HTC Values within Conduction Solver

The Cool (FEM) conduction solver does not use a 3-stage HTC. It uses the packing HTC value for the cooling phase. This is based on the assumption that the filling phase is much smaller compared to the packing phase. Moreover, cool analysis cannot determine whether the part has detached or not. The whole part or a particular area can be selected and assigned local heat transfer coefficients through part surface properties option.

7.3.2 Flow Solver

In the flow solver apart from melt and mould temperatures filling and packing parameters can also be specified. During the analysis pressure in the cavity is computed at each time step, therefore the detached condition is also known. Flow analysis involves an iteration solution between the mould temperatures, the part temperatures and cartridge heaters temperatures. Each is updated in turn until convergence is achieved overall. In case of the flow solver, the part temperatures are solved by the flow (fill and pack) solver, therefore they are output of that solver. The part temperature distribution results are available by setting Cool (FEM) + Fill + Pack analysis. However, the temperature results from the Fill + Pack solver output the mould temperature at the interface rather that the polymer temperature for surface nodes. The

polymer temperature on the surface nodes is available by modification of the software dat files. This adds an extra function for the Fill + Pack solver, which writes an additional time series (XY) result for selected nodes representing true polymer temperature on the surface nodes. The modified dat files were kindly provided by Dr. Franco Costa, senior research leader at Autodesk. Table 7.2 shows processing parameters for flow solver.

Table 7.2 Simulation parameters that were used with flow solver.

Runs	Melt T (°C)	Cartridge heaters T (°C)	Flow rate (cm^3/s)	Packing (MPa) PP/PS		Ambient T (°C)
1	220	60	3.93	30	50	25
2	220	60	3.93	60	100	
3	220	60	9.82	30	50	
4	220	60	9.82	60	100	
5	220	80	3.93	30	50	
6	220	80	3.93	60	100	
7	220	80	9.82	30	50	
8	220	80	9.82	60	100	
9	240	60	3.93	30	50	
10	240	60	3.93	60	100	
11	240	60	9.82	30	50	
12	240	60	9.82	60	100	
13	240	80	3.93	30	50	
14	240	80	3.93	60	100	
15	240	80	9.82	30	50	
16	240	80	9.82	60	100	

Other parameters were kept default:

- Transient, part heat flux calculation - flow analysis on every iteration.
- Transient mould temperature convergence tolerance for each time step = 0.01.
- Maximum number of transient mould temperature iterations for each time step = 50.

- Maximum %volume to fill per time step = 4%, with maximum iteration per time step = 50 and convergence tolerance = 1.
- Maximum packing time step = 2 s, with maximum iterations per time step = 50 and convergence tolerance = 1.

7.3.2.1 HTC Values within Flow Solver

The flow solver employs 3-stage HTC values, for filling, packing and detached condition which is intended to provide more accurate results compared to the conduction solver. If the HTC values are not changed software will use default values of 5000 W/m^{2}C for filling, 2500 W/m^{2}C for packing and 1250 W/m^{2}C for detached phase. These values can be changed through part surface properties option, by assigning local HTC values as shown in Figure 7.4.

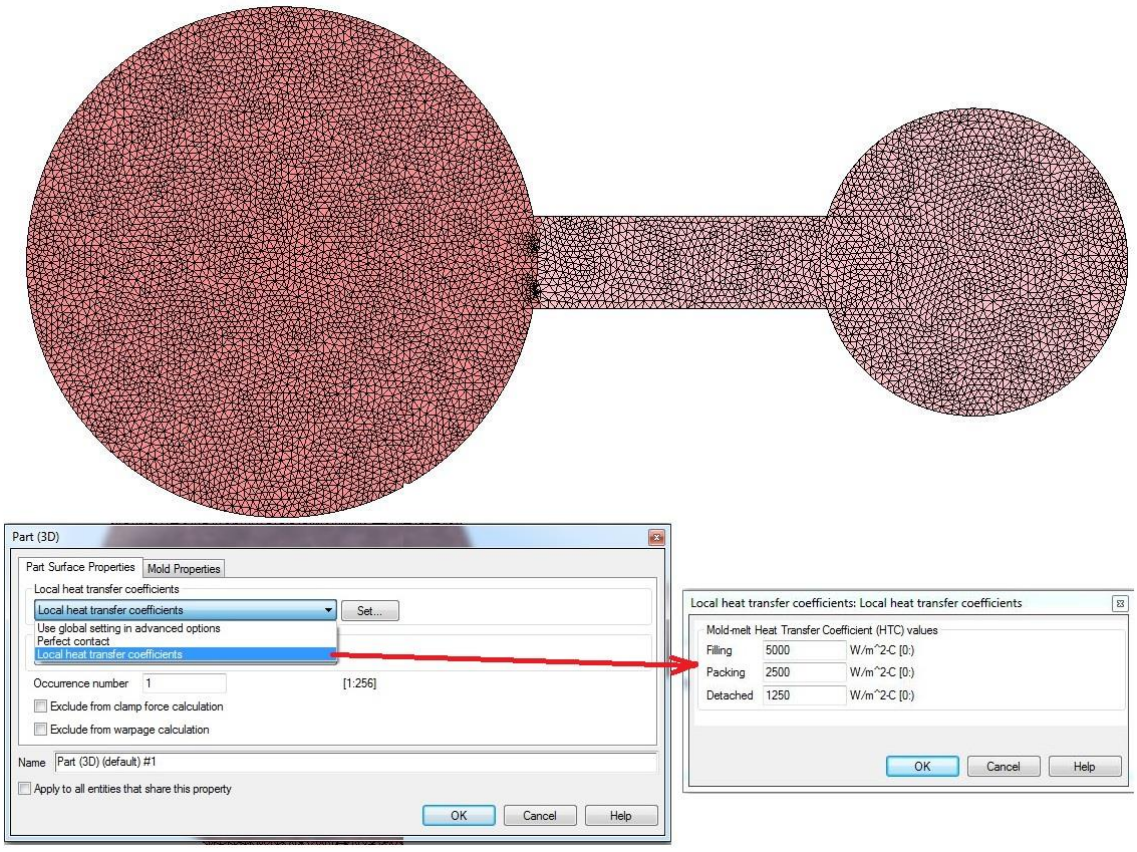

Figure 7.4 Local heat transfer coefficients in part surface properties.

7.4 One Dimensional Finite Difference Model of the Heat Transfer

Prior to the Moldflow simulations a one dimensional finite difference model of the heat transfer was used to estimate HTC values. The model was implemented by Professor John Sweeney at the University of Bradford. The model uses standard techniques and is summarised in Appendix 3. It has a three layer structure consisting of a polymer layer, a fictitious layer and a sapphire window layer which is shown in Figure 7.5. The polymer layer has a fully insulated boundary whereas, the sapphire layer takes into account convection effects on its outer boundary. The fictitious layer represents the polymer/sapphire interface and is of a particular interest here. It has two heat transfer values for melt and solid states. The switch-over from melt to solid state was based on the DSC results of solidification for both polypropylene and polystyrene. Figure 7.6 demonstrates a range of predicted cooling profiles for polystyrene with melt temperature of 220 °C and mould temperature 60 °C. The melt and solid HTC were set to the same value ranging from 1250 W/m²C to 25000 W/m²C. Experimental cooling profiles were compared to the predicted profiles obtained with the one dimensional finite difference model. A range of experiments were performed for both polystyrene and polypropylene where melt and solid HTC values of the fictitious layer were changed to match experimentally obtained cooling curves. Figure 7.7 shows experimental and predicted cooling curves of polystyrene. Values of 7700 W/m²C for melt state and 6600 W/m²C for solid showed the closest matching to the experimental cooling curve. Values in the similar range also demonstrated better prediction for polypropylene. It has demonstrated that value higher than the Moldflow default value has to be used to better predict cooling profiles. Improvements in prediction were also observed when melt temperature was set to 240 °C and mould temperature set to 80 °C. The values obtained were used as the basis for input data for the Moldflow thermal calculations discussed below.

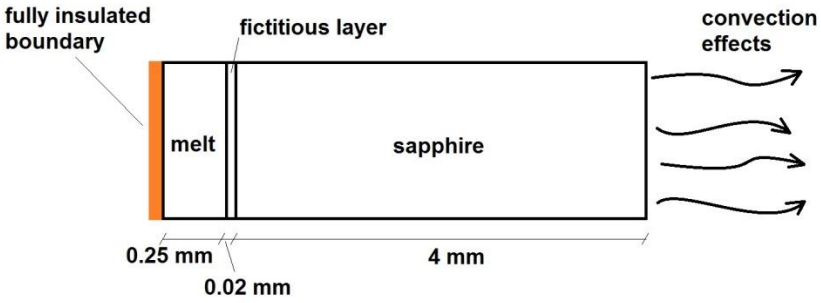

Figure 7.5 A three layer structure of one dimensional finite difference model of the heat transfer.

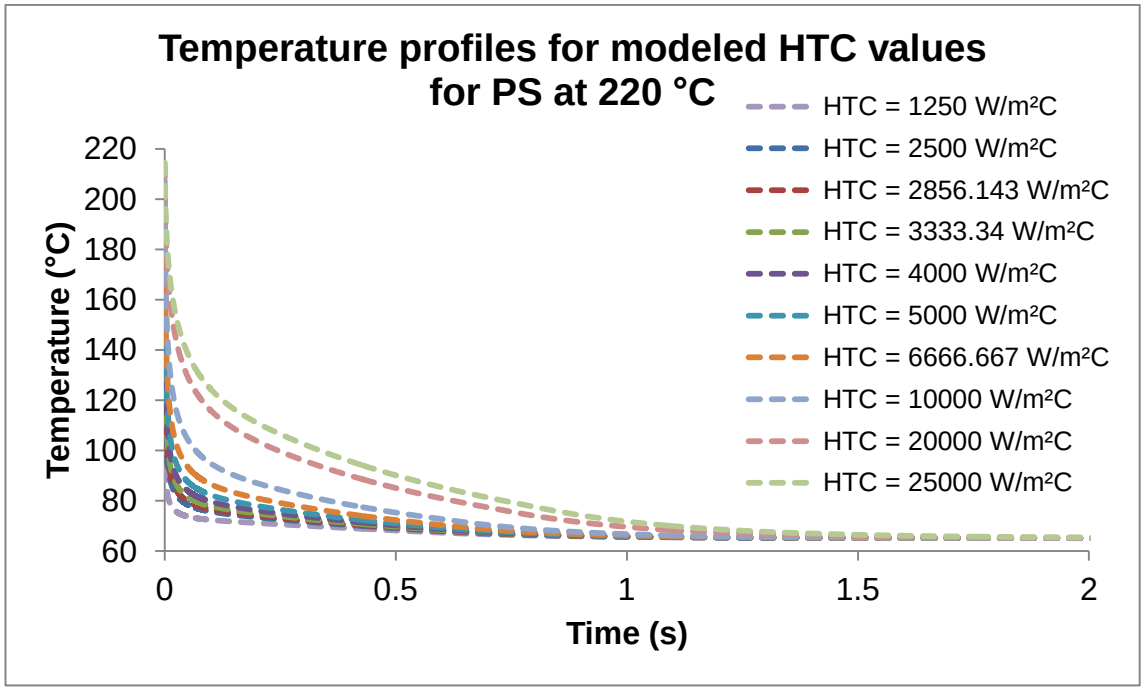

Figure 7.6 Predicted cooling profiles of PS with one dimensional finite difference model.

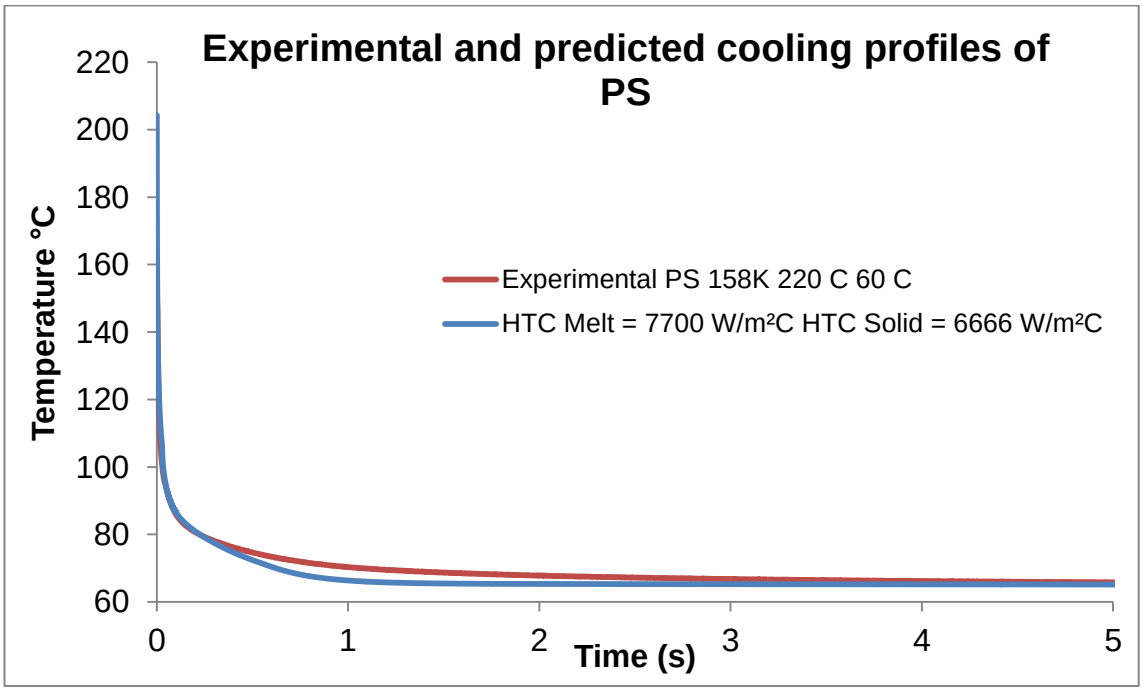

Figure 7.7 Experimental and predicted cooling profiles of polystyrene.

7.5 Conduction Solver Results of CB PP and CB PS

Results from the Moldflow simulation software were compared to the experimentally obtained cooling profiles recorded through polished sapphire window. Cooling from simulated results starts from melt set temperatures therefore at t = 0 s temperatures are 220 °C fro runs 1 and 5, and 240 °C for runs 9 and 13. Experimentally obtained peak temperatures for CB PP were 140 °C for run 1, 144 °C for run 5, 149 °C for run 9 and 154 °C for run 13. measured peak temperatures for CB PS were 146 °C for run 1, 152 °C for run 5, 155 °C for run 9 and 159 °C for run 13. From Figures 7.8 - 7.15 it can be clearly seen that default value of HTC does not predict polymer cooling well for both materials. Large deviations are observed from the start of the cooling till approximately two seconds. Increase of heat transfer coefficient from 2500 W/m^2C to 7700 W/m^2C consistently improves cooling profile prediction at different processing conditions. Table 7.3 shows experimentally obtained and predicted temperatures for CB PP at four times steps that were used for statistical analysis of the experimentally obtained cooling profiles. These were t = 0.25 s, t = 0.5 s, t = 1 s and t = 1.5 s starting from peak temperatures. Use of the default HTC value showed that maximum temperature difference was at t = 0.25 s ranging from 22.8 °C to 25.1 °C. An increase of the HTC value showed a reduction of temperature difference in the range of 1.3 °C to 3.7 °C. Table 7.4 shows experimentally acquired and simulated data for CB PS temperature at t = 0.25 s, t = 0.5 s, t = 1 s and t = 1.5 s. Similarly to CB PP there was big temperature difference observed at t = 0.25 s when comparing experimental temperature and Moldflow predicted temperature using conduction solver with default HTC values. Prediction of temperature of CB PS at t = 0.25 s, t = 0.5 s, t = 1 s and t = 1.5 s was improved by employing higher HTC value.

Generally improvements in temperature prediction were observed for both materials with conduction solver and HTC equal to 7700 W/m^{2}C.

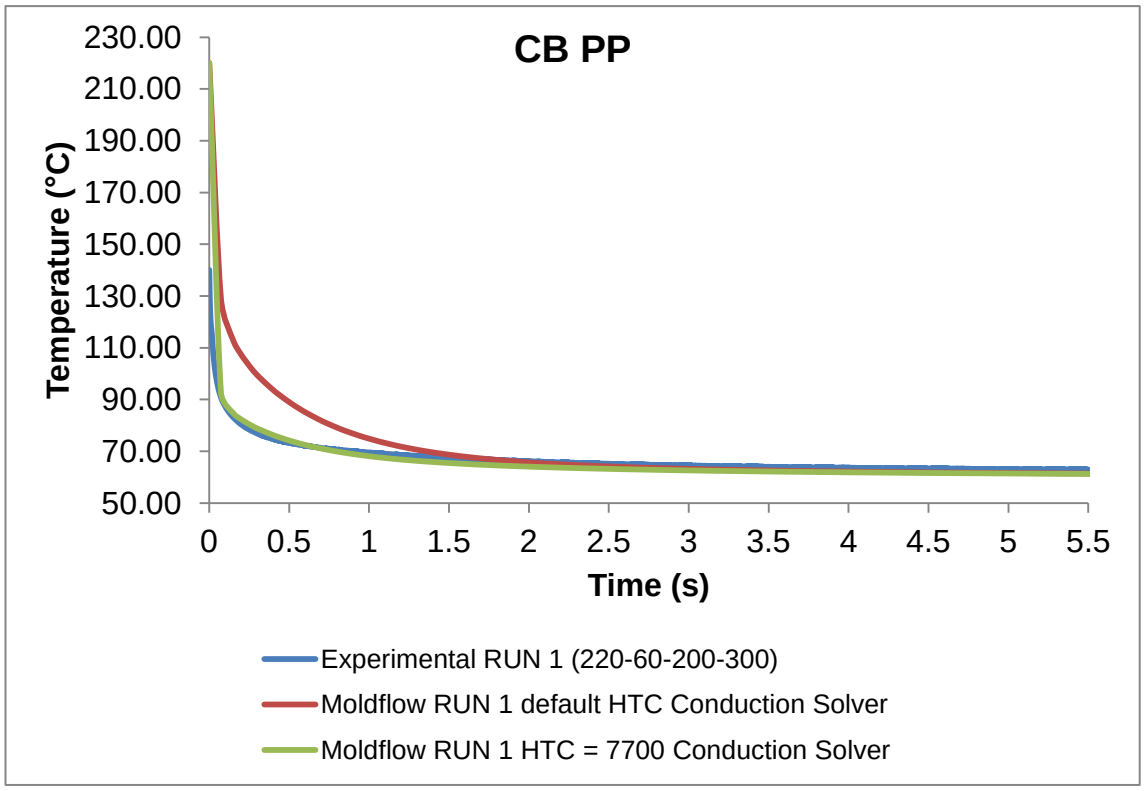

Figure 7.8 Cooling curves plot of CB PP - experimental and conduction solver results for RUN 1.

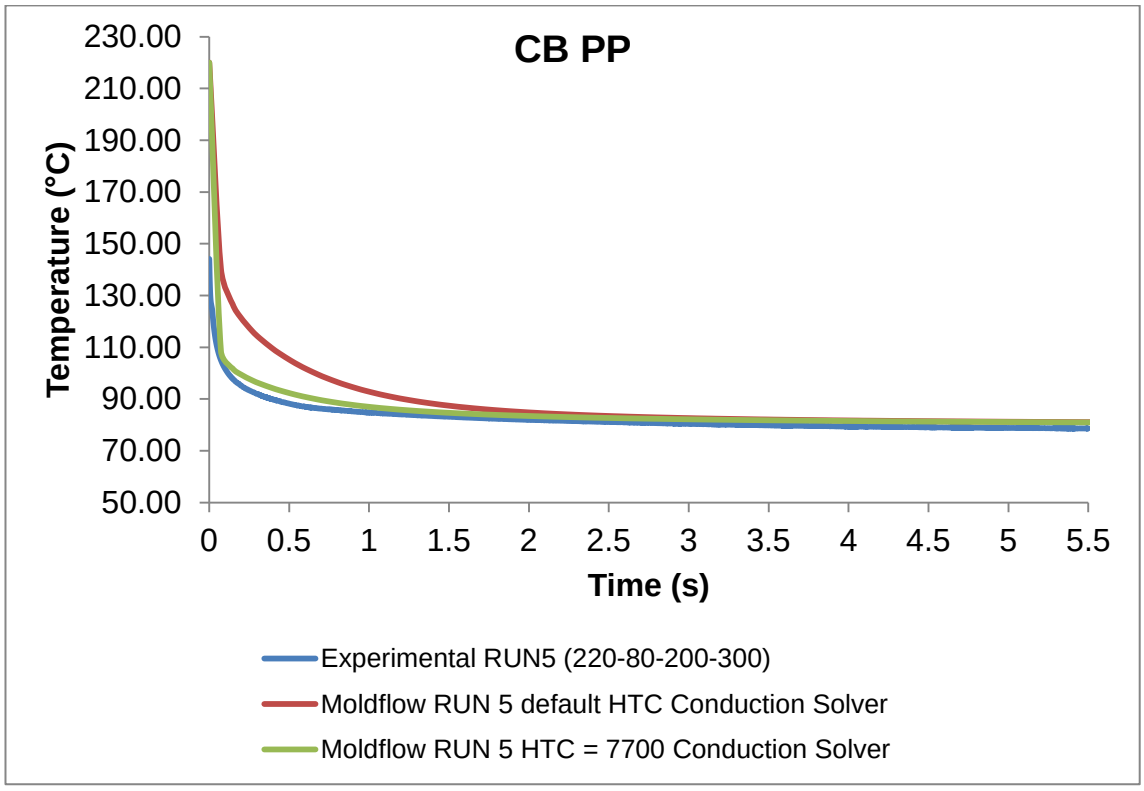

Figure 7.9 Cooling curves plot of CB PP - experimental and conduction solver results for RUN 5.

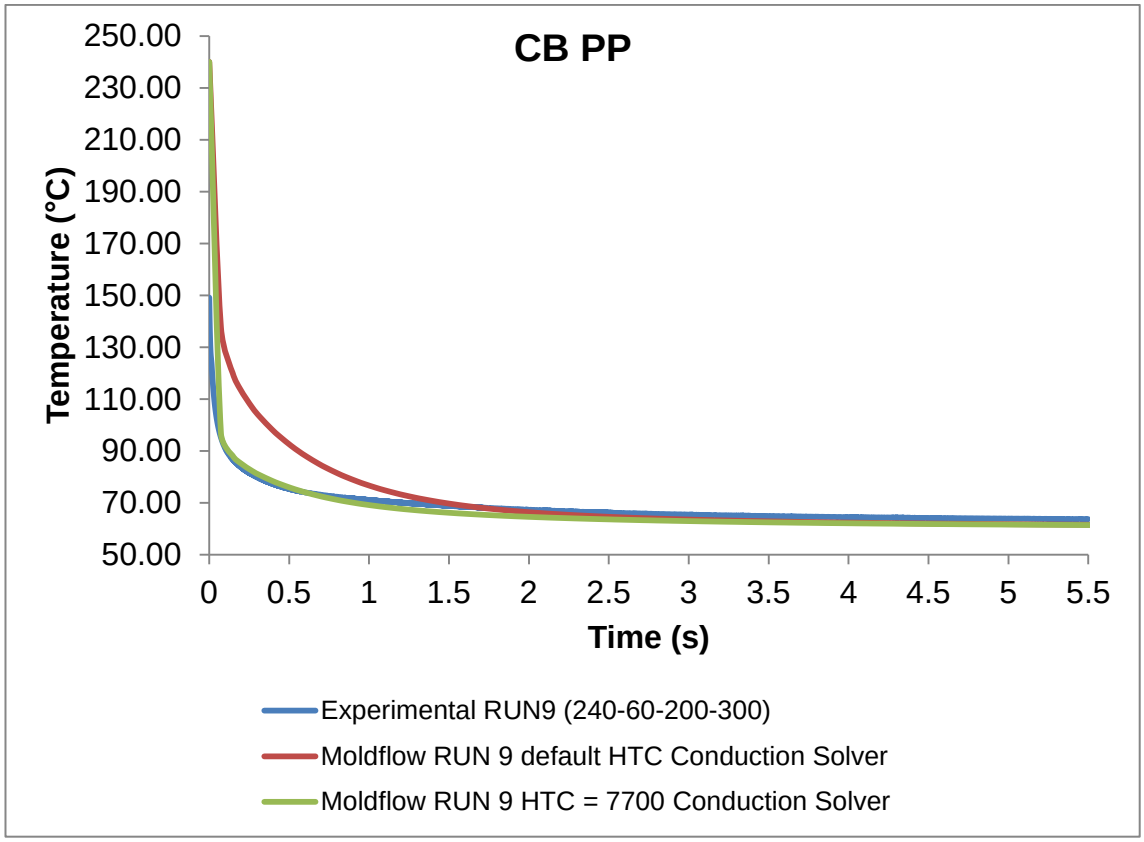

Figure 7.10 Cooling curves plot of CB PP - experimental and conduction solver results for RUN 9.

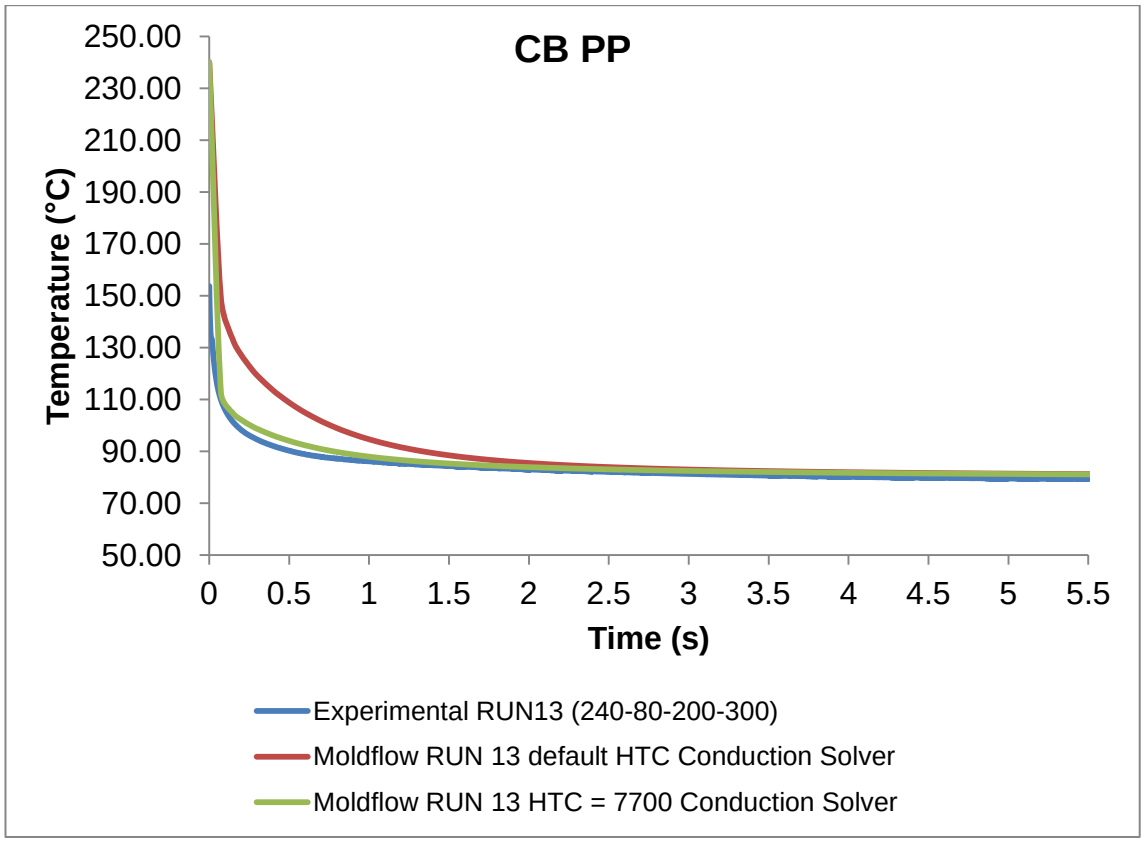

Figure 7.11 Cooling curves plot of CB PP - experimental and conduction solver results for RUN 13.

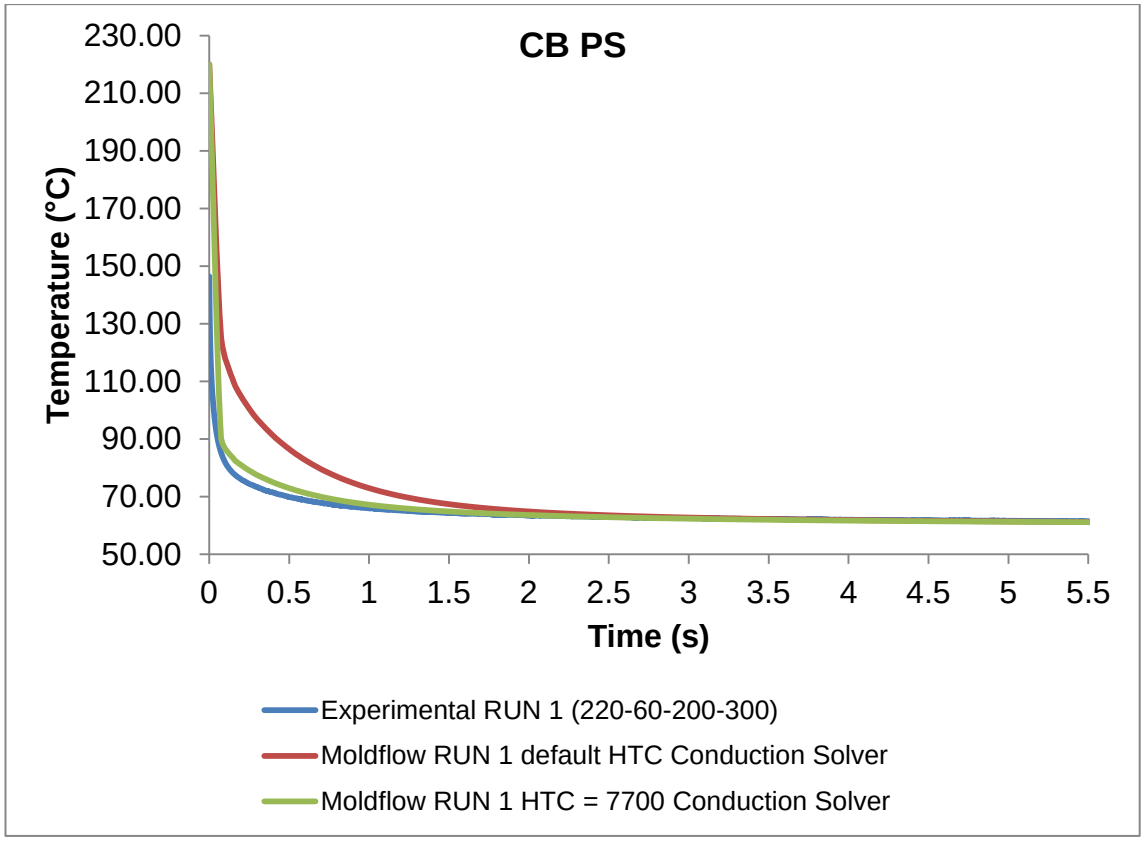

Figure 7.12 Cooling curves plot of CB PS - experimental and conduction solver results for RUN 1.

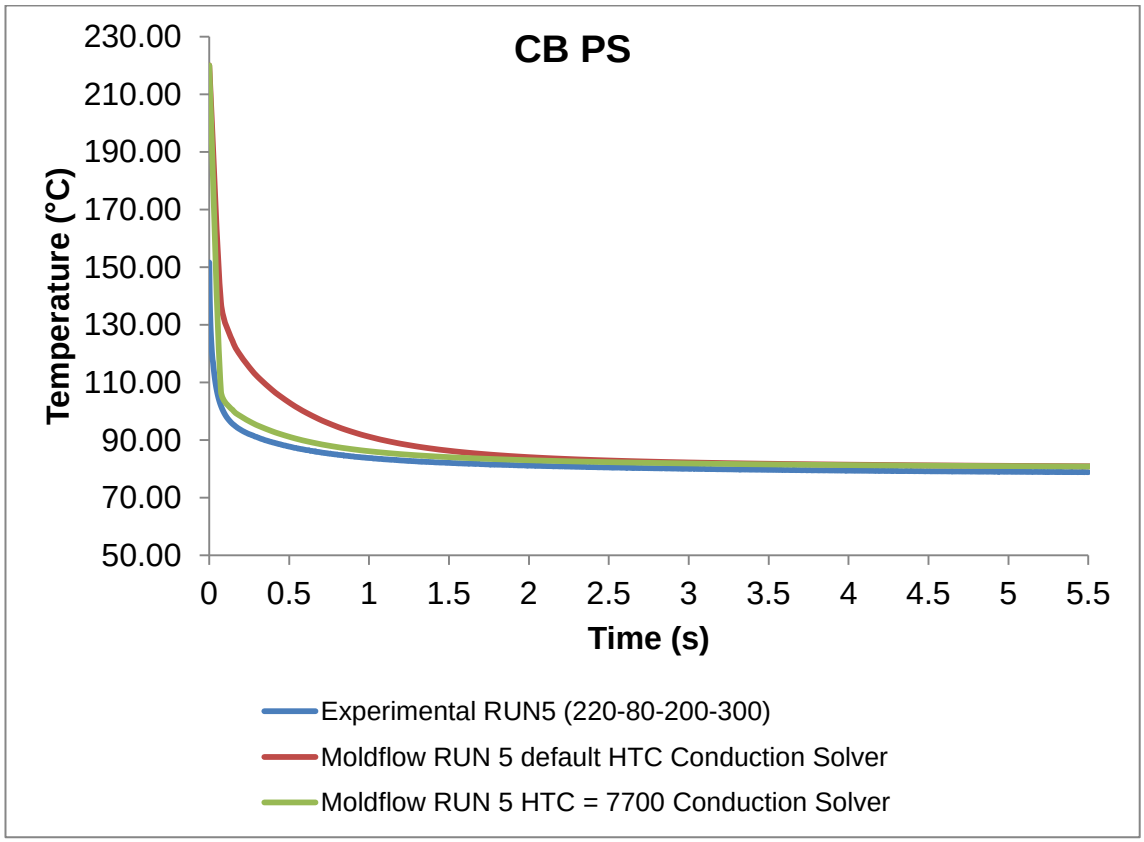

Figure 7.13 Cooling curves plot of CB PS - experimental and conduction solver results for RUN 5.

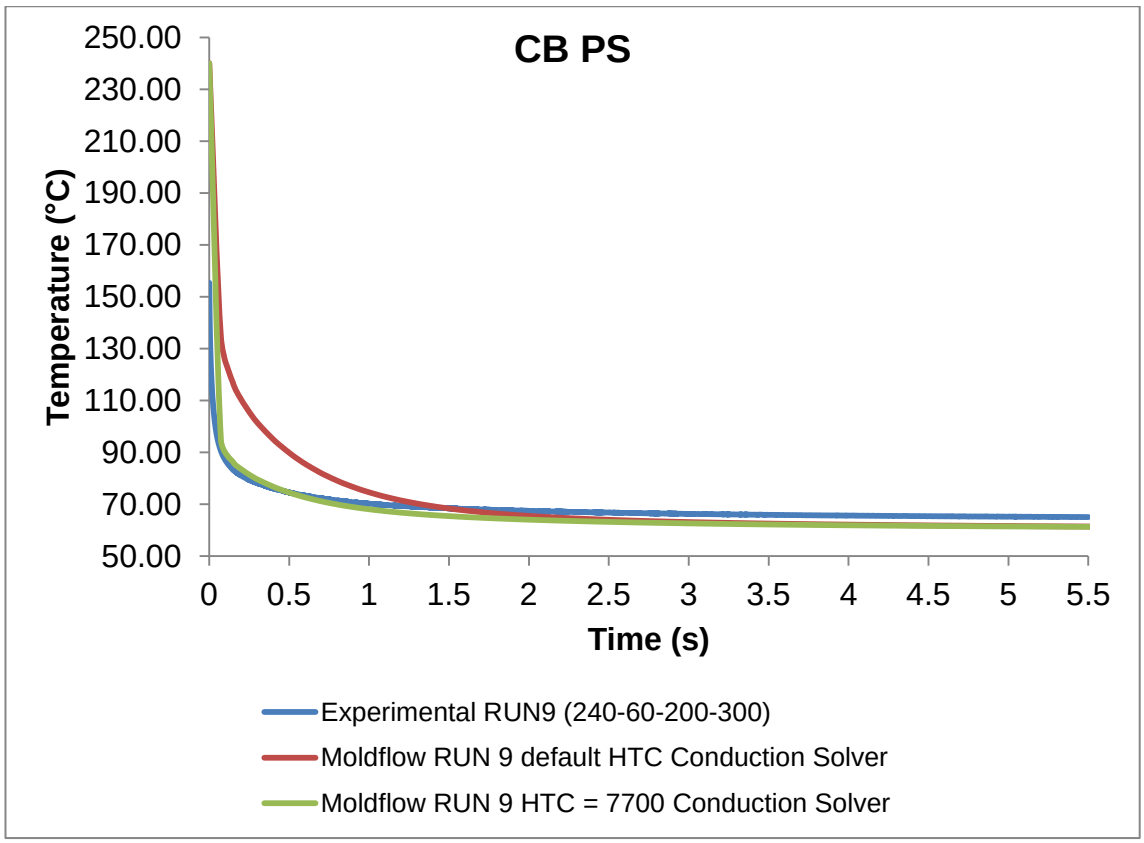

Figure 7.14 Cooling curves plot of CB PS - experimental and conduction solver results for RUN 9.

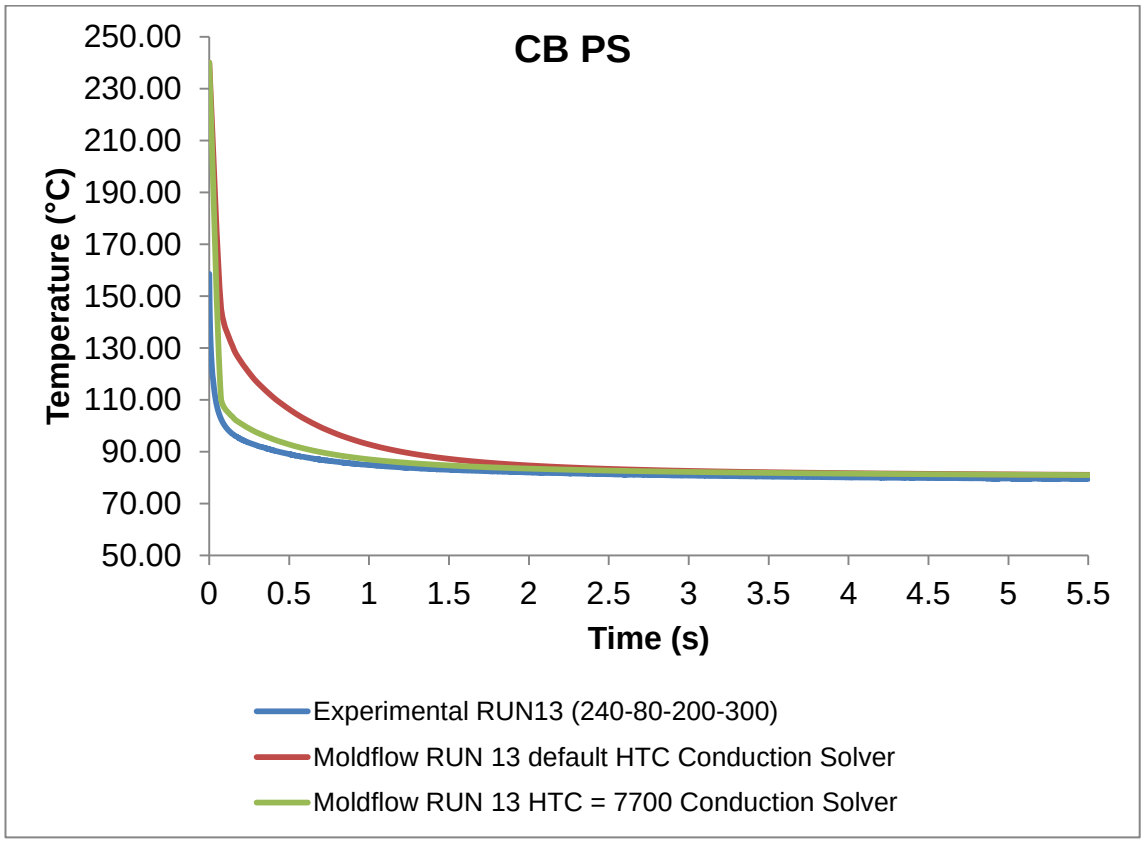

Figure 7.15 Cooling curves plot of CB PS - experimental and conduction solver results for RUN 13.

Table 7.3 Experimentally obtained and predicted temperatures for CB PP at four times steps.

		T at 0.25 s	T at 0.5 s	T at 1 s	T at 1.5 s
RUN 1	Experimental (°C)	78.50	73.28	69.52	67.56
	Moldflow default HTC (°C)	101.64	88.50	74.02	68.38
	Moldflow HTC = 7700 (°C)	79.78	73.94	67.74	65.32
	Temperature Difference default HTC (°C)	23.13	15.21	4.50	0.83
	Temperature Difference HTC = 7700 (°C)	1.28	0.66	-1.79	-2.24
RUN 5	Experimental (°C)	93.48	88.27	84.80	83.15
	Moldflow default HTC (°C)	116.29	104.78	92.10	87.16
	Moldflow HTC = 7700 (°C)	97.21	92.09	86.66	84.54
	Temperature Difference default HTC (°C)	22.80	16.51	7.30	4.01
	Temperature Difference HTC = 7700 (°C)	3.72	3.83	1.86	1.39
RUN 9	Experimental (°C)	81.70	75.42	71.11	68.84
	Moldflow default HTC (°C)	106.79	92.01	75.73	69.39
	Moldflow HTC = 7700 (°C)	82.29	75.72	68.74	66.02
	Temperature Difference default HTC (°C)	25.09	16.60	4.62	0.55
	Temperature Difference HTC = 7700 (°C)	0.59	0.30	-2.37	-2.82
RUN 13	Experimental (°C)	96.30	90.30	86.15	84.33
	Moldflow default HTC (°C)	121.45	108.29	93.80	88.16
	Moldflow HTC = 7700 (°C)	99.63	93.79	87.58	85.17
	Temperature Difference default HTC (°C)	25.15	17.99	7.66	3.84
	Temperature Difference HTC = 7700 (°C)	3.34	3.49	1.44	0.84

Table 7.4 Experimentally obtained and predicted temperatures for CB PS at four times steps.

		T at 0.25 s	T at 0.5 s	T at 1 s	T at 1.5 s
RUN 1	Experimental (°C)	74.57	69.96	65.95	64.37
	Moldflow default HTC (°C)	99.07	86.00	72.17	67.13
	Moldflow HTC = 7700 (°C)	78.45	72.71	66.88	64.73
	Temperature Difference default HTC (°C)	24.50	16.04	6.22	2.76
	Temperature Difference HTC = 7700 (°C)	3.88	2.75	0.93	0.35
RUN 5	Experimental (°C)	92.14	87.77	83.77	82.08
	Moldflow default HTC (°C)	114.04	102.58	90.47	86.06
	Moldflow HTC = 7700 (°C)	95.97	90.94	85.83	83.95
	Temperature Difference default HTC (°C)	21.90	14.81	6.70	3.99
	Temperature Difference HTC = 7700 (°C)	3.83	3.17	2.06	1.88
RUN 9	Experimental (°C)	79.50	74.56	70.20	68.44
	Moldflow default HTC (°C)	103.99	89.28	73.73	68.06
	Moldflow HTC = 7700 (°C)	80.70	74.24	67.69	65.27
	Temperature Difference default HTC (°C)	24.49	14.71	3.53	-0.38
	Temperature Difference HTC = 7700 (°C)	1.21	-0.32	-2.51	-3.17
RUN 13	Experimental (°C)	93.52	89.10	84.88	83.03
	Moldflow default HTC (°C)	118.95	105.86	92.03	86.99
	Moldflow HTC = 7700 (°C)	98.30	92.56	86.73	84.58
	Temperature Difference default HTC (°C)	25.43	16.76	7.15	3.95
	Temperature Difference HTC = 7700 (°C)	4.78	3.45	1.85	1.54

7.5 Flow Solver Results of CB PP and CB PS

Results from the Moldflow flow solution were compared to the experimentally obtained cooling profiles recorded through the polished sapphire window. Since the flow solver employs 3-stage HTC values, the regions when HTC values change from filling stage, to packing stage and then to detached stage can be observed when default HTC values were used. Figure 7.16 shows experimental cooling profile together with predicted cooling profile and pressure profile simulated with default HTC values. Figure 7.17 demonstrates the same data but between the start of the filling and one second. Figures 7.16 and 7.17 show predicted temperature and pressure profiles for a single node which is located in the centre of the part geometry shown in Figure 7.3. As described previously, the temperature of the polymer surface during the simulation with flow solver was available through modification of the software dat files, which added an extra result called "Temperature trace". Temperature tracing begins with the start of cavity filling which is t = 0 s in Figure 7.17. However, central node is located some distance away from the injection location. Figure 7.17 demonstrates that polymer melt reaches the central node at t = 0.04 s after the start of the injection. The temperature trace result is meant to be polymer temperature, but central node is not yet filled with polymer before t = 0.04 s, therefore software outputs a phantom polymer temperature (220 °C) before the node was filled. This phantom temperature should be ignored, therefore in further analyses it was removed. It has to be clarified that "Temperature trace" result is not an officially supported result but rather a work around which enables to see the polymer temperature on the surface nodes at each time-step.

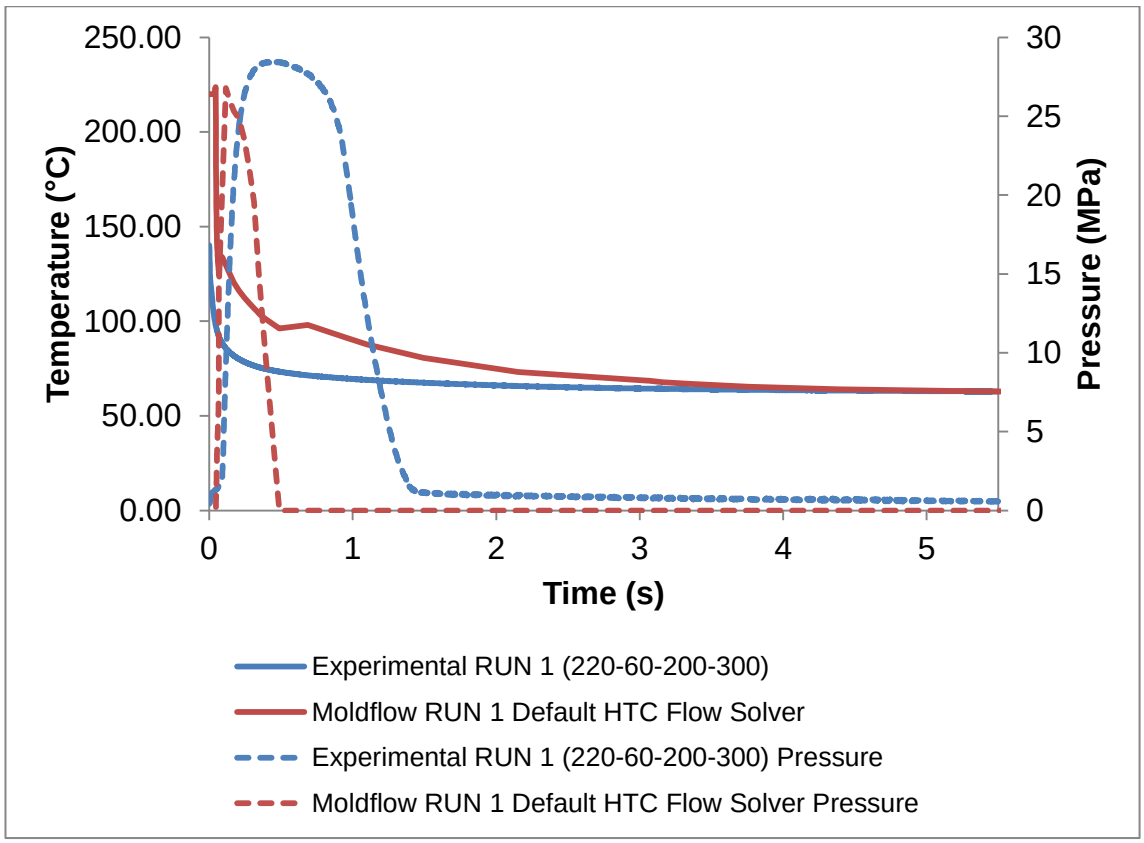

Figure 7.16 Experimental cooling and pressure curves compared to predicted cooling and pressure curves simulated with default HTC values.

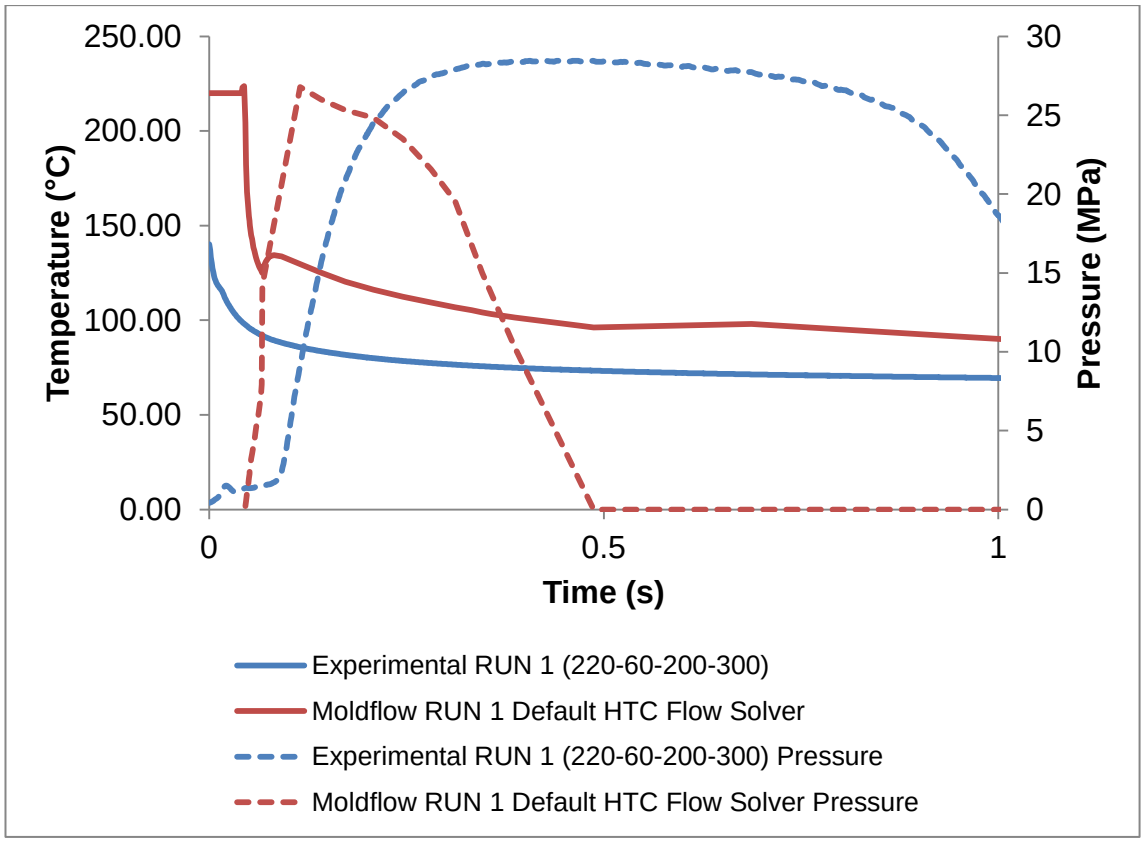

Figure 7.17 Experimental cooling and pressure curves compared to predicted cooling and pressure curves simulated with default HTC values (between 0 and 1 second).

Figure 7.18 demonstrated first bump or reheat of the polymer surface at t = 0.068 s and this corresponds with predicted filling time of 0.067 s. It could be reasonable to conclude that this a compressive heating effect, however peak pressure predicted was at 0.115 s. Moreover, experimentally reheat of the surface with an increase of cavity pressure was not observed. To test this observation, another simulation was performed where HTC values for filling, packing and detached phases were set to 5000 W/m^{2}C, which is a default value for filling phase. Figure 7.18 demonstrates that compressive heating was also predicted with the same HTC value for all three stages. It also has shown that reheat effect strongly depends on HTC set value for each stage. When filling HTC was set to 5000 W/m^{2}C and packing to 2500 W/m^{2}C observed reheat at the surface was 9.46 °C, comparing to 0.32 °C when both filling and packing HTC were set to 5000 W/m^{2}C.

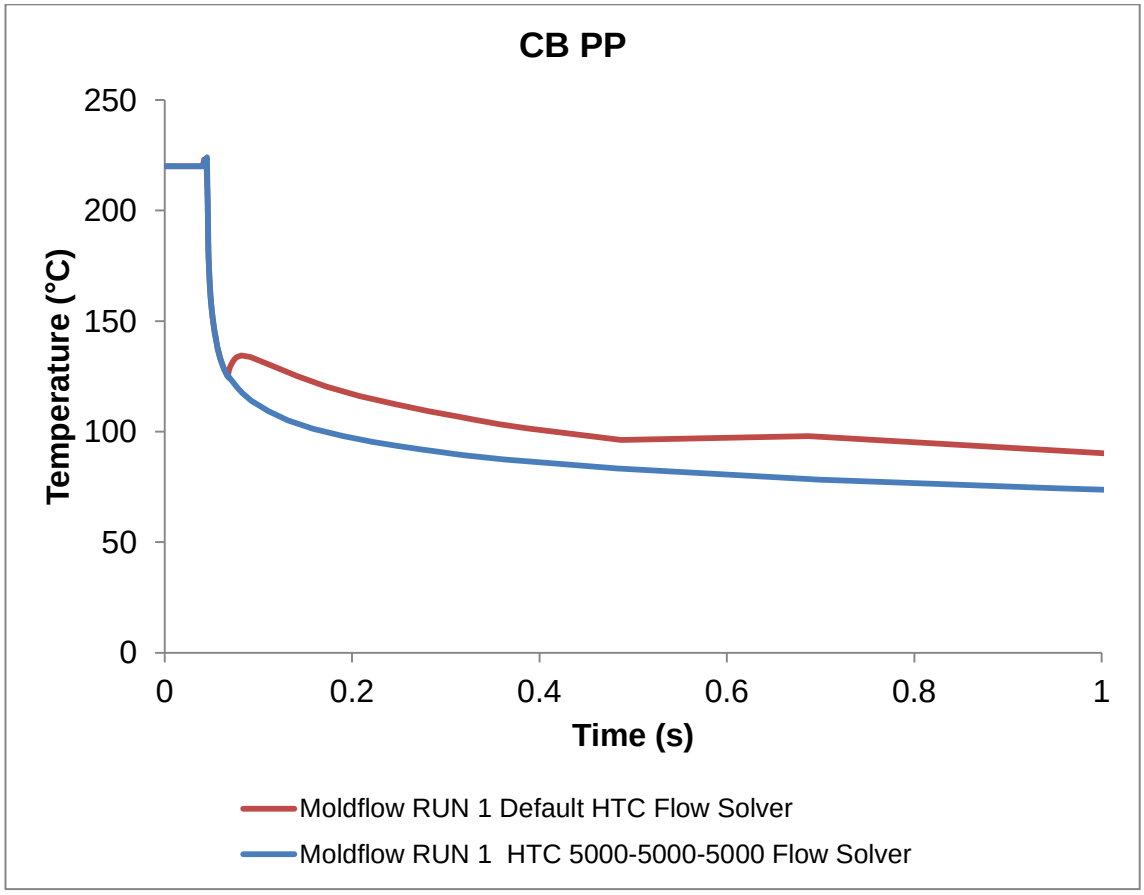

Figure 7.18 Results from flow solver with default HTC values and changed HTC value to 5000 W/m^{2}C for filling, packing and detached condition.

A second reheat was observed at t = 0.487 s and corresponded with the pressure dropping to zero at the same time-step (see Figure 7.16). Flow analysis considers that an element has entered into the detached condition when the local pressure has reached zero. Similarly to the first reheat at the surface it was governed by the change of the default HTC values from 2500 W/m^{2}C (packing) to 1250 W/m^{2}C (detached). If HTC value changes from higher value to lower, solver predicts some reheat at the surface because heat flux slows down, consequently temperature gradient from the core to the skin becomes shallower. Figure 7.19 demonstrates that reheat due to the drop of pressure disappears once the same HTC value is used for packing and detached stages.

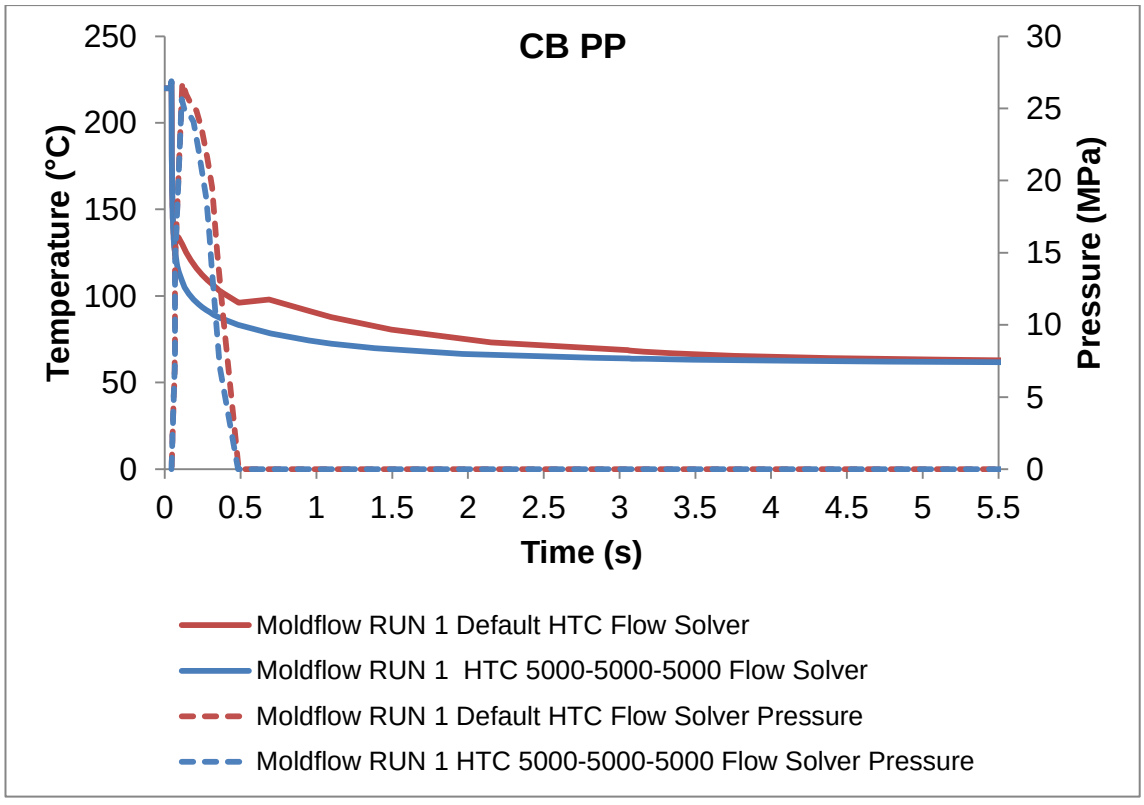

Figure 7.19 Predicted cooling and pressure curves simulated with default HTC values and changed HTC values to 5000 W/m^{2}C for filling, packing and detached condition.

Figure 7.20 demonstrates experimentally obtained cooling profile and Moldflow predicted cooling profile with default values of HTC of CB PS. Additionally, it

shows experimental and predicted cavity pressure distributions. Figure 7.21 represents the same data between the start of the filling and two seconds.

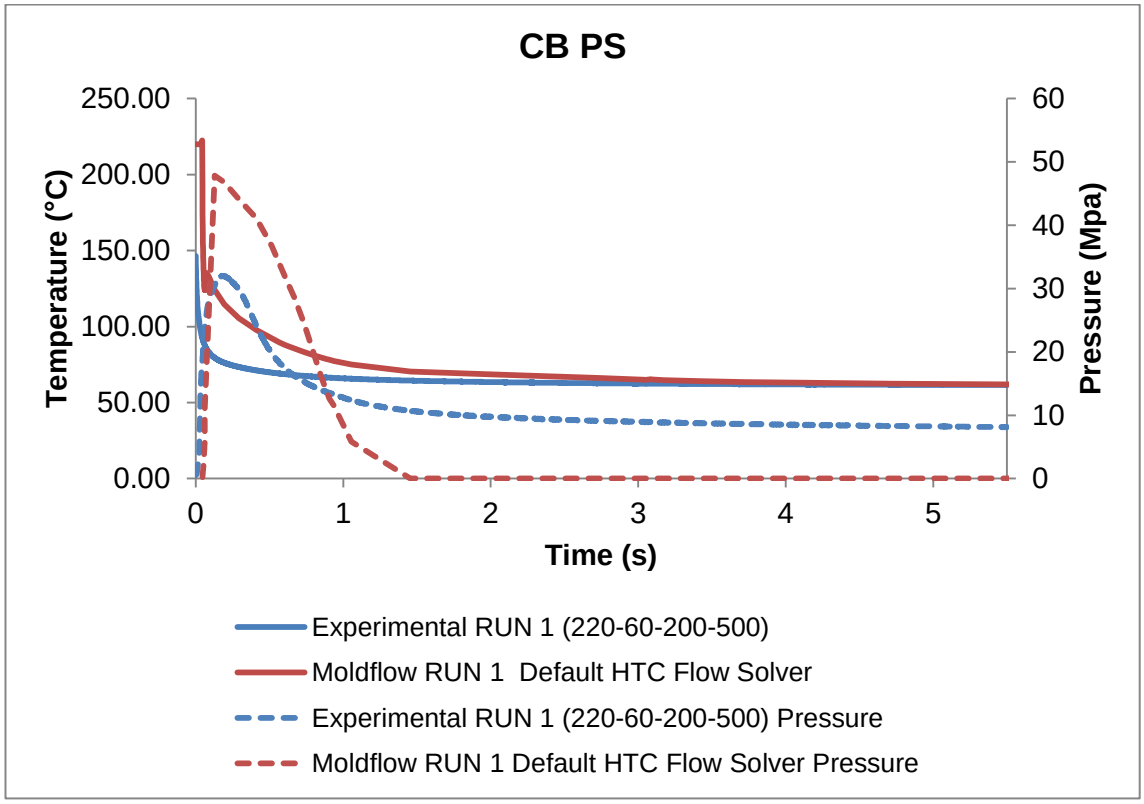

Figure 7.20 Experimental cooling and pressure curves compared to predicted cooling and pressure curves simulated with default HTC values.

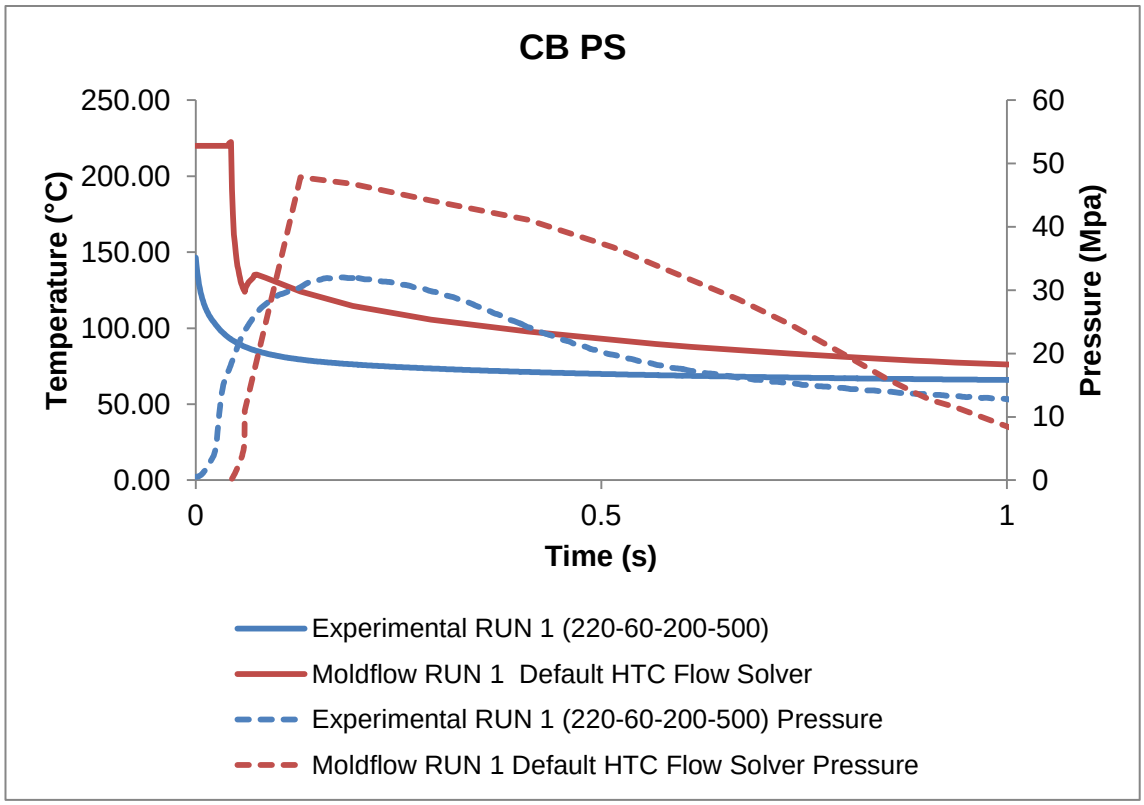

Figure 7.21 Experimental cooling and pressure curves compared to predicted cooling and pressure curves simulated with default HTC values (between 0 and 2 seconds).

Similarly to CB PP, a reheat of 11°C was observed at t = 0.061 s, which corresponded with the end of the filling time equal to 0.061 s. The second reheat due to the drop of cavity pressure and change to detached condition was not observed with default values of HTC. From Figures 7.19 and 7.20 it can be seen that CB PP drops to zero cavity pressure quicker comparing to CB PS and temperatures at those time-step are different. It can be seen in Figure 7.22 that the core temperature of CB PP when the cavity pressure drops to zero is equal to 173.58 °C, comparing to 95.72 °C for CB PS. This justifies why CB PP is subjected to higher reheat when changing from packing phase to detached phase. In CB PP part there is still a large temperature difference between the core and the skin layer. Heat still flows from the core to the skin, but once HTC is reduced from 5000 W/m^{2}C to 1250 W/m^{2}C, not as much of the heat leaves the polymer, meaning it accumulates at the skin and generates a reheat of the surface.

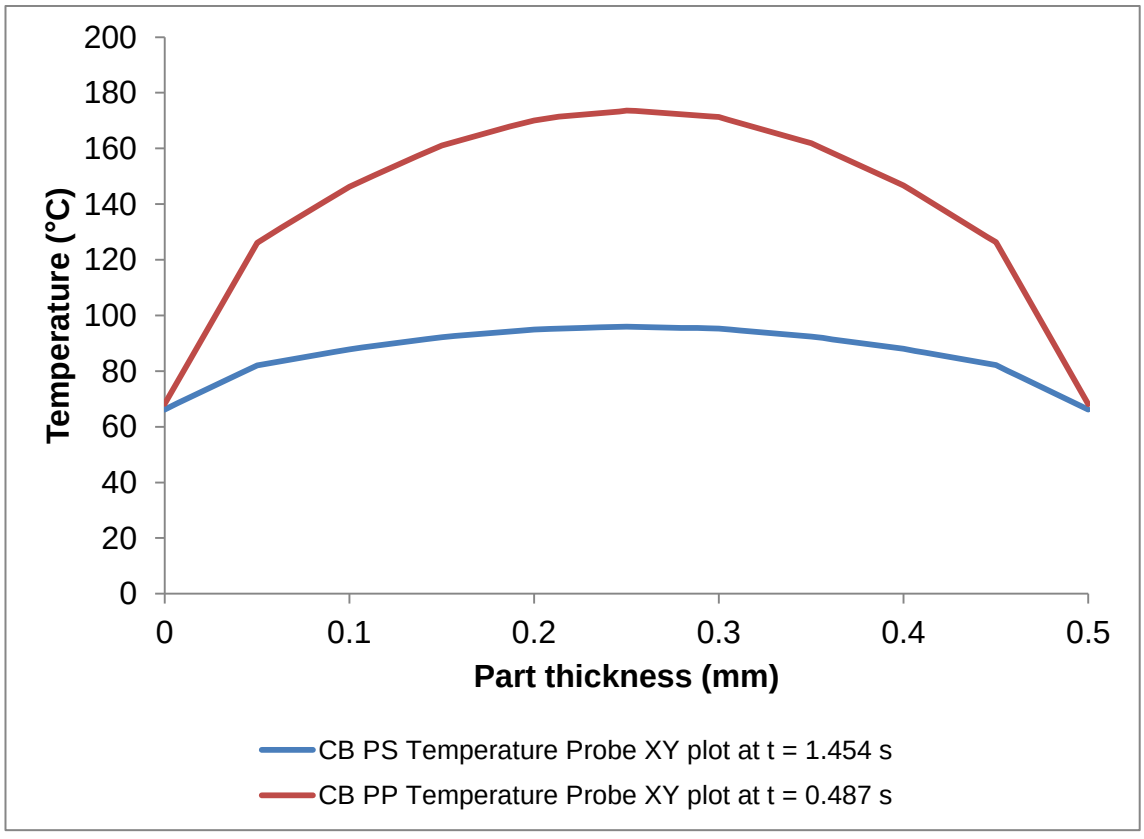

Figure 7.22 Predicted temperature through the part thickness of CB PS and CB PP when cavity pressure dropped to zero.

The reason why the CB PP pressure drops to zero quicker than CB PS lies in the PVT properties of the materials. The PVT properties of the polymers denote the relationship between pressure (P), volume (V) and temperature (T) of the polymer. Density is an important property of materials in the simulation, because it affects both mass and heat transfer. Moreover, density of the polymers vary with pressure and temperature. Thermoplastics have different PVT behaviours across its transition temperature depending on type of polymer, shown in Figure 7.23. Semi-crystalline polymers have significant and sharp pressure drop due to the sudden decrease in specific volume around transition temperature, whereas amorphous thermoplastics have only a change in slope in its specific volume-temperature curve without a sudden transition from melt to solid. (Zhou, 2013).

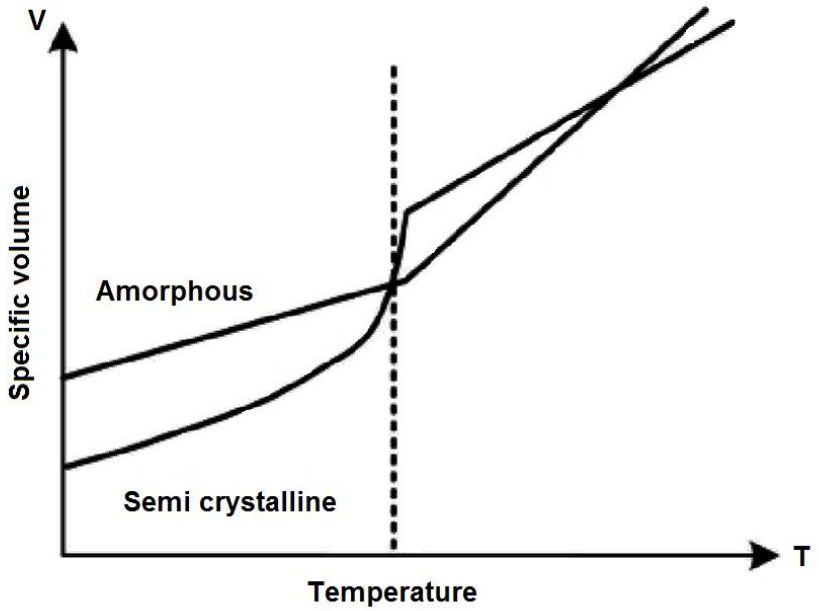

Figure 7.23 Specific volume-temperature curves of semicrystalline thermoplastic and amorphous thermoplastic (Zhou, 2013).

Figures 7.24 - 7.27 show average experimental cooling curves and average of 25 central nodes Moldflow predicted cooling curves. Predicted temperature distributions include flow solution with default HTC values and flow solution where packing HTC was changed to 7700 W/m^{2}C, keeping filling and detached

HTC default. It can clearly be seen that default HTC values do not predict cooling well. On experimental cooling profiles there was no reheat observed, however there was a slight change of slope present which corresponded with end of filling and build-up of the cavity pressure. This is more visible in Figures 7.25 and 7.27 where mould temperature was set to 80 °C.

Predicted cooling profiles demonstrate the effect of HTC values during the change from filling to packing and packing to detached phases. In Figures 7.24 - 7.27 filling HTC was set to 5000 W/m^{2}C. A reheat at the surface can be observed when HTC value for packing phase is lower than filling HTC, on the other hand increase of HTC for packing phase changes the slope or one could say increases the cooling rate. A value of 7700 W/m^{2}C for the packing phase improves the cooling prediction from the start of the cavity filling till it reaches detached condition. Maximum reheat during the change from packing to detached phase was 1.7 °C with default HTC values, comparing to 12.19 °C with packing HTC increased to 7700 W/m^{2}C.

Another simulation was performed with CB PP where, filling HTC was kept unchanged and both packing HTC and detached HTC changed to 7700 W/m^{2}C. Figure 7.28 shows a comparison between experimental cooling curve, predicted cooling curve using conduction solver, predicted using flow solver where only packing HTC was changed to 7700 W/m^{2}C, and results from flow solver where both packing and detached HTC values were changed to 7700 W/m^{2}C. Results prove that reheat around 0.5 s is purely due to the reduction of HTC value from packing to detached phase. Moreover, no reheating due to the detachment of part was observed experimentally. Elimination of the reheat by setting packing and detached HTC values to 7700 W/m^{2}C was also present in run 5, run 9 and run 13.

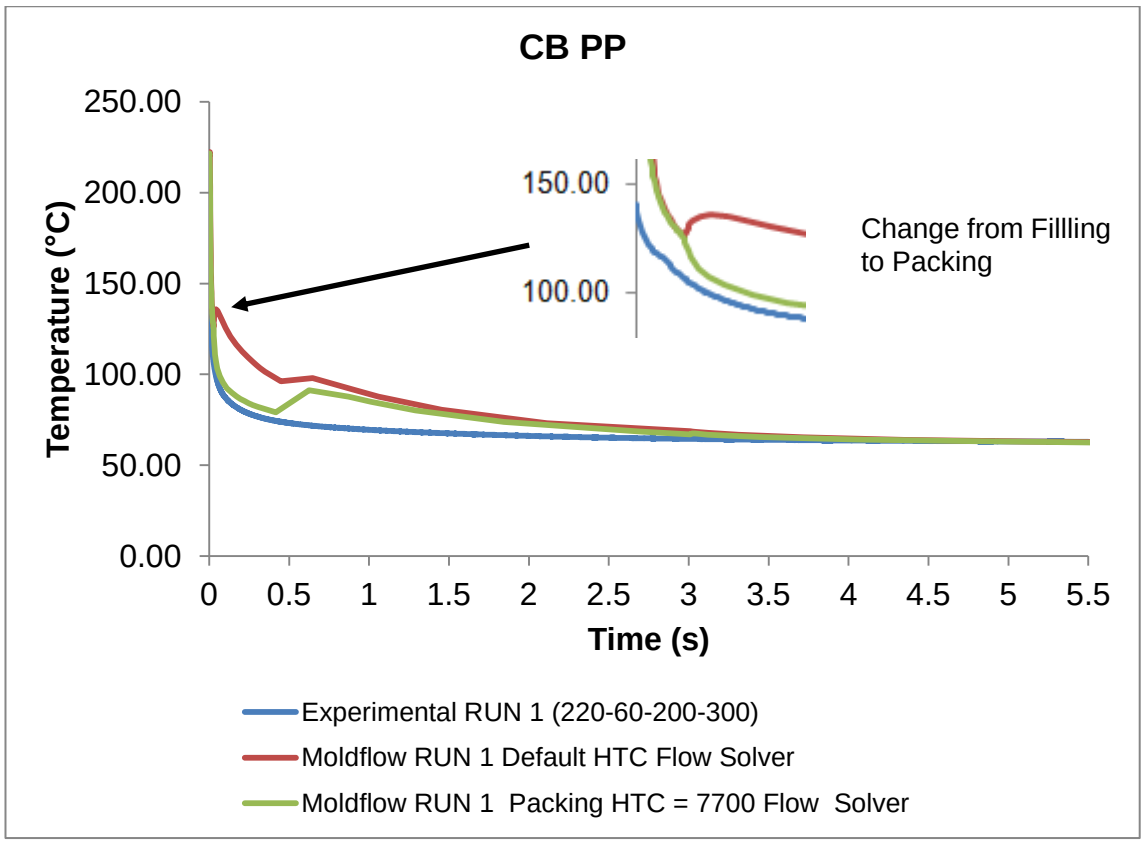

Figure 7.24 Cooling curves plot of CB PP - experimental and flow solver results for RUN 1.

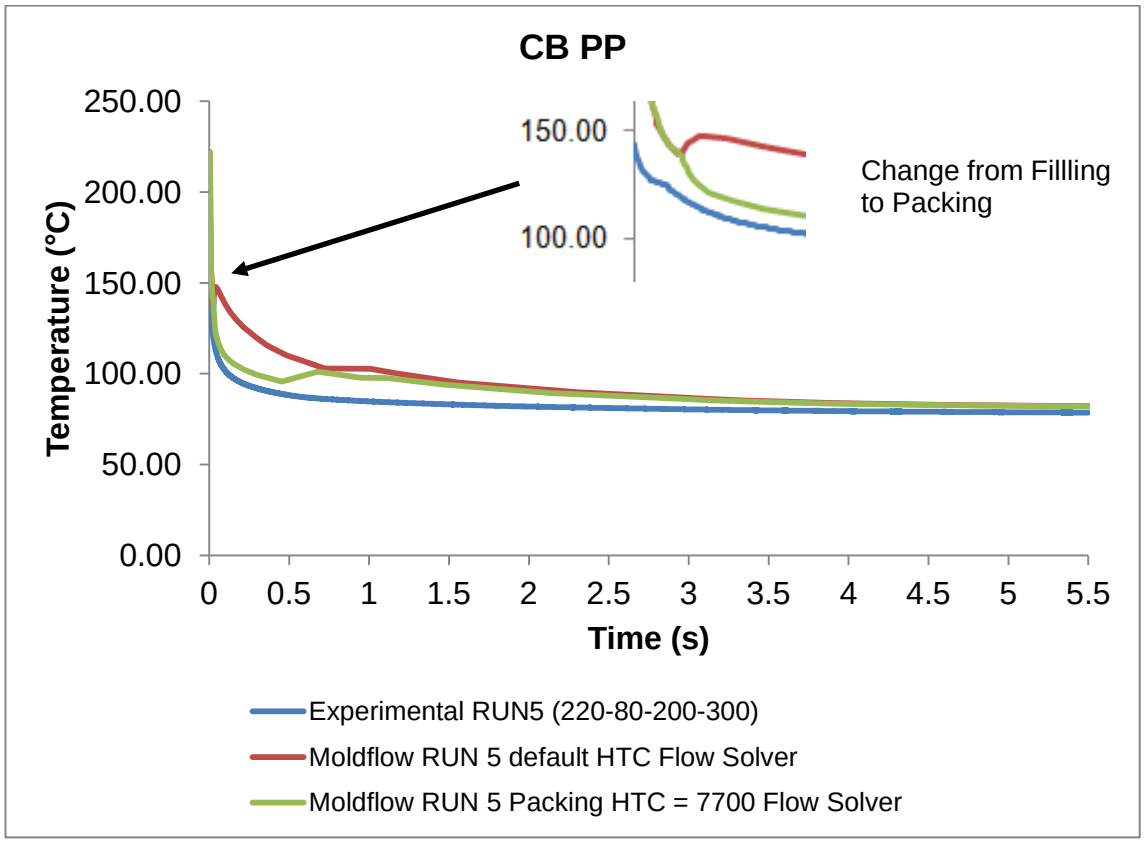

Figure 7.25 Cooling curves plot of CB PP - experimental and flow solver results for RUN 5.

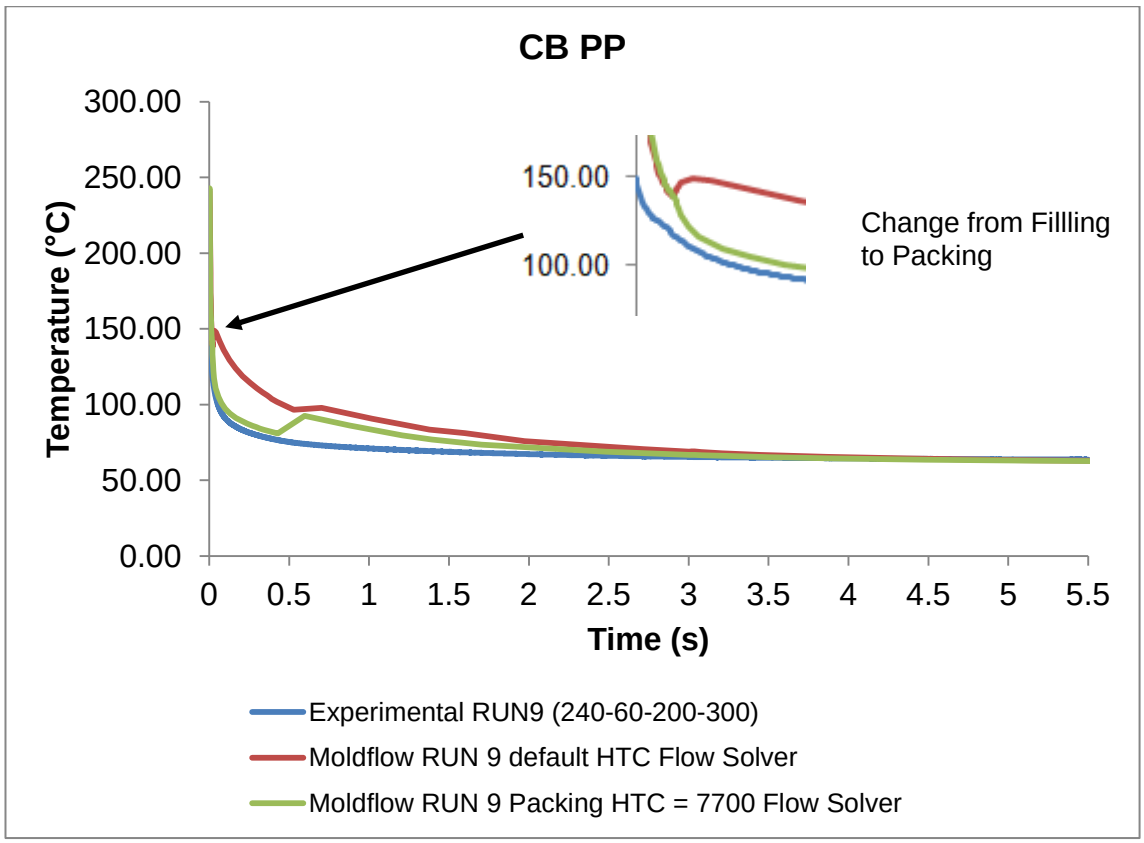

Figure 7.26 Cooling curves plot of CB PP - experimental and flow solver results for RUN 9.

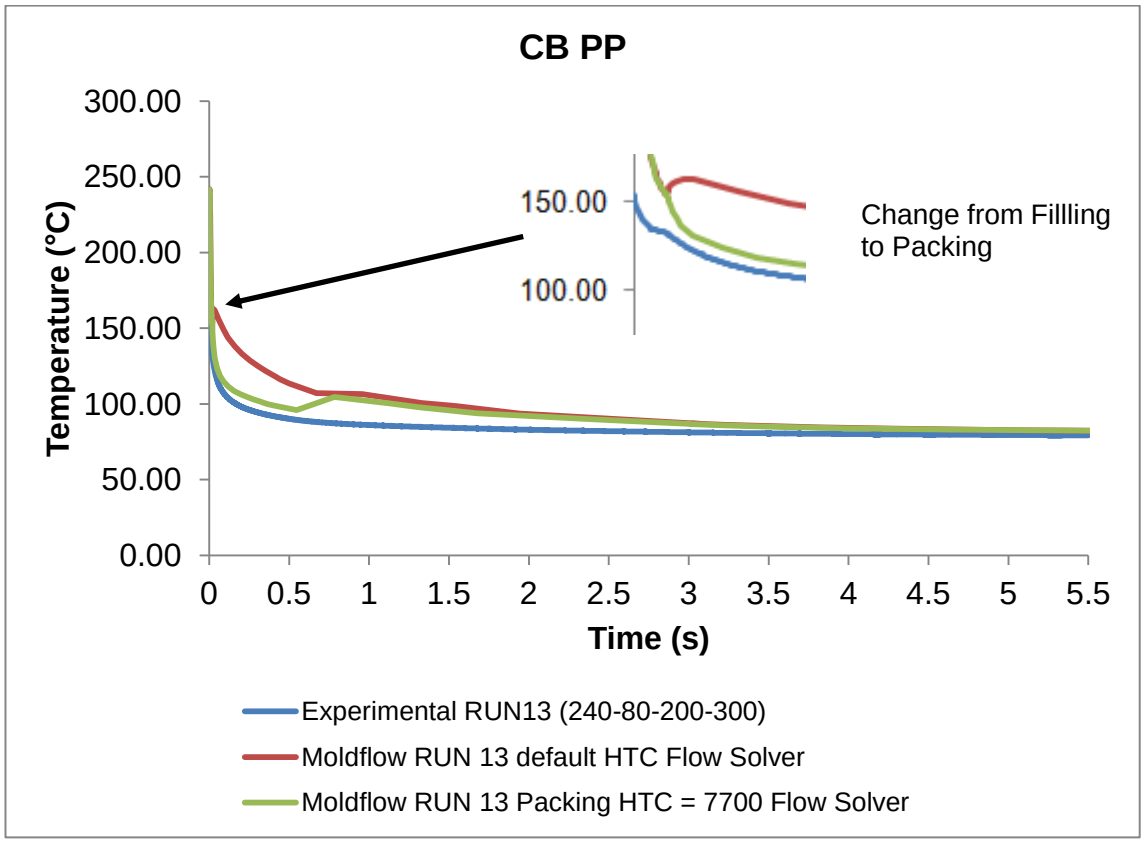

Figure 7.27 Cooling curves plot of CB PP - experimental and flow solver results for RUN 13.

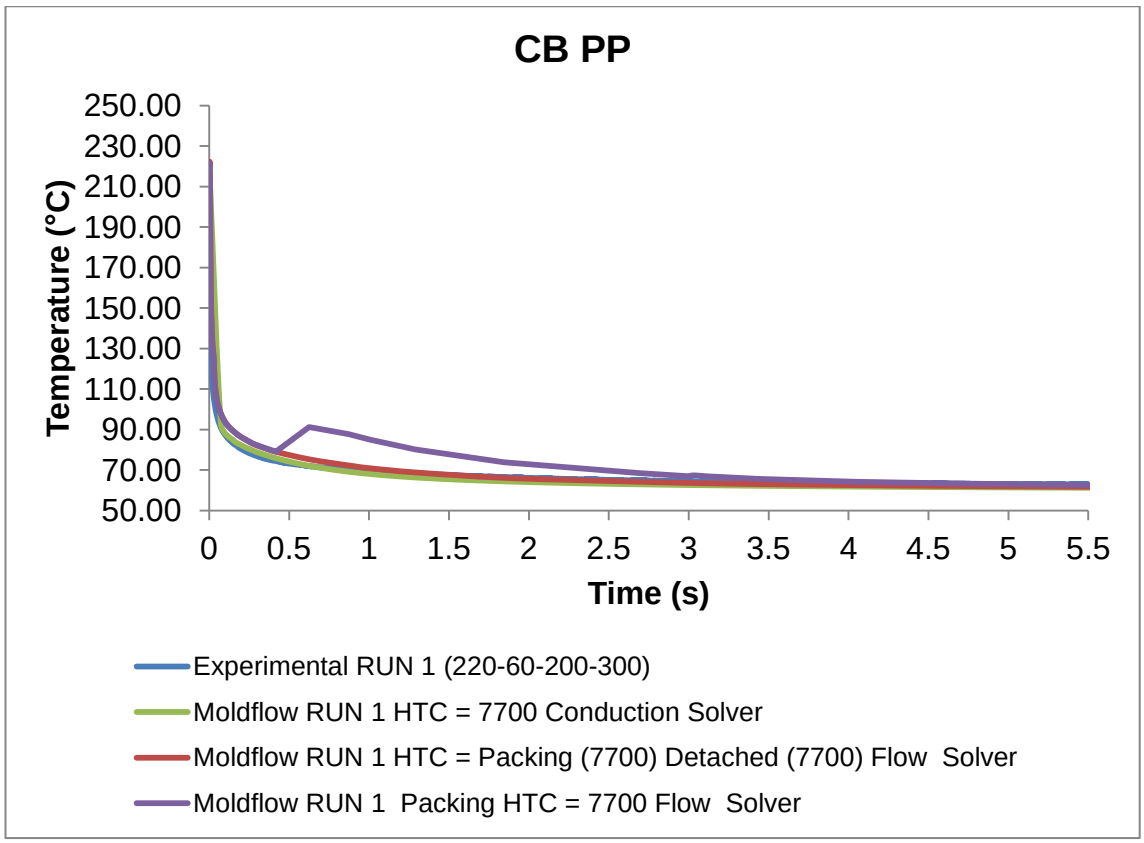

Figure 7.28 Cooling curves plot of CB PP - experimental, conduction solver and flow solver results for RUN 1.

Figures 7.29 - 7.32 demonstrate experimental cooling curves and average of 25 central nodes Moldflow predicted cooling curves of CB PS. Predicted temperature distributions include flow solution with default HTC values and flow solution where packing HTC was changed to 7700 W/m^{2}C, keeping filling and detached HTC default. A reheat can be observed in predicted cooling curves with default HTC values during the phase change from filling to packing. Similarly to CB PP this is an effect of the decrease of HTC value from 5000 W/m^{2}C to 2500 W/m^{2}C. Experimentally there was no reheat regions observed throughout the cycle. In predicted curves with default HTC values there was no reheat observed during the phase change from packing to detached. As described previously, zero pressure was reached when temperature of the part was close to the mould set temperature.

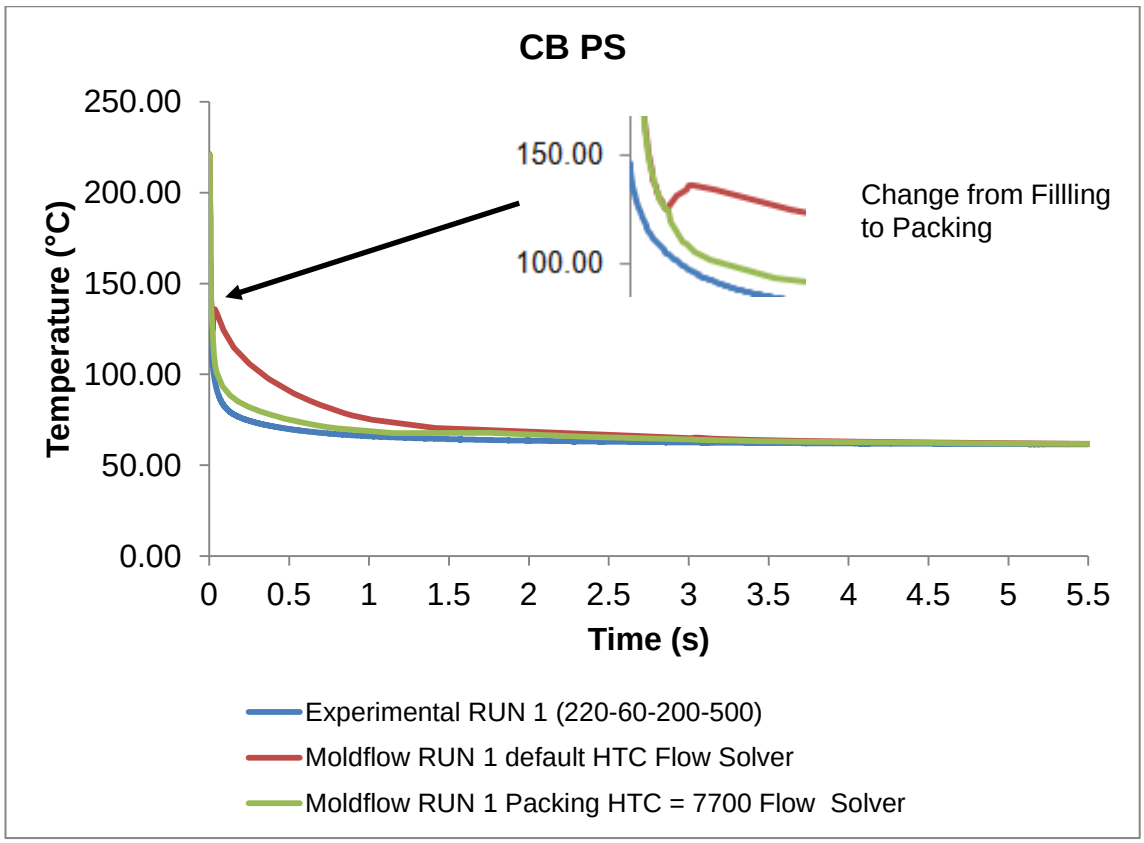

Figure 7.29 Cooling curves plot of CB PS - experimental and flow solver results for RUN 1.

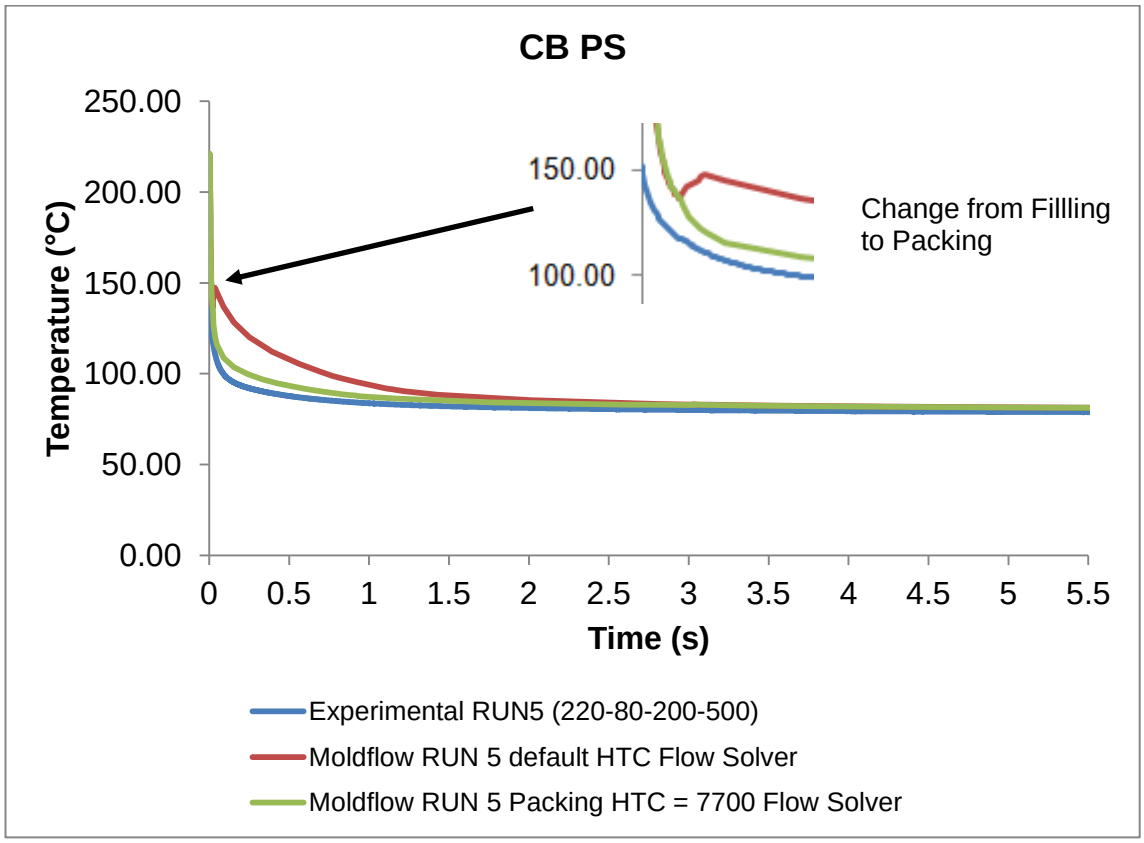

Figure 7.30 Cooling curves plot of CB PS - experimental and flow solver results for RUN 5.

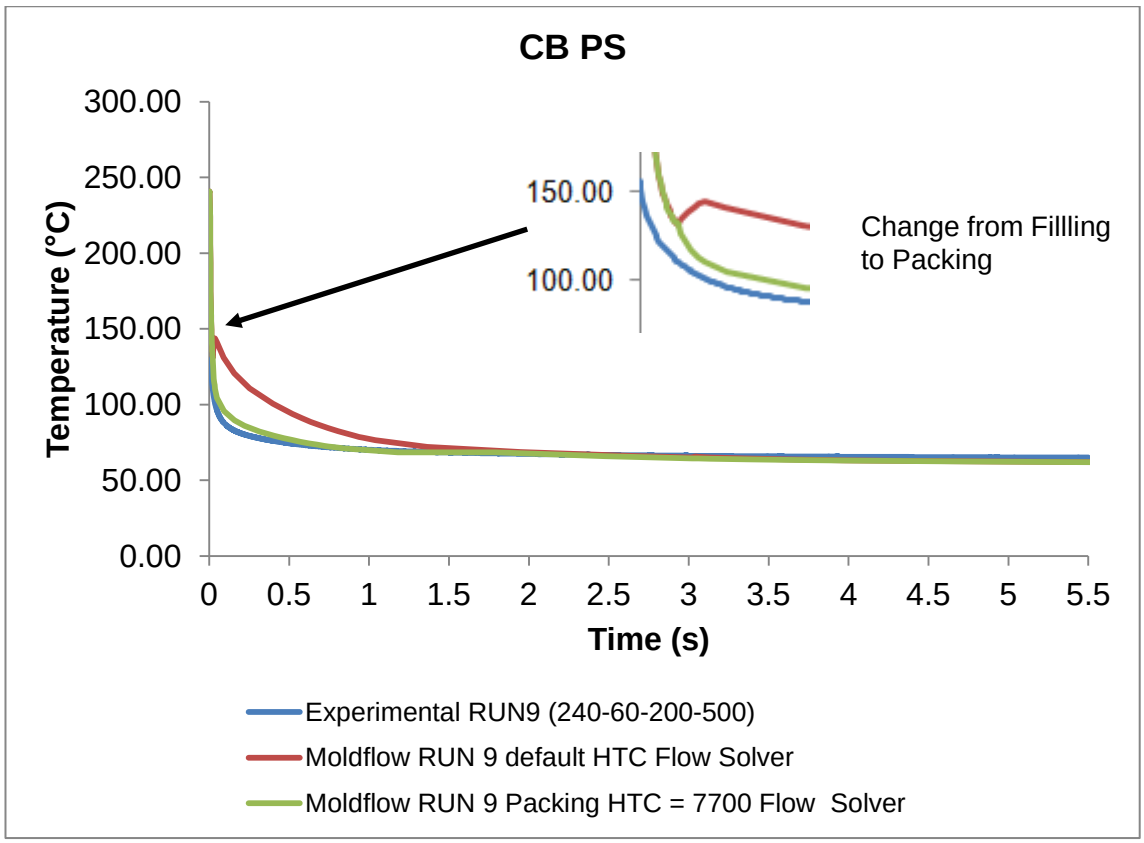

Figure 7.31 Cooling curves plot of CB PS - experimental and flow solver results for RUN 9.

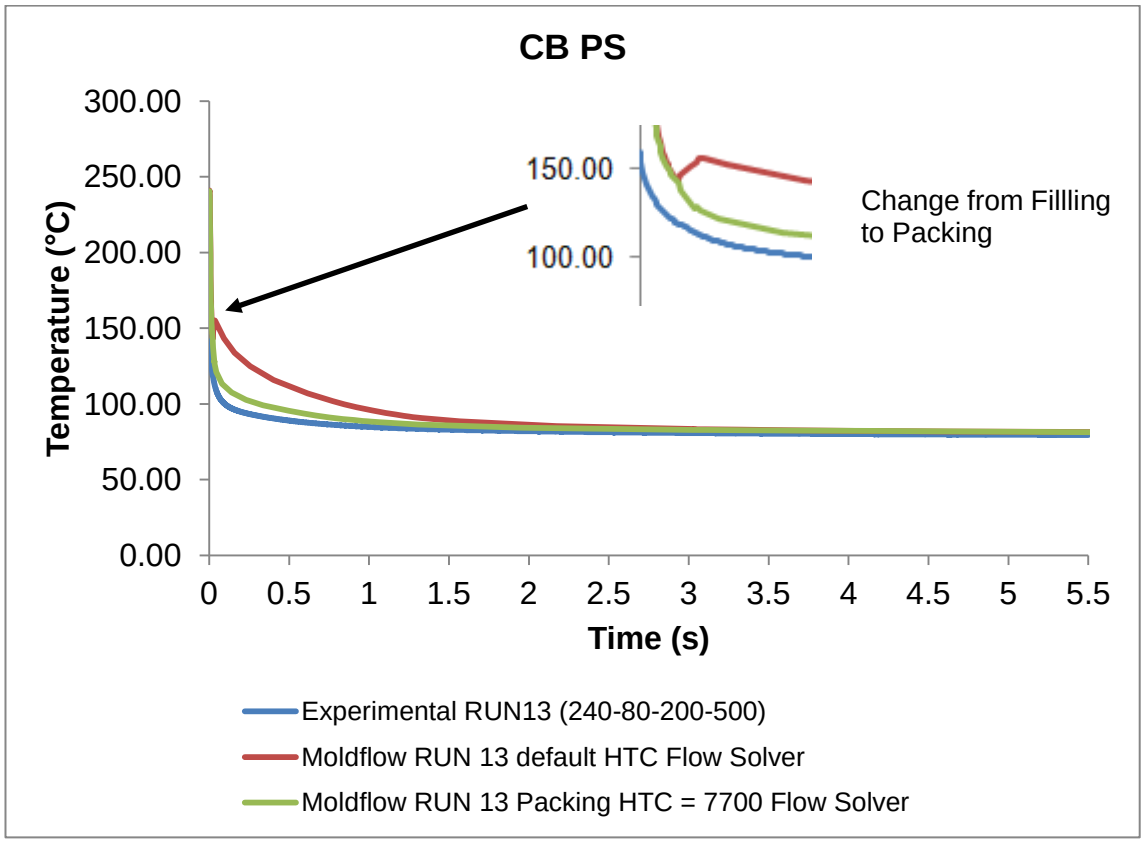

Figure 7.32 Cooling curves plot of CB PS - experimental and flow solver results for RUN 13.

7.7 Conclusion

This chapter reports a simulation study of polymer cooling during microinjection moulding process. Simulation process and available cooling analysis solvers within Moldflow simulation software were discussed. Results from conduction solver and flow solver were compared to experimentally obtained cooling curves. Different HTC values were used within both solvers to predict temperature of the polymer surface during filling, packing and cooling. The following conclusions can be made based on the obtained results:

- Both solvers predicted that temperature of the polymer surface when it starts cooling was equal to the melt set temperature in case of conduction solver or it was even higher than the melt set temperature using flow solver. The data gathered experimentally suggests that surface temperature of the polymer equal to melt set temperature cannot be assumed.
- In the conduction solver where a single value of HTC was used, improvements in cooling prediction were observed for both materials with an increase of the HTC values from 2500 W/m^{2}C (default) to 7700 W/m^{2}C. The highest temperature difference between experimental and predicted temperature with both materials was observed at t = 0.25 s from the start of the cooling. An increase of the HTC value showed a reduction of temperature difference in the range of 1.3 °C to 3.7 °C, comparing to 21.9 °C - 25.43 °C predicted with default HTC value and showed improvements at other time-steps.
- The flow solver which uses 3-stage HTC has advantages and disadvantages. Using default HTC values it predicts reheat at the surface due to the phase change from filling to packing and from packing to

detached condition. It was shown experimentally that CB PP reheating with an increase of cavity pressure (entering packing phase) was actually a real effect, however no reheat was observed with CB PS. In predicted cooling curves materials also responded differently to reheat during change from packing to detached phase due to their PVT properties. No reheat due to the detachment of the part from the mould surface was observed experimentally, therefore in flow solver it is advisable to keep filling and detached HTC of equal values.

- Generally, both solvers failed to predict surface temperature accurately using default HTC values. Prediction can be improved with higher HTC value and conduction solver appears to be advantageous comparing to flow solver. Firstly, the conduction solver is faster, taking 1 hour and 11 minutes to perform one simulation, compared to 3 hours and 41 minutes with the flow solver. Secondly, because injection speed and packing pressure were not statistically significant for cooling of the polymer and there was no detachment observed, there is no need for complicated flow analysis which includes 3-stage HTC.

Chapter 8 Conclusions and Recommendations

The cooling of polymers was investigated with respect to simulation of heat transfer at polymer-cavity interfaces during microinjection moulding. The thermal characteristics of the boundary between the polymer melt and mould tool are important considerations for injection moulding. They are particularly relevant for microinjection moulding due to the high surface area to volume ratio. The thermal field can have a significant influence on internal structure, morphology and resulting physical properties of the part. Understanding of heat flux from the part during microinjection moulding is essential for prediction of the final product quality.

Measurement of melt temperature is a difficult task for microinjection moulding. Commercially available cavity pressure/temperature sensors are impractical to use due to their physical size, relatively slow response time and because they may influence the temperature measurement by acting as a heat sink. A mould was designed based on a flow visualisation tool developed at the University of Bradford. A sapphire window forms the fixed half of the mould cavity, which allows thermal measurements of the melt temperature using a non-invasive, non-contact IR technique. To investigate the effects of surface finish, a number of sapphire windows were laser machined to generate a range of surface topographies.

The majority of organic polymers are selective emitters and appear semi-transparent to the IR camera. Employing Fourier transform infrared spectroscopy has shown that the addition of 4 wt% of carbon black masterbatch makes polypropylene and polystyrene IR opaque. This allowed melt surface temperatures to be measured with a high speed infrared camera. Prior to microinjection moulding experiments, thermal properties of the compounded

and neat polypropylene and polystyrene were analysed using DSC. The DSC results showed that the T_g of polystyrene and the T_m of polypropylene were not affected by the addition of carbon black masterbatch. The heat capacity of polymers was measured using MDSC. Results showed that the addition of pigment to polystyrene was statistically insignificant. In the case of polypropylene, the increase of heat capacity was observed with an addition of carbon black masterbatch. Highest increase of heat capacity (12.7 %) was observed at low temperature of 16.85 °C. With an increase of temperature difference in heat capacities between carbon black filled and neat polypropylene was reducing down to 6.8 % at 186.85 °C.

The surface energy of sapphire and mould steel was examined. Sapphire and steel are both high surface energy solids and have good wettability by liquids. Therefore, they are efficient mould materials for microinjection moulding. The surface energy of sapphire was determined to be slightly higher than the surface energy of steel. However, the rate of spreading of polymers on both substrates has shown that difference was not significant.

The optical train of the experiment is complex due to the reflection at surfaces, absorption in optical components and different emissivities of target materials. This makes it impractical to compensate for the IR attenuation analytically. For that reason, prior to experimental investigation carbon black filled polypropylene and polystyrene were calibrated in-situ. A design of experiments was carried out on a microinjection moulding machine, where surface finish effects and process parameters such as melt temperature, mould temperature injection speed and packing pressure were investigated. The cooling curves were statistically analysed. The parametric study has established that during filling injection speed was the most significant parameter, following

by the temperature of the melt and temperature of the mould. During polymer cooling, temperature of the mould was the most significant parameter following by the temperature of the melt. Cooling did not show dependence on packing pressure and injection speed. The effects of surface roughness on material cooling were inconclusive as there were no trends observed with an increase of effective surface area.

Two cooling solutions within the Moldflow simulation software were investigated for prediction of polymer cooling during the microinjection moulding cycle. These were the conduction solver, which employs a single value of HTC and flow solver which employs 3-stage HTC for filling, packing and detached condition. Polymer peak surface temperatures were over predicted when compared to experimentally obtained peak temperatures. Default values of HTC were not able to predict cooling well and showed that temperature difference between experimentally obtained cooling profiles and predicted could be as high as 25 °C. A more accurate cooling prediction was obtained with higher value of HTC using the conduction solver. Moreover, predicted cooling curves for polypropylene and polystyrene showed no significant difference with both default and changed HTC values. Therefore, the results can be generalised to cover both amorphous and semicrystalline thermoplastics with similar properties within conduction solver. The flow solver has to be used with caution as it requires good understanding of the materials behaviour during the cycle. The reheat at interface due to the polymer-mould separation was observed in experimental study by Bendada et al. (2004b) and it corresponded to the cavity pressure dropping to the atmospheric pressure. This reheat was also predicted by the flow solver when HTC values are kept at their default values. Bendada et al. (2004) have performed their experiments with polypropylene on a 400-ton

injection moulding machine and their component had a thickness of 2.3 mm and average dimensions of 330 x 200 x 180 mm. The reheat due to separation was not observed in this work, which suggests that packing and detached HTC should be set to the same value. Moreover, it was shown that semi-crystalline and amorphous materials respond differently to reheat due to their PVT properties.

The simulation results have shown that the heat transfer coefficient is a significant parameter in the computer simulation of the microinjection moulding. The default values of heat transfer coefficients might predict cooling better for conventional injection moulding simulations, however for microinjection moulding these values produce significant errors.

This study has revealed a few open-ended questions that require further investigation for better understanding of heat transfer coefficients in microinjection moulding and prediction of cooling in simulation software. Among the areas that are suggested for further work are:

- Experimental measurement of cooling profiles for thinner polymer specimens (thickness bellow 0.5 mm) and comparison of these profiles with simulated results.
- Perform a study without packing pressure to identify significance of the reheat of the surface due to the shrinkage and detachment from the cavity wall. These results can be compared with Moldflow flow solver that uses 3-stage HTC.
- Perform a study with unfilled materials but with a spectrally adapted IR camera. This requires a narrowband pass filter which transfers infrared light in the wavelength range in which polymer is highly opaque.

- Perform a study with unfilled polymers and without a filter. Some of the polymers are semi-transparent for the radiation, this suggests that not only surface temperature can be measured but also core temperature which can lead to better understanding of the heat flux from the part.
- Simulation of the part surface temperature can be improved by importing temperature dependant heat capacity and thermal conductivity data. Materials that has been used in this study had a single value of heat capacity and thermal conductivity in the Moldflow materials database. Also, prediction can be improved by importing rheological data that can better describe polymer melt behaviour during microinjection moulding.

References

AGA infrared systems AB, (1984). Operation manual, thermovision 782, AGA infrared systems AB, Secaucus, New Jersey. pp. 6-23.

Anastasiadis, Spiros K., and Hatzikiriakos, Savvas G., (1998). The work of adhesion of polymer/wall interfaces and its association with the onset of wall slip. *Journal of Rheology,* 42(2), pp. 795-812.

ASTM Committee E20 on temperature measurement, (1993). Manual on the use of thermocouples in temperature measurement. Philadelphia, PA, ASTM.

Autodesk Moldflow Insight (2012). AMI Cool Analysis Products. [online] Available at: http://de0qmbqba3hfm.cloudfront.net/attachments/49230/0 [Accessed 25.08.2015].

Autodesk, (2012a). Autodesk Simulation Moldflow, Plastic made perfect, brochure. Available at: http://images.autodesk.com/adsk/files/simulation_moldflow_detail_brochure_en_us_v3.pdf [Accessed: 17 Dec 2012].

Aveyard, R., and Haydon, D. A., (1973). An introduction to the principles of surface chemistry. Cambridge [Eng.], University Press.

Bahrami, M., Culham, J.R., Yovanovich, M.M., Schneider, G.E., (2006). Review of Thermal Joint Resistance Models for Nonconforming Rough Surfaces. *Applied Mechanics Review,* 59, 1.

Bahrami, M., Yovanovich, M. M., and Culham J. R., (2004). Thermal joint resistance of conforming rough surfaces with gas-filled gaps. *Journal of Thermophysics and Heat Transfer,* 18(3), pp. 318-325.

Bansal, R. and Goyal, M., (2005). *Activated carbon adsorption*. Boca Raton: Taylor & Francis. Pp. 25-26.

Barnes, G., and Gentle, I., (2011). Interfacial science: an introduction. 2nd ed. New York, Oxford University Press. pp. 15, 17-18.

Bart, J., (2006). Plastics additives. Amsterdam: IOS Press, pp. 20-21.

Battenfeld, (2003). Operating manual: Injection moulding machine Microsystem50, chapter 3, pp. 1-2.

Battenfeld, (no date). Micro-moulding: Battenfeld injection molding, brochure. Available at: http://www.battenfeld.ru/fileadmin/templates/docs/imm/microsystem_presentation.pdf [Accessed: 9 Dec 2013].

Bendada, A., Cole, K., Lamontagne, M., and Simard, Y., (2004a). A hollow waveguide infrared thermometer for polymer temperature measurement during injection moulding. *Journal of Optics A: Pure and Applied Optics,* 5, pp. 464-470.

Bendada, A., Cole, K., Lamontagne, M., and Simard, Y., (2004b). Analysis of thermal contact resistance between polymer and mold in injection molding. *Applied Thermal Engineering,* 24, pp. 2029-2040.

Blume-Peytavi, U., Tosti, A. And Whiting, D., (2008). Hair, hair growth and hair disorders. 1st ed. Dordrecht, Springer. pp. 9.

Bohler-Uddeholm, (2000). Impax Hi Hard P20 prehardened mould steel, properties sheet. Available at: http://www.uddeholm.hu/hungarian/files/Impaxhh_en.pdf [Accessed: 08 Apr 2013].

Bowden F.P. and Tabor D., (1950). The Friction and Lubrication of Solids.

Breitenstein, O., Watra, W., and Langenkamp, M, (2010). Lock-in Thermography - Basics and Applications to Functional Diagnostics of Electronic Components. 2nd Ed. Berlin, Springer. pp. 7-14.

Bruce Cassel, R., (no date). How Tzero technology improves DSC Performance. Part III: the measurement of specific heat capacity. TA Instruments Publication TA 279.

Buehler, (2012). Buehler buyer's guide 2012, Germany, Buehler GmbH. p. 30, 40, 42-43.

Cabot Corporation, (2012). PLASBLACK UN2014. Product datasheet.

Chen, Tai-Chang, Darling, R.B., (2005). Parametric studies on pulsed near ultraviolet frequency tripled Nd: YAG laser micromachining of sapphire and silicon. Journal of Materials Processing Technology, pp. 214-218.

Chen, Z., and Turng, L.-S., (2005). A review of current developments in process and quality control for injection molding. *Advances in Polymer Technology,* 24(3), 165-182.

Coates, P.D., Whiteside, B. R., Martyn, M. T., Spares, R., and Gough, T., (2006). Micromoulding - precision processing for controlled products. In: *Proceeding of the Seconds International Conference on Multi-material micro manufacture (4M)* 2006, pp. 13-15.

Comyn, J., (1997). Adhesion science. Cambridge, Royal Society of Chemistry, Information Services. pp. 103-110.

Cooper, M., Mikic, B.B. and Yovanovich, M.M., (1969). Thermal Contact Conductance. *International Journal of Heat and Mass Transfer,* 12, pp. 279-300.

Costa, F.S., Tosello, G., Whiteside, B.R., (2009). Best practice strategies for validation of micro moulding process simulation, P D Coates and authors, Polymer Process Engineering 09, Enhanced Polymer Processing, The University of Bradford, pp. 331-364.

Delaunay, D., and Le Bot, P., (2000). Nature of contact between polymer and mold in injection molding. Part 1: influence of a non-perfect thermal contact. *Polymer Engineering and Science,* 40(7), pp. 1682-1691.

Dininger, J., (1994). Three critical measurements on injection molding processes. Elyria, The United States of America 2-6 Oct 1994., 3, pp. 2159 - 2164.

Dobrovinskaya, E., Lytvynov, L. and Pishchik, V. (2009). *Sapphire*. New York: Springer. P. 85.

Erbil, H. Y., (2006). Surface chemistry of solid and liquid interfaces. Oxford, Blackwell Pub. pp. 85, 223, 231-234, 284, 308-315, 336.

Finn, K. H., (2004). The measurement of surface energy of polymers by means of contact angles of liquids on solid surfaces, a short review of frequently used methods. University of Oslo.

FLIR Advanced Thermal Solutions, (2013). R&D advanced course, EMEA region, version D-2013. p. 99, 129.

FLIR Systems, (2014). FLIR X6540sc specifications, brochure.

Fontes, J., (2005). Chapter 20: temperature sensors. In: Wilson, J.S., 2005. *Sensor Technology Handbook,* Amsterdam, Elsevier. pp. 531-563.

Fraden, J., (2010). Handbook of modern sensors: physics, designs, and applications. New York, Springer. pp. 549-550.

Fuller, J. J., and Marotta, E. E., (2001). Thermal contact conductance of metal/polymer joints: an analytical and experimental investigation. *Journal of Thermophysics and Heat Transfer,* 15(2), pp. 228-238.

Gaur, U., and Wunderlich, B., (1982a). Heat capacity and other thermodynamic properties of linear macromolecules. V. Polystyrene. *Journal of Physical and Chemical reference Data,* 11(2), pp. 313 - 325.

Gaur, U., and Wunderlich, B., (1982b). Heat capacity and other thermodynamic properties of linear macromolecules. IV. Polypropylene. *Journal of Physical and Chemical reference Data,* 10(4), pp. 1051 - 1064.

Gautschi, G., (2002). Piezoelectric sensorics: force, strain, pressure, acceleration and acoustic emission sensors, materials and amplifiers. Berlin, Springer. pp. 159-161.

Globalopticsuk, (2012). Sapphire - Al1O3 properties sheet. Available at: http://www.globalopticsuk.com/pdf/sapphire.pdf [Accessed: 08 Apr 2013].

Grujicic, M., Zhao, C. and Dusel, E. (2005). The effect of thermal contact resistance on heat management in the electronic packaging. *Applied Surface Science*, 246(1-3), pp.290-302.

help.autodesk.com, (2015). Autodesk Simulation Moldflow Insight 2015 Help. [online] Available at: http://help.autodesk.com/view/MFIA/2015/ENU/ [Accessed 25.08.2015].

Johannaber. F., (2007). Injection Molding Machines, A User's Guide, 4th edition, Munich: Carl Hanser Verlag.

Kamal M. R., Agassant J.-F., (2009). Injection molding technology and fundamentals. Munich, Hanser.

Kaplan, H., (2007). Practical applications of infrared thermal sensing and imaging equipment. Bellingham, Wash, Spie Press. pp. 13-20, 22-29, 37.

Karnakis, D.M., Knowles M.R.H., Petkov P.V.,Dobrev, T., Dimov, S.S., (2007b). Surface integrity otimisation in ps-laser milling of advanced engineering

materials. Proceedings of the Fourth International WLT-Conference on Lasers in Manufacturing.

Karnakis, D.M., Mortimer, V., Knowles M.R.H., (2007a). Recent advances in ultrafast laser micromachining systems for material micromanufacturing. In: 8th International Conference and Exhibition on Lser Metrology, Machine Tool, CMM & Robotic Performance, Cardiff, Wales.

Kelly, A. L., Woodhead, M., and Coates P. D., (2005). Comparison of injection molding machine performance. *Polymer Engineering and Science,* 45(8), pp. 857-865.

Khan, W.A., Culham, J.R., and Yovanovich M.M., (2005). Modeling of cylindrical pin-fin heat sinks for electronic packaging. In: *proceedings 2005 IEEE/CPMT 21st Semiconductor Thermal Measurement & Management Symposium.*

Khurana, I., (2008). Essentials of medical physiology. New Delhi, Elsevier, pp. 74.

Kistler, (2011a). p-T-Sensor for mold cavity and temperature with front diameter 1 mm, data sheet. Available at: http://www.kistler.com/uk/en/product/pressure/6188AA0,4 [Accessed: 16 Feb 2013].

Kistler, (2011b). p-T-Sensor for mold cavity and temperature with front diameter 2.5 mm, data sheet. Available at: http://www.kistler.com/uk/en/product/pressure/6189A0,4 [Accessed: 22 Apr 2013].

Koenig, J., (1999). *Spectroscopy of polymers*. Amsterdam: Elsevier, pp. 35-47.

Lambert, M. A., and Fletcher, L.S., (1995). Experimental investigation of the thermal contact conductance of electroplated silver coatings. *Journal of Thermophysics and Heat Transfer,* 9(1), pp. 79-87.

Lau, W. and Burns, C., (1973). Kinetics of spreading. Polystyrene melts on plane glass surfaces.*Journal of Colloid and Interface Science*, 45(2), pp.295-302.

Leach, R., (2010). *Fundamental principles of engineering nanometrology*. Oxford: William Andrew. P. 236.

Lienhard J.H. IV and Lienhard J.H. V, (2002). A heat transfer texbook. 3rd ed. Cambridge, U.S.A.: Phlogiston Press. p. 65.

Madhusudana C.V. , (1996). Thermal Contact Resistance.

Manero., F., (1996). Cavity temperature measurement and control in thermoplastics injection moulding. Ph. D. McGill University.

Mantelli, M. B., and Yovanovich, M. M., (2002). Thermal contact resistance. In: David G. Gilmore, 1994. *Spacecraft Thermal Control Handbook, Volume I: Fundamental Technologies.* AAI (American Institute of Aeronautics and Ast; 2 edition), pp. 599-638.

Marotta, E. E. and Fletcher, L. S., (1998). Thermal contact conductance for aluminium and stainless-steel contacts. *Journal of Thermophysics and Heat Transfer,* 12(3), pp. 374-381.

Marotta, E. E., and Fletcher L. S., (1996). Thermal contact conductance of selected polymeric materials. *Journal of Thermophysics and Heat Transfer,* 10(2), pp. 334-342.

Masse, H., Arquis, E., Delaunay, D., Quilliet, S., and Le Bot, P.H., (2004). Heat transfer with mechanically driven thermal contact resistance at the polymer-mold interface in injection molding of polymers. *International Journal of Heat and Mass Transfer,* 47, pp. 2015-2027.

McWaid, T., and Marschall, E., (1992). Thermal contact resistance across pressed metal contacts in a vacuum environment. *International Journal of Heat and Mass Transfer,* 35(11), pp. 2911-2920.

Measurement specialties, (2003). Temperature sensors: advantages and disadvantages, Application note, TD034. Available at: http://www.meas-spec.com/downloads/Temperature_Sensor_Advantages.pdf [Accessed: 19 Feb 2013].

Meiron, T., Marmur, A. and Saguy, I., (2004). Contact angle measurement on rough surfaces.*Journal of Colloid and Interface Science*, 274(2), pp.637-644.

Micronics.net, (2012). Micronics Microfluidics: Lab Automation & Nanotechnology. [online] Available at: http://www.micronics.net/technology [Accessed: 8 Dec 2012].

Mikic, B.B., (1974). Thermal Contact Conductance; Theoretical Considerations. *International Journal of Heat and Mass Transfer*, 17, pp. 205-214.

Montgomery, D., Runger, G. and Hubele, N., (2007). Engineering statistics. Hoboken, NJ: John Wiley. P.342.

Montgomery, R.R. and Sauerwein, J.C., (2011). *NIST SP 260 - 2011 standard reference materials catalog.* Washington, USA: U.S. Goverment Printing Office.

Moses, W. M., and Johson, R. R., (1989). Experimental results for the quasisteady heat transfer through periodically contacting surfaces. *International Journal of Thermophysics,* 3(4), pp. 474-476.

Mtdmicromolding.com, (2012). Ejector Ring. [online] Available at: http://www.mtdmicromolding.com/node/43 [Accessed: 8 Dec 2012].

Murphy, J., (2001). *Additives for plastics handbook*. Oxford, UK: Elsevier Advanced Technology. Pp. 84, 90-92.

Narh, K. A., and Sridhar, L., (1997). Measurement and modeling of thermal contact resistance at a plastic metal interface. ANTEC'97 (Toronto, Canada), pp. 2273-2277.

Narh, K.A., and Sridhar, L., New Jersey Institute of Technology, (2000). *Apparatus and Method for Simultaneously Determining Thermal Conductivity and Thermal Contact Resistance.* U.S. Pat. 6,142,662.

Olympus-ims.com, (2015a). Height Parameters (amplitude mean in the height direction). Available at: http://www.olympus-ims.com/en/knowledge/metrology/roughness/3d_parameter/ [Accessed: 06/052015].

Olympus-ims.com, (2015b). Roughness (3D) parameter. [image online] Available at: http://www.olympus-ims.com/en/knowledge/metrology/roughness/3d_parameter/ [Accessed: 06/052015].

Parihar, Shailendra K., and Wright Neil T., (1997). Thermal contact resistance at elastomer to metal interfaces. *International Communications in Heat and Mass Transfer,* 24(8), pp. 1083-1092.

Peterson, P. P., and Fletcher, L.S., (1988). Evaluation of thermal contact conductance between mold and heat spreader materials. *Journal of Heat Transfer,* 110, pp. 996-998.

Piotter, V., Finnah, G., Hanemann, T., and Ruprecht, R., (2009). Micro Injection molding. In: Kamal, Musa R., 2009. *Injection Molding: Technology and Fundamentals,* Munich, Hanser. pp. 341-389.

Piotter, V., Mueller, K., Plewa, K., Ruprecht, R., and Hausselt J., (2002). Performance and simulation of thermoplastic micro injection molding. *Microsystem technologies*, 8(6), pp. 387-390.

Pocius, A. V., (2002). Adhesion and adhesives technology: an introduction. Munich, Hanser. pp. 94-96.

Priamus, (2013). Cavity pressure sensors type 6008A/6008Ax,x-102, data sheet. Available at: http://www.priamus.com/english/pdf/Datenblaetter_pdf_e/DS6008_069e.pdf [Accessed: 16 Feb 2013].

Reed, R. P., (1999). Thermocouple thermometers. In: Webster, J. G., 1999. *The measurement, instrumentation, and sensors handbook,* Boca Raton, Fla, CRC Press published in cooperation with IEEE Press. pp. 32-41 - 32-53.

Rogers, K., Takacs, E. and Thompson, M., (2005). Contact angle measurement of select compatibilizers for polymer-silicate layer nanocomposites. *Polymer Testing*, 24(4), pp.423-427.

Rosato, D., Rosato, D. and Rosato, M., (2000). *Injection molding handbook*. Boston: Kluwer Academic Publishers. P. 128.

Rosato, D.V., and Rosato, D. V., (2000). injection molding handbook: the complete molding operation, technology, performance, economics. New York, Van Nostrand. pp. 691-692.

Rothon, R., (2003). *Particulate-filled polymer composites*. Shrewsbury, UK: Rapra Technology. Pp.78-81.

Rudawska, A. and Jacniacka, E., (2009). Analysis for determining surface free energy uncertainty by the Owen–Wendt method. *International Journal of Adhesion and Adhesives*, 29(4), pp.451-457.

Rulison, C., (1999). So you want to measure surface energy? KRUSS Technical Note TN306e

Runciman, H. M., (1999). Thermal imaging. In: Webster, J. G., 1999. *The measurement, instrumentation, and sensors handbook,* Boca Raton, Fla, CRC Press published in cooperation with IEEE Press. p. 35-1.

Samant, N. Anoop, B. Dahotre Narendra, (2009). Laser machining of structural ceramics—a review. Journal of the European Ceramic Society, 29 (6), pp. 969–993.

Sandler, S., (1998). *Polymer synthesis and characterization*. San Diego: Academic Press, pp. 120-124.

Sauer, B. and Dee, G., (2002). Surface Tension and Melt Cohesive Energy Density of Polymer Melts Including High Melting and High Glass Transition Polymers. *Macromolecules*, 35(18), pp.7024-7030.

Schick, C., (2009). Differential scanning calorimetry (DSC) of semicrystalline polymers. *Anal Bioanal Chem*, 395(6), pp.1589-1611.

Scholz, S. G., (2011). Micro injection moulding: process monitoring and optimisation. Ph. D. Cardiff University.

Schonhorn, H., (1966). Kinetics of Wetting of Surfaces by Polymer Melts. *J. Appl. Phys.*, 37(13), p.4967.

Silberzan, P. and Leger, L., (1992). Spreading of high molecular weight polymer melts on high-energy surfaces. *Macromolecules*, 25(4), pp.1267-1271.

Smith, B., (2011). *Fundamentals of Fourier transform infrared spectroscopy*. Boca Raton, FL: CRC Press. Pp. 1-8, 41-49.

Snaith, B., Probert, S. D., and O'Callaghan, P.W., (1986). Thermal resistances of pressed contacts. *Journal of Applied Energy,* 22(1), pp. 31-84.

Sommer, R., and Engeler, P., (2005). Piezoelectric pressure sensors. In: Wilson, J. S., 2005. *Sensor technology book,* Amsterdam, Elsevier. pp. 433-457.

Song, S., Yovanovich, M.M., (1988). Relative contact pressure: dependence on surface roughness and Vickers microhardness. *International Journal of Thermophysics,* 2(1), pp. 43-47.

Sovrin.com, (2011a). Medical Devices Manufacturer, brochure. Available at: http://www.sovrin.com/services [Accessed: 8 Dec 2012].

Sovrin.com, (2011b). Wound closure device. [image online] Available at: http://www.sovrin.com/case-studies/micromouldingwound-closure-device [Accessed: 8 Dec 2012].

Sridhar L., (1999). Investigation of Thermal Contact Resistance at a Plastic-Metal Interface in Injection Molding. Ph .D. New Jersey Institute of Technology.

Sridhar, L., and Narh, K. A., (1999). Computer simulation of the effect of thermal contact resistance on cooling in injection molding. *Simulation,* 73(3), pp. 144-148.

Sridhar, L., Sedlak, B. M., and Narh, K. A., (2000). Parametric study of heat transfer in injection molding - effect of thermal contact resistance. *Journal of Manufacturing Science and Engineering,* 122(4), pp. 698-705.

Sridhar, M. R., and Yovanovich, M. M., (1994). Review of elastic and plastic contact conductance models: comparison with experiment. *Journal of Thermophysics and Heat Transfer,* 8(4), pp. 633-640.

Sridhar, M. R., and Yovanovich, M. M., (1996a). Elastoplastic contact conductance model for isotropic conforming rough surfaces and comparison with experiments. *Journal of Heat Transfer,* 18, pp. 3-9.

Sridhar, M. R., and Yovanovich, M. M., (1996b). Thermal contact conductance of tool steel and comparison with model. *International Journal of Heat and Mass Transfer,* 39(4), pp. 831-839.

Stalder, A., Kulik, G., Sage, D., Barbieri, L. and Hoffmann, P., (2006). A snake-based approach to accurate determination of both contact points and contact angles. *Colloids and Surfaces A: Physicochemical and Engineering Aspects*, 286(1-3), pp.92-103.

Stemmer Imaging GmbH, (2010). The imaging and vision handbook. Puchheim, SIS STEMMER IMAGING Services GmbH. pp. 152-153.

Stuart, B., (2004). Infrared spectroscopy. Chichester, Eng.: J. Wiley, pp. 5-10.

Sunil Kumar, S. and Ramamurthi, K., (2003). Influence of flatness and waviness of rough surfaces on surface contact conductance. *Journal of Heat Transfer,* 125(3), pp. 394-402.

Support.minitab.com, (2015). Minitab 17 Support - Minitab. [online] Available at: http://support.minitab.com/en-us/minitab/17/ [Accessed 15.08.2015].

Surace, R.,Trotta, G., Bellantone, V. And Fassi, I., (2012). Chapter 4: The micro injection moulding process for polymeric components manufacturing. In: Volosencu, C., 2012. New technologies - trends, innovations and research. 1st ed. Rijeka, InTech. pp 67-68.

TA Instruments, (2013). TRIOS Online Help.

Thermo Scientific, (no date). Transmission sampling techniques in OMNIC 9 software help files.

Unger, P., (2006). Gastrow injection molds. Munich, Hanser. pp. 23-29.

Van Anda, J., (no date). IR technology parameters and tradeoffs, technical notes (14). Available at: http://gs.flir.com/uploads/file/tech-

notes/tech%20note14%20-%20ir%20technology%20parameters.pdf [Accessed: 15 Apr 2013].

Vollmer, M, and Mollman, K.-P., (2010). Infrared Thermal Imaging: Fundamental, research and Applications. Weinheim, Wiley-VCH Verlag GmbH & Co. pp. 101-105, 108-114, 139-142, 150-154, 160.

Vorburger T. V., Raja J., (1990). Surface Finish Metrology Tutorial (NISTIR 89-4088), U.S. Department of Commerce, National Institute of Standards and Technology. pp. 1-4.

Wahid, Syed M.S., and Madhusudana C.V., (2000). Gap conductance in contact heat transfer. *International Journal of Heat and Mass Transfer,* 43, pp. 4483-4487.

Watlow Ltd, (2013). FIREROD cartridge heaters, specifications sheet. Available at: http://www.watlow.co.uk/downloads/en/specsheets/stlfrc0413.pdf [Accessed: 16 Apr 2013].

Whiteside, B. R., Martyn M. T., Coates P. D., Greenway, G., Allen, P., and Hornsbury, P., (2003). Micromoulding: process characteristics and product properties. *Plastics, Rubber and Composites,* 32(6), pp. 231-239.

Whiteside, B. R., Martyn, M. T., and Coates P. D., (2006). Introduction to micromolding. In: Greener, J., and Wimberger-Friedl, R., 2006. *Precision Injection Molding: Process, Materials, and Applications,* Munich, Hanser. pp. 239-264.

Wu, S., (1982). *Polymer interface and adhesion*. New York: M. Dekker. pp.11-12.

Yu, Chi J., Sunderland, J. E., and Poli, C., (1990). Thermal contact resistance in injection molding. *Polymer Engineering and Science,* 30(24), pp. 1599-1606.

Zenkiewicz, M., (2007). Methods for the calculation of surface free energy of solids. *Journal of Achievements in Materials and Manufacturing Engineering*, 24(1), pp. 137-145.

Zhang, X., Cong, P. Z. and Fujii, M., (2006). A study on thermal contact resistance at the interface of two solids. *International Journal of Thermophysics,* 27(3), pp. 880-895.

Zhao, J., Chen, G., and Juay, Y. K., (2003). Development of process monitoring technologies for polymer micro moulding process. Available at: http://citeseerx.ist.psu.edu/viewdoc/download?doi=10.1.1.2.609&rep=rep1&type=pdf [Accessed: 14 Feb 2013].

Zhou, H. (2013). *Computer modeling for injection molding*. Hoboken, N.J.: Wiley. p. 245

Appendix 1: Publications

Bigot, S., Lacan, F., Hirshy, H, Petkov, P.V., Babenko, M., González Castro, G., Sweeney, J., Ugail, H. and Whiteside, B.R., 2014. Micro and Nano Structuring of Sapphire for Micro Injection Process Investigation. *9th International Conference on MicroManufacturing* (Nanyang Technological University (NTU) and National University of Singapore, Singapore).

Babenko, M., Whiteside, B.R, Sweeney, J., González Castro, G., Norris, K., and Bigot S., 2014. Estimation of Thermal Contact Conductance at Polymer Melt and Mold surface interface in microinjection molding. *30th International Conference of the Polymer Processing Society (*Cleveland, Ohio, USA).

Babenko, M., Whiteside, B.R., Norris, K., González Castro, G., Sweeney, J., and Bigot S., 2013. Temperature Measurements at the Polymer Melt and Mould Cavity Interface Using High Speed Thermal Camera. *Polymer Processing Engineering 13.* The University of Bradford.

Babenko, M., Whiteside, B.R., Norris, K., González Castro, G., Sweeney, J., and Coates P.D., 2013. The Usage of Thermal Imaging for Temperature Measurements during Microinjection Moulding. *10th International Conference on Multi-Material Micro Manufacture* (San Sebastián, Spain), pp. 69-72.

Whiteside, B.R., Babenko, M., Norris, K., González Castro, G., Sweeney, J., Bigot, S. and Coates P.D., 2013. High Speed Visualisation of Cooling Phenomena in Micromoudling Processes. *29th International Conference of the Polymer Processing Society (*Nuremberg, Germany).

González Castro, G., Babenko, M., Bigot, S., Sweeney, J., Ugail, H. and Whiteside B.R., 2011. Thermal Contact Resistance in Micromoulding. *Polymer Processing Engineering 11: Enhanced Polymer Processing*, The University of Bradford, pp.236-250.

Appendix: 2 Effect of Carbon Black Masterbatch on C_p - Two-sample T-test Results

PP and CB PP

Two-Sample T-Test and CI: 16.85, 16.85_1

```
Two-sample T for 16.85 vs 16.85_1

          N    Mean   StDev  SE Mean
16.85     3  1.4404  0.0165   0.0095
16.85_1   3  1.6240  0.0319    0.018


Difference = mu (16.85) - mu (16.85_1)
Estimate for difference:  -0.1836
95% CI for difference:  (-0.2728, -0.0944)
T-Test of difference = 0 (vs not =): T-Value = -8.86  P-Value = 0.013  DF = 2
```

Two-Sample T-Test and CI: 26.85, 26.85_1

```
Two-sample T for 26.85 vs 26.85_1

          N    Mean   StDev  SE Mean
26.85     3  1.5060  0.0173    0.010
26.85_1   3  1.6908  0.0305    0.018


Difference = mu (26.85) - mu (26.85_1)
Estimate for difference:  -0.1848
95% CI for difference:  (-0.2493, -0.1203)
T-Test of difference = 0 (vs not =): T-Value = -9.12  P-Value = 0.003  DF = 3
```

Two-Sample T-Test and CI: 36.85, 36.85_1

```
Two-sample T for 36.85 vs 36.85_1

          N    Mean   StDev  SE Mean
36.85     3  1.5710  0.0160   0.0093
36.85_1   3  1.7645  0.0319    0.018


Difference = mu (36.85) - mu (36.85_1)
Estimate for difference:  -0.1935
95% CI for difference:  (-0.2821, -0.1048)
T-Test of difference = 0 (vs not =): T-Value = -9.39  P-Value = 0.011  DF = 2
```

Two-Sample T-Test and CI: 46.85, 46.85_1

```
Two-sample T for 46.85 vs 46.85_1

          N    Mean   StDev  SE Mean
46.85     3  1.6507  0.0142   0.0082
46.85_1   3  1.8534  0.0321    0.019
```

```
Difference = mu (46.85) - mu (46.85_1)
Estimate for difference:  -0.2027
95% CI for difference:  (-0.2899, -0.1155)
T-Test of difference = 0 (vs not =): T-Value = -10.00  P-Value = 0.010  DF = 2
```

Two-Sample T-Test and CI: 56.85, 56.85_1

```
Two-sample T for 56.85 vs 56.85_1

         N    Mean   StDev  SE Mean
56.85    3  1.7412  0.0111   0.0064
56.85_1  3  1.9443  0.0263    0.015


Difference = mu (56.85) - mu (56.85_1)
Estimate for difference:  -0.2031
95% CI for difference:  (-0.2740, -0.1323)
T-Test of difference = 0 (vs not =): T-Value = -12.34  P-Value = 0.007  DF = 2
```

Two-Sample T-Test and CI: 66.85, 66.85_1

```
Two-sample T for 66.85 vs 66.85_1

         N     Mean    StDev  SE Mean
66.85    3  1.83429  0.00881   0.0051
66.85_1  3   2.0408   0.0239    0.014


Difference = mu (66.85) - mu (66.85_1)
Estimate for difference:  -0.2065
95% CI for difference:  (-0.2698, -0.1432)
T-Test of difference = 0 (vs not =): T-Value = -14.04  P-Value = 0.005  DF = 2
```

Two-Sample T-Test and CI: 76.85, 76.85_1

```
Two-sample T for 76.85 vs 76.85_1

         N     Mean    StDev  SE Mean
76.85    3  1.92977  0.00530   0.0031
76.85_1  3   2.1409   0.0213    0.012


Difference = mu (76.85) - mu (76.85_1)
Estimate for difference:  -0.2111
95% CI for difference:  (-0.2655, -0.1567)
T-Test of difference = 0 (vs not =): T-Value = -16.69  P-Value = 0.004  DF = 2
```

Two-Sample T-Test and CI: 86.85, 86.85_1

```
Two-sample T for 86.85 vs 86.85_1

         N     Mean    StDev  SE Mean
86.85    3  2.03140  0.00633   0.0037
86.85_1  3   2.2485   0.0197    0.011
```

```
Difference = mu (86.85) - mu (86.85_1)
Estimate for difference:  -0.2171
95% CI for difference:  (-0.2684, -0.1658)
T-Test of difference = 0 (vs not =): T-Value = -18.21  P-Value = 0.003  DF = 2
```

Two-Sample T-Test and CI: 96.85, 96.85_1

```
Two-sample T for 96.85 vs 96.85_1

         N     Mean    StDev  SE Mean
96.85    3  2.15037  0.00470   0.0027
96.85_1  3   2.3691   0.0186    0.011


Difference = mu (96.85) - mu (96.85_1)
Estimate for difference:  -0.2187
95% CI for difference:  (-0.2664, -0.1711)
T-Test of difference = 0 (vs not =): T-Value = -19.75  P-Value = 0.003  DF = 2
```

Two-Sample T-Test and CI: 106.85, 106.85_1

```
Two-sample T for 106.85 vs 106.85_1

          N     Mean    StDev  SE Mean
106.85    3  2.29962  0.00470   0.0027
106.85_1  3   2.4742   0.0175    0.010


Difference = mu (106.85) - mu (106.85_1)
Estimate for difference:  -0.1745
95% CI for difference:  (-0.2196, -0.1295)
T-Test of difference = 0 (vs not =): T-Value = -16.66  P-Value = 0.004  DF = 2
```

Two-Sample T-Test and CI: 176.85, 176.85_1

```
Two-sample T for 176.85 vs 176.85_1

          N    Mean   StDev  SE Mean
176.85    3  2.4703  0.0235    0.014
176.85_1  3  2.6288  0.0126   0.0073


Difference = mu (176.85) - mu (176.85_1)
Estimate for difference:  -0.1585
95% CI for difference:  (-0.2075, -0.1094)
T-Test of difference = 0 (vs not =): T-Value = -10.29  P-Value = 0.002  DF = 3
```

Two-Sample T-Test and CI: 186.85, 186.85_1

```
Two-sample T for 186.85 vs 186.85_1

          N     Mean    StDev  SE Mean
186.85    3   2.4868   0.0135   0.0078
186.85_1  3  2.65625  0.00895   0.0052
```

```
Difference = mu (186.85) - mu (186.85_1)
Estimate for difference:  -0.16947
95% CI for difference:  (-0.19916, -0.13978)
T-Test of difference = 0 (vs not =): T-Value = -18.16  P-Value = 0.000  DF = 3
```

PS and CB PS

Two-Sample T-Test and CI: 16.84, 16.84_1

```
Two-sample T for 16.84 vs 16.84_1

          N    Mean   StDev  SE Mean
16.84     3  1.1874  0.0155   0.0089
16.84_1   3  1.1789  0.0235    0.014


Difference = mu (16.84) - mu (16.84_1)
Estimate for difference:  0.0084
95% CI for difference:  (-0.0432, 0.0601)
T-Test of difference = 0 (vs not =): T-Value = 0.52  P-Value = 0.639  DF = 3
```

Two-Sample T-Test and CI: 26.84, 26.84_1

```
Two-sample T for 26.84 vs 26.84_1

          N    Mean   StDev  SE Mean
26.84     3  1.2311  0.0166   0.0096
26.84_1   3  1.2245  0.0235    0.014


Difference = mu (26.84) - mu (26.84_1)
Estimate for difference:  0.0066
95% CI for difference:  (-0.0462, 0.0595)
T-Test of difference = 0 (vs not =): T-Value = 0.40  P-Value = 0.716  DF = 3
```

Two-Sample T-Test and CI: 36.84, 36.84_1

```
Two-sample T for 36.84 vs 36.84_1

          N    Mean   StDev  SE Mean
36.84     3  1.2761  0.0161   0.0093
36.84_1   3  1.2694  0.0231    0.013


Difference = mu (36.84) - mu (36.84_1)
Estimate for difference:  0.0067
95% CI for difference:  (-0.0450, 0.0584)
T-Test of difference = 0 (vs not =): T-Value = 0.41  P-Value = 0.709  DF = 3
```

Two-Sample T-Test and CI: 46.84, 46.84_1

```
Two-sample T for 46.84 vs 46.84_1

          N    Mean   StDev  SE Mean
```

```
46.84    3  1.3206  0.0169   0.0098
46.84_1  3  1.3178  0.0211    0.012


Difference = mu (46.84) - mu (46.84_1)
Estimate for difference:  0.0028
95% CI for difference:  (-0.0469, 0.0526)
T-Test of difference = 0 (vs not =): T-Value = 0.18  P-Value = 0.868  DF = 3
```

Two-Sample T-Test and CI: 56.84, 56.84_1

```
Two-sample T for 56.84 vs 56.84_1

         N    Mean   StDev  SE Mean
56.84    3  1.3626  0.0180    0.010
56.84_1  3  1.3656  0.0226    0.013


Difference = mu (56.84) - mu (56.84_1)
Estimate for difference:  -0.0030
95% CI for difference:  (-0.0560, 0.0501)
T-Test of difference = 0 (vs not =): T-Value = -0.18  P-Value = 0.869  DF = 3
```

Two-Sample T-Test and CI: 66.84, 66.84_1

```
Two-sample T for 66.84 vs 66.84_1

         N    Mean   StDev  SE Mean
66.84    3  1.4098  0.0192    0.011
66.84_1  3  1.4183  0.0226    0.013


Difference = mu (66.84) - mu (66.84_1)
Estimate for difference:  -0.0085
95% CI for difference:  (-0.0631, 0.0460)
T-Test of difference = 0 (vs not =): T-Value = -0.50  P-Value = 0.653  DF = 3
```

Two-Sample T-Test and CI: 76.84, 76.84_1

```
Two-sample T for 76.84 vs 76.84_1

         N    Mean   StDev  SE Mean
76.84    3  1.4586  0.0193    0.011
76.84_1  3  1.4768  0.0218    0.013


Difference = mu (76.84) - mu (76.84_1)
Estimate for difference:  -0.0181
95% CI for difference:  (-0.0717, 0.0354)
T-Test of difference = 0 (vs not =): T-Value = -1.08  P-Value = 0.360  DF = 3
```

Two-Sample T-Test and CI: 86.84, 86.84_1

```
Two-sample T for 86.84 vs 86.84_1

         N    Mean   StDev  SE Mean
86.84    3  1.5159  0.0204    0.012
```

```
86.84_1  3  1.5415  0.0220    0.013


Difference = mu (86.84) - mu (86.84_1)
Estimate for difference:  -0.0256
95% CI for difference:  (-0.0808, 0.0296)
T-Test of difference = 0 (vs not =): T-Value = -1.48  P-Value = 0.237  DF = 3
```

Two-Sample T-Test and CI: 106.84, 106.84_1

```
Two-sample T for 106.84 vs 106.84_1

          N    Mean   StDev  SE Mean
106.84    3  1.8856  0.0195    0.011
106.84_1  3  1.8572  0.0273    0.016


Difference = mu (106.84) - mu (106.84_1)
Estimate for difference:  0.0283
95% CI for difference:  (-0.0333, 0.0900)
T-Test of difference = 0 (vs not =): T-Value = 1.46  P-Value = 0.240  DF = 3
```

Two-Sample T-Test and CI: 116.84, 116.84_1

```
Two-sample T for 116.84 vs 116.84_1

          N    Mean   StDev  SE Mean
116.84    3  1.9098  0.0212    0.012
116.84_1  3  1.8717  0.0264    0.015


Difference = mu (116.84) - mu (116.84_1)
Estimate for difference:  0.0381
95% CI for difference:  (-0.0242, 0.1004)
T-Test of difference = 0 (vs not =): T-Value = 1.95  P-Value = 0.147  DF = 3
```

Two-Sample T-Test and CI: 126.84, 126.84_1

```
Two-sample T for 126.84 vs 126.84_1

          N    Mean   StDev  SE Mean
126.84    3  1.9423  0.0223    0.013
126.84_1  3  1.9047  0.0277    0.016


Difference = mu (126.84) - mu (126.84_1)
Estimate for difference:  0.0375
95% CI for difference:  (-0.0278, 0.1028)
T-Test of difference = 0 (vs not =): T-Value = 1.83  P-Value = 0.165  DF = 3
```

Two-Sample T-Test and CI: 136.84, 136.84_1

```
Two-sample T for 136.84 vs 136.84_1

          N    Mean   StDev  SE Mean
136.84    3  1.9733  0.0225    0.013
136.84_1  3  1.9358  0.0289    0.017
```

```
Difference = mu (136.84) - mu (136.84_1)
Estimate for difference:  0.0375
95% CI for difference:  (-0.0298, 0.1049)
T-Test of difference = 0 (vs not =): T-Value = 1.77  P-Value = 0.174  DF = 3
```

Two-Sample T-Test and CI: 146.84, 146.84_1

```
Two-sample T for 146.84 vs 146.84_1

          N    Mean   StDev  SE Mean
146.84    3  2.0028  0.0273    0.016
146.84_1  3  1.9665  0.0293    0.017


Difference = mu (146.84) - mu (146.84_1)
Estimate for difference:  0.0363
95% CI for difference:  (-0.0373, 0.1098)
T-Test of difference = 0 (vs not =): T-Value = 1.57  P-Value = 0.215  DF = 3
```

Two-Sample T-Test and CI: 156.84, 156.84_1

```
Two-sample T for 156.84 vs 156.84_1

          N    Mean   StDev  SE Mean
156.84    3  2.0358  0.0287    0.017
156.84_1  3  1.9987  0.0282    0.016


Difference = mu (156.84) - mu (156.84_1)
Estimate for difference:  0.0371
95% CI for difference:  (-0.0368, 0.1111)
T-Test of difference = 0 (vs not =): T-Value = 1.60  P-Value = 0.208  DF = 3
```

Two-Sample T-Test and CI: 166.84, 166.84_1

```
Two-sample T for 166.84 vs 166.84_1

          N    Mean   StDev  SE Mean
166.84    3  2.0721  0.0284    0.016
166.84_1  3  2.0346  0.0227    0.013


Difference = mu (166.84) - mu (166.84_1)
Estimate for difference:  0.0374
95% CI for difference:  (-0.0294, 0.1043)
T-Test of difference = 0 (vs not =): T-Value = 1.78  P-Value = 0.173  DF = 3
```

Two-Sample T-Test and CI: 176.84, 176.84_1

```
Two-sample T for 176.84 vs 176.84_1

          N    Mean   StDev  SE Mean
176.84    3  2.1036  0.0291    0.017
176.84_1  3  2.0696  0.0201    0.012
```

```
Difference = mu (176.84) - mu (176.84_1)
Estimate for difference:  0.0340
95% CI for difference:  (-0.0310, 0.0990)
T-Test of difference = 0 (vs not =): T-Value = 1.67  P-Value = 0.194  DF = 3
```

Two-Sample T-Test and CI: 186.84, 186.84_1

```
Two-sample T for 186.84 vs 186.84_1

          N    Mean   StDev  SE Mean
186.84    3  2.1322  0.0289    0.017
186.84_1  3  2.0998  0.0160   0.0093


Difference = mu (186.84) - mu (186.84_1)
Estimate for difference:  0.0324
95% CI for difference:  (-0.0282, 0.0931)
T-Test of difference = 0 (vs not =): T-Value = 1.70  P-Value = 0.188  DF = 3
```

Two-Sample T-Test and CI: 196.84, 196.84_1

```
Two-sample T for 196.84 vs 196.84_1

          N    Mean   StDev  SE Mean
196.84    3  2.1570  0.0278    0.016
196.84_1  3  2.1277  0.0134   0.0078


Difference = mu (196.84) - mu (196.84_1)
Estimate for difference:  0.0293
95% CI for difference:  (-0.0474, 0.1059)
T-Test of difference = 0 (vs not =): T-Value = 1.64  P-Value = 0.242  DF = 2
```

Two-Sample T-Test and CI: 206.84, 206.84_1

```
Two-sample T for 206.84 vs 206.84_1

          N     Mean    StDev  SE Mean
206.84    3   2.1843   0.0254    0.015
206.84_1  3  2.15689  0.00912   0.0053


Difference = mu (206.84) - mu (206.84_1)
Estimate for difference:  0.0274
95% CI for difference:  (-0.0396, 0.0945)
T-Test of difference = 0 (vs not =): T-Value = 1.76  P-Value = 0.220  DF = 2
```

Appendix 3: 1D Finite Difference Model of the Heat Transfer

For time t, distance x and temperature u, the heat flow equation in one dimension is given by (O'Neil 2012)

$$C\frac{\partial u}{\partial t} = K\frac{\partial^2 u}{\partial x^2} \qquad (1)$$

where C is the product of specific heat and density (i.e. the specific heat in terms of material volume) and K is the conductivity, assumed in this case to be constant with respect to x. More generally, we may write

$$C\frac{\partial u}{\partial t} = \frac{\partial^2}{\partial x^2}(Ku) \qquad (2)$$

which applies when K varies with x.

The model consists of three material layers a, b and c, each with constant C and K, with values C_a, C_b, C_c and K_a, K_b, K_c respectively. Each of the three layers a, b and c is divided into a number of equal intervals, respectively L, M and N, which are of lengths Δx_a, Δx_b, and Δx_c. The model is illustrated in Figure 1. The integer i represents a generic point and varies

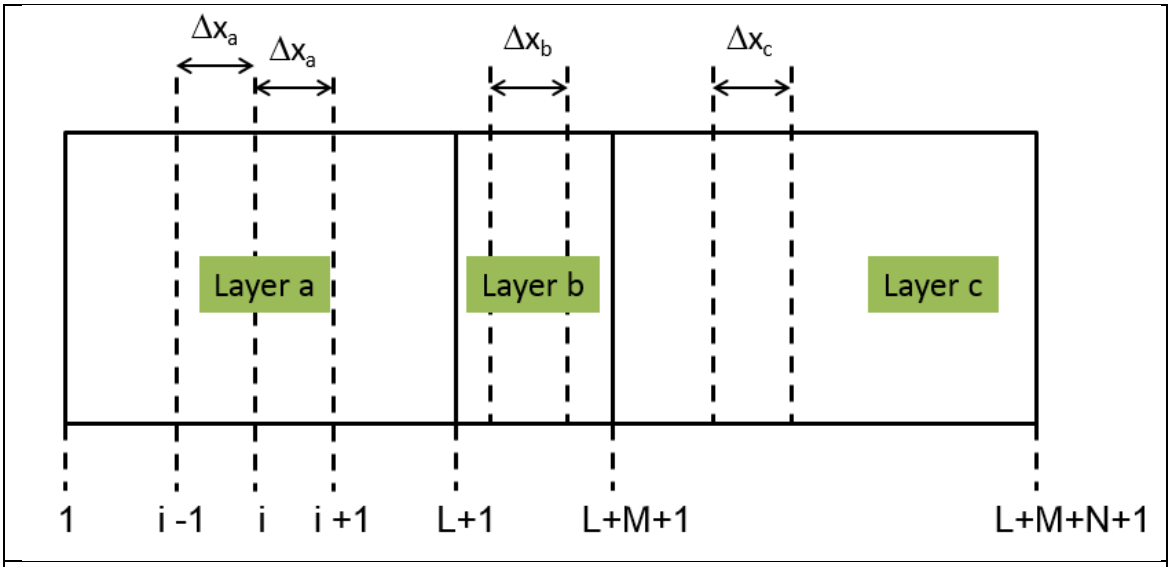

Figure 1. Diagram of model

between 1 and L+M+N+1. At the point i, the current temperature at time t is u_i and the temperature in the immediately previous time, t - Δt, is $\bar{u}_i$. We use first differences in time and the second derivative midpoint formula (Burden and Faires 2011) in x to approximate equations (1) and (2) with finite difference expressions. When the point i is not at a boundary or interface (i.e. for values other than 1, L+1, L+M+1 and L+M+N+1) or at i = 2 (see below) equation (1) is used to create the difference equation

$$C\frac{u_i - \bar{u}_i}{\Delta t} = K\frac{u_{i+1} - 2u_i + u_{i-1}}{\Delta x^2} \qquad (3)$$

where C = C_a, C_b, or C_c; K = K_a, K_b, or K_c ;and $\Delta x = \Delta x_a$, Δx_b, or Δx_c., depending on whether the point i is in layer a, b or c.

At the interface between a and b (i.e. i = L+1) equation (2) is adapted similarly, but the second derivative is approximated having regard to the nonconstant conductivities:

$$C\frac{u_{L+1}-\bar{u}_{L+1}}{\Delta t}=\frac{K_b(u_{L+2}-u_{L+1})/\Delta x_b-K_a(u_{L+1}-u_L)/\Delta x_a}{(\Delta x_a+\Delta x_b)/2} \qquad (4)$$

where C is the weighted average

$$C=(\Delta x_a C_a+\Delta x_b C_b)/(\Delta x_a+\Delta x_b) \qquad (5)$$

Similarly, at the interface between layers b and c

$$C\frac{u_{L+M+1}-\bar{u}_{L+M+1}}{\Delta t}=\frac{K_c(u_{L+M+2}-u_{L+M+1})/\Delta x_c-K_b(u_{L+M+1}-u_{L+M})/\Delta x_b}{(\Delta x_b+\Delta x_c)/2} \qquad (6)$$

where

$$C=(\Delta x_b C_b+\Delta x_c C_c)/(\Delta x_b+\Delta x_c) \qquad (7)$$

Equations (3), (4) and (6) relate the current unknown temperatures u_i to the known previous temperatures $\bar{u}_i$ and form a set of simultaneous equations. Equation (3) becomes

$$-u_{i-1}+\left(2+\frac{C\Delta x^2}{K\Delta t}\right)u_i-u_{i+1}=\frac{C\Delta x^2}{K\Delta t}\bar{u}_i \qquad (8)$$

The coefficients of the current temperatures are assigned to elements of vectors $D1_i$, $D2_i$ and $D3_i$, and the right hand sides are assigned to the vector R_i such that (8) becomes

$$D3_{i-1}u_{i-1}+D2_i u_i+D1_{i+1}u_{i+1}=R_i \qquad (9)$$

In the model the layers a, b and c represent respectively the polymer melt, interface and sapphire. The model is of half the mould with the left-hand boundary i = 1 the symmetry boundary. Here, the derivative $\frac{\partial u}{\partial x}=0$ and this is represented as $u_2=u_1$. The first equation (8) then corresponds to i = 2 and becomes

$$\left(1+\frac{C\Delta x^2}{K\Delta t}\right)u_2-u_3=\frac{C\Delta x^2}{K\Delta t}\bar{u}_2 \qquad (10)$$

or alternatively

$$D2_2 u_2+D1_3 u_3=R_2 \qquad (11)$$

where

$$
\begin{aligned}
D2_2 &= 1+\frac{C_a\Delta x_a^2}{K_a\Delta t}\\
D1_3 &= -1\\
R_2 &= \frac{C_a\Delta x_a^2}{K_a\Delta t}\bar{u}_2
\end{aligned}
\qquad (12)
$$

For the remainder of the layer a, inspection of equations (8) and (9) gives for equation (9)

$$
\begin{aligned}
D1_i &= -1,\ 4 \le i \le L+1\\
D2_i &= 2+\frac{C_a\Delta x_a^2}{K_a\Delta t},\ 3 \le i \le L\\
D3_i &= -1,\ 2 \le i \le L-1\\
R_i &= \frac{C_a\Delta x_a^2}{K_a\Delta t}\bar{u}_i,\ 3 \le i \le L
\end{aligned}
\qquad (13)
$$

At the interface i = L+1, equation (4) applies. This can be rewritten as

$$
-u_L\frac{K_a\Delta x_b}{K_b\Delta x_a}+\left(\frac{K_a\Delta x_b}{K_b\Delta x_a}+1+\frac{C\Delta x_b(\Delta x_a+\Delta x_b)}{2K_b\Delta t}\right)u_{L+1}-u_{L+2}=\frac{C\Delta x_b(\Delta x_a+\Delta x_b)}{2K_b\Delta t}\bar{u}_{L+1}
\qquad (14)
$$

where C is given by equation (5). It is now in the form of equation (9), with

$$
D3_L u_L + D2_{L+1}u_{L+1} + D1_{L+2}u_{L+2} = R_{L+1}
\qquad (15)
$$

Comparison of equations (14) and (15) gives expressions for the vector coefficients.

In the layer b the coefficients of (9) are given as

$$
\begin{aligned}
D1_i &= -1,\ L+2 \le i \le L+M+1\\
D2_i &= 2+\frac{C_b\Delta x_b^2}{K_b\Delta t},\ L+1 \le i \le L+M\\
D3_i &= -1,\ L \le i \le L+M-1\\
R_i &= \frac{C_b\Delta x_b^2}{K_b\Delta t}\bar{u}_i,\ L+1 \le i \le L+M
\end{aligned}
\qquad (16)
$$

At the interface i = L+M+1, equation (6) applies. This can be rewritten as

$$
-u_{L+M}\frac{K_b\Delta x_c}{K_c\Delta x_b}+\left(\frac{K_b\Delta x_c}{K_c\Delta x_b}+1+\frac{C\Delta x_c(\Delta x_b+\Delta x_c)}{2K_c\Delta t}\right)u_{L+M+1}-u_{L+M+2}=\frac{C\Delta x_c(\Delta x_b+\Delta x_c)}{2K_c\Delta t}\bar{u}_{L+M+1}
\qquad (17)
$$

where C is given by equation (7). It is now in the form of equation (9), with

$$
D3_{L+M}u_{L+M} + D2_{L+M+1}u_{L+M+1} + D1_{L+M+2}u_{L+M+2} = R_{L+M+1}
\qquad (18)
$$

Comparison of equations (17) and (18) gives expressions for the vector coefficients.

In the layer c, the right-hand boundary i = L+M+N+1 is assumed to lose heat to the atmosphere by convection. The heat flux at the boundary is assumed to be proportional to the difference in temperature between the boundary and the air, the latter assumed to be at temperature u_a. The condition takes the form

$$K_c \frac{\partial u}{\partial x} = -\beta(u - u_a) \tag{19}$$

where β is a constant of proportionality. As a difference equation this becomes

$$K_c \left(\frac{u_{L+M+N+1} - u_{L+M+N}}{\Delta x_c} \right) = -\beta(u_{L+M+N+1} - u_a) \tag{20}$$

which becomes

$$-u_{L+M+N} + \left(1 + \frac{\beta \Delta x_c}{K_c} \right) u_{L+M+N+1} = \frac{\beta \Delta x_c}{K_c} u_a \tag{21}.$$

For the interior of layer c equation (9) applies with the coefficients given by

$$\begin{aligned}
&D1_i = -1, \quad L+M+3 \le i \le L+M+N+1 \\
&D2_i = 2 + \frac{C_c \Delta x_c^2}{K_c \Delta t}, \quad L+M+2 \le i \le L+M+N \\
&D3_i = -1, \quad L+M+1 \le i \le L+M+N-1 \\
&R_i = \frac{C_c \Delta x_c^2}{K_c \Delta t} \bar{u}_i, \quad L+M+2 \le i \le L+M+N
\end{aligned} \tag{22}.$$

Finally we complete the definition of the coefficients by rewriting equation (21) as

$$D3_{L+M+N} u_{L+M+N} + D2_{L+M+N+1} u_{L+M+N+1} = R_{L+M+N+1} \tag{23}$$

where

$$\begin{aligned}
&D3_{L+M+N} = -1 \\
&D2_{L+M+N+1} = 1 + \frac{\beta \Delta x_c}{K_c} \\
&R_{L+M+N+1} = \frac{\beta \Delta x_c}{K_c} u_a
\end{aligned} \tag{24}$$

We may now write the set of equations (9), (11), (15), (18) and (23) in matrix form:

$$\begin{bmatrix} D2_2 & D1_3 & 0 & 0 & . & . & .0 & 0 & 0 & 0 \\ D3_2 & D2_3 & D1_4 & 0 & & & & & 0 & 0 \\ 0 & D3_3 & D2_4 & D1_5 & & & & & & 0 \\ 0 & 0 & D3_4 & . & & & & & & . \\ 0 & & & & . & & & & & . \\ 0 & & & & & . & & & & . \\ . & & & & & & & & & 0 \\ . & & & & & & & D2_{L+M+N-1} & & 0 \\ 0 & & & & & & & D3_{L+M+N-1} & D2_{L+M+N} & D1_{L+M+N+1} \\ 0 & 0 & . & . & . & . & . & 0 & D3_{L+M+N} & D2_{L+M+N+1} \end{bmatrix} \begin{bmatrix} u_2 \\ u_3 \\ u_4 \\ . \\ . \\ . \\ . \\ u_{L+M+N-1} \\ u_{L+M+N} \\ u_{L+M+N+1} \end{bmatrix} = \begin{bmatrix} R_2 \\ R_3 \\ R_4 \\ . \\ . \\ . \\ . \\ R_{L+M+N-1} \\ R_{L+M+N} \\ R_{L+M+N+1} \end{bmatrix}$$

(25)

The system was solved by performing row and column operations to produce an upper-triangular left-hand matrix, and then performing Gaussian elimination (Burden and Faires 2011).

The method was programmed in FORTRAN 90. Runtime was insignificant and resources negligible. Initial conditions were set as constant temperatures in the three layers. Temperature dependence in K and C was introduced by making these quantities functions of $\bar{u}_i$ and running the process iteratively.

References

O'Neil PV, *Advanced Engineering Mathematics*, 7th Edn. Cengage Learning International Edition 2012.

Burden RL, Faires JD, Numerical Analysis. 9th Edn. Brookes/Cole Cengage Learning, Boston MA 2011